Hydrodynamic Forces on Pusher-Barge Convoys in Deep and Shallow Water

Von der Fakultät für Ingenieurwissenschaften, Abteilung Maschinenbau und Verfahrenstechnik

der

Universität Duisburg-Essen

zur Erlangung des akademischen Grades

eines

Doktors der Ingenieurwissenschaften

Dr.-Ing.

genehmigte Dissertation

von

Lahbib Zentari
aus
Azrou, Marokko

Gutachter: Univ.-Prof. Dr.-Ing. Bettar Ould el Moctar
Prof. Dr.-Ing. Milovan Perić

Tag der mündlichen Prüfung: 19. September 2023

Abstract

The present thesis focuses on experimental and numerical investigations of hydrodynamic forces and moments acting on pusher-barge convoys in deep and shallow waters. For this purpose, a typical inland waterway pushed convoy was designed and tested in three representative configurations. The experimental tests consisting of captive tests such as resistance and propulsion tests, steady drift variation tests, and steady rudder variation tests were conducted in both deep and shallow waters. Furthermore, optical measurements were performed to capture and analyze the complex flow pattern in the gap between the pusher and a barge under deep and shallow water conditions. The experimental results were used to define the limits and validate the numerical methods

In this work, a numerical procedure based on the Reynolds Averaged Navier-Stokes equations was used to gain insight into the complex flow around multibody ships in deep and shallow waters. In general, numerical and measured hydrodynamic forces and moments agreed favorably. Furthermore, two-equation turbulence models and Improved Delayed Detached Eddy Simulation technique were used to predict the gap flow in deep and shallow waters. The latter technique was found to be the most reliable, especially for predicting the velocity field in fully separated flow regions. The extensive and systematic experimental and numerical investigations showed that the water depth restriction has major effects on the hydrodynamic performance of such multibody ships.

Zusammenfassung

Die vorliegende Arbeit befasst sich mit experimentellen und numerischen Untersuchungen der hydrodynamischen Kräfte und Momente, die auf Schubverbände in tiefen und flachen Gewässern wirken. Zu diesem Zweck wurde ein für die Binnenschifffahrt typischer Schubverband entworfen und in drei repräsentativen Konfigurationen getestet. Die experimentellen Versuche, bestehend aus Widerstands- und Propulsionsversuchen, Schrägschleppversuchen und Rudervariationsversuchen, wurden sowohl in tiefen als auch in flachen Gewässern durchgeführt. Zusätzlich wurden optische Messverfahren eingesetzt, um das komplexe Strömungsfeld in der Spalte zwischen Schubschiff und Leichter unter Tiefen- und Flachwasserbedingungen zu erfassen und zu analysieren. Die experimentellen Ergebnisse wurden zur Validierung der numerischen Methoden verwendet.

In dieser Arbeit wurde eine numerische Methode auf der Grundlage der Reynolds-gemittelten-Navier-Stokes-Gleichungen verwendet, um einen detaillierten Einblick in die komplexe Strömung um Schubverbände in tiefen und flachen Gewässern zu erhalten. Im Allgemeinen stimmten die numerischen und gemessenen hydrodynamischen Kräfte und Momente gut überein. Es wurden Zweigleichungs-Turbulenzmodelle und die Improved Delayed-Detached Eddy Simulation Technik zur Vorhersage der Spaltströmung in tiefen und flachen Gewässern verwendet. Die letztgenannte Methode erwies sich als die zuverlässigste, insbesondere für die Vorhersage des Geschwindigkeitsfeldes in vollständig abgelösten Strömungsbereichen. Die umfangreichen und systematischen experimentellen und numerischen Untersuchungen haben gezeigt, dass die Einschränkung der Wassertiefe einen bedeutenden Einfluss auf das hydrodynamische Verhalten solcher Mehrkörperschiffe hat.

Declaration

Part of the work in the present thesis has been published in the following references:

- Zentari, L., el Moctar, O., Lassen, J., Hallmann, R., and Schellin, T. E. Experimental and numerical investigation of shallow water effects on resistance and propulsion of coupled pusher-barge convoys. *Applied Ocean Research*, 121:103048, 2022. doi: 10.1016/j.apor.2022.103048

- Zentari, L., Tödter, S., el Moctar, O., Neugebauer, J., and Schellin, T. E. Experimental and numerical investigation of the gap flow between a pusher and a barge in deep and shallow water. *Applied Ocean Research*, 132:103466, 2023. doi: 10.1016/j.apor.2023.103466

Acknowledgement

Completing my PhD journey was long and arduous, but I was fortunate to have received invaluable guidance and support from so many incredible individuals.

First and foremost, I extend my sincerest and warmest thanks to Professor Bettar Ould el Moctar, who was an unwavering source of support and knowledge. He provided me with invaluable advice and much needed constructive criticism. Furthermore, I am deeply grateful to Professor Milovan Perić for accepting to review my manuscript and for his guidance in navigating the challenges of CFD modeling.

I would like to express my sincerest gratitude to the Bundesanstalt für Wasserbau for their financial and material support, and to Thorsten Dettmann and Dr. Michael Schröder for their warm welcome and continuous support throughout my time at the institution. I also extend my thanks to Dr. Philipp Mucha for his continuous support from the very beginning, even after he moved to the other side of the planet. To my colleagues Chris, Nicole, Caro, Sabine, Sandra and Andreas thank you for making my time in the department W4 an enjoyable experience. Special thanks to Dr. Jacek Jankowski for reviewing my manuscript and to Dr. Lydia Schulze for her invaluable advice on managing my work duties and my PhD. I am especially grateful to my friend and colleague Jakob Rzeszutko, who helped me improve my plotting skills using Python and for reviewing my manuscript.

I also want to express my appreciation to my former colleagues in Duisburg at the institute of ship technology and transport systems. Special thanks go to my friends and former colleagues Dr. Andreas Peters and Guillermo Chillcce, who provided me with invaluable knowledge and mental support. I am grateful to Guillermo for the fruitful exchange of ideas during our weekly PhD meetings. Besides, our discussions extended well beyond technical subjects. I warmly thank Andreas for his broad knowledge in physics and CFD. He always pushed me forward, finding the right words to motivate me. Besides, I hope that one day direct numerical simulations will become affordable, for that is the only way he can be satisfied with the accuracy of CFD results. I would also like to thank Dr. Simon Mewes for his helpful insights regarding uncertainty analysis. I thank Dr. Thomas E. Schellin for reviewing my publications and this thesis.

Validation was an essential part of my work, and I extend my sincerest thanks to Benjamin Friedhoff from DST for the support during the design phase, Jan Lassen from HSVA for the deep water tests, Rink Hallmann from MARIN for the shallow water tests,

and Simon Tödter and Dr. Jens Neugebauer from ISMT for the optical measurements. They provided me with excellent results, which greatly benefited this work.

Finally, I am deeply grateful to the many friends I made along the way, since I landed in Germany from Morocco back in 2008. Thanks to David, Malen, and Philipp in Bremen, to Felix, Lisa, Maike, and Denise in Hamburg, and to Hermann, Saskia, and Caro in Karlsruhe, to Martina in Genova, to Fadoua in Rome and to all my friends back in Casablanca. I of course apologize to anyone I forgot. Special thanks go to my partner Sara, who supported me through my mood swings and pulled me out of my self-doubts many times in the last year. Last but not least, I warmly thank my family in Morocco, France, and elsewhere, for their unconditional support, especially my mother Ouafa and my sister Maria, my aunt Bouthaina and my uncle Cyrille, and of course my cousin Miya. To them I say "choukrane bezzaf, merci beaucoup"!

Contents

List of Figures

List of Tables

Nomenclature

Acronyms

AFBS	Aft body side vortex
CFD	Computational Fluid Dynamics
CFL	Courant-Friedrichs-Lewy number
CPMC	Computerized Planar Motion Carriage
CV	Control volume
DDES	Delayed Detached Eddy Simulation
DES	Detached Eddy Simulation
EARSM	Explicit Algebraic Reynolds Stress model
FBSV	Fore body side vortex
FVM	Finite Volume Method
GIS	Grid induced separation
HRIC	High Resolution Interface Capturing
IDDES	Improved Delayed Detached Eddy Simulation
ITTC	International Towing Tank Conference
KCS	KRISO Container Ship
LDV	Laser Doppler Velocimetry
LES	Large Eddy Simulation
LLM	Log-layer mismatch
MRF	Moving reference frame
MSD	Modeled stress depletion
MUSCL	Monotonic Upstream-Centered Scheme for Conservation Law
PIV	Particle Image Velocimetry
PMM	Planar Motion Mechanism

RANSE	Reynolds-Averaged Navier-Stokes Equations
SIMMAN	Workshop on Verification and Validation of Ship Manoeuvring Simulation Methods
UKC	Under Keel Clearance
VoF	Volume of fluid
ZKR	Zentrale Komission für die Rheinschifffahrt

Greek Symbols

α	Volume fraction	–
Δ	Displacement	m^3
η	Kinematic viscosity	m^2/s
η_0	Propeller open-water efficiency	–
η_D	Propulsion efficiency	–
$\mathbf{\Omega_0}$	Rotation velocity vector	rad/s
μ	Dynamic viscosity	Pa s
μ_t	Eddy-viscosity	Pa s
ω	Specific turbulent dissipation rate	m^2/s^3
ϕ	Roll angle	rad
ψ	Heading angle	rad
ρ	Fluid density	kg/m^3
θ	Pitch angle	rad
ε	Turbulent dissipation rate	m^2/s^3

Roman Symbols

$\mathbf{b}$	Body force vector	N
$\mathbf{D}$	Deformation tensor	m
$\mathbf{F}$	External force vector	N
$\mathbf{H}$	Angular momentum	N m
$\mathbf{I_x}$	Moment of inertia with respect to x-axis	kg^2 m
$\mathbf{I_y}$	Moment of inertia with respect to y-axis	kg^2 m

$\mathbf{I_z}$	Moment of inertia with respect to z-axis	$\mathrm{kg^2\,m}$
$\mathbf{I}$	Unit tensor	–
$\mathbf{M}$	External moments vector	$\mathrm{N\,m}$
$\mathbf{n}$	Normal vector of the CV surface	-
$\mathbf{r_g}$	Location of ship's center of mass	m
$\mathbf{S}(\psi,\theta,\phi)$	Transformation matrix	–
$\mathbf{T}$	Stress tensor	Pa
$\mathbf{T}(\psi,\theta,\phi)$	Transformation matrix	–
$\mathbf{U}$	Translation velocity vector	m/s
$\mathbf{u}$	Fluid velocity vector	m/s
$\mathbf{u'}$	Fluctuating fluid velocity vector	m/s
$\overline{\mathbf{u}}$	Reynolds averaged fluid velocity vector	m/s
ϕ_i	Numerical solution on grid i	–
B	Ship breadth	m
C_f	Frictional resistance coefficient	–
C_p	Pressure coefficient	–
D_P	Propeller diameter	m
f	Cell face	$\mathrm{m^2}$
F_H	Hydrodynamic forces acting on the hull	N
F_P	Hydrodynamic forces acting on the propeller	N
F_R	Hydrodynamic forces acting on the rudder	N
Fn	Froude number	–
Fn_h	Froude depth number	–
g	Gravitational acceleration	$\mathrm{m/s^2}$
h	Water depth	m
J	Propeller advance ratio	–
K	Hydrodynamic roll moment	$\mathrm{N\,m}$
k	Turbulent kinetic energy	$\mathrm{m^2/s^2}$
K_Q	Non-dimensional torque coefficient	–
K_{TD}	Duct non-dimensional thrust coefficient	–

K_{TP}	Propeller non-dimensional thrust coefficient	–
K_{TT}	Total non-dimensional thrust coefficient	–
l_{LES}	LES length scale	m
l_{HYBRID}	Hybrid length scale	m
l_{RANS}	RANSE length scale	m
L_{OA}	Length overall	m
L_{PP}	Length between perpendiculars	m
M	Hydrodynamic pitch moment	N m
N	Hydrodynamic yaw moment	N m
n	Propeller revolution rate	1/s
P	Cell center	m
p	Pitch velocity	rad/s
p	Pressure	Pa
P_{DM}	Delivered power	W
P_{EM}	Effective power	W
q	Roll velocity	rad/s
r	Yaw velocity	rad/s
R_k	Convergence ratio	–
r_k	Refinement ratio	–
S	CV's surface	m^2
T	Ship draft	m
t	Time	s
T_P	Propeller thrust	N
u	Surge velocity	m/s
u^+	Dimensionsless wall velocity	–
V	CV's volume	m^3
v	Sway velocity	m/s
w	Heave velocity	m/s
X	Longitudinal hydrodynamic force	N
Y	Transversal hydrodynamic force	N

y^+	Dimensionless wall distance	–
Z	Vertical hydrodynamic force	N

1 Introduction

In the ambit of energy efficiency, inland waterway shipping in Germany is gaining an increased interest. Owing to a more favorable environmental impact compared to other transport means, more than 7% of all transported goods are shipped on inland waterways, as reported by the german federal statistical office (Statistisches Bundesamt (2022), in German). According to the Central Commission for Navigation on the Rhine River (ZKR - Zentrale Komission für die Rheinschifffahrt (2003), in German), most of the traffic takes place on the Rhine river. Pushed convoys account for a significant portion of the traffic. Indeed, according to the Federal Association of German Inland Shipping (Bundesverband der Deutschen Binnenschifffahrt e.V. (2022), in German), pushed barges account for nearly 26% of the total dry cargo tonnage capacity available in Germany's inland waterway fleet. Recently, however, due to the negative impact of extreme temperature periods, water levels have been lower for extended periods of time. The ensuing logistic shortcomings have negatively impacted regions and industries highly dependent on inland waterway transport. The need for renewed policies allowing ships and convoys to sail with smaller **U**nder **K**eel **C**learances (UKC) in critical areas is, therefore, mandatory. Navigability analyses are an essential tool upon which such policies and rules are based. For this purpose, ship handling simulators are increasingly utilized. These devices combine a realistic operating environment with an adequate mathematical model to predict the real time motion behavior of a vessel. The reliability of these predictions depends on accurately predicted hydrodynamic forces and moments acting on a vessel. At the moment, the most reliable method is based on full-scale trials in deep water, whereby the associated hydrodynamic forces and moments are obtained via indirect parameter identification. In extremely shallow waters, however, this method is not applicable, given the higher grounding and collision risks. Nonetheless, to improve and develop suitable mathematical models for maneuverability analyses in restricted waters for inland waterway vessels, an accurate quantification of hydrodynamic forces and moments is necessary. Recently, due to the phenomenal rise in computing power, **C**omputational **F**luid **D**ynamics (CFD) represents a promising alternative to full-scale trials in shallow waters. The numerical simulation of maneuvering motions in shallow waters is a challenging task as there are a number of additional uncertainties associated with the geometrical particularities of inland waterway vessels and water depth restrictions. Furthermore, benchmark data are relatively scarce. This holds particularly true for pushed convoys because the flow passing by multi-body vessels is substantially more complex than the flow around their monohull counterparts. The need to validate data is particularly relevant, considering that pusher-barge convoys are an important part of the German inland waterway fleet. Indeed, due to their unique capability of transporting a combination of different goods,

they offer noteworthy advantages from a logistical point of view. Consequently, the need for improved navigability analyses and, thus, adequate benchmark data for deep and shallow water conditions is evident. Thereupon, the suitability of CFD techniques to predict the flow around multi-body vessels has to be assessed.

1.1 State of the art

From a broader point of view, the maneuverability of a vessel has always been a relevant research topic. The foundation of the mathematical model serving as a starting point was formulated by Abkowitz (1964). This model relies on the approximation of hydrodynamic forces and moments acting on a vessel expressed as representative Taylor series expansions. These forces and moments, in six or three degrees of freedom, can be approximated as body-motion dependent polynomials. The use of a **P**lanar **M**otion **M**echanism (PMM) to identify the so-called maneuvering coefficients characterizes these models. Such PMM devices allow the execution of large amplitude motions or prescribed trajectories in a towing tank. In Germany, a **C**omputerized **P**lanar **M**otion **C**arriage (CPMC) was installed in Hamburg in the context of the *Sonderforschungsbereich Schiffbau 98*. Accounting for the capabilities of the CPMC device, Oltmann and Sharma (1984) made notable contributions to mathematical maneuvering models. Sutulo and Guedes Soares (2011) documented an extensive overview of mathematical models and their suitability, and Brix (1993) covered practical aspects of maneuvering.

The use of CFD to virtually reproduce PMM tests is gaining considerable momentum in the maritime research community. While numerical resistance tests for vessel speed and power predictions are nowadays an industry standard according to Bertram (2012), maneuvering still poses considerable challenges. el Moctar (2001) performed steady drift and yaw tests for different sea-going vessels in deep water using CFD. A particular attention was given to rudder and propeller modeling. Cura-Hochbaum (2006) replicated a complete set of virtual PMM tests for the **K**RISO **C**ontainer**s**hip (KCS) model in deep water, including accounting for the free surface. Subsequent validation and verification was documented in the Proceedings of the workshop on verification and validation of ship **Man**oeuvring **Sim**ulation (SIMMAN); see Stern et al. (2011). While the initial computations were limited to double-body setups, i.e. with the omission of the free surface and ship motions, the development of CFD codes and the corresponding computing power allowed more complex setups. More recently, direct maneuvering simulations with fully appended vessels in deep water were performed by el Moctar et al. (2014). In their study, they performed numerical zig-zag and turning circle maneuvers for a fully appended vessel, i.e. including the motions of steering and propulsive devices. A satisfactory agreement with measured data was reached. Similarly, Carrica et al. (2016) performed shallow water direct maneuvering simulations for self-propulsion and zig-zag cases. While their self-propulsion simulations agreed favorably with experimental data, zig-zag maneuvers were more challenging computationally. More recently, Kim et al.

(2022) performed direct maneuvering simulations of the KCS in shallow waters. In their study, good agreement was reached between experiments and their computations for both kinematic and trajectory parameters. These computations, although becoming more feasible nowadays, nevertheless require substantial computational resources.

The extension of the maneuvering problem to shallow and confined waters was initially limited to the prediction of resistance; see Tuck (1978). One of the first relevant formulations of adequate mathematical models in restricted waters was given by Norrbin (1971). An extensive and systematic experimental study of shallow water effects on maneuvering was presented by Gronarz (1997). A thorough overview of mathematical models in shallow waters can be found in Eloot (2006). On the experimental front, a few notable studies dealt with shallow water PMM tests for sea-going vessels; see Eloot et al. (2015). CFD computations dealing with ships sailing in shallow waters have naturally been focused on the prediction of resistance and squat. The latter phenomenon is significant because it represents the major cause of speed restriction in confined waterways. Studies by Mucha et al. (2016), Tezdogan et al. (2016), Bechthold and Kastens (2020) and Chillcce and el Moctar (2022) provided useful insights on CFD capabilities in this regard.

For inland waterway vessels, despite the increased research interest, benchmark data for validation purposes remain scarce. Mucha et al. (2017, 2018, 2019), Quadvlieg et al. (2018), Zeng et al. (2018) and Oud and Bedos (2022) presented benchmark data of monohull inland waterway vessels. Zeng et al. (2019) relied on CFD methods to improve the prediction of viscous resistance in shallow water of an inland waterway monohull. Oud and Bedos (2022) presented numerical and experimental investigations of the effect of water depth on maneuvering forces for inland ships. They validated CFD simulations against experimental measurements of hydrodynamic forces and moments acting on a typical 110 m inland waterway vessel. On the other hand, only few studies dealt with pusher-barge vessels. King et al. (2008) performed captive model tests on nine pusher-barge configurations to obtain hydrodynamic derivatives. Maimun et al. (2011) extended this investigation by determining maneuvering characteristics in deep and shallow waters. Yuba and Tannuri (2013) investigated the effect of different maneuvering and propulsion devices for different configurations. Sano et al. (2017) analyzed the effect of loading conditions and water depth on maneuverability of a pusher-barge convoy by varying the draft of the barge. Grassi et al. (2013) performed CFD simulations to obtain hydrodynamic coefficients for three configurations of pusher-barge systems using a double-body setup. Du et al. (2020) used CFD methods to predict the resistance and to analyze the generated waves in restricted waters of two inland waterway vessels consisting of one pusher boat coupled with one barge and with two barges. Zentari et al. (2022) published an extensive study dealing with experimental and numerical investigations of shallow water effects on resistance of and the associated propulsive power required for pusher-barge convoys. More recently, Delefortrie et al. (2022) obtained hydrodynamic coefficients from experimental PMM tests for different pusher-barge convoys in deep and shallow water. The obtained coefficients were subsequently used to populate a mathematical model implemented in their ship-handling simulator.

1.2 Objectives and organization of the thesis

Despite the fact that the maneuverability of ships in shallow waters is very relevant nowadays, the research output treating the maneuverability of pushed-convoys is still very limited. First, the models used in the above cited studies are relatively small, up to a scale of 1:25, which poses substantial difficulties from a measurement point of view. Second, numerical analyses of the flow passing by this kind of vessels remain very scarce. The hydrodynamic characteristics of multi-body pushed convoys are therefore not well known. The main research questions arising from this problem statement are:

1. How accurate are state-of-the-art experimental and numerical techniques in quantifying the hydrodynamic forces and moments acting on pusher barge vessels in both deep and shallow water?
2. How does shallow water affect the hydrodynamic forces and moments acting on pusher-barge convoys?
3. What is the impact of the flow in the gap between pusher and barge on the hydrodynamic performance of pushed convoys?

In addressing these research questions, this thesis aims to present a contribution towards a better quantification of hydrodynamic forces and moments acting on pusher-barge convoys in deep and shallow water using state-of-the-art experimental and numerical techniques. Two parts summarize the main objective of the present work. The first part describes an extensive procedure to experimentally quantify hydrodynamic loads acting on pusher-barge convoys in deep and shallow waters. The considered convoys comprised three configurations, namely, a pusher coupled with one barge, a pusher coupled with two barges, and a pusher coupled with four barges. The second part presents a robust computational procedure, based on the numerical solution of the **R**eynolds-**A**veraged-**N**avier-**S**tokes **E**quations (RANSE) to replicate the above mentioned experimental tests. An additional objective was to experimentally and numerically quantify the impact of the gap between the pusher and barge on the flow passing by such convoys using optical measurement methods and numerical scale-resolving techniques. The thesis is organized as follows:

- Chapter 2 presents the theoretical background, drawing upon currently applied maneuvering models. An Abkowitz-type model presented by Mucha (2017) constituted the starting point of the analysis. External forces and moments acting on the vessel are presented and discussed, with an emphasis on shallow water effects.
- Chapter 3 provides an overview of the theoretical basis for the numerical method used in this thesis. It covers the introduction of the Navier-Stokes equations and

discusses key aspects of the method, such as turbulence models, discretization techniques, solution algorithms, and error quantification procedures.

- Chapter 4 offers a detailed description of the geometric characteristics of the pusher-barge convoys, including their propulsion and steering devices. The chapter also describes the experimental setup used to obtain validation data, which included resistance and propulsion tests, as well as steady drift and steady rudder variation tests, conducted in both deep and shallow waters.
- In chapter 5, the results of the resistance and propulsion tests conducted in both deep and shallow waters are presented. The CFD results of virtual resistance tests for all three configurations are validated against experimental data. The chapter also provides a thorough discussion on the effects of restricted water depth and configuration arrangement on resistance and propulsion.
- Chapter 6 focuses on the investigation of gap flow between a pusher and a barge, based on the previous chapter's findings. This chapter briefly describes the use of **P**article **I**mage **V**elocimetry (PIV) and **L**aser **D**oppler **V**elocimetry (LDV) techniques for the quantitative analysis of the gap flow. These experiments are numerically reproduced using various turbulence modeling approaches, consisting of RANSE and the **I**mproved **D**elayed **D**etached **E**ddy **S**imulation technique (IDDES). The chapter further discusses the effects of water depth restriction on the gap flow and its impact on the hydrodynamic performance of the convoy.
- Chapter 7 covers steady drift and steady rudder variation tests on pusher-barge configurations in deep and shallow waters. Herein, the numerical procedure used to replicate these tests is detailed, along with sensitivity analyses. Experimental and numerical results are thoroughly described, emphasizing how water depth impacts the hydrodynamic forces and moments acting on a convoy's hull. Both experimental and numerical findings are presented.
- Chapter 8 offers a summary of the thesis, emphasizing the key findings and the author's contributions. Additionally, possible directions for future works are provided.

2 Theoretical background

The main objective of this thesis is the accurate prediction of hydrodynamic forces and moments acting on pusher-barge convoys in maneuvering conditions in deep and shallow water. This task is essential, as it constitutes the groundwork of both the formulation of an adequate maneuvering mathematical model and populating it with so-called hydrodynamic coefficients. It is thus appropriate to present the theoretical background leading to the formulation of these maneuvering mathematical models. However, the scope of this work is not to retrieve hydrodynamic coefficients in order to conduct maneuvering simulations, but rather to use the required captive model tests to analyze the flow surrounding maneuvering pushed convoys, in deep and shallow water. Indeed, captive model tests, besides their primary use for the derivation of hydrodynamic coefficients, offer particular incentives regarding the analysis of the flow around vessels in maneuvering conditions, under the systematic variation of speed, drift angle, rotating rate and rudder deflection.

Therefore, in this chapter, the theoretical background regarding the maneuverability of a surface vessel is briefly discussed. First, the coordinate system and the equations of motion are derived and described. An Abkowitz-type mathematical model is then introduced, as it constitutes the starting point of the investigation presented in this work. External hydrodynamic forces and moments acting on a vessel's hull are discussed, including the shallow water effect. Finally, the relevant captive model tests, which were performed both experimentally and numerically, are presented and discussed.

2.1 Coordinate system and reference frame

The motion of a surface vessel may be treated as a rigid-body motion. Obeying the fundamentals of Newtonian physics, one must define an inertial reference frame from which the ship motions can be described, hence the differentiation between the inertial earth-fixed O, X_0, Y_0, Z_0 and ship-fixed S, x, y, z cartesian coordinate system. Figures 2.1 and 2.2 depict a schematic representation of the ship-fixed and earth-fixed coordinate system in six and three degrees of freedom respectively. In the reference frame considered in this work, Z_0 and z axes point downward, x and y axes point towards the bow and to starboard. The coordinate system is located on the calm water-plane amidship. The translatory motions of the vessel in the x, y, z directions are denoted u, v, w for surge, sway, and heave respectively. The rotational motions around the axes are denoted p, q, r

for roll, pitch and yaw. Variables of interest are the position and orientation of the vessel relative to the inertial system. Expressing the ship's position relative to the inertial coordinate system depends upon a spatial relation between both systems. Variables of interest in maneuvering predictions are the ship's instantaneous translatory and angular velocities. These are expressed in the ship's body-fixed coordinate system; hence, a coordinate transformation is applied to express the translatory velocity vector $\mathbf{u_s}$, defined by its components $[u, v, w]^T$ in the inertial coordinate system as $\mathbf{u_0}$:

$$\mathbf{u_0} = \mathbf{T}(\psi, \theta, \phi)\mathbf{u_s} \tag{2.1}$$

with the transformation matrix $\mathbf{T}$ defined as:

$$\mathbf{T}(\psi, \theta, \phi) = \begin{bmatrix} \cos\psi\cos\theta & (\cos\psi\sin\theta\sin\phi - \sin\psi\cos\phi) & (\cos\psi\sin\theta\cos\phi - \sin\psi\sin\phi) \\ \sin\psi\cos\theta & (\sin\psi\sin\theta\sin\phi - \cos\psi\cos\phi) & (\sin\psi\sin\theta\cos\phi - \cos\psi\sin\phi) \\ \sin\psi & \cos\theta\sin\phi & \cos\theta\cos\phi \end{bmatrix} \tag{2.2}$$

Analogously, the same procedure is applied to the rotational velocity vector $\mathbf{\Omega_S}$, expressed in the ship-fixed coordinate system consisting of components $[r, q, p]^T$. A somewhat more advantageous mathematical formulation is obtained by defining the angular velocities as the rate of change of the Eulerian angles $[\dot{\psi}, \dot{\theta}, \dot{\phi}]^T$. This formulation allows the use of the non-orthogonal transformation matrix $\mathbf{S}(\psi, \theta, \phi)$ to define $\mathbf{\Omega_S}$ in the inertial coordinate system as $\mathbf{\Omega_0}$ as follows:

$$\mathbf{\Omega_0} = \mathbf{S}(\psi, \theta, \phi)\mathbf{\Omega_S} \tag{2.3}$$

Using the Euler-angle convention, the matrix $\mathbf{S}(\psi, \theta, \phi)$ can be defined as:

$$\mathbf{S}(\psi, \theta, \phi) = \begin{bmatrix} 1 & \sin\phi\tan\theta & \cos\phi\tan\theta \\ 0 & \cos\phi & -\sin\phi \\ 0 & \frac{\sin\phi}{\cos\theta} & \frac{\cos\phi}{\cos\theta} \end{bmatrix} \tag{2.4}$$

Fossen (2021) covers theoretical considerations regarding ship-fixed and inertial reference frames.

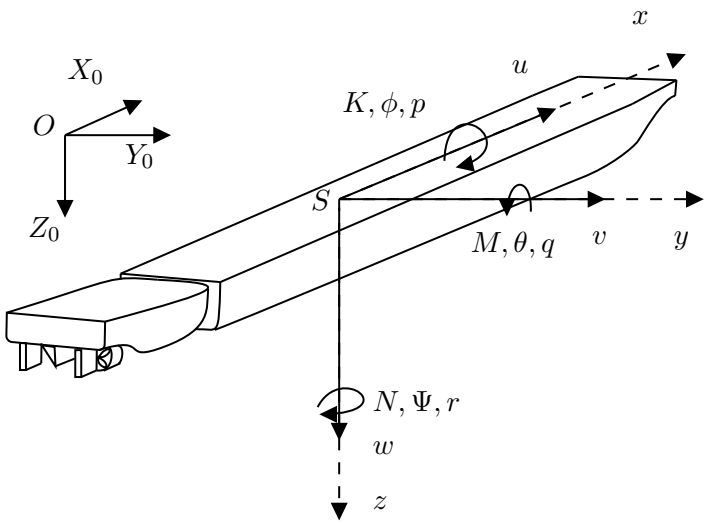

Figure 2.1: Schematic representation of reference frame with six degrees of freedom.

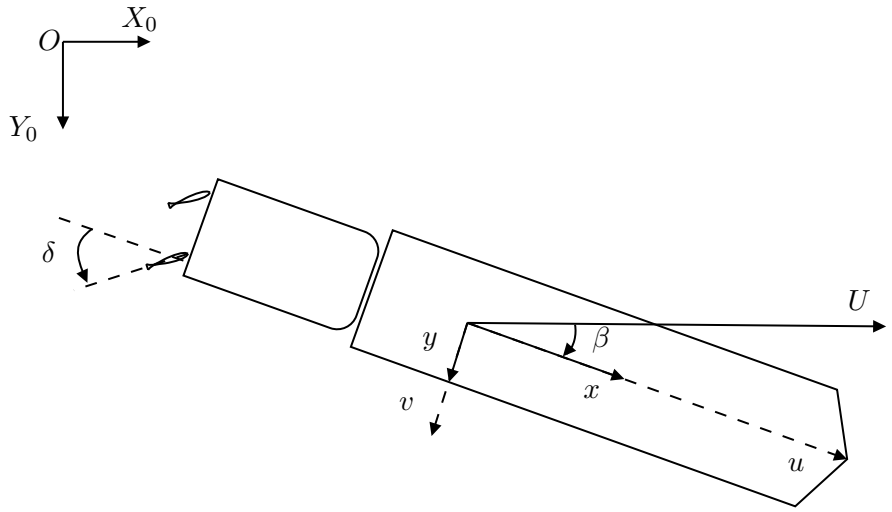

Figure 2.2: Schematic representation of reference frame with three degrees of freedom.

2.2 Equation of motion

The description of the maneuverability of a surface vessel draws upon rigid body dynamics, such as a constant ship mass and an unchanged hull shape. The common ground for such purposes is based on classical Newtonian mechanics represented by the momentum conservation equation. Conservation of linear momentum can be written as follows:

$$\mathbf{F} = m\frac{d}{dt}\left(\mathbf{u_0} + \mathbf{\Omega_0} \times \mathbf{r_g}\right) \tag{2.5}$$

where $\mathbf{u_0}$ is the inertial referenced velocity vector $[u, v, w]^T$, $\mathbf{\Omega_0}$ is the inertial referenced rotation vector $[p, q, r]^T$, and $\mathbf{r_g}$ is the location of the ship's center of mass. The force vector $\mathbf{F}$ represents the resulting forces acting on the ship $[X, Y, Z]^T$. The angular momentum conservation equation is obtained in a similar manner. The conservation of angular momentum $\mathbf{H}$ is defined as follows:

$$\mathbf{M} = \frac{d}{dt}\mathbf{H} + \mathbf{r_g} \times \mathbf{F} \tag{2.6}$$

where $\mathbf{M}$ is the resulting moment vector $[K, M, N]^T$ and $\mathbf{H}$ the angular momentum. Considering a rigid body being the sum of discrete points with a masses m_i, the moments of inertia with respect to the body fixed coordinate system S, x, y, z are defined as:

$$I_{xx} = \sum_i (y_i^2 + z_i^2)m_i \tag{2.7}$$

$$I_{yy} = \sum_i (x_i^2 + z_i^2)m_i \tag{2.8}$$

$$I_{zz} = \sum_i (x_i^2 + y_i^2)m_i \tag{2.9}$$

$$I_{xy} = I_{yx} = \sum_i m_i x_i y_i \tag{2.10}$$

$$I_{xz} = I_{zx} = \sum_i m_i x_i z_i \tag{2.11}$$

$$I_{yz} = I_{zy} = \sum_i m_i y_i z_i \tag{2.12}$$

Employing vector decomposition, algebraic rearrangement and including the definition of moments of inertia into equations (2.5) and (2.6) yields:

$$X = m\left[\dot{u} + qw - rv + \dot{q}z_g - \dot{r}y_g + (qy_g + rz_g)\,p - (q^2 + r^2)x_g\right] \tag{2.13}$$
$$Y = m\left[\dot{v} + ru - pw + \dot{r}x_g - \dot{p}z_g + (rz_g + px_g)\,q - (r^2 + p^2)y_g\right] \tag{2.14}$$
$$Z = m\left[\dot{w} + pv - qu + \dot{p}y_g - \dot{q}x_g + (px_g + qy_g)\,r - (p^2 + q^2)z_g\right] \tag{2.15}$$

$$K = I_{xx}\dot{p} + I_{xy}\dot{q} + I_{xz}\dot{r} + (I_{zz} - I_{yy})\,rq + Iyz\left(q^2 - r^2\right) + I_{xz}pq - I_{xy}pr + \\ + m\left[y_g\left(\dot{w} + pv + qu\right) - z_g\left(\dot{v} + ru + pw\right)\right] \tag{2.16}$$
$$M = I_{yx}\dot{p} + I_{yy}\dot{q} + I_{yz}\dot{r} + (I_{xx} - I_{zz})\,pr + Ixz\left(r^2 - p^2\right) + I_{xy}qr - I_{yz}qp + \\ + m\left[z_g\left(\dot{u} + qw + rv\right) - x_g\left(\dot{w} + pv + qy\right)\right]pmb \tag{2.17}$$
$$N = I_{zx}\dot{p} + I_{zy}\dot{q} + I_{zz}\dot{r} + (I_{yy} - I_{xx})\,pq + Ixy\left(r^2 - p^2\right) + I_{yz}pr - I_{xz}qr + \\ + m\left[x_g\left(\dot{v} + ru + pw\right) - y_g\left(\dot{u} + qw + rv\right)\right] \tag{2.18}$$

Equations (2.13) to (2.18) describe the motion of a rigid body in six degrees of freedom, see Fossen (2021). Accounting for ship symmetry at $y = 0$ and the limited influence of heave, pitch and roll for inland waterway vessels, see Gronarz (1997), the problem can be reduced to three degrees of freedom motions X, Y and N; see figure 2.2. The governing equations in ship fixed coordinate system can thus be simplified as:

$$X = m\left(\dot{u} - vr - x_g r^2\right) \tag{2.19}$$
$$Y = m\left(\dot{v} + ur - x_g\dot{r}\right) \tag{2.20}$$
$$N = I_{zz} + mx_g\left(\dot{v} + ur\right) \tag{2.21}$$

2.3 Hydrodynamic forces and moments

Equations (2.19) to (2.21) are sufficient to describe the response of a surface vessel to rudder maneuvers. The right hand side of the equation contains variables dependent on the shape and mass of a vessel, while the left hand side encloses all external forces and moments, including the action of the fluid. In recent years, the solution of the RANS equations offers the possibility to directly resolve the flow around a maneuvering vessel, see el Moctar et al. (2014), Carrica et al. (2016) and Kim et al. (2022). This process is, however, highly resource intensive. Thus, such a technique is not feasible to predict maneuvers using real-time ship handling simulators. A viable approach has been formulated by Abkowitz (1964) and expanded further by Norrbin (1971). Herein, hydrodynamic forces and moments are assumed to be dependent on the motion variables and their derivative:

$$F = f\left(x_0, y_0, \Psi, u, v, r, \dot{u}, \dot{v}, \dot{r}, \delta\right) \tag{2.22}$$

Forces and moments can be modeled using Taylor-series expansion of the velocity and acceleration variables. This approach is valid in ship hydrodynamics, as the time scale of a vessel's motion is relatively slow. Following the approach by Abkowitz (1964), a vessel is analyzed in its equilibrium state at a given velocity u_0, in which the longitudinal force is balanced by a thrust at a constant propeller revolution rate n. Small perturbations from the equilibrium state are denoted Δu, such as $\Delta u = u - u_0$. Using a Taylor-series expansion, one can obtain the so-called hydrodynamic derivatives. To exemplify the application of this method, the surge force X first order and second order hydrodynamic derivatives depending to the forward velocity Δu are written as:

$$X_u = \frac{\partial X}{\partial u}\Delta u \qquad\qquad X_{uu} = \frac{\partial^2 X}{\partial u^2}\Delta u^2 \tag{2.23}$$

Depending on the velocity and acceleration component, terms up to the second or third order derivative are sufficient to describe, with acceptable accuracy, the motion of a surface vessel in the calm water case, see Sutulo and Guedes Soares (2011). Required PMM tests to populate an adequate mathematical model with maneuvering coefficients offer a satisfying approximation to consider the vessel in a quasi steady maneuvering situation. For this purpose, the starting point is to consider the mathematical model established by Mucha (2017), valid in deep and shallow water. This model draws upon the work of Wolff (1981). He carried out extensive model tests to determine the response of different vessels, and he proposed an appropriately reduced maneuvering model:

$$X = X_{\dot{u}}\dot{u} + X_u\Delta u + X_{uu}\Delta u^2 + X_{\delta\delta}\delta^2 + X_{vv}v^2 + X_{rr}r^2 + X_{vr}vr \tag{2.24}$$

$$\begin{aligned} Y = {} & Y_{\dot{v}}\dot{v} + Y_{\dot{r}}\dot{r} + Y_0 + Y_v v + Y_{vvv}v^3 + Y_r r + Y_{rrr}r^3 + Y_\delta\delta + \\ & + Y_{\delta\delta\delta}\delta^3 + Y_{vrr}vr^2 + Y_{rvv}rv^2 + Y_{\delta u}\delta\Delta u \end{aligned} \tag{2.25}$$

$$\begin{aligned} N = {} & N_{\dot{v}}\dot{v} + N_{\dot{r}}\dot{r} + N_0 + N_v v + N_{vvv}v^3 + N_r r + N_{rrr}r^3 + N_\delta\delta + \\ & + N_{\delta\delta\delta}\delta^3 + N_{vrr}vr^2 + N_{rvv}rv^2 + N_{\delta u}\delta\Delta u \end{aligned} \tag{2.26}$$

This mathematical model, described in equations (2.24) to (2.26), formulates with satisfactory accuracy the forces acting on a surface vessel, while avoiding the complexity of over-identification. However, a few drawbacks have to be taken into account. Hull, propulsion and rudder forces are not separated by their effect, but rather included in the global external forces. The vessel is assumed advancing at a constant velocity, and the model tests required to identify derivatives are conducted at a predetermined operational propulsion point. This method, while offering good understanding of a ship's behavior

under certain conditions, fails to offer a proper definition for each effect separately. Furthermore, its validity is restricted to a limited perturbation range from the ship's initial condition. The concept of a modular model has been introduced to address these limitations. External forces are separated into several modules interacting with each other. These are mainly hull forces F_H, propulsion forces F_P, and rudder forces F_R:

$$X = X_H + X_P + X_R \tag{2.27}$$

$$Y = Y_H + Y_P + Y_R \tag{2.28}$$

$$N = N_H + N_P + N_R \tag{2.29}$$

Although modular models provide more possibilities in terms of maneuvering simulations, the physical description of each effect and their interaction is often based on approximations and empirical assumptions, which may decrease the quality of the simulations. Several modular models are available, such as Oltmann and Sharma (1984) or the **M**aneuvering **M**odeling **G**roup (MMG) model of Yasukawa and Yoshimura (2015). While they are substantially similar in their approach, differences are present in the characterization of each effect. In the present work, the forces acting on the hull were measured and computed for the fully appended ship operating at propulsion point. For resistance experiments and computations, the bare hull of the combined pusher-barge convoys was considered.

2.4 Shallow water effects

Shallow water effects can be summarized as an increase in forces and moments acting on the vessel due to reduced distance between keel and channel bottom. Accurately quantifying these effects on maneuverability is essential to ensure the safety of the ship and the waterway. An immediate effect of decreased water depth is a significantly higher resistance. The flow accelerates past the stagnation point on the fore part of the vessel, particularly at a small UKC. The ensuing pressure distribution is characterized by a higher pressure at the bow area and larger low-pressure zones in areas where the flow is accelerated, resulting in higher longitudinal forces and increased squat. While squat has a significant influence on resistance, it becomes an environmental issue as it increases the risk of grounding; see Mucha et al. (2016), Tezdogan et al. (2016) and Bechthold and Kastens (2020). A feasible solution is a required reduction of the forward speed in shallow-water areas. Computation of shallow water resistance is a challenging task because the bottom of the channel and its interaction with the ship's bottom include complex physical effects between the associated boundary layer regions, as highlighted by Chillcce and el Moctar (2022). This observation is particularly important for inland waterway vessels; Zeng et al. (2019).

In shallow waters, the Froude depth number $Fn_h = u/\sqrt{gh}$ characterizes the flow regime surrounding a vessel at a forward speed u, where g is the acceleration of gravity, and h is the water depth. According to Pompée (2015), one differentiates between the subcritical ($Fn_h < 1$), the critical ($Fn_h = 1$), and the supercritical speed range ($Fn_h > 1$). At $Fn_h < 0.6$, the wave-making resistance of a vessel is comparable to the wave resistance under deep water conditions. As a vessel approaches its critical speed, the wave pattern changes drastically. The flow around the vessel is then highly unsteady, and a dramatic increase of the wave-making resistance occurs, attaining a maximum value at $Fn_h = 1$. Most inland waterway vessels operate at a speed range well below this critical value.

Propulsion of sea going vessels and inland waterway vessels differs mainly in that inland waterway vessels operate in relatively shallow waters. In shallow waters, a smaller UKC dictates the arrangement of the propellers. Consequently, smaller semi-submerged propellers have to be accommodated in the aft part of the pusher boat, and these propellers are usually situated inside a tunnel. A higher propeller loading is required to keep the forces balanced. The ensuing interactions between hull, propeller and rudder change the flow dynamics around the hull. As the propeller operates in the wake of the ship, blockage effect can lead to a modified propeller inflow, which can reduce the propulsion effectiveness. This is compensated by the arrangement of nozzles and tunnels in the aft part of inland waterway vessels; see Friedhoff et al. (2019) and Radojčić et al. (2021). Consequently, the effort needed to reach a particular velocity increases drastically in shallow water condition. Higher propeller loads can lead to increased noise and vibrations which may cause structural damage; see Schevchuk (2018).

A significant change on rudder forces is not clearly visible under shallow water conditions. However, these forces are highly sensitive to propeller action. The dynamics of these forces then change, due to higher propeller loading and modified inflow velocities. Other than their course keeping abilities, inland waterway vessels must provide a higher maneuverability than their seagoing counter parts. This necessitates larger rudders. Often double rudder systems are situated ahead or behind of the nozzle; see Liu (2017). This holds particularly true for pusher boats because their operational mode often requires them to be able to push differently sized convoys.

Owing to the blockage effect induced by shallow to very shallow waters, the UKC, defined as $(h - T)/h$, where h is the water depth, and T is the draft, has a decisive effect on the yaw moment N and the lateral force Y. Depending on the drift angle and the vessel's shape, blockage of the cross flow between port- and starboard side increases. This obstruction causes an unbalance in the pressure distribution and, therefore, a different force and moment balance. According to Vantorre et al. (2017), in shallow waters, this effect is accentuated, particularly in very shallow water, e.g. at a UKC of 20%. Considering pusher-barge models, King et al. (2008) found out that a decreased water depth induces a smaller turning radius. However, free running maneuver tests for pusher-barge convoys needs to be performed in order to directly quantify shallow water effect

on maneuverability. To the author's best knowledge, such tests are unavailable at the moment.

2.5 Captive maneuvering tests

A range of experimental tests are necessary to obtain a full set of maneuvering coefficients for a ship. One can decide between direct and indirect parameter identification, each method having its drawbacks and advantages. In the latter, the hydrodynamic derivatives in equation (2.24), (2.25) and (2.26) are obtained by regression based on analyses of ship motions in standard maneuvers. Literature on this method can be found in Fossen (2021). Direct parameter identification aims to obtain the hydrodynamic derivatives by measuring the forces and moments acting on a vessel resulting from a certain input in a test basin, using a PMM or CPMC device. Due to the dependency between forces and the corresponding variables introduced in equation (2.24), (2.25) and (2.26), the latter is varied as to reconstruct the coefficients by fitting a polynomial through linear regression. Oltmann and Sharma (1984), and more recently Eloot (2006) described the experimental procedure for PMM or CPMC captive maneuvering tests.

The coefficients depending on the longitudinal velocity u can be easily determined from a classical resistance test by selecting appropriate parameters. Details of resistance tests can be found in Bertram (2012). The propulsion point for a certain operational range can be determined via the British method, as described by the **I**nternational **T**owing **T**ank **C**onfecerence (ITTC) (1999). Here, the ship model is towed through the basin at a constant velocity, while the propeller loading is varied. Thrust, torque, and longitudinal force is measured. The equilibrium point, i.e., the point when thrust and resistance cancel each other, is determined by interpolation. Oblique towing tests, performed to determine coefficients depending on velocity component v, are executed in a similar manner. The ship is towed at a fixed position, and a given drift angle β is specified. The tests are carried out with the fully appended ship at a revolution rate n obtained from the propulsion tests. External forces induced by the variation of rudder angle, expressed by the coefficient with the subscript δ, can be investigated with relative ease by towing the vessel in a straight line. The rudder angle δ is then varied over an appropriate range of values, corresponding typically to the operational range of the candidate ship. To account for the curvature of the path of the maneuvering vessel and the oration rate r, rotating arm tests are executed. The ship is fixed to an arm that describes a circular motion about a fixed axis. Forces and moments acting on the hull are measured during each run. A drift angle is also specified to determine cross coupled coefficients. In this work, these quasi-steady tests were reproduced numerically and validated for deep and shallow water cases, with the exception of rotating arm tests. Given the nature of the task at hand, i.e., analyzing the flow around pusher-barge systems, only a few quasi-steady maneuvering tests were numerically reproduced in this work. Table 2.1 lists the associated parameters of these tests.

Table 2.1: Overview of captive maneuvring tests performed numerically and experimentally as well as corresponding varied parameter.

Test	**Kinematic parameter**	**Symbol**	**Unit**
Resistance	Surge velocity	U	[m/s]
Propulsion	Propeller revolution rate	n	[1/s]
Oblique towing	Drift angle	β	[°]
Rudder variation	Rudder angle	δ	[°]

Although the preferred method considers only quasi-steady tests, dynamic tests are usually carried out in test facilities. The particular ship is towed on a sinusoidal path while forces and moments are measured. Depending on the mathematical model at hand, pure sway, pure yaw, or combined sway/yaw tests are conducted. The force is then assumed to be periodic and approximated as a function of the oscillatory motion. The ITTC (2005) gives recommendations regarding the parameters for harmonic tests. More details on the efficient design of captive model tests and the choice of appropriate parameters can be found in Eloot (2006) and Sutulo and Guedes Soares (2011).

3 Numerical Method

3.1 Introduction

The majority of the numerical simulations presented in this work are based on the numerical solution of the RANS equations. A more advanced hybrid technique, combining a RANSE solution near a test body and **L**arge-**E**ddy-**S**imulation (LES) solution in the far field, was used in selected cases. The aim of the following chapter is to provide an overview of the numerical methods applied in this thesis. The Navier-Stokes equations are briefly introduced, followed by a presentation and brief discussion of turbulence modeling approaches. Spatial and temporal discretization techniques are then described, followed by a description of boundary conditions, solution algorithms, and error quantification techniques. All simulations presented in this work were performed using the commercial software Simcenter STAR-CCM+; see Siemens (2022). The **F**inite **V**olume **M**ethod (FVM) is implemented within it, thus the Navier-Stokes equations are formulated in integral form. An in-depth descritpion of turbulent flows can be found in Pope (2000). A thorough description of computational methods for fluid dynamics can be found in Ferziger et al. (2019).

3.2 The Navier-Stokes equations

The Navier-Stokes equations are a set of equations that describe the motion of fluids. Expressed for an incompressible Newtonian fluid and an arbitrary fixed **c**ontrol **v**olume (CV), these equations take the form of mass and momentum conservation equations. For a CV with a volume V and a surface S, in a Cartesian reference frame (x, y, z), the conservation of mass can be written as:

$$\frac{\partial}{\partial t}\int_V \rho \mathrm{d}V + \int_S \rho \mathbf{u}\cdot\mathbf{n}\mathrm{d}S = 0 \tag{3.1}$$

Where ρ is the density of the fluid, $\mathbf{n}$ the normal vector of the surface pointing outwards, $\mathbf{u}$ the fluid velocity and t the time. For the same CV, the equation of momentum conservation can be written as:

$$\frac{\partial}{\partial t}\int_V \rho \mathbf{u} \mathrm{d}V + \int_S \rho \mathbf{u}\mathbf{u} \cdot \mathbf{n} \mathrm{d}S = \int_S \mathbf{T} \cdot \mathbf{n} \mathrm{d}S + \int_V \rho \mathbf{b} \mathrm{d}V \tag{3.2}$$

The right hand side of the above equation comprises external forces acting on the CV. One differentiates between body forces such as gravity, and surface forces due to pressure and viscous stresses. The term $\mathbf{T}$ in equation (3.2) indicates the stress tensor, $\mathbf{b}$ the body force vector describing a force per unit mass. The stress tensor $\mathbf{T}$ can be written as:

$$\mathbf{T} = 2\mu\mathbf{D} - \Big(p - \frac{2}{3}\mu\Big(\nabla \cdot \mathbf{u}\Big)\Big)\mathbf{I} \tag{3.3}$$

where μ is the dynamic viscosity, $\mathbf{I}$ the unit tensor, p the pressure. The deformation tensor $\mathbf{D}$ is defined as:

$$\mathbf{D} = \frac{1}{2}(\nabla \mathbf{u} + (\nabla \mathbf{u})^T) \tag{3.4}$$

3.3 Turbulence modeling

3.3.1 Reynolds-Averaged Navier-Stokes Equations

Flows in maritime applications are often considered turbulent, characterized by sudden variations in pressure and velocity, seemingly chaotic behavior, and the presence of eddies at various spatial and temporal scales. The Navier-Stokes equations can predict the motion of turbulent fluids with sufficient accuracy within a defined domain, however, simulating these flows using **D**irect **N**umerical **S**imulation (DNS) requires a very fine spatial and temporal discretization, which is computationally expensive and infeasible for most maritime flows. To overcome this limitation, simplifications are necessary in order to reduce computational costs. In the cases relevant to this work, the quantities of interest were typically the mean values of forces and moments acting on a convoy's hull. To this end, the goal of the simulations was to solve the RANS equations. The Reynolds decomposition involves splitting a flow quantity ϕ into a time-averaged component $\overline{\phi}$ and a fluctuating component ϕ'.

$$\phi(\mathbf{x}, t) = \overline{\phi(\mathbf{x})} + \phi'(\mathbf{x}, t) \tag{3.5}$$

with:

$$\overline{\phi(\mathbf{x})} = \lim_{T\to\infty} \frac{1}{T} \int_0^T \phi(\mathbf{x}, t)\mathrm{d}t \tag{3.6}$$

t is the time, while T denotes the averaging interval. The latter needs to be large enough in relation to the time scale of flow fluctuations. In cases where the flow is not statistically steady, the velocity or any other flow variable of interest can be decomposed into an averaged and a fluctuating component over a specific number of realizations N, see equation 3.5, where:

$$\overline{\phi(\mathbf{x}, t)} = \lim_{N\to\infty} \frac{1}{N} \sum\nolimits_1^N \phi_n(\mathbf{x}, t) \tag{3.7}$$

Considering the Navier-Stokes equations, applying Reynolds averaging to velocity and pressure leads to the following expressions for mass and momentum conservation:

$$\frac{\partial}{\partial t} \int_V \rho \mathrm{d}V + \int_S \rho \overline{\mathbf{u}} \cdot \mathbf{n} \mathrm{d}S = 0 \tag{3.8}$$

$$\begin{gathered} \frac{\partial}{\partial t} \int_V \rho \overline{\mathbf{u}} \mathrm{d}V + \int_S \rho(\overline{\mathbf{u}}\,\overline{\mathbf{u}} + \overline{\mathbf{u}'\mathbf{u}'}) \cdot \mathbf{n} \mathrm{d}S = \\ \int_S \mu(\nabla \overline{\mathbf{u}} + (\nabla \overline{\mathbf{u}})^T) \cdot \mathbf{n} \mathrm{d}S + \int_S \overline{p}\mathbf{I} \cdot \mathbf{n} \mathrm{d}S + \int_V \rho \mathbf{b} \mathrm{d}V \end{gathered} \tag{3.9}$$

In equation (3.9), the term $\rho\overline{\mathbf{u}'\mathbf{u}'}$ is known as the Reynolds stress tensor. This term, accounting for the turbulent fluctuations in fluid momentum, is unknown and results in the so-called closure problem, i.e. there are more unknown variables than equations at hand. Therefore, approximations and empirical assumptions are required to close the system of equations and account for turbulence. The approach proposed by Boussinesq (1877) states that turbulence enhances the mixing of fluid quantities and can be treated as an additional diffusion. This leads to the following expression for the Reynolds stress tensor:

$$-\rho\overline{\mathbf{u}'\mathbf{u}'} = \mu_t(\nabla \overline{\mathbf{u}} + (\nabla \overline{\mathbf{u}})^T) + \frac{2}{3}\rho k l \tag{3.10}$$

here μ_t is the so-called eddy viscosity, l the characteristic turbulence length scale and k the turbulent kinetic energy, defined as:

$$k = \frac{1}{2}(\overline{\mathbf{u}' \cdot \mathbf{u}'}) \tag{3.11}$$

The suitability of a turbulence model for certain engineering problems depends on various factors, such as the presence of strong curvatures and/or large recirculation zones in the flow. For most marine applications, so-called two-equation models are frequently used. The $k-\varepsilon$ turbulence model, introduced by Jones and Launder (1972) and further improved by Launder and Sharma (1974), is one such model. It consists of two additional transport equations for the scalar quantities of turbulent kinetic energy k and the turbulent dissipation rate ε. In index notation, the Reynolds averaged velocity is written as $\overline{u_i}$ with indices i denoting the velocity components i, j, k in a Cartesian coordinate system. The transport equations for turbulent kinetic energy k and turbulent dissipation rate ε thus read:

$$\frac{\partial(\rho k)}{\partial t} + \frac{\partial(\rho\overline{u_i}k)}{\partial x_i} = \frac{\partial}{\partial x_j}\Big[\Big(\mu + \frac{\mu_t}{\sigma_k}\Big)\frac{\partial k}{\partial x_j}\Big] + P_k - \rho\varepsilon \tag{3.12}$$

$$\frac{\partial(\rho\varepsilon)}{\partial t} + \frac{\partial(\rho\overline{u_i}\varepsilon)}{\partial x_i} = C_{\varepsilon 1}P_k\frac{\varepsilon}{k} - \rho C_{\varepsilon 2}\frac{\varepsilon^2}{k} + \frac{\partial}{\partial x_j}\Big[\Big(\mu + \frac{\mu_t}{\sigma_\varepsilon}\Big)\frac{\partial \varepsilon}{\partial x_j}\Big] \tag{3.13}$$

here, P_k represents the production rate of turbulent kinetic energy. The turbulent viscosity, also known as eddy-viscosity, μ_t is defined as:

$$\mu_t = \rho C_\mu \frac{k^2}{\varepsilon} \tag{3.14}$$

with the model constants $C_{1_\varepsilon} = 1.44$, $C_{2_\varepsilon} = 1.92$, $C_\mu = 0.09$, $\sigma_k = 1.0$ and $\sigma_\varepsilon = 1.3$. According to Pope (2000), $k-\varepsilon$ models performs well in free stream regions, but fails for highly recirculating wall bounded flows. In this regard, the $k-\omega$ model, introduced by Wilcox (1988), offers better solutions. Analogous to the $k-\varepsilon$ model, two transport equations accounting for the turbulent kinetic energy k and the specific turbulent dissipation rate ω close the system of equations. These are respectively described by the following equations:

$$\frac{\partial(\rho k)}{\partial t} + \frac{\partial\rho\overline{u_j}k}{\partial x_j} = P_k - \rho\beta^*\rho\omega k + \frac{\partial}{\partial x_j}\Big[\Big(\mu + \sigma_k\frac{\rho k}{\omega}\Big)\frac{\partial k}{\partial x_j}\Big] \tag{3.15}$$

$$\frac{\partial(\rho\omega)}{\partial t} + \frac{\partial\rho\overline{u_j}\omega}{\partial x_j} = \frac{\alpha\omega}{k}P_k - \rho\beta\omega^2 + \frac{\partial}{\partial x_i}\Big[\Big(\mu + \sigma_\omega\frac{\rho k}{\omega}\Big)\frac{\partial \omega}{\partial x_j}\Big] \tag{3.16}$$

The turbulent viscosity μ_t is defined in $k-\omega$ turbulence model as:

$$\mu_t = \rho C_\mu \frac{k}{\omega} \tag{3.17}$$

with the different parameters being $\alpha_\omega = \frac{5}{9}$, $\beta = 0.075$, $\beta^* = 0.09$. $\sigma_k = 2.0$. While the $k-\varepsilon$ model is supposedly more suitable for the prediction of flows in free-stream regions, the $k-\omega$ model is more accurate in predicting turbulent flows in near wall regions, but performs poorly in free-stream regions. In maritime applications, the $k-\omega-$SST model, introduced by Menter (1994), is widely used and validated for a variety of hull shapes, see Larsson et al. (2013). This model combines the advantages of both models, switching to a $k-\varepsilon$ behavior in free stream regions and $k-\omega$ in near wall regions. Two-equations models can lead to substantial shortcomings when predicting flows with very strong curvatures, large recirculation zones and flow separation. In such cases, the **R**eynolds-**S**tress-equation **M**odel (RSM) tends to be more accurate. The eddy-viscosity assumption is neglected, and each component of the Reynolds stress tensor is computed. RSM offers more accuracy while keeping the computational cost lower than DNS or LES. The mathematical formulation involves a transport equation for each individual component of the Reynold's stress tensor, amounting for an additional 6 equations. Its use remains however limited due to a comparatively more demanding grid quality for convergence to be reached. Some applications of the RSM model can be found in Hadzic (1999).

A crucial issue in predicting the forces acting on a ship hull is correctly modeling the behavior of the fluid in the vicinity of the wall. This region, known as the boundary layer, is characterized by the presence of multiple layers and a correlation between tangential velocity and wall distance. According to Schlichting and Gersten (2000), one can differentiate between the viscous sublayer, where viscous stresses are dominant, and the turbulent layer, where turbulent stresses are dominant. There is also a buffer layer in between. Integrating the RANS equations down to the wall requires a fine spatial grid resolution, leading to increased computational effort. One way to overcome this issue is by using the so-called law of the wall, first introduced by von Kármán (1930). This approach introduces a dimensionless wall distance n^+ as a variable to evaluate the boundary layer:

$$n^+ = \frac{u_\tau n}{\nu} \tag{3.18}$$

where $\nu = \mu/\rho$ is the kinematic viscosity, and n is the normal distance from the wall. The shear stress velocity u_τ is defined as:

$$u_\tau = \sqrt{\frac{\tau_w}{\rho}} \tag{3.19}$$

The flow regime in the near wall region can be characterized by the dimensionless wall velocity u^+ defined as:

$$u^+ = \frac{\overline{u_{ta}}}{u_\tau} \tag{3.20}$$

where $\overline{u_{ta}}$ is the mean wall tangential velocity. The viscous sublayer is located in the region where $n^+ \leq 5$. In this region, the assumption that $u^+ = n^+$ is considered valid, as the velocity varies linearly with the distance from the wall. The logarithmic wall region is located where $n^+ \geq 30$, where the dimensionless velocity u^+ is obtained as:

$$u^+ = \frac{1}{\kappa} \ln n^+ + B \tag{3.21}$$

where τ_w is the wall shear stress, κ is the von Karman's constant and B a constant accounting for the wall roughness. In the buffer layer region, located where $5 < n^+ < 30$, the relationship between u^+ and n^+ is not well understood and its approximations can lead to inaccurate results. To achieve a more accurate simulation, it is preferable to fully resolve the boundary layers. However, this requires a finer grid resolution in the near-wall region, which can be computationally expensive. On the other hand, for simulations of flows in extreme shallow waters, it is often necessary to fully resolve the boundary layers as the interaction between the bottom and the ship can disrupt the assumptions made by the law of the wall.

3.3.2 Large Eddy Simulation

Large **E**ddy **S**imulation (LES) aims to resolve the larger scale eddies in the flow and model the smaller eddies using subgrid-scale models. The underlying assumption is that the energy contained in large-scale structures has a greater impact on the flow field and therefore plays a more significant role in the transport of flow quantities than smaller eddies. The complexity of LES models lies in the definition of a filter to determine which fluctuations in the flow field should be modeled. To this end, a low-pass filtering operation is applied to the governing equations. Roughly speaking, the filtering operation removes small eddies from the solution based on a filter width related to the grid spacing. Eddies larger than the filter size are resolved, smaller eddies are modeled. Applying the filtering operation to the Navier-Stokes equations for an incompressible fluid yields:

$$\frac{\partial(\rho\overline{u}_i)}{\partial x_i} = 0 \tag{3.22}$$

$$\frac{\partial(\rho\overline{u}_i)}{\partial t} + \frac{\partial(\rho\overline{u_i}\,\overline{u_j})}{\partial x_j} = \frac{\partial {\tau_{ij}}^s}{\partial x_j} - \frac{\partial \overline{p}}{\partial x_i} + \frac{\partial}{\partial x_j}\left[\mu\left(\frac{\partial \overline{u}_i}{\partial x_j} + \frac{\partial \overline{u}_j}{\partial x_i}\right)\right] \tag{3.23}$$

The term τ_{ij}^{s} refers to the subgrid-scale Reynolds stress, which represents the impact of small-scale structures on larger scales of the flow. To close the governing equations, this tensor must be modeled. Similar to RANS equations, appropriate closure models are needed to close the system of equations. To accomplish this, approximations referred to as subgrid-scale or subfilter-scale stress models are introduced. The main difference between RANS and LES lies in the domain considered for the filtering operation. In LES, only the locally-averaged velocity field is considered to obtain the parameters for the closure model. There are various models available in the literature, with the most commonly used ones being the Smagorinsky and dynamic models; see Sagaut (2006). In this specific study, dynamic models were implemented. Dynamic models, as introduced by Germano et al. (1991), rely on the scale similarity model. This approach assumes that the smallest resolved eddies behave similarly to the largest modeled eddies. In other words, information obtained from the smallest resolved eddies can be used to model the largest modeled eddies and so on. This approach presents advantages over Smagorinsky models, which assume isotropy of the modeled eddies, see Smagorinsky (1963).

3.3.3 Hybrid methods

Despite the widespread use of RANS methods in maritime applications, there are certain scenarios where a more detailed resolution of the turbulence is needed. Some studies, such as Arslan et al. (2016) and Liefvendahl and Fureby (2017) succesfully used LES to predict hydrodynamic forces acting on ships. However, the prohibitive computational cost of LES and the minimal gain in accuracy compared to other methods limits its use for further complex investigations. Promising alternatives are hybrid RANS/LES methods as they combine the best of both techniques. Simply put, RANS equations are solved in the boundary layer region of a test body, while LES resolves the flow in the detached far field. At the interface between RANS and LES regions, flow quantities are transferred from one region to another. The most prominent technique is the **D**etached **E**ddy **S**imulation (DES) introduced by Spalart et al. (1997), which combines a classic Smagorinsky LES model with a Spalart-Allmaras RANS model, as introduced in Spalart and Allmaras (1994), in the near-wall region. Next section briefly introduces the mechanisms governing DES and their limitations.

Detached Eddy Simulation

The Detached Eddy Simulation (DES) method, as originally formulated by Spalart et al. (1997), aims to combine the benefits of RANS and LES by using RANS near the wall and LES in the far-field separated regions. The original DES formulation, also known as DES97, employs a one-equation Spalart-Allmaras RANS model in the near-wall region and LES in the separated flow regions (Spalart et al., 1997, Spalart and Allmaras, 1994).

Later, Strelets (2001) extended the DES97 model by implementing the $k-\omega-$ SST turbulence model in the RANS region.

In DES, the transition from RANS to LES occurs using a turbulent length-scale l. Turbulent eddies characterized by a length scale smaller than the grid size are modeled using the RANS model, while those larger than the grid size are resolved using LES. This distinction is based solely on a comparison between the turbulent length scale and the grid size. To further clarify this concept, the specific dissipation rate ω in equation 3.16 is replaced by a modified dissipation rate $\tilde{\omega}$, which smoothly transitions between the RANS and LES dissipation rates across the interface between the two regions:

$$\tilde{\omega} = \omega\Phi \tag{3.24}$$

Where Φ is a variable which can equate unity, or the scale length ratio l_{ratio}:

$$\Phi = \max(l_{\text{ratio}}, 1) \tag{3.25}$$

and

$$l_{\text{ratio}} = \frac{l_{\text{RANS}}}{l_{\text{LES}}} \tag{3.26}$$

The LES length scale l_{LES} corresponds to:

$$l_{\text{LES}} = C_{\text{DES}}\Delta \tag{3.27}$$

where Δ is the largest distance between the cell center under consideration and the cell centers of the neighboring cells. The coefficient C_{DES} is determined depending on a blending function which considers both the $k-\varepsilon$ coefficient $C_{\text{DES}}^{k-\varepsilon}$ and the $k-\omega$ coefficient $C_{\text{DES}}^{k-\omega}$. The blending function reads:

$$C_{\text{DES}} = C_{\text{DES}}^{k-\omega}F_1 + C_{\text{DES}}^{k-\varepsilon}(1-F_1) \tag{3.28}$$

where F_1 is the blending function as described in Menter (1994). The RANS length scale l_{RANS} is defined as:

$$l_{\text{RANS}} = \frac{\sqrt{k}}{\beta * \omega} \tag{3.29}$$

with k the turbulent kinetic energy, β the turbulence model coefficient and ω the specific dissipation rate. The value of $\Phi = 1$ indicates a solution covered by the RANSE method, while a value of $\Phi < 1$ indicates a solution covered by the LES definition. As stated above, the models by Spalart et al. (1997) and Strelets (2001) depend only on the grid resolution. While these models demonstrated some advantages, they may lead to some issues for complex geometries:

- **Grid Induced Separation**: For an accurate implementation of DES, it is crucial to locate the interface between the RANS and LES regions outside of the boundary layer. This is typically achieved by assuming that the grid spacing in the near-wall region is significantly higher than the size of the boundary layer. At the time when DES was first developed, this assumption was reasonable due to computational limitations and the prohibitive cost of excessively fine grids. However, in cases of weakly separated flows, this ambiguous grid definition can lead to an incorrect prediction of the separation point, resulting in the RANS-LES interface being located inside the boundary layer. This phenomenon is referred to as **G**rid-**I**nduced **S**eparation (GIS).

- **Modeled Stress Depletion**: GIS has a major influence over the predicted skin friction, leading to a phenomenon known as **M**odeled **S**tress **D**epletion (MSD). When the LES solution invades the boundary layer, it reduces the modeled eddy viscosity in the RANS model, resulting in a lower predicted skin friction than expected.

- **Grey Area**: The "grey area problem" arises when neither RANS nor LES method is implemented correctly. With a sufficiently small grid resolution, the transition from the statistically averaged near-wall flow to the turbulent separated flow should occur instantaneously. However, in certain cases, this transition is delayed because of weak separation, leading to the aforementioned "grey area problem."

To overcome the limitations mentioned above, **D**elayed **D**etached **E**ddy **S**imulation (DDES) and **I**mproved **D**etached **E**ddy **S**imulation (IDDES) were developed.

Delayed Detached Eddy Simulation

The DDES method was introduced by Spalart et al. (2006) to address grid-dependent issues such as GIS and MSD. The method is a refinement of the formulation proposed by Menter and Kuntz (2004) based on the SST turbulence model. The key novelty of DDES is the introduction of velocity-dependency in the DES filtering criteria. This is achieved by using a flow-dependent shielding function f_d, that preserves the RANS solution within the attached boundary layer. Thus, DDES has been shown to be less sensitive to grid resolution than other turbulence modeling methods, making it a reliable

option for practical engineering simulations. DDES enables the use of RANS equations in a region where the wall distance d is smaller than the boundary layer thickness.

$$\tilde{d} = d - f_d \max(0, d - \psi C_{\mathrm{DES}} \Delta) \tag{3.30}$$

where C_{DES} is the model coefficient and Δ the largest distance between the cell center under consideration and the cell centers of the neighboring cells. The function f_d reads:

$$f_d = 1 - \tanh\left[(8 r_d)^3\right] \tag{3.31}$$

where:

$$r_d = \frac{\tilde{\nu}}{\sqrt{\nabla \mathbf{u} : \nabla \mathbf{u}^T} \kappa^2 d^2} \tag{3.32}$$

with κ being the von Karman constant. The function f_d equals 0 in the boundary layer and 1 outside of it. In that way, an incursion of the LES solution in the boundary layer is prevented.

Improved Delayed Detached Eddy Simulation

While the DDES formulation offers significant advantages in differentiating the zonal distribution of RANS and LES, an issue arises when considering the flow near the boundary layer. When the requirements for grid spacing in the boundary layer are excessively fine, the separation between LES and RANS takes place inside it. The location of the RANS/LES interface contrasts with the definition of DES, which aims to locate the LES solution outside of the boundary layer. In literature, this phenomenon is called **L**og-**L**ayer **M**ismatch (LLM). The main effect is that the solution develops two logarithmic boundary layers, hence the name LLM. Shur et al. (2008) proposed an improved formulation of the DDES approach. The core idea is to propose an alternative formula for the subgrid length scale. In this approach, the specific dissipation rate $\tilde{\omega}$ is defined as:

$$\tilde{\omega} = \frac{\sqrt{k}}{l_{\mathrm{HYBRID}} f_{\beta*} \beta*} \tag{3.33}$$

where $f_{\beta*}$ is the free-shear modification factor and $\beta*$ the $k-\omega-SST$ model coefficient. l_{HYBRID} is defined as:

$$l_{\text{HYBRID}} = \tilde{f}_d(1 + f_e)l_{\text{RANS}} + (1 - \tilde{f}_d)C_{\text{DES}}\Delta_{\text{IDDES}} \tag{3.34}$$

The main difference between DDES and IDDES lies in the introduction of **W**all-**M**odeled LES (WMLES) capabilities in the code. The length scale l_{HYBRID} determines the transition between RANS and LES in the wall region, where the function f_e is an elevating function. Its aim is to compensate the stress loss when the RANS/LES transition takes place inside the boundary layer by intensifying the RANS component in the transition zone. $\tilde{f}_d$ is an empirical function controlling the switch, defined as:

$$\tilde{f}_d = \min\left[2\exp(-9\alpha^2), 1\right] \tag{3.35}$$

where α is a constant defined as:

$$\alpha = 0.25 - \frac{d}{\Delta} \tag{3.36}$$

The parameters d and Δ depend on the grid resolution. The elevating function f_e is also of empirical nature:

$$f_e = \max\left[(f_{e1} - 1), 0\right]\Psi f_{e2} \tag{3.37}$$

with f_{e1} and f_{e2} are defined as follows:

$$f_{e1} = \begin{cases} 2\exp(-11.09\alpha^2), \alpha \geq 0 \\ 2\exp(-9\alpha^2), \alpha < 0 \end{cases} \tag{3.38}$$

$$f_{e2} = 1 - \max(f_t, f_l) \tag{3.39}$$

and

$$f_t = \tanh\left[(C_t^2 r_{dt})^3\right] \tag{3.40}$$

$$f_l = \tanh\left[(C_l^2 r_{dl})^1 0\right] \tag{3.41}$$

with r_{dl} and r_{dt} as the laminar and turbulent parts of rd, defined as:

$$r_{dl} = \frac{\nu}{\sqrt{\nabla\overline{\mathbf{u}} : \nabla\overline{\mathbf{u}}}\kappa^2 d^2} \tag{3.42}$$

$$r_{dt} = \frac{\nu_t}{\sqrt{\nabla\overline{\mathbf{u}} : \nabla\overline{\mathbf{u}}}\kappa^2 d^2} \tag{3.43}$$

where ν is the kinematic viscosity, $\nu_t = \frac{\mu_t}{\rho}$ with μ_t the turbulent eddy viscosity, κ the von Karman constant and d the distance to the wall. c_l and c_t are model coefficients. Finally, the mesh length scale Δ_{IDDES} is altered as to introduce a linear variation of the length scale depending on the wall distance d.

$$\Delta_{\text{IDDES}} = \min(\max(0.15d, 0.15\Delta, \Delta_{\min}), \Delta) \tag{3.44}$$

Here, $\Delta_{\min}$ represents the smallest distance between the cell center under consideration and the cell centers of the neighboring cells. In this work, IDDES is used for a specific case, i.e. the numerical prediction of the flow in the gap between pusher-boat and barge. The vast majority of the simulations were performed using RANSE with the $\mathrm{k}-\omega-\mathrm{SST}$ turbulence model.

3.4 Multiphase flow

When considering surface vessels, it becomes necessary to capture the deformation of the free surface to include its effect on hydrodynamic forces and moments acting on the hull. In this work, free surface simulations were performed using the **V**olume of **F**luid (VoF) method. This interface-capturing method defines a volume fraction α in the CV as the ratio between the phase volume V_α and the total CV's volume V_{CV}:

$$\alpha = \frac{V_\alpha}{V_{CV}} \tag{3.45}$$

Necessarily, the overall sum of all phases volumes in the CV equals to its volume, and therefore, the sum of all volume fractions yields:

$$\sum_i \frac{V_{\alpha_i}}{V_{CV}} = 1 \tag{3.46}$$

An additional transport equation has to be solved for the volume fraction. α being a scalar quantity, the equation reads:

$$\frac{\partial}{\partial t}\int_V \alpha \mathrm{d}V + \int_S \alpha \mathbf{u}\cdot\mathbf{n}\mathrm{d}S = 0 \tag{3.47}$$

Particular attention should be paid to spatial and temporal discretization to avoid undesirable smearing of the free surface. In this work, the **H**igh **R**esolution **I**nterface **C**apturing scheme (HRIC) is utilized to ensure interface sharpness, see Muzaferija and Perić (1997).

3.5 Discretization methods

Approximations in time and space are needed to obtain a discretized form of the Navier-Stokes equations. While numerous methods are available, the **F**inite **V**olume **M**ethod (FVM) as implemented in Simcenter STAR-CCM+ is used in this thesis. The spatial discretization consists in dividing the computational domain into CVs of arbitrary shape. In each CV, the conservation principles must be satisfied. For transient simulations, a temporal discretization is also required. To illustrate the method, a generic transport equation for a scalar quantity ϕ is considered. The equation reads:

$$\underbrace{\frac{\partial}{\partial t}\int_V \phi \mathrm{d}V}_{\text{Transient term}} + \underbrace{\int_S \rho\phi\mathbf{u}\cdot\mathbf{n}\mathrm{d}S}_{\text{Convective term}} = \underbrace{\int_S \Gamma\nabla\phi\cdot\mathbf{n}\mathrm{d}S}_{\text{Diffusive term}} + \underbrace{\int_V \mathbf{S}_\phi \mathrm{d}V}_{\text{Source term}} \tag{3.48}$$

where Γ is a constant diffusion coefficient and S_ϕ is a source term of the variable ϕ. This equation contains surface and volume integrals as well as time and space derivatives. The goal is to transform these terms into discrete expressions in order to obtain an algebraic system of equations for the variable values at cell centers.

3.5.1 Approximation of surface and volume integrals

Considering the scalar quantity ϕ, the volume integral can be approximated simply as the product of the CV's volume ΔV and the mean value of the quantity stored at the CV's center P:

$$\int_V \phi \mathrm{d}V \approx \phi_P \Delta V \tag{3.49}$$

This method, known as the midpoint rule, requires no further interpolation since the distribution of ϕ is assumed to be constant or linear. Higher order approximations can

be used to minimize the truncation error, see Ferziger et al. (2019). The surface integral of a CV's surface, denoted as S, can be represented as the sum of the surface integral over each individual face of the CV, denoted as f. Similar to equation (3.49), the midpoint rule is utilized to create a discrete expression. The integrand in this case is the value of the flow quantity ϕ at the center of the control volume's face f, resulting in the following expression:

$$\int_S \phi \mathrm{d}S \approx \sum_f (\phi_f S_f) \tag{3.50}$$

As mentioned above, the values of a variable are stored at the center of each CV. Therefore, the value of ϕ at the CV's face center can be interpolated from the values of the variable in neighboring control volumes. Any interpolation technique relies on an assumed progression of ϕ between two neighboring CV. To maintain second-order accuracy, a linear interpolation scheme may be used. For a face with index f and two neighboring CVs P and N, as shown in figure 3.1, the formula is as follows:

$$\phi_f = \phi_P + \frac{\phi_P - \phi_N}{(\mathbf{x}_P - \mathbf{x}_N) \cdot \mathbf{n}} (\mathbf{x}_f - \mathbf{x}_P) \cdot \mathbf{n} \tag{3.51}$$

whereas ϕ_P and ϕ_N are the values of ϕ in cell P with position $\mathbf{x}_P$ and its neighbor cell N with position $\mathbf{x}_N$, $\mathbf{x}_f$ is the position of the face f. Henceforth, linear interpolation constitutes the foundation of the so-called **C**entral **D**ifferencing **S**cheme (CDS), used for the approximation of gradients of diffusive fluxes:

$$\left(\frac{\partial \phi}{\partial x}\right)_f \approx \frac{\phi_N - \phi_P}{x_N - x_P} \tag{3.52}$$

Further interpolation techniques of same or higher order can be found in literature, see (Ferziger et al. (2019)).

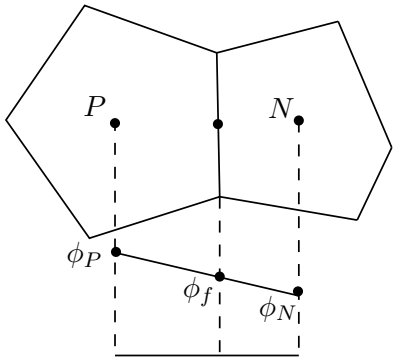

Figure 3.1: Schematic representation of interpolation of ϕ_f at the face f between two cells using the linear interpolation.

3.5.2 Discretization of convective and diffusive fluxes

The surface integral for a CV's face f in the convective term in equation (3.48) is approximated according to the method described in the previous section:

$$\int_S \rho\phi\mathbf{u}\cdot\mathbf{n}\mathrm{d}S \approx \sum_f \phi\rho(\mathbf{u}\cdot\mathbf{n}S)_f = \dot{m}_f\phi_f \tag{3.53}$$

The term $\dot{m}_f$ represents the mass flow rate. The convective flux is therefore defined as the transport of the variable ϕ through the face f of the CV via mass flow. The value of ϕ_f can be interpolated using the scheme described in the previous section. Other techniques may be utilized to enhance the stability of the numerical solution. The solver in this method chooses the techniques based on the formulation of the flow problem. Techniques such as **F**irst-**O**rder **U**pwind (FOU), **S**econd-**O**rder **U**pwind (SOU), CDS, or hybrid schemes are used. Applying the same procedure to the diffusive term results in:

$$\int_S \Gamma\nabla\phi\cdot\mathbf{n}\mathrm{d}S \approx \sum_f(\Gamma\nabla\phi\cdot\mathbf{n}S)_f \approx \sum_f\left(\frac{\partial\phi}{\partial\mathbf{n}}S\right)_f \tag{3.54}$$

where Γ is the diffusion coefficient, $\nabla\phi$ is the gradient of the scalar quantity ϕ. The derivative in the direction of the face normal $\mathbf{n}$ can be approximated using CDS, as stated above.

3.5.3 Approximation of temporal derivatives

For transient flows, it is necessary to approximate the temporal derivative in order to compute the variable ϕ at the next time step, denoted as $t_{N+1} = t_N + \Delta t$. This can be achieved by using an appropriate time discretization scheme, which can be either explicit or implicit. Explicit schemes rely on the past solutions to compute the desired value at t_{N+1}, while implicit schemes take into account both expressions from previous and current time steps. Therefore, they require the solution of a linear system of equations. In this work, simulations were performed using the **T**hree-**T**ime-**L**evel (TTL) method, an implicit second-order time integration scheme, which discretizes the transient term as follows:

$$\frac{\partial}{\partial t}\int_V \rho\phi \mathrm{d}V = \frac{3(\rho\phi)^{N+1} - 4(\rho\phi)^N + (\rho\phi)^{N-1}}{2\Delta t}V \tag{3.55}$$

This scheme considers flow variables from three time steps, $N-1$, N, and $N+1$, which leads to higher memory requirements. However, it ensures stability and tends to yield non-oscillatory solutions. A useful metric to assess whether the time step in a simulation is appropriate is the **C**ourant-**F**riedrichs-**L**ewy (CFL) number, defined as:

$$\mathrm{CFL} = \frac{u\Delta t}{\Delta x} \tag{3.56}$$

Where Δx is the grid spacing. To ensure the stability of explicit time discretization methods, the CFL number should usually be less than unity. When used in conjunction with the **H**igh **R**esolution **I**nterface **C**apturing (HRIC) scheme for free-surface flows and a second-order scheme, the CFL number should be less than 0.5, to ensure sharpness of the interface. A detailed review of temporal discretization techniques can be found in reference Ferziger et al. (2019).

3.6 Boundary conditions

Simulations of fluid flows are mathematical problems that require the definition of a domain in which conservation laws are satisfied. However, the algebraic system of equations can only yield a solution by defining suitable boundaries for the domain. This issue is referred to as the boundary value problem. There are two types of boundary condition:

- **Neumann condition** : The gradient of ϕ is defined at a location x_i. For instance:

$$\frac{\partial\phi(x_i)}{\partial x} = f(\mathbf{x}, t) \tag{3.57}$$

- **Dirichlet condition** : The value of ϕ is defined at a location x_i. For instance:

$$\phi(x_i) = f(\mathbf{x}, t) \tag{3.58}$$

Dirichlet and Neumann conditions are mathematical tools used to express an assumptions, such as a wave at the inlet. Following boundary conditions are used in this work:

- **Inlet**: A fixed value for velocity, volume fraction and turbulence is set. A pressure gradient is defined.

- **Outlet**: In this case, the pressure is defined as a function of the hydrostatic pressure. As for velocity, volume fraction and turbulence, a gradient is defined.

- **No-Slip Wall**: The velocity a the cell face corresponding to a wall is set to wall velocity, as to take the no-slip condition into account. Pressure at the wall is obtained by interpolation from interior points. Turbulence variables are computed according to a wall function in case one is used.

- **Symmetry**: The normal component of velocity is zero. Zero gradient conditions are specified for the tangential component of the velocity and for the remaining variables.

3.7 Pressure velocity coupling

The momentum and mass conservation equations do not contain a distinct expression for the calculation of pressure, despite the pressure gradient ∇p in the momentum conservation equation. Additionally, the mass conservation equation serves more as a condition that needs to be satisfied when solving the momentum conservation equation. However, an expression for the pressure can be derived by combining the conservation equations, in the form of the Poisson equation. For an incompressible Newtonian flow, the following Poisson equation for pressure is obtained by taking the divergence of the vector form of the momentum equation:

$$\frac{\partial}{\partial x_i}\left(\frac{\partial p}{\partial x_i}\right) = -\frac{\partial}{\partial x_i}\left[\frac{\partial\left(\rho u_i u_j\right)}{\partial x_j}\right] \tag{3.59}$$

The solution method implemented in the solver used in this work uses a pressure-correction equation. This equation is derived from a discretized continuity and momentum equation, see Ferziger et al. (2019). The set of equations to be solved includes

the three equations for the conservation of momentum and the pressure correction equation. Solving them all simultaneously requires a significant amount of computing power. The solver used in this work employs the **S**emi-**I**mplicit **M**ethod for **P**ressure-**L**inked **E**quations (SIMPLE) to solve the conservation equations in a segregated manner, as described in Patankar (1980). The main steps of the SIMPLE algorithm can be summarized as follows:

- An initial pressure field is used to solve the momentum equation. An intermediary velocity field $\mathbf{u}^*$ is created. This velocity field does not satisfy the continuity equation.
- The intermediary velocity field $\mathbf{u}^*$ is used to solve a pressure correction equation.
- The pressure correction is used to compute an updated pressure field p^*.
- The gradient of the pressure correction field is used to compute updated velocities $\mathbf{u}^{**}$, which satisfy the continuity equation, but not the momentum equation.
- The velocity and pressure fields are iteratively corrected by solving in turn momentum equations and the pressure-correction equation, until both the momentum equations and the continuity equation are satisfied simultaneously.
- The converged values are used to initialize the next time step.

3.8 Error estimation

It is important to conduct an uncertainty analysis on numerical results to ensure their validity and reliability. The process of error quantification is crucial for estimating uncertainties. According to Eça and Hoekstra (2009), errors can be classified into categories such as modeling, discretization, iterative, input, and round-off errors.

Modeling errors are associated with the mathematical formulation of a physical phenomenon and the necessary simplifications made to decrease computational cost. This is particularly relevant for simulations of turbulent flows. Different simulations in marine hydrodynamics often involve empirical assumptions about turbulence, such as ship resistance in shallow water. In other cases, the use of scale-resolving methods may be more appropriate. Modeling errors can be assessed through comparison with robust experimental data, a process called validation. This process also requires an uncertainty analysis of the experimental results.

Round-off in a computer refers to the difference between the exact value of a number and its representation. However, modern CFD codes typically use double-precision represen-

tation, minimizing thus round-off errors. Iterative errors denote the difference between the approximated and exact solutions of the algebraic system of equations. The residuals provide a useful tool for controlling the iterative convergence of a simulation. In this work, convergence is considered to have been reached when the residuals have fallen by at least two orders of magnitude for unsteady problems. Similar indications are given in Ferziger et al. (2019).

Discretization errors arise from the representation of governing equations in algebraic expressions in a discrete temporal and spatial domain. Several quantification procedures are available, see Eça and Hoekstra (2009). The procedure suggested by Oberhagemann (2017) and el Moctar et al. (2021) is used in this work. Mewes (2021) demonstrated the validity of this method for free surface flows. Time-step and grid size are refined using the same refinement ratio r_k, to keep the CFL number constant in all considered solutions, a minimum of three successive refinements with a fixed r_k value is needed for error estimation.

$$r_k = \frac{\Delta h_{k_2}}{\Delta h_{k_1}} = \frac{\Delta h_{k_3}}{\Delta h_{k_2}} \tag{3.60}$$

where Δh_{k_i} is the base size of a grid or a time step, with indexes $i = 1, 2, 3$ identifying, respectively, the fine, medium, and coarse grids. The convergence ratio R_k is defined as follows:

$$R_k = \frac{\phi_2 - \phi_1}{\phi_3 - \phi_2} \tag{3.61}$$

where ϕ_i is the solution obtained on grid i. The solution's convergence is monotonic when $0 < R_k < 1$; oscillatory, when $-1 < R_k < 0$; and diverging, when $R_k > 1$. Following the procedure by Oberhagemann (2017), the grid-independent solution ϕ_0 corresponds to a solution obtained on a grid of infinitesimally small grid spacing. The discretization error δ is then defined as follows:

$$\epsilon \approx \delta = \phi_i - \phi_0 = a_1 \Upsilon_i + a_2 \Upsilon_i^2 + \dots \tag{3.62}$$

where Υ_i is the dimensionless scalar refinement ratio defined as:

$$\Upsilon_i = \sqrt{\frac{1}{4}\left[\left(\frac{1}{r_x}\right)^{2(i-1)} + \left(\frac{1}{r_y}\right)^{2(i-1)} + \left(\frac{1}{r_z}\right)^{2(i-1)} + \left(\frac{1}{r_t}\right)^{2(i-1)}\right]} \tag{3.63}$$

where r_x, r_y, r_z and r_t are the refinement factors in x, y, z direction and in time. In our case, this factor is constant in space and time. Least-square minimization is applied to first- and second order polynomial of equation (3.62):

$$S_1\left(\phi_0, a\right) = \sqrt{\sum_{i=1}^{n_g} \left(\phi_i - \left(\phi_0 + a\Upsilon_i\right)\right)^2} \tag{3.64}$$

$$S_2\left(\phi_0, a_1, a_2\right) = \sqrt{\sum_{i=1}^{n_g} \left(\phi_i - \left(\phi_0 + a_1\Upsilon_i + a_2\Upsilon_i^2\right)\right)^2} \tag{3.65}$$

with n_g the number of refinement levels. Oscillatory convergence may be acceptable if the differences between the solutions are small. In this work, extrapolation of grid independent solutions was performed only in case of monotonic convergence.

4 Candidate Ship and Experimental Setup

This chapter presents the candidate pusher-barge combination and the experimental setup used to measure the hydrodynamic forces and moments acting on a pushed convoy. The first section provides an overview of the main design features of the pusher-boat and barges, including the steering and propulsion systems. The experimental setup for each of the steady maneuvering tests, including resistance and propulsion, drift, and rudder variation, is then described and discussed. Detailed information on the test basins, location of load cells, and the experimental conditions used is provided. The content of this chapter has been partly published in Zentari et al. (2022), with partly exact wording.

4.1 Candidate ship

The pusher boat was designed in collaboration with the Development Centre for Ship Technology and Transport Systems (DST - Entwicklungszentrum für Schiffstechnik und Transportsysteme e. V., in German), see Guesnet (2017). The pusher boat model was equipped with two nozzles, two ducted propellers, and a single rudder placed behind each propeller. Each nozzle was located underneath a tunnel situated in the aft part of the pusher boat (see figure 4.7). A wedge shaped bow characterized each barge. Figure 4.1 depicts the lines plans of the pusher boat and one of the barges, and table 4.1 summarizes their full-scale principal particulars. Model tests were performed at a scale of $\lambda = 16$. The combinations of pusher boat and barges represented typical convoy configurations navigating on the Rhine river. A two digit code designated each configuration. The first digit indicated the longitudinal arrangement of the barges; the second digit, the transverse arrangement. The following three configurations were tested:

- configuration 1:1, characterized by a bow-stern coupling between pusher boat and one barge;
- configuration 2:1, characterized by a bow-bow coupling between pusher boat and aft barge and a stern-stern coupling between first barge and aft barge;
- configuration 2:2, characterized by a bow-bow coupling between pusher boat and aft two barges and a stern-stern coupling between two aft barges and two first barges.

Figure 4.2 shows a top view of the three arrangements of the pusher boat and the barges as models tested at the Hamburg ship model basin (**H**amburgische **S**chiffbau **V**ersuchs**A**nstalt HSVA, in German). The dot marks the location of the six-component reference frame. For each configuration, for the pusher boat itself, and for one barge alone, Table 4.2 lists coordinates x_{pmm}, y_{pmm}, z_{pmm}, of the load cells, mass m of the modeled pusher-barge configurations and coordinates x_G, y_G, z_G of their center of gravity about the x, y, z coordinates. These coordinates refer to a coordinate system with its origin located amidships of each configuration, on the center line of the pusher boat, and on the calm waterline plane. The x-axis points forward, the y-axis to starboard, and the z-axis downward. The centers of gravity depended on the location of the load cells. All entries in table 4.1 refer to the models tested.

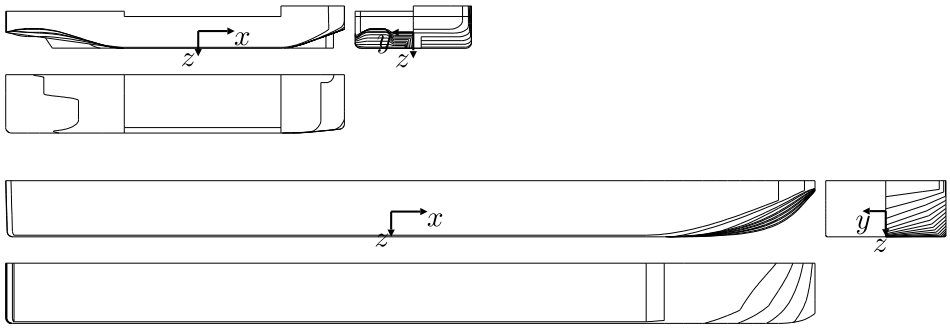

Figure 4.1: Lines plan and coordinate system of the pusher boat (without rudders, nozzles, and propellers) and one of the barges.

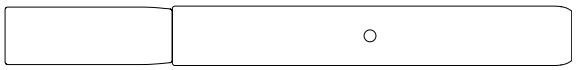

(a) Configuration 1:1

(b) Configuration 2:1

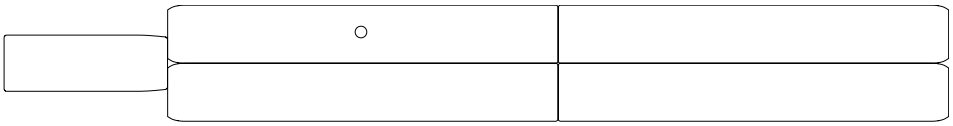

(c) Configuration 2:2

Figure 4.2: Top view of the three tested configurations of the pusher-barge convoy and the respective position of the six-component force balance.

Table 4.1: Principal particulars of the pusher-boat and of the barge at full scale.

Description	Symbol	Unit	Pusher Boat	Barge
Length over all	L_{OA}	[m]	32.00	76.45
Breadth	B	[m]	11.00	11.36
Draft	T	[m]	1.60	2.80
Volume	V	[m^3]	405.286	2245.71
Wetted surface	S_W	[m^2]	434.60	1246.60
Longitudinal center of gravity	x_G	[m]	1.609	-2.718

Table 4.2: Coordinates of the load cells, masses of the pusher-barge systems and coordinates of the centers of gravity of each configuration, of the pusher boat itself, and of one barge alone at model scale.

Symbol	Unit	Conf. 1:1	Conf. 2:1	Conf. 2:2	Pusher Boat	Barge
x_{pmm}	[m]	-0.186	-0.203	-0.203		
y_{pmm}	[m]	0.000	0.000	-0.355		
z_{pmm}	[m]	-0.090	-0.090	-0.090		
m	[kg]	646.600	1194.300	2289.700	98.800	547.700
x_G	[m]	0.3533	0.5301	0.7549		
y_G	[m]	0.000	0.000	0.000	0.000	0.000
z_G	[m]	-0.010	0.0005	0.006		

The coupling system between pusher boat and one barge or two barges, which allowed relative heave and pitch motions between pusher boat and barge or barges, consisted of three vertical poles that were attached to mobile transverse beams sliding along these poles as shown in figure 4.3. A 2.0 mm gap was left between pusher boat and barge or barges to avoid collisions in case of sudden motions. To constrain relative motions between barges in configurations 2:1 and 2:2, they were rigidly fixed to each other using a wooden beam mounted at their edges. Propulsion and steering devices consisted of two four-bladed outward turning ducted propellers and two fishtail rudders. Figure 4.7 shows a detailed view of the pusher-boats aft body, and figure 4.8 depict principal dimensions and particulars of the fish-tail rudder. Type 19-A Wageningen series nozzles surrounded the propellers. The corresponding servo engines and gear boxes were mounted, respectively, inside and outside the aft ends of the pusher boat. Two poles mechanically coupled the port and starboard shafts. Propellers and ducts were identical to the ones used for the inland waterway test case of Mucha et al. (2017). Open water characteristics of propellers and nozzles, as well as geometries, were provided. Rudders had a fishtail transverse profile with a fixed plate around the base. Tables 4.3, 4.4, and 4.5 list, respectively, principal particulars of propellers, rudders, and nozzles, all referred to the tested scale models.

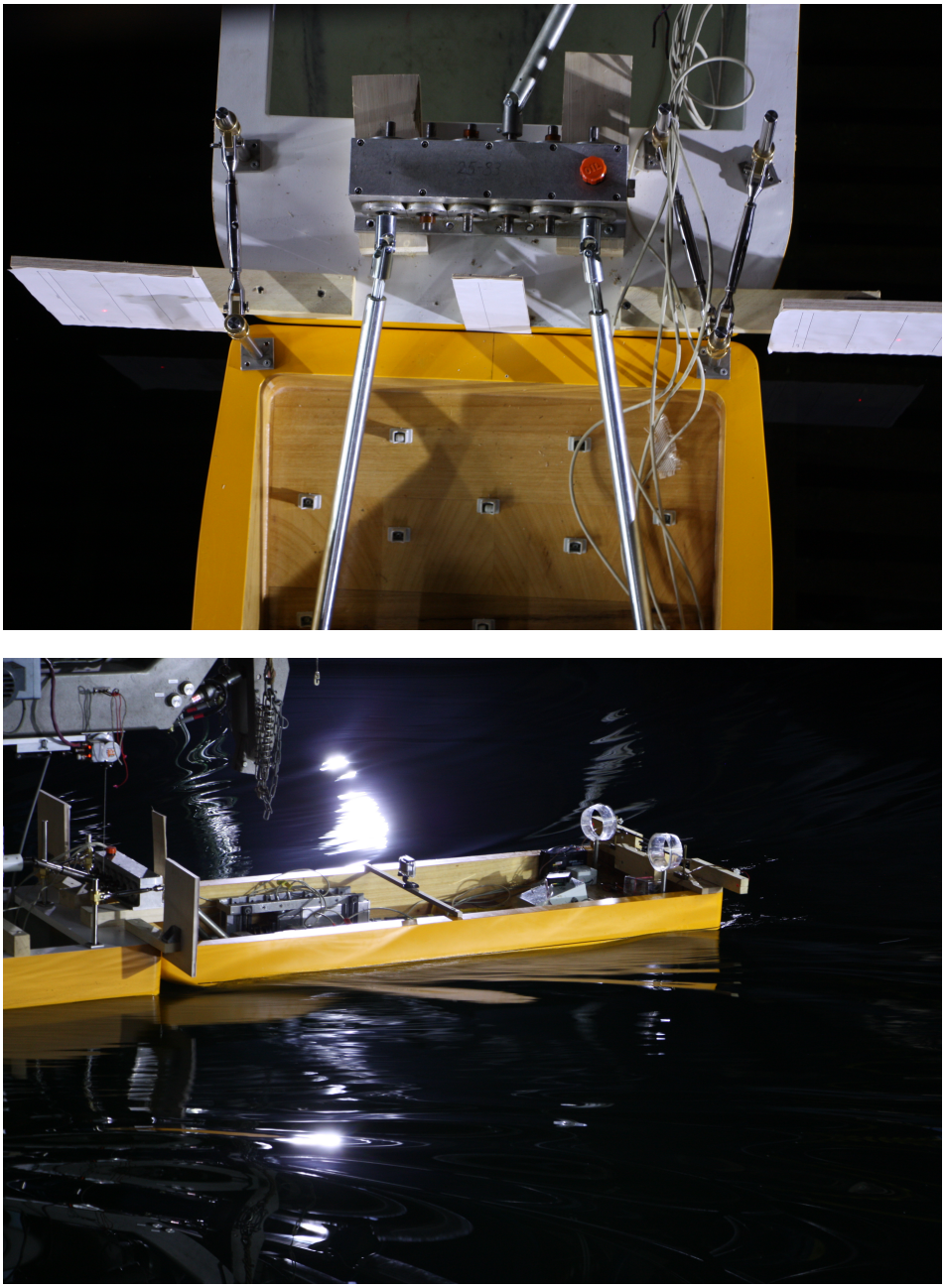

Figure 4.3: Top view and side view of the coupling system.

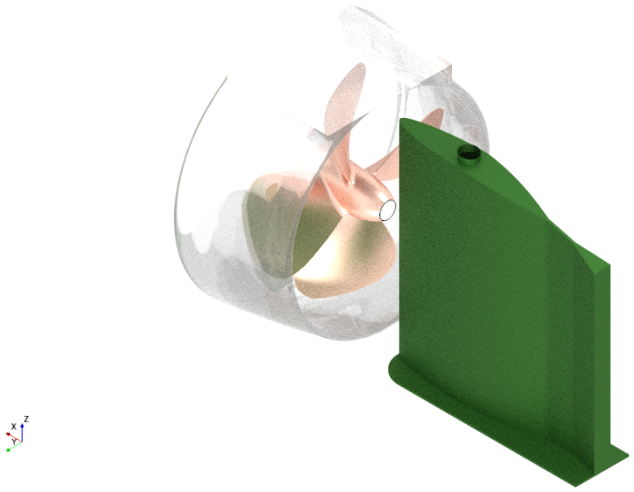

Figure 4.4: Rendered view of propulsive and steering devices arranged in the tunnels of the pusher-boat.

Figure 4.5: Detailed side view of the propulsive and steering devices arrangement.

Figure 4.6: Detailed stern view of the propulsive and steering devices arranged in the tunnels of the pusher-boat.

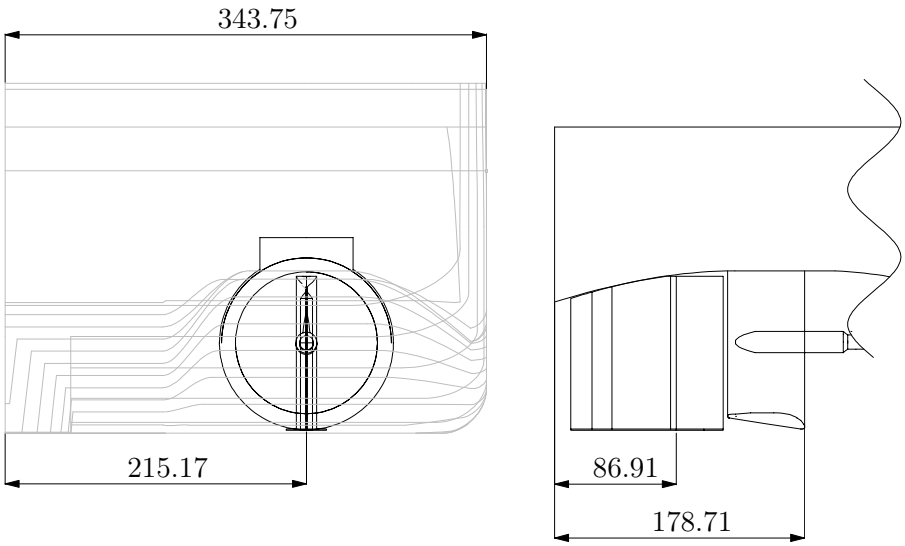

Figure 4.7: View of the after body of the pusher boat showing one of the ducted propellers with its rudder, all units in mm.

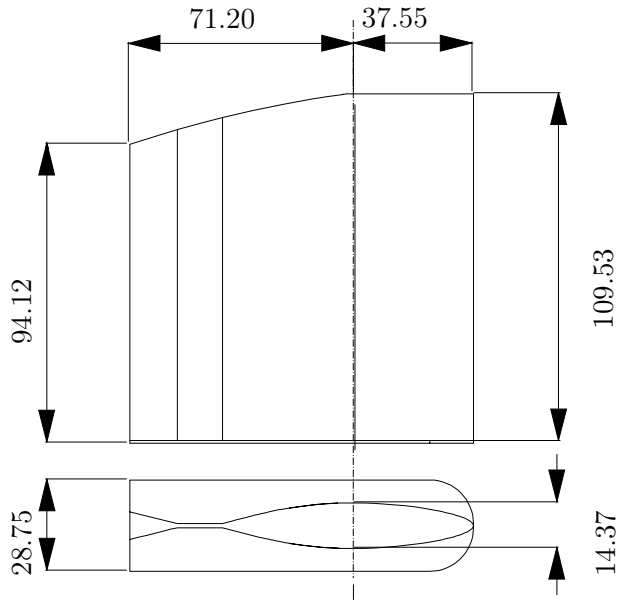

Figure 4.8: Principal particulars of rudder, all units in mm.

Table 4.3: Principal particulars of the modeled propellers.

Description	Symbol	Unit	Value
Scale factor	λ	[-]	16
Diameter	D_p	[m]	0.100
Pitch ratio	P_{07}/D_p	[-]	1.052
Disc Ratio	A_E/A_0	[-]	0.710
Chord length	C_{07}	[m]	0.040
Non-dimensional hub diameter	d_h/D_P	[-]	0.185
Number of blades	Z	[-]	4
Position to keel	Z_p	[m]	0.059

Table 4.4: Principal particulars of the modeled rudders.

Description	Symbol	Unit	Value
Scale factor	λ	[-]	16
Lateral ruder area	A_r	[m^2]	0.0115
Chord length	c	[m]	0.108
Aspect ratio	Λ_r	[-]	0.903
Thickness	t	[m]	0.0114

Table 4.5: Principal particulars of the modeled ducts.

Description	Symbol	Unit	Value
Scale factor	λ	[-]	16
Duct length	L_D	[m]	0.0550
Inner diameter	D_i	[m]	0.102
Length to diameter ratio	L_D/D_i	[-]	0.5392
Diameter at entry	D_{DEN}	[m]	0.1194
Diameter at exit	D_{DEX}	[m]	0.1046

4.2 Experimental setup

4.2.1 Overview of the performed tests

Within the scope of this work, the primary focus was to examine the influence of shallow water on hydrodynamic forces and moments acting on inland pusher-barge configuration. To achieve this, a systematic experimental investigation was carried out. The experimental tests involved typical captive maneuvering tests to determine hydrodynamic coefficients for a mathematical model. Table 4.6 lists all the tests performed, including the type of test, water depth ratio h/T, ship velocity U, drift angle β, rudder angle δ, and propeller revolution rate n. The listed parameters are applicable for all tested configurations, except for the propeller revolution rate, which varies based on the corresponding configuration. The first value in the column n represents the propulsion point of configuration 1:1; the second value corresponds to configuration 2:1; and the third value corresponds to configuration 2:2.

Table 4.6: Overview of the experimental test matrix in deep and shallow water. The listed parameters are valid for all tested configurations.

Test	h/T [-]	U [m/s]	β [°]	δ [°]	n [1/s]
Resistance	∞	0.556; 0.8329; 1.106	0	0	0
	2.0				
	1.5	0.556; 0.694			
	1.2				
Propulsion	∞	0.556; 0.8329; 1.106	0	0	varied
	2.0				
	1.5	0.556; 0.694			
	1.2				
Drift	∞	0.556	4; 8; 12; 16	0	9.70; 10.90; 12.90
	2.0				11.09; 12.29; 15.75
	1.5				
	1.2				
Rudder	∞	0.556	0	0:5:60	9.70; 10.90; 12.90
	2.0			5; 10; 20; 30; 45; 60	11.09; 12.29; 15.75
	1.5				
	1.2				

4.2.2 Resistance and propulsion

Deep water tests were carried out in the large towing tank of HSVA. A large six-component force balance measured the forces. The location of the six-component force balance differed for each configuration (see figure 4.2). For configuration 1:1, this balance was situated in the one barge being pushed; for configuration 2:1, in the aft barge of the two barges being pushed; for configuration 2:2, in the aft port barge of the four barges being pushed. The resistance tests were performed at design draft under deep water conditions for three speeds, corresponding to Froude numbers ranging from $Fn = 0.052$ to 0.136. The associated full-scale speeds of 8, 12, and 16 km/h corresponded to a typical forward speed range of inland waterway vessels in German waterways. During these tests, the water temperature was 18.9 °C, the water density was 999.983 kg/m^3. Resistance tests were run under bare hull conditions with mounted rudders at 0°. The models were free to heave and pitch, but otherwise constrained, and the pusher boat was free to heave and pitch relative to the barges. An optical tracking device, consisting of two laser

pointers mounted on the aft part of the pusher boat and pointing at a displayed range fastened to the bow of the pusher boat, measured the relative motion of the pusher boat. During these test runs, a camera fixed on the pusher boat captured the position of the laser relative to the global coordinate system of the six-component force balance. The raw video material was then analyzed using an algorithm that monitored the relative position of the pusher boat.

Shallow water tests were carried out in the shallow water basin at the **M**aritime **R**esearch **I**nstitute **N**etherlands (MARIN). The basin is 220 m long, 15.8 m wide, and 1.15 m deep. The facility is equipped with PMM capabilities. The basin is particularly adapted for resistance and self-propulsion tests in shallow water for inland waterway vessels and large push-tow fleets. Three water depth to draft ratios h/T were tested: 2, 1.5, and 1.2. The model setup was identical to the one used at HSVA. Two time two potentiometers measured heave and pitch motions of the pusher and barge independently. Full scale speeds of 8.0 km/h and 10.0 km/h were tested, corresponding to typical velocities of convoys sailing in shallow to extreme shallow waters.

Propulsion tests were conducted following the ITTC (1999) performance prediction method. The pusher boat was fitted with the two rudders situated behind the two ducted propellers. For a specified constant carriage velocity U, the total resistance force X was measured for four propeller rotation rates n.

4.2.3 Steady drift tests

Drift tests were conducted in the large towing tank of HSVA using the CPMC facility, as described in Oltmann and Sharma (1984), to measure the forces acting on a pusher-barge system in deep water conditions. A six-component force balance was used to measure the forces and its location was adjusted for each configuration, as shown in Figure 4.2, which was the same as the resistance and propulsion tests described earlier. The tests were conducted at a design draft of $T = 0.175$ m, under deep water conditions at a velocity of $U = 0.556$ m/s, which corresponds to a typical inland waterway convoy velocity of 8 km/h at full scale. Four drift angles were tested for each configuration: 4°, 8°, 12°, and 16°. These tests were also run with fully appended pusher with rudders at 0° deflection angle. The tests were performed at the previously determined propulsion point using the British method. Similar to the resistance tests, the models were allowed to pitch, heave and roll, while the pusher was allowed to heave and pitch relative to the barges. Prior to each run, the tested configuration was set to the appropriate drift angle using the CPMC facility, as illustrated in figure 4.9. In each run, four drift angles were tested for 50 s each. Mean values of total longitudinal force X, total transverse force Y and total yaw moment N in relation to the ship-fixed coordinate system were obtained by averaging over the last 20 s of each measurement interval.

Drift tests in shallow waters were conducted in the shallow water maneuvering basin at MARIN, equipped with PMM capabilities. Using the same experimental setup as the deep water tests, three water depth to draft ratios were tested: $h/T = 2.0$, $h/T = 1.5$, and $h/T = 1.2$. The models were free to move in the heave, pitch, and roll directions, while the pusher was free to move in the heave and pitch directions relative to the barges. For each water depth, four drift angles of $4°$, $8°$, $12°$, and $16°$ were tested at a model speed of $U = 0.556$ m/s. The convoys were fully appended, with the propeller delivering the thrust previously determined in propulsion tests. Forces X, Y and moment N were measured in each run for a single drift angle over a measurement time of 300 s. The mean value of forces and moments was determined by averaging over an interval of 150 s. In shallow waters, some drift tests were repeated.

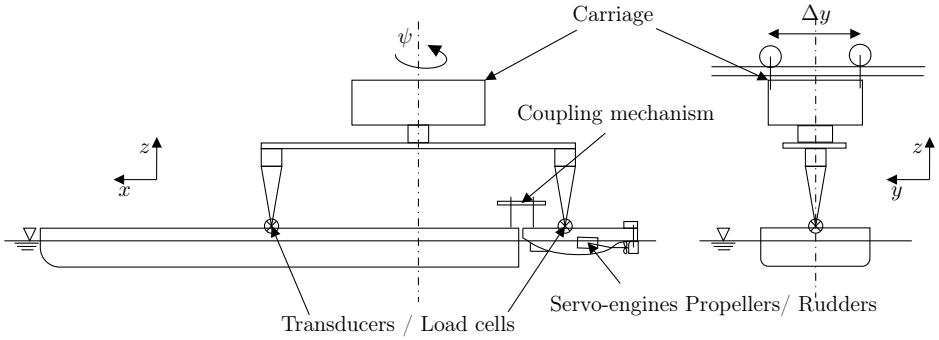

Figure 4.9: Schematized side (left) and front (right) view of the experimental setup for captive maneuvering tests in deep and shallow waters.

4.2.4 Steady rudder variation tests

Steady rudder variation tests in deep water were carried out in the same test conditions as drift tests. The models were fully appended, operating at propulsion point. Two synchronized servo-motors were used to modify the rudder angle δ. The models were towed in a constrained straight ahead position with a drift angle of $0°$. During a measurement time of 300 s, the rudder position was varied each 20 s, starting from a rudder angle of $5°$ up to $65°$ amounting to a total of 12 rudder angles. Averaging over an interval of 10 seconds yielded the mean value of forces and moments. No repeatability is available for these tests.

In shallow water, the experimental setup for rudder tests is identical to drift tests. While operating at propulsion point, the models were carried out in a constrained straight ahead position over a measurement time of 300 s. Two rudder positions were investigated during this measurement time. In total, forces and moments were measured for 6 distinct rudder position of respectively $5°, 10°, 20°, 30°, 40°, 65°$, for a total of three runs for water depth to draft ratios of $h/T = 2.0,\ 1.5$ and 1.2. The average value of forces and moments was

determined over an interval of 100 s. In extreme shallow waters, some rudder variation tests were repeated.

Figure 4.10 shows a photograph of configuration 1:1 being tested using the CPMC facility at HSVA, while figure 4.11 illustrates a photograph of the same configuration being tested in the PMM facility at MARIN.

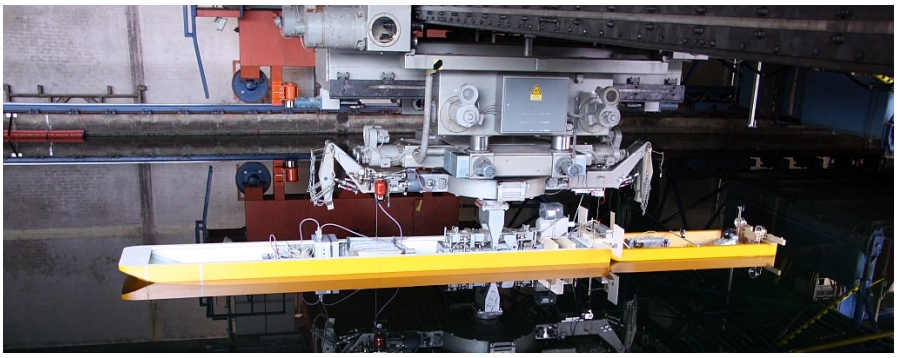

Figure 4.10: Side view of the experimental setup for deep water captive maneuvering tests with configuration 1:1.

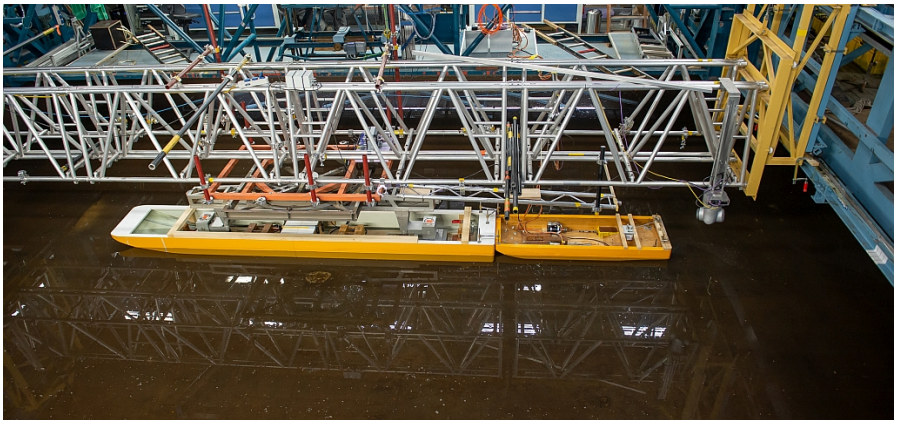

Figure 4.11: Side view of the experimental setup for shallow water captive maneuvering tests with configuration 1:1.

4.3 Concluding remarks

In this chapter, an overview of the experimental setup and the tested pushed convoy model is provided. The focus of the experimental campaign was to quantify the impact of water depth on the forces and moments acting on a maneuvering convoy. However, certain aspects of the procedure are worth noting. According to the ITTC guidelines,

the model size should not exceed a certain limit to minimize interactions with the basin's side walls. This is particularly important in shallow waters to avoid overlapping lateral and horizontal water restriction effects on forces and moments. However, choosing a smaller model would have meant sacrificing the size of the propellers and rudders, which are essential in assessing the maneuverability of a vessel. Another aspect to consider is the way drift and rudder variation tests were conducted in deep waters. Varying the drift or rudder angle over one run may lead to the so-called memory effect, where the ship model is towed in turbulent waters and measurements are partially distorted. This effect is mitigated in shallow water tests, where only one drift angle per run was investigated. Repeatability of experiments was also considered in some cases. Quantification of uncertainty in PMM tests is given in Yoon et al. (2015). Examples of efficient design of PMM tests in shallow waters are given by Eloot (2006).

5 Resistance and Propulsion

This chapter presents an investigation on the resistance and propulsion of pusher-barge systems in deep and shallow water. Specifically, the emphasis was placed on the experimental and numerical quantification of the shallow water effect on resistance and propulsion. Herein, experimental results of resistance and propulsion tests, obtained via the procedure presented in chapter 4, are presented and discussed. Thereafter, the numerical procedure used to numerically reproduce the resistance tests is introduced. These results were validated against experimental data for configurations 1:1, 2:1 and 2:2 and four different water depths, ranging from deep to extreme shallow water. Finally, noticeable physical effects are explained and discussed. The content of this chapter has been partly published in Zentari et al. (2022), with partly exact wording.

5.1 Computational procedure

The purpose of numerical simulations was to validate a computational procedure adopted to reliably predict the resistance of pusher-barge systems in deep and shallow waters. Preliminary calculations highlighted the fact that, despite the low Froude numbers encountered for the tested convoys, the free surface significantly affected integral quantities, especially for shallow water cases. Although relative motions between coupled bodies were neglected, flow-induced trim and sinkage were accounted for by changing the floating position of each vessel in the convoy. For shallow water cases, geometry and dimensions of the test basin defined the computational domain required to capture wall effects and wave reflections at boundaries. Figures 5.2 and 5.1 depict the computational domains for, respectively, shallow and deep water resistance cases. A distance of $2.0 \cdot L_{OA}$ was specified between inlet and test body; a distance of $3.5 \cdot L_{OA}$, between test body and outlet. For shallow water cases, a distance of 7.54 m was specified between test body and side wall; for deep water cases, this distance was $2.5 \cdot L_{OA}$. A distance of $3.5 \cdot L_{OA}$ was specified between a test body's keel and the domain's bottom; a distance of $1.5 \cdot L_{OA}$ between calm waterline and the domain's top. The computational mesh was coarsened toward the outlet to avoid backflow and wave reflection at boundaries. Symmetry conditions were assumed to exist about a configuration's centerline. For deep water cases, the domain's side and the bottom were modeled as slip boundaries. For shallow water cases, side and bottom were modeled as walls with a no-slip condition and a relative velocity equal to the inlet velocity. The free surface deformation was resolved using a minimum of 10 control volumes in the vertical direction. Refinement zones were arranged around

the bodies and between barge and pusher boat to accurately simulate the flow in the vicinity surrounding a convoy. Two additional refinement zones, depicted in figures 5.4 and 5.3, were created to more accurately capture the wave pattern. A coarsened mesh idealized the air part of the domain as the air flow was hardly of interest.

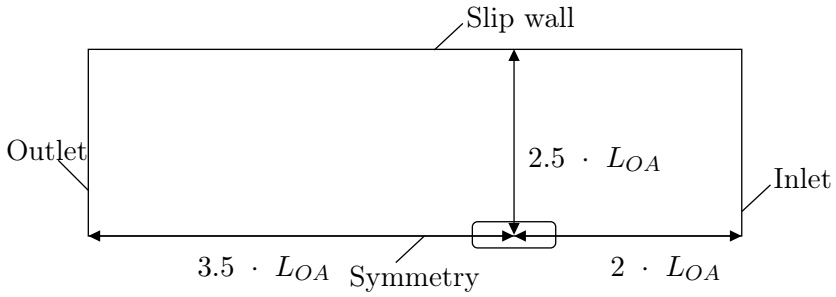

Figure 5.1: Schematic representation of the computational domain for deep water resistance simulations.

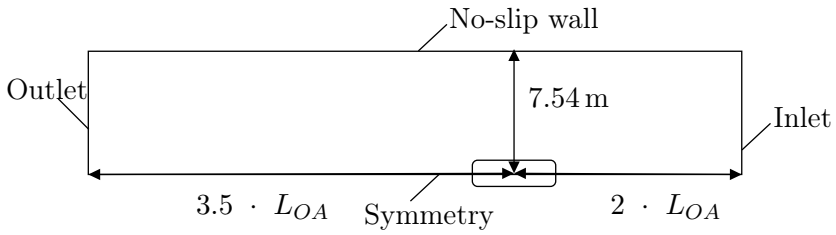

Figure 5.2: Schematic representation of the computational domain for shallow water resistance simulations.

Figure 5.3: Overview of surface mesh of configuration 1:1 for shallow water resistance simulation at $h/T = 1.5$.

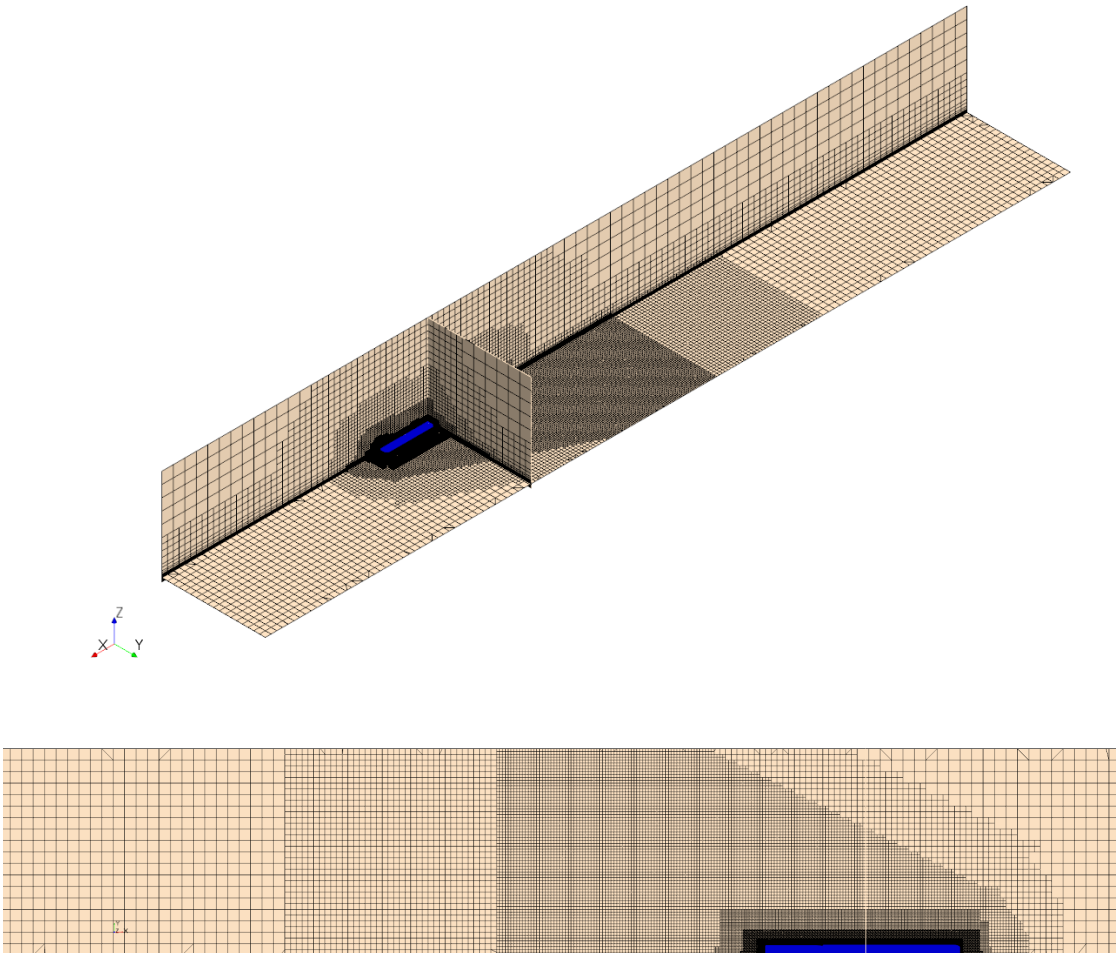

Figure 5.4: Overview of domain mesh for shallow water resistance simulation at $h/T = 1.5$.

The method of Oberhagemann (2017) and el Moctar et al. (2021) was used to perform a sensitivity and convergence analysis. The grid refinement factor for spatial and temporal discretizations was the same to ensure a constant CFL number. Simulations were conducted on three successively finer grids, based on a constant refinement ratio $r_k = \sqrt{2}$. For configuration 1:1 at $U = 0.556$ m/s in waters of $h/T = 1.2$, three successively finer grids were generated. The time step was selected to keep the CFL number below 0.5. For each time-step, six outer SIMPLE iterations were considered. Table 5.1 gives an overview of the grids and time steps considered. The coarsest grid comprised $4.13 \cdot 10^6$ control volumes; the finest grid, $23.9 \cdot 10^6$. For these three grids, this table lists also the number of control volumes CV, the time step size Δt, the resulting total longitudinal force X, and the percentage difference between X and the total longitudinal force obtained on the finest grid. According to the resulting ratio of $R_k = -0.824$, the solution's

convergence was oscillatory. Figure 5.5 plots the intermittent continuous values of total longitudinal force X obtained by averaging these over the last 50 s of the simulation. As seen, these values converge after a simulation time of about 150 s. Figure 5.6 plots comparative time series of the experimentally measured longitudinal force X_{EFD} and numerically computed longitudinal force X_{CFD} for this case. As seen, the oscillatory behavior of the measured resistance, marked by the black line in this figure, is not replicated in the computations marked by the red line. This difference was due to the inherent flow simplifications of the turbulence model implemented in the RANSE solver as well as the error sources associated with the experiment measurements, e.g. carriage vibrations and velocity variation, see Figure 5.7. Figure 5.8 depicts the distribution of y^+ values over the bottom surface of the pusher-barge configuration 1:1 at $U = 0.556$ m/s. The mean y^+ value for both bodies was about 2.04 at $h/T = 1.2$.

Table 5.1: Sensitivity analysis for longitudinal force X, shallow water $h/T = 1.2$, $U = 0.556$ m/s.

CV $\cdot$ 10^6	Δt [s]	X [N]	**Diff. in** %	R_k
4.13	0.005	-3.849	0.41 %	
9.25	0.0035	-3.758	-1.99 %	
23.9	0.0025	-3.833		
-	-	-		-0.824

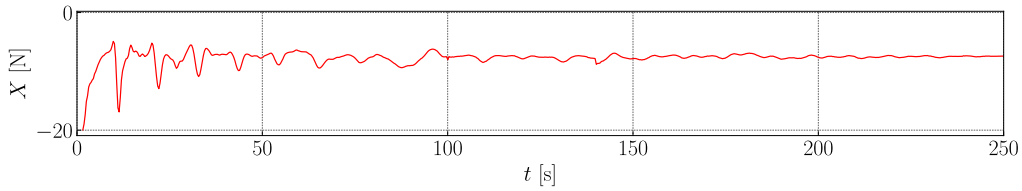

Figure 5.5: Time history of longitudinal force X in numerical resistance simulation for $h/T = 1.2$ and $U = 0.556$ m/s.

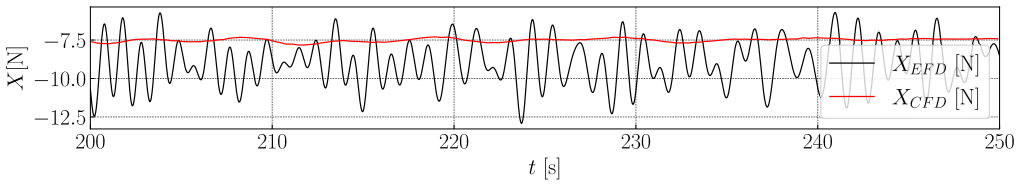

Figure 5.6: Time history comparison of measured and computed longitudinal force X for $h/T = 1.2$ and $U = 0.556$ m/s.

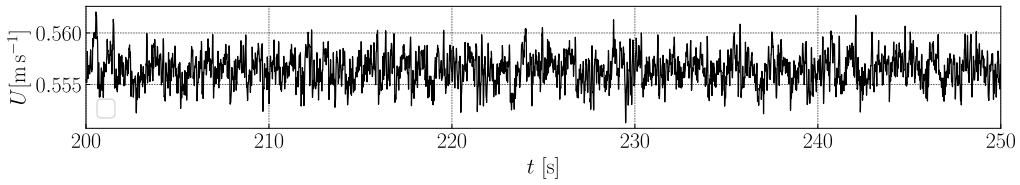

Figure 5.7: Time history of carriage velocity U for $h/T = 1.2$ and $U = 0.556$ m/s.

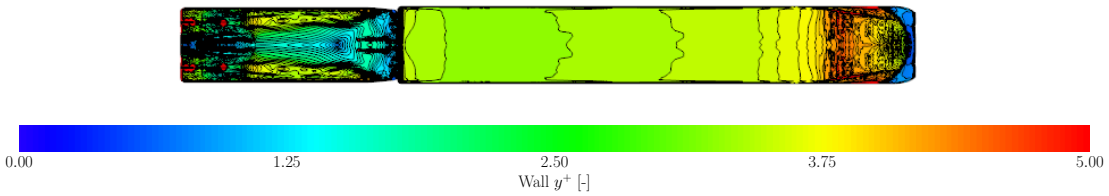

Figure 5.8: y^+ values distributed over the bottom surface of the pusher-barge configuration 1:1 at $U = 0.556$ m/s in water of $h/T = 1.2$.

5.2 Experimental results

5.2.1 Resistance

To put the obtained resistances into perspective, resistance coefficient C_T versus carriage velocity U are plotted for each configuration in Figure 5.9. In this figure, coefficients for the inland waterway test case of Mucha et al. (2017) were also included, to ease the comparison with a full-bodied vessel of similar main particulars as configuration 2:1. As seen, the largest resistance coefficient is attributable to configuration 1:1, followed by configuration 2:1. Considering their hull forms, the arrangement of the barges seems to have influenced the efficiency of the entire convoy. In configuration 1:1, the stern of the barge connected to the pusher boat, which caused an unsteady flow around the pusher boat's bow. The gap between the two bodies created a considerable geometric discontinuity. It is presumed that this affected the flow around the convoy. In configurations 2:1 and 2:2, the bow of the aft barge was connected to the pusher boat, while the two barges were joined at their respective sterns. These configurations represented a relatively smooth hull form compared to configuration 1:1. Consequently, the fewer flow disturbances surrounding the vessels led to a reduced resistance coefficient. Furthermore, in configurations 2:1 and 2:2, the gap between pusher boat and barge might have had less influence on the resistance coefficient than in configuration 1:1. In configurations 2:1 and 2:2, the gap lengths were the same, and the ratios of gap length to convoy length were equal. As seen in Figure 5.9, differences between the comparative resistance coef-

ficients for the full-bodied vessel of Mucha et al. (2017) and configuration 2:1 are small, suggesting that gap effects on resistance for this configuration could be relatively small.

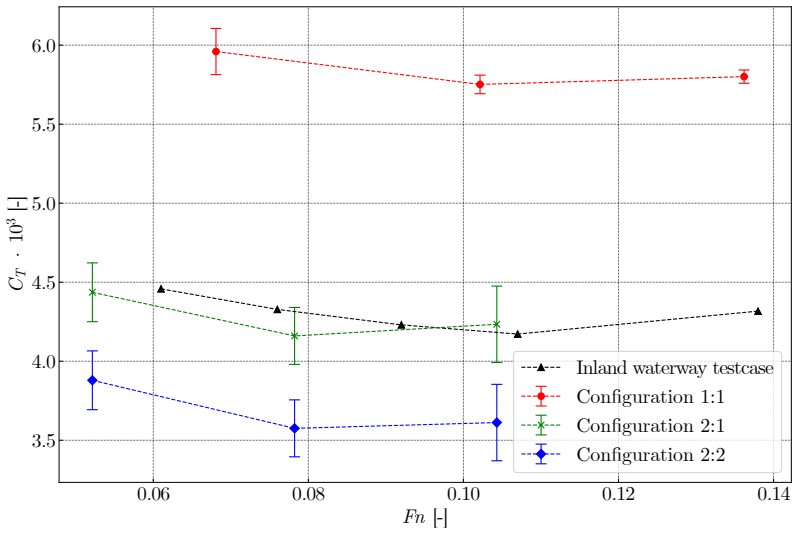

Figure 5.9: Resistance coefficient C_T versus Froude number Fn in deep water for configurations 1:1, 2:1, and 2:2 and for the inland waterway testcase of Mucha et al. (2017).

Figure 5.10 depicts the resistance coefficient C_T versus water depth to draft ratio h/T for configurations 1:1, 2:1, and 2:2 at $U = 0.556$ m/s. Although in shallow water of $h/T = 1.2$, convoy 2:1 is seen to be the most efficient configuration as its resistance coefficient is lowest, in deep waters of $h/T > 30.0$, convoy 2:2 with its even lower resistance coefficient is more efficient.

The overall increase of resistance with decreasing water depth is a well documented phenomenon, attributable to the blockage effect causing an increase of flow velocities surrounding the vessel and a change of the frictional coefficient due to the interactions of the vessel and the waterway's bottom. The mixing of two boundary layers and its effect on frictional resistance has been recently addressed by Zeng et al. (2019).

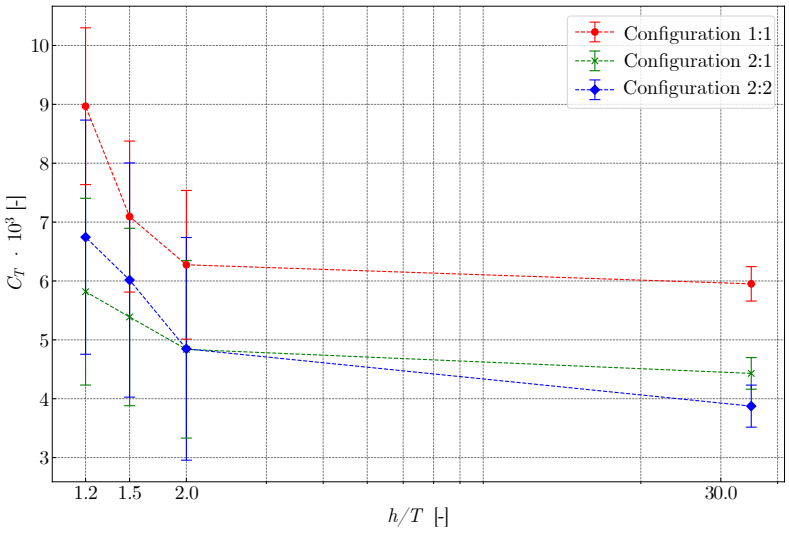

Figure 5.10: Resistance coefficient C_T versus water depth to draft ratio h/T for configurations 1:1, 2:1, and 2:2 at $U = 0.556$ m/s.

From resistance tests for configuration 1:1 at $U = 0.556$ m/s in deep water and shallow water of $h/T = 1.2$, figures 5.11 and 5.12 plot time series of total longitudinal force X acting on the whole system and carriage velocity U. The time series in deep water show an oscillatory behavior, but their standard deviations are acceptably small compared to their mean values. Although high-frequency small amplitude oscillations are seen to be superimposed on the carriage velocity as well as the associated longitudinal force X, these oscillations are small enough to be considered irrelevant. Several factors could have caused these oscillations. Among them were sudden variations of carriage velocity that initiated inertial forces leading to force variations. While deep water tests were conducted with the bare hull and mounted rudders, shallow water tests were performed with the bare hull and with an idling propeller delivering zero thrust. As depicted in Figure 5.12, the difference between both tests is barely noticeable. Nevertheless, the amplitude of the oscillations is larger than its deep water counterpart, suggesting a strong shallow water effect. However, the standard deviations are relatively small. A sensitivity analysis of the tests in deep and shallow water was unavailable.

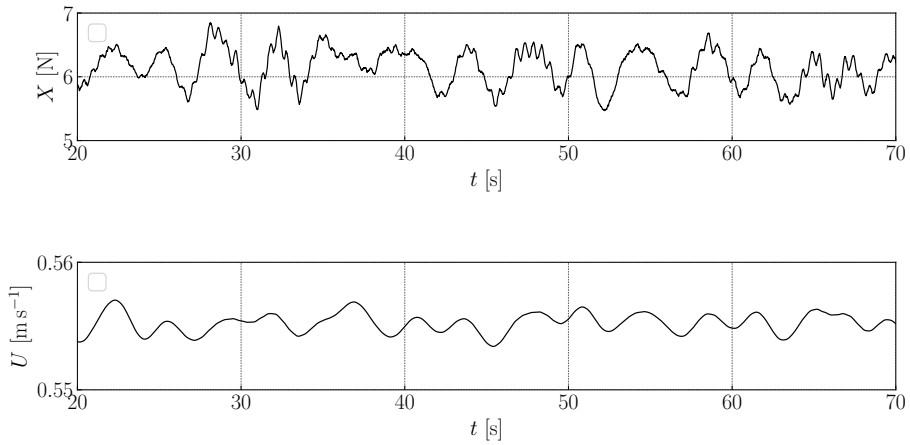

Figure 5.11: Time series of total longitudinal force X and carriage velocity U over time t for bare hull for configuration 1:1 at $U = 0.556$ m/s.

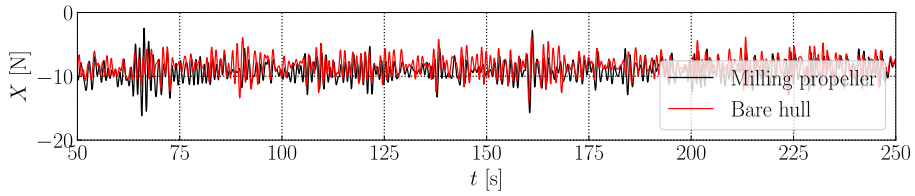

Figure 5.12: Comparison of total longitudinal force X over time t for shallow water resistance tests at $h/T = 1.2$ and $U = 0.556$ m/s, configuration 1:1.

The influence of shallow water on resistance was backtracked to changes in the pressure field around the vessels. Owing to the blockage effect, the flow accelerated past the stagnation point in the bow area. The pressure then decreased, causing a change of the dynamic floating position. Typically, a monohull is subject to sinkage and trim. This consequence was highlighted by Mucha et al. (2016), Tezdogan et al. (2016), Bechthold and Kastens (2020) and Chillcce and el Moctar (2022). The pusher-barge model experienced this phenomenon as well, albeit to a lesser extent. Figure 5.13 depicts the barge sinkage z_{barge} versus Froude number Fn in deep water for configurations 1:1, 2:1 and 2:2. Figure 5.14 portrays the influence of water depth on barge sinkage at $U = 0.556$ m/s for configurations 1:1, 2:1 and 2:2. In deep water, the highest sinkage is attributable to configuration 1:1, whereas it is barely noticeable for configuration 2:2. However, in shallow water, barge sinkage increases, with the highest value attributable to configuration 2:2 at $h/T = 1.2$.

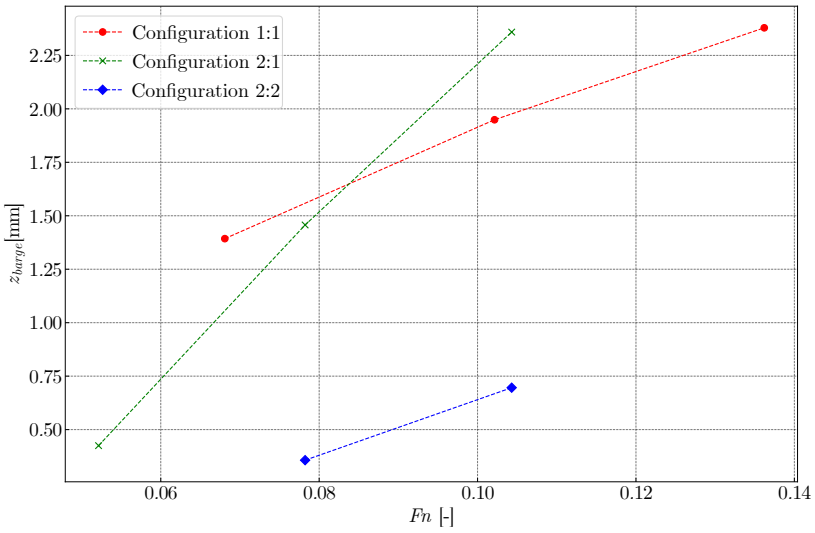

Figure 5.13: Barge sinkage z_{barge} versus Froude number Fn in deep water for configurations 1:1, 2:1, and 2:2.

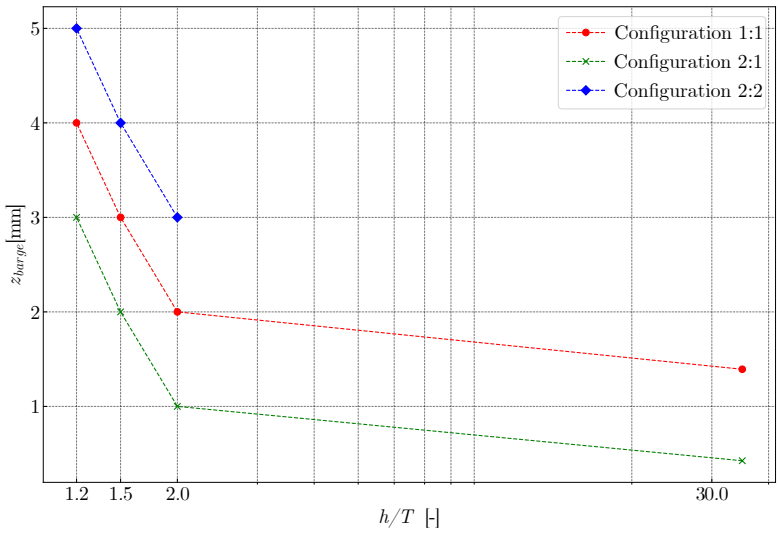

Figure 5.14: Barge sinkage z_{barge} versus water depth to draft ratio h/T for configurations 1:1, 2:1, and 2:2 at $U = 0.556$ m/s.

The speeds considered always corresponded to a depth Froude number of less than $Fn_h = 0.48$, well below the critical value of $Fn_h = 1$. Therefore, it was concluded that the wave making resistance was of minor importance. At the speed regimes considered in this work, viscous and frictional resistances were the dominant components. Recent research has focused on the estimation of the frictional resistance coefficient C_f and the form factor k, both of which account for the viscous resistance. Using CFD methods, Raven (2016) and Zeng et al. (2019) focused on the prediction of C_f for different kinds of ships, including an inland waterway vessel. As the classical ITTC 57 formula does not account for water depth, using this formula tends to underestimate the C_f for shallow water predictions. Although various empirical methods have been utilized to estimate shallow water effects on ship resistance, such as Schilchting (1934), Lackenby (1963), and Millward (1999), no results were extrapolated by deducting the associated form factor of the pusher-barge convoy.

5.2.2 Propulsion

Open-water propeller tests were performed as documented by Mucha et al. (2017). The propulsors mounted on the pusher boat were identical to the ones installed on the inland waterway vessel they tested. Propeller and nozzle characteristics can be taken from the aforementioned publication. The non-dimensional thrust coefficient K_T is defined as follows:

$$K_T = \frac{T}{\rho n^2 D_P^4} \tag{5.1}$$

where n is the propeller revolution rate and D_P the propeller diameter. As the propeller rotated inside the duct, the total thrust coefficient K_{TT} was split into the propeller thrust coefficient K_{TP} and the duct thrust coefficient K_{TD} as follows:

$$K_{TT} = K_{TP} + K_{TD} \tag{5.2}$$

The non-dimensional torque coefficient K_Q and the propeller open-water efficiency η_0 are then written as follows:

$$K_Q = \frac{Q}{\rho n^2 D_P^5} \tag{5.3}$$

$$\eta_0 = \frac{K_T J}{K_Q 2\pi} \tag{5.4}$$

Propulsion tests were conducted following the ITTC (1999) performance prediction method. To illustrate the application of this method, figure 5.15 portrays the associated time series of port and starboard thrust T_{PS} and thrust T_{STB} and port and starboard torques Q_{PS} and Q_{STB} for each tested velocity for configuration 1:1. A progressive increase of thrust and torque values characterized a consistent response to the gradual increase of propeller revolution rate. Self-propulsion points for each velocity were determined via linear interpolation between thrust and residual force. Based on these interpolated quantities, the delivered power P_D, the effective power P_E, and the propulsion efficiency η_D were obtained as follows:

$$P_D = 2\pi n Q_{TT} \tag{5.5}$$

$$P_E = R_{TM} U \tag{5.6}$$

$$\eta_D = \frac{P_E}{P_D} \tag{5.7}$$

where Q_{TT} is the total torque. The propulsion related criteria comprised the required power P_D and the effective power P_E. For each of the three configurations, figures 5.16 and 5.17 plot these criteria versus carriage velocity U. These plots demonstrate that these criteria depend on the number of barges being pushed. It seemed reasonable that increased power was required to attain a given speed with more barges coupled to the pusher boat. Nevertheless, the effective power required at the lower speed of 0.5552 m/s did not differ significantly compared to the effective power required at the higher speed of 0.8329 m/s. The comparative values of P_D and P_E for configurations 2:1 and 2:2 at their corresponding carriage velocities of 0.5552 m/s and 0.8329 m/s accentuated this trend.

The transported volume was compared to assess the transport effectiveness of the three pusher-barge configurations. Based on barge displacement Δ_B and the interpolated required power P_D, the ratio P_D/Δ_B expressed the power required to move a unit payload at a given speed. Figure 5.16 plots this ratio versus speed. As seen, at low speeds, the difference between these ratios for each configuration is relatively small. However, at higher speeds this ratio increases noticeably, not only between configurations 1:1 and 2:1, but also for configuration 2:2 itself.

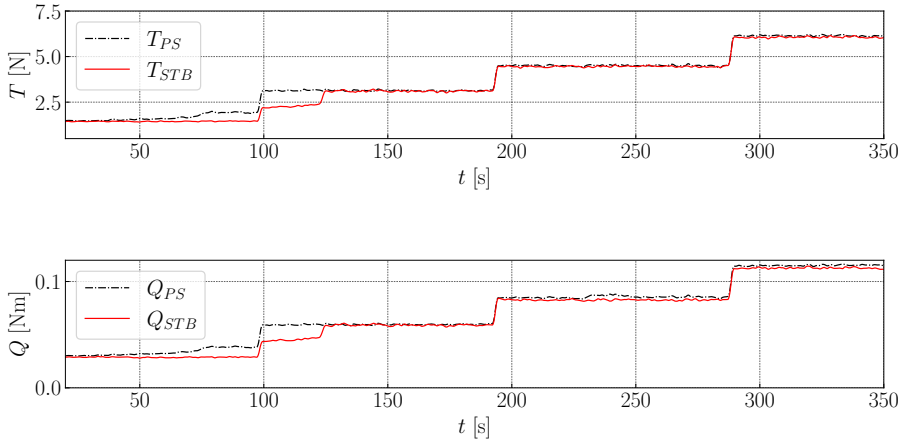

Figure 5.15: Time series of thrust T and torque Q over time in seconds at a carriage velocity of $U = 0.5552$ m/s for configuration 1:1.

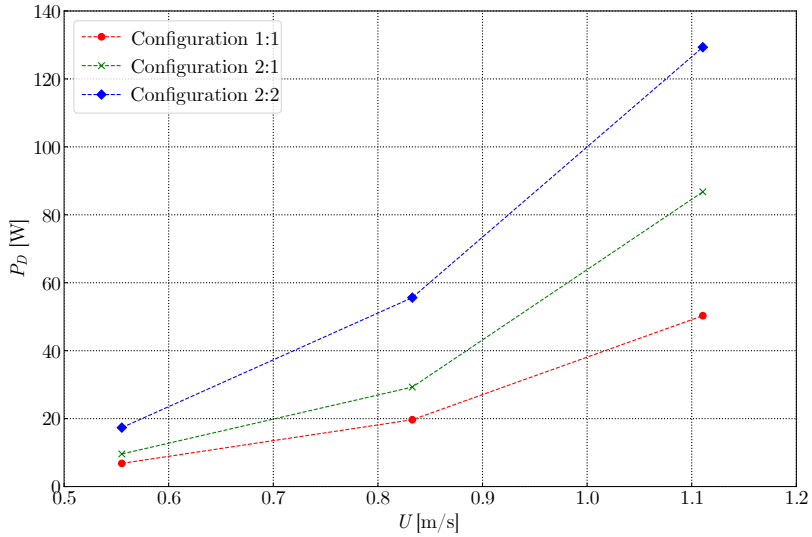

Figure 5.16: Delivered power P_D over carriage velocity U for configurations 1:1, 2:1, 2:2.

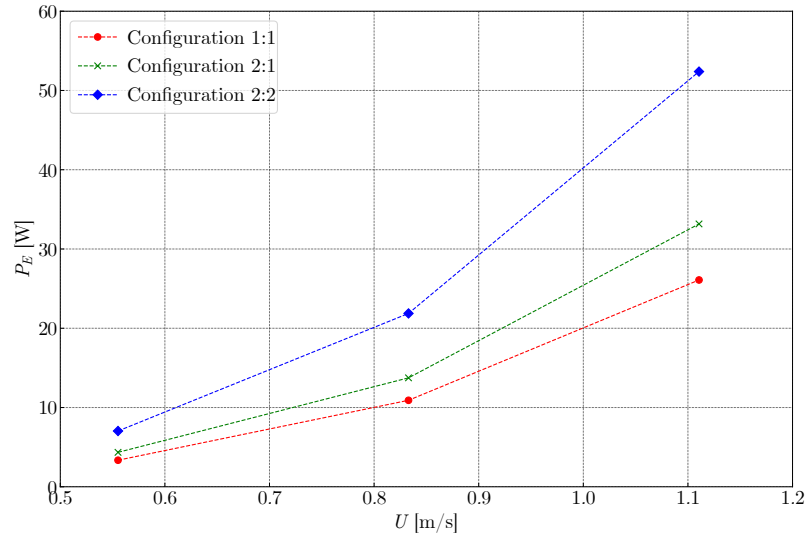

Figure 5.17: Required power P_E over carriage velocity U for configurations 1:1, 2:1, 2:2.

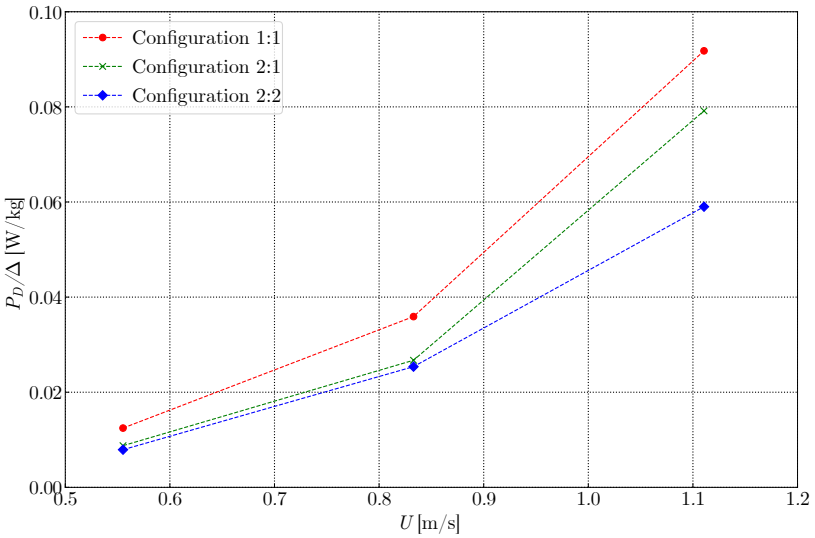

Figure 5.18: Delivered power to displacement ratio P_D/Δ over carriage velocity U for configurations 1:1, 2:1, 2:2.

Shallow water propulsion point at $h/T = 2.0$ was calculated using the same method as in deep water. The propeller rate was then the same for $h/T = 1.5$ and 1.2. The measured overall resistance resulted in the longitudinal force X. The increase of this force caused by the depth restriction was measured. For $h/T = 2.0$, force X is nearly zero, indicating sufficient thrust was available for self propulsion. For $h/T = 1.5$, the increase of X is somewhat more moderate compared with the larger resistance for $h/T = 1.2$. This meant that in shallow water, the propeller had to be overloaded to maintain a near constant velocity. The results from the experimental propulsion tests were used to plot the effective power versus displacement ratio P_E/Δ for the carriage velocity of 0.556 m/s shown in figure 5.19. This demonstrates that, in deep water, less power was required for the configuration consisting of four barges; however, in moderate to extreme shallow water, configuration 2:1 appeared to be more advantageous as it needed somewhat less power. Recall that all considered barges were characterized by a large flat bottom, a feature that increases the frictional resistance in shallow waters.

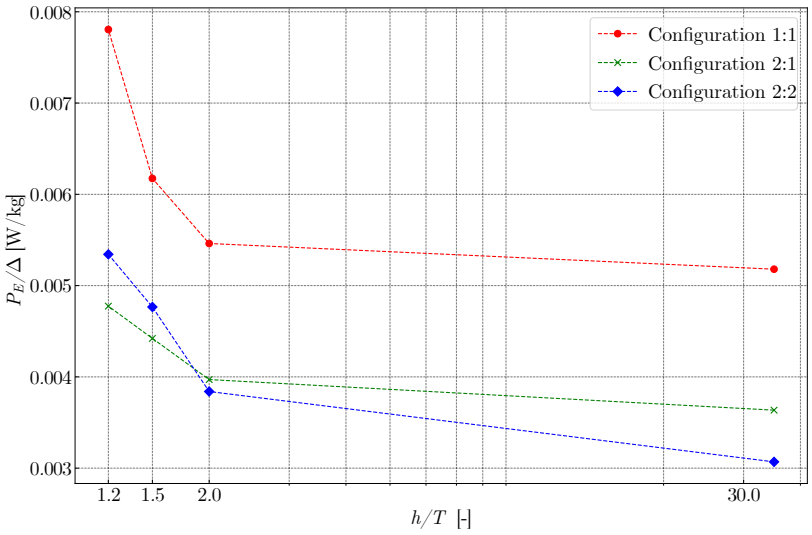

Figure 5.19: Effective power to displacement ratio P_E/Δ over water depth to draft ratio h/T at 0.556 m/s for configurations 1:1, 2:1, 2:2

Propulsion of sea going vessels and inland waterway vessels differs mainly in that inland waterway vessels operate in relatively shallow waters. In shallow waters, a smaller UKC dictates the arrangement of the propellers. Consequently, smaller semi-submerged propellers have to be accommodated in the aft part of the pusher boat, and these propellers are usually situated inside a tunnel. Furthermore, locating the propellers in a tunnel has a negative effect on the propeller inflow, leading to decreased efficiency. According to

Pompée (2015), the propulsive efficiency as defined by equation 5.7 lies between 0.7 and 0.8 for conventional seagoing ships, and it can be as low as 0.3 to 0.4 for pusher boats; see Radojčić et al. (2021). The experimentally obtained values confirm these observations, and the arrangement of the barges affected this efficiency significantly. For configuration 1:1 at $U = 0.5552$ m/s, the efficiency η_D is about 0.49 and at $U = 1.1156$ m/s, η_D attains a value as high as high as 0.51. For configuration 2:1 at $U = 0.5552$ m/s, $\eta_D = 0.452$; and at $U = 1.1156$ m/s, $\eta_D = 0.382$. These results revealed that the efficiency for all tested velocities was nearly the same. It turned out that the propulsion efficiency η_D was lowest for configuration 2:2. At a carriage velocity of $U = 0.5552$ m/s, its efficiency was $\eta_D = 0.405$; and at a carriage velocity of $U = 1.1156$ m/s, its efficiency was $\eta_D = 0.404$. It can be concluded that the arrangement of the barges, specifically, the number of barges in front of the pusher led to a lower propulsion efficiency. As stated above, configuration 2:2 was less efficient at the velocities $U = 0.5552$ m/s and $U = 0.8329$ m/s. The four barges ahead of the pusher boat and the larger overall breadth of the convoy had a massive influence on the propellers' inflow. Larger recirculation zones as well as less streamlined propeller inflows were a cause for poor propulsion performance. In shallow waters, torque and thrust were not measured; consequently, propulsive efficiency could not be determined. However, estimates of Pompée (2015) showed that this efficiency may be as low as 0.2 to 0.3 for inland waterway vessels. Considering the added resistance in shallow waters at $h/T = 1.2$, an increase of 39, 25, and 54% was obtained for, respectively, configurations 1:1, 2:1, and 2:2 compared with the deep water resistance at a carriage velocity of $U = 0.5552$ m/s. For configuration 1:1, the increased resistance lies within an acceptable range. The increased resistance obtained for configuration 2:1, as it was the lowest resistance coefficient within this velocity range, demonstrated a more favorable, i.e., higher propulsive efficiency. Considering the blockage effect and the disruptive flow in shallow waters, it can be concluded that the propulsive efficiency in shallow water can only decrease. However, these considerations should take into account the overall transport efficiency. Configuration 2:2, despite the above observations, proved to be the most profitable transport mode, followed closely by configuration 2:1. Regarding the maneuverability of such convoys, configuration 2:1 is the most favorable transport mode as it represents a compromise between transport and propulsion efficiency. This configuration is also the most frequently encountered kind of convoy in German waterways.

5.3 Numerical results

Figures 5.20, 5.21 and 5.22 plot the CFD computed and the comparative experimentally measured resistance coefficient C_T versus Froude number Fn of all cases for, respectively, configurations 1:1, 2:1 and 2:2, on the medium grid. Red markings identify deep water values; blue markings, values in shallow water of $h/T = 2.0$; green markings, values in shallow water of $h/T = 1.5$; and black markings, values in shallow water of $h/T = 1.2$. Vertical bars with horizontal limit lines specify the deviation range of measured values. In deep water, for configuration 1:1, the computed coefficient at $Fn \approx 0.102$

($U = 0.8329$ m/s) and at $Fn \approx 0.137$ ($U = 1.1156$ m/s) deviated respectively by only 1.4% and 1.7% from the experimental value, whereas at $Fn \approx 0.068$ ($U = 0.5552$ m/s) the computed value deviated by about 8.0% from the experimental values. For configuration 2:1, the computed values at $Fn \approx 0.102$ ($U = 0.8329$ m/s) and at $Fn \approx 0.137$ ($U = 1.1156$ m/s) deviated respectively by 5.5% and 6.2% from the experimental value, whereas at $Fn \approx 0.068$ ($U = 0.5552$ m/s) the computed value deviated by only 3.3% from the experimental values. For configuration 2:2, the computed values deviated by approximately 9.9%, 6.6% and 5.3% at respectively $Fn \approx 0.068$ ($U = 0.5552$ m/s), $Fn \approx 0.068$ ($U = 0.5552$ m/s) and $Fn \approx 0.137$ ($U = 1.1156$ m/s). As seen, the agreement between computed and experimental resistance coefficients is satisfactory. In most cases, the computed values lay within the experimental uncertainty.

In shallow water of $h/T = 2.0$, the influence of water depth was moderate as the computed values differ only slightly from the ones obtained in deep water. Specifically, the difference between computed and experimental values was 7.9% at $Fn \approx 0.068$ ($U = 0.556$ m/s) and 5.1% at $Fn \approx 0.085$ ($U = 0.694$ m/s) for configuration 1:1. For configuration 2:1, the computed coefficients deviated from the experimental values by 6.9% at $Fn \approx 0.068$ ($U = 0.556$ m/s) and 7.6% at $Fn \approx 0.085$ ($U = 0.694$ m/s). As for configuration 2:2, the deviations from the experimental values were within the same range. At $Fn \approx 0.068$ ($U = 0.556$ m/s) the deviation was about 9.8%; at $Fn \approx 0.085$ ($U = 0.694$ m/s) about 10.4%.

The deviations were similar in shallow water of $h/T = 1.5$, being 8.1% at $Fn \approx 0.068$ ($U = 0.556$ m/s) and 9.03% at $Fn \approx 0.068$ ($U = 0.694$ m/s) for configuration 1:1. For configuration 2:1, the numerical results deviated from the experimental results by 8.3% at $Fn \approx 0.068$ ($U = 0.556$ m/s) and 9.8% at $Fn \approx 0.085$ ($U = 0.694$ m/s). The deviations were slightly larger at this water depth for configuration 2:2. Specifically, 9.8% at $Fn \approx 0.068$ ($U = 0.556$ m/s) and 12.9% at $Fn \approx 0.085$ ($U = 0.694$ m/s)

In the shallowest water of $h/T = 1.2$, the difference between computed and experimental values was greatest, being 15.16% at $Fn \approx 0.068$ ($U = 0.556$ m/s) and 8.9% at $Fn \approx 0.068$ ($U = 0.694$ m/s) for configuration 1:1. This trend was also observed for configuration 2:1, with deviations of 8.6% at $Fn \approx 0.068$ ($U = 0.556$ m/s) and 10.5% at $Fn \approx 0.068$ ($U = 0.694$ m/s). For configuration 2:2, the deviations were also within this range, being 9.6% at $Fn \approx 0.068$ ($U = 0.556$ m/s) and 14.9% at $Fn \approx 0.068$ ($U = 0.694$ m/s).

Although no noticeable trim and sinkage were measured during the experiments, the prediction of resistance in shallow water required an accurate representation of the flow between the bottom of the pusher barge convoy and the bottom of the channel. Moreover, the coupling arrangement between pusher and barge added to the complexity of the numerical simulations because the flow in the gap did influence the overall resistance of the convoys.

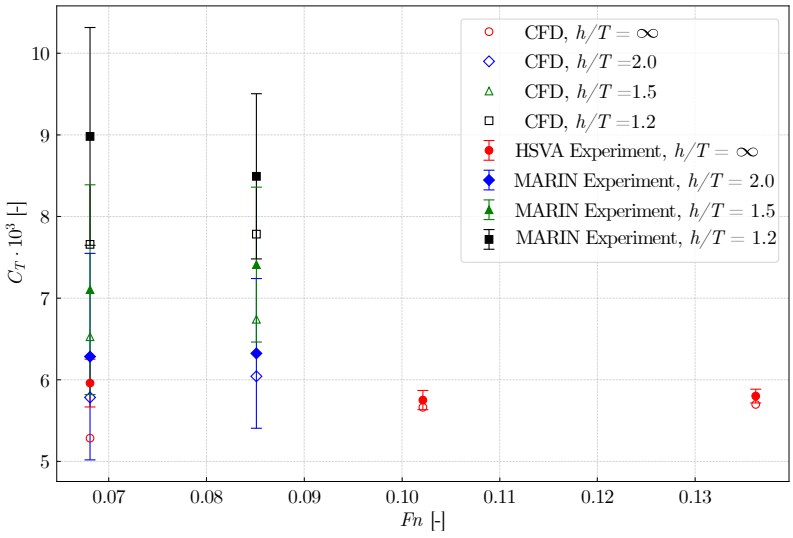

Figure 5.20: Validation of numerical resistance results for configuration 1:1 in deep and shallow waters.

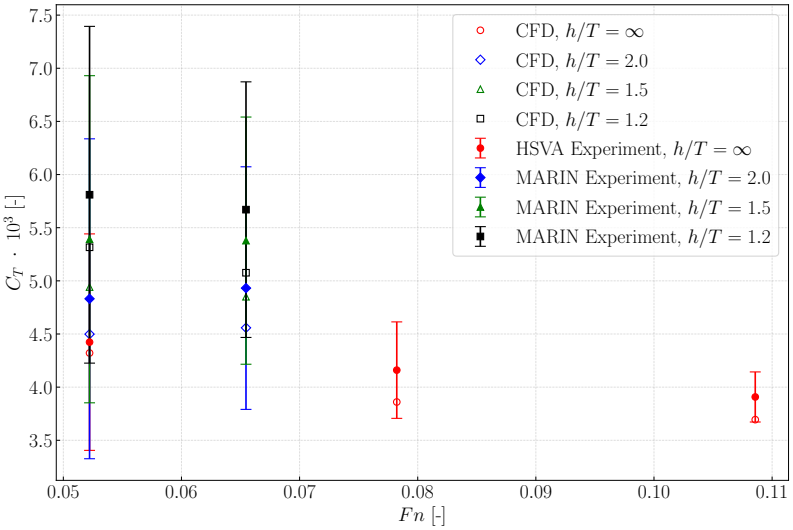

Figure 5.21: Validation of numerical resistance results for configuration 2:1 in deep and shallow waters.

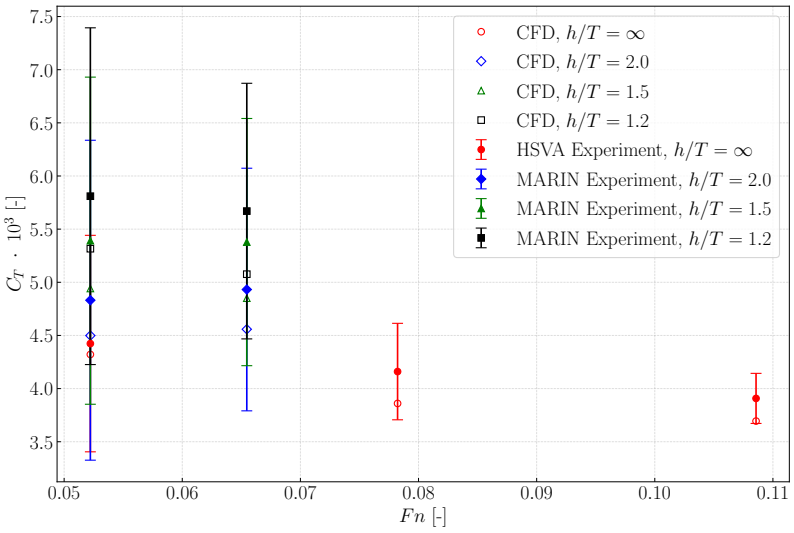

Figure 5.22: Validation of numerical resistance results for configuration 2:2 in deep and shallow waters.

For the majority of cases, the computed resistances revealed the dominance of shear forces over pressure forces. Investigations of Zeng et al. (2019) on river-going vessels led to similar conclusions, emphasizing the need for reliable models to predict friction forces. Indeed, shortcomings of the method recommended by the by the ITTC, where the frictional resistance coefficient $C_{f_{ITTC}}$ is obtained via equation (5.8), include the omission of accounting for full-bodied sharp edged vessels and blockage effects in shallow waters. Zeng et al. (2019) proposed an improved semi-empirical frictional resistance coefficient $C_{f_{Zeng}}$ determined via equation (5.9):

$$C_{f_{ITTC}} = \frac{0.0075}{(\log Re - 2)^2} \tag{5.8}$$

$$C_{f_{Zeng}} = \frac{0.0086}{(\log Re - 1.631)^2} \cdot \left(1 + \frac{c_1}{(\log Re + c_2)^2} \cdot \left(\frac{h}{T}\right)^{c_3}\right) \tag{5.9}$$

In equation (5.9), Re is the Reynolds number, h/T is the water depth to draft ratio, and c_1, c_2 , and c_3 are factors calculated by Zeng et al. (2019) for three ship types, including the full bodied inland waterway vessel "Rhine Ship." This ship's geometric features, similar to those of an Europa type barge, include a large flat bottom, sharp edged bilges, and a quasi-vertical transom. For additional details concerning the "Rhine Ship", see Zeng

et al. (2018) and Zeng et al. (2019). Figure 5.23 plots comparative values of frictional resistance coefficients $C_{f_{CFD}}$, $C_{f_{ITTC}}$, and $C_{f_{Zeng}}$ versus depth to draft ratio h/T for the barge in configuration 1:1 advancing at $U = 0.556$ m/s. Coefficient $C_{f_{CFD}}$ was obtained via CFD; coefficient $C_{f_{ITTC}}$ via equation (5.24a); coefficient $C_{f_{Zeng}}$, via equation (5.9). The abscissa plots values of h/T on a logarithmic scale to demonstrate the relatively favorable correlation of numerical and empirical values based on the modified correlation value of the ITTC. Nevertheless, an increase of roughly 12% for the frictional resistance coefficient under shallow water conditions is noteworthy. These data reinforced the need for further research regarding inland waterway vessels sailing in shallow waters.

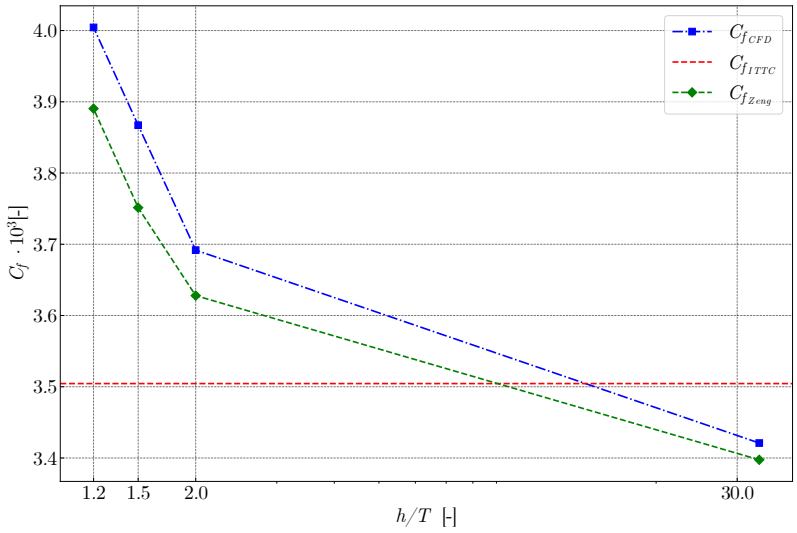

Figure 5.23: Influence of shallow water on frictional resistance for configuration 1:1 and $U = 0.556$ m/s at different water depths.

Conclusions based on figure 5.23 were substantiated also in figure 5.24. Herein, bottom views of shear stresses distributed over the bottom surfaces of pusher-barge configuration 1:1 advancing at $U = 0.556$ m/s in deep water and in water depths of $h/T = 2.0, 1.5,$ and 1.2 are depicted. The effect of decreasing water depth is clearly visible. In the bow area, the red colored area identifies greater shear stress zones. With decreasing h/T ratios, these areas became larger, highlighting the increasing friction associated with the shallower water depths. The large flat bottom area was also subject to increased shear stresses, albeit less pronounced visually. On the other hand, the gap effect is distinctly apparent, considering the shear stress distribution over the pusher's surface. The low shear stress zone corresponded to a flow separation and recirculation zone, here described as a "dead water" zone. This zone becomes significantly larger with decreasing

water depth. In the extremely shallow water depth of $h/T = 1.2$, a large portion of the pusher's bottom is engulfed by the dead water zone although the pusher operated at a higher water depth to draft ratio than the barge. The unfavorable arrangement of the pusher behind the vertical transom of the barge turned out to be decisive.

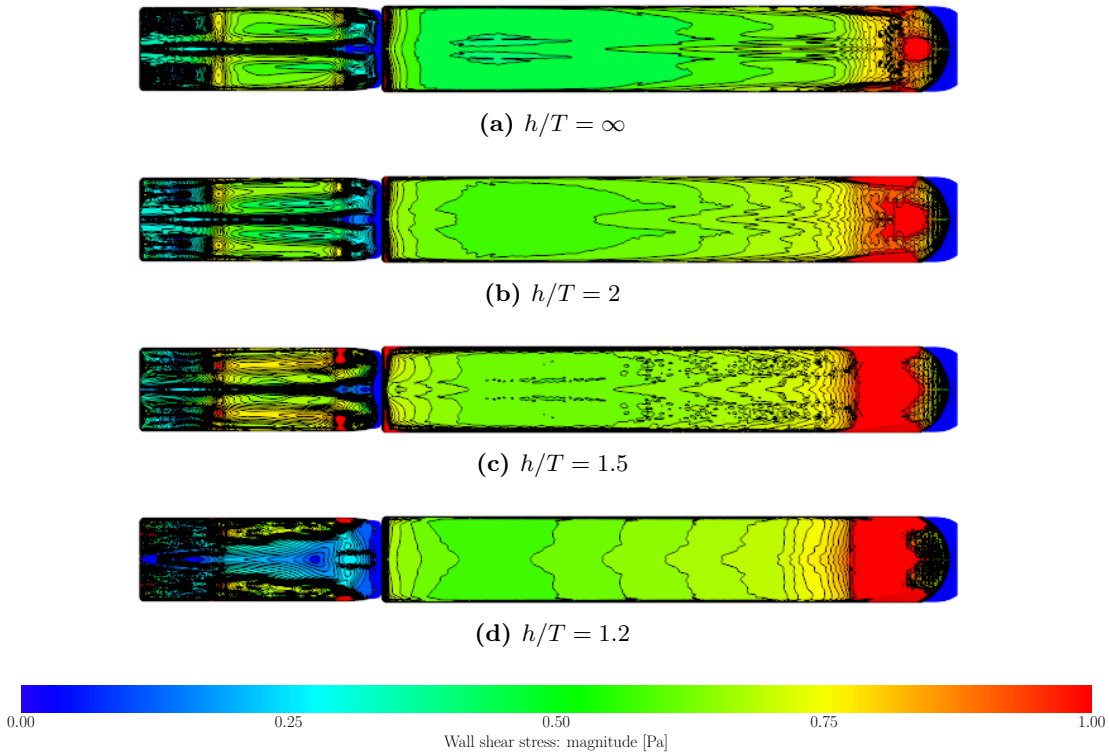

(a) $h/T = \infty$

(b) $h/T = 2$

(c) $h/T = 1.5$

(d) $h/T = 1.2$

Figure 5.24: Influence of shallow water on wall shear stress over pusher and barge hull surface for configuration 1:1 at $U = 0.556\,\mathrm{m/s}$ and different water depths.

Barge arrangement is a crucial aspect when considering the resistance on pusher-barge systems. Figure 5.25 depicts bottom view of shear stress distribution over the bottom surfaces of pusher-barge configurations 1:1, 2:1 and 2:2 advancing at 0.556 m/s at a water depth ratio of $h/T = 1.2$. In the bow area, shear stress distribution is fairly consistent. The red area at the bow, highlighting higher shear stresses, is visible in all three configurations. The most extreme case is represented by configuration 2:2, where this area is more pronounced, as a result of the increased breadth and the geometrical unsteadiness of the fore ship region. While configurations 2:2 and 2:1 are charcterized by a bow-bow coupling between pusher and barge, the bow-stern coupling between pusher and barge in configuration 1:1 clearly impacts the flow around the pusher and thus, the shear stress distribution around the pusher. In configuration 2:1, the flow separation is less abrupt than in configuration 1:1, resulting in higher stresses over the pusher. Configuration 2:2 presents the least advantageous arrangement, as shown by the low stresses around the pusher, indicating a larger "dead water zone".

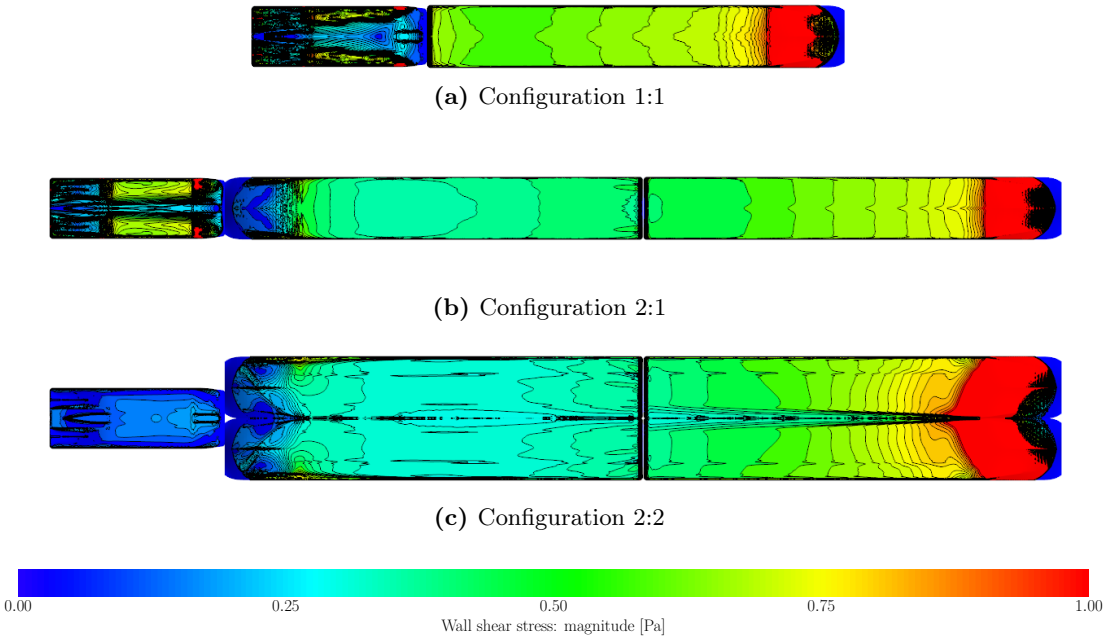

(a) Configuration 1:1

(b) Configuration 2:1

(c) Configuration 2:2

Figure 5.25: Influence of barge arrangement on wall shear stress over pusher and barge hull surface for configuration 1:1, 2:1 and 2:2 at $U = 0.556$ m/s and $h/T = 1.2$.

While frictional resistance seemed to be dominant, it was nonetheless meaningful to assess the pressure field around configuration 1:1 based on the associated wave pattern as depicted in figure 5.26. First and foremost, the wave pattern differed from the classical Kelvin wake field associated with highly optimized modern seagoing vessels. In all water depths, a distinctive surface elevation in the bow area is visible in all four graphs of

figure 5.26. The high pressure zone, corresponding to the stagnation point at the bow of the barge, becomes larger and is more visible with decreasing water depth. The so-called shoulder effect, although barely visible under deep water conditions, is drastically amplified as water depth decreased. This effect is particularly visible in the shallowest water depth of $h/T = 1.2$. Alongside the barge's parallel body, a relatively large low pressure zone develops. A disturbance on the water surface is also visible in the gap area between pusher and barge, and this effect is also amplified in extreme shallow waters.

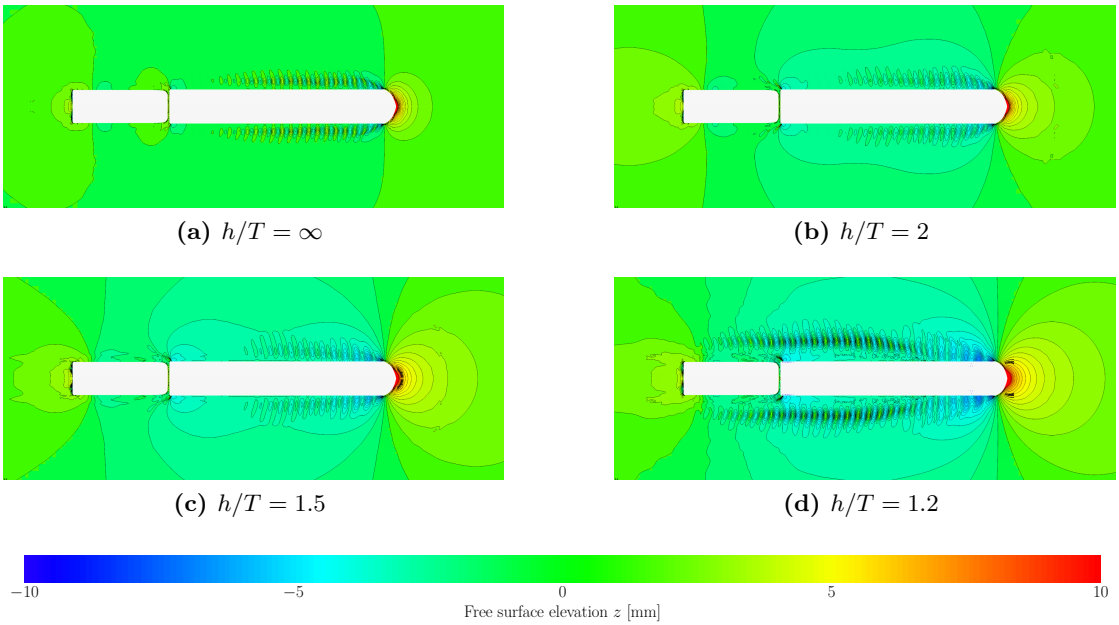

(a) $h/T = \infty$ **(b)** $h/T = 2$

(c) $h/T = 1.5$ **(d)** $h/T = 1.2$

Figure 5.26: Free surface elevation for configuration 1:1 at $U = 0.556$ m/s and different water depths.

Figure 5.27 depicts the wave pattern associated with, respectively, configurations 1:1, 2:1 and 2:2 at a velocity of $U = 0.556\,\mathrm{m/s}$ and $h/T = 1.2$. Similar to the previous observations, a distinct elevation of the water surface in the bow area is visible for all three configurations. This effect is even more present for configuration 2:2, where the junction between the two front barges causes a significantly larger stagnation point, as seen in figure 5.27c. The shoulder effect is also noticeably larger for configuration 2:2, underlining the high pressure and velocity difference induced by this particular geometry. Similar to configuration 1:1, the gaps between pusher and barge or barges cause a disruption of the free surface. In configuration 2:1 and 2:2, a secondary wave pattern is visible at the barge-barge coupling point. The convoy's shape, characterized by geometrical discontinuities, likely caused this phenomena. The flow around the pusher at the shallowest water depth of $h/T = 1.2$ is greatly impacted by the number of barges constituting the convoy. For

configuration 2:2, the large flat-bottomed area of the barges combined with blockage effect associated with this water depth greatly disrupted the flow around the pusher. As seen in figure 5.27c, the tunnels accommodating the propulsion devices are not entirely filled with water, whereas they are fully submerged in configuration 1:1 and 2:1. Even though this effect disappears at propulsion point and mounted propellers, this observation confirms the insights gained from the experimental campaign. Indeed, configuration 2:2 has the lowest propulsive efficiency in shallow waters.

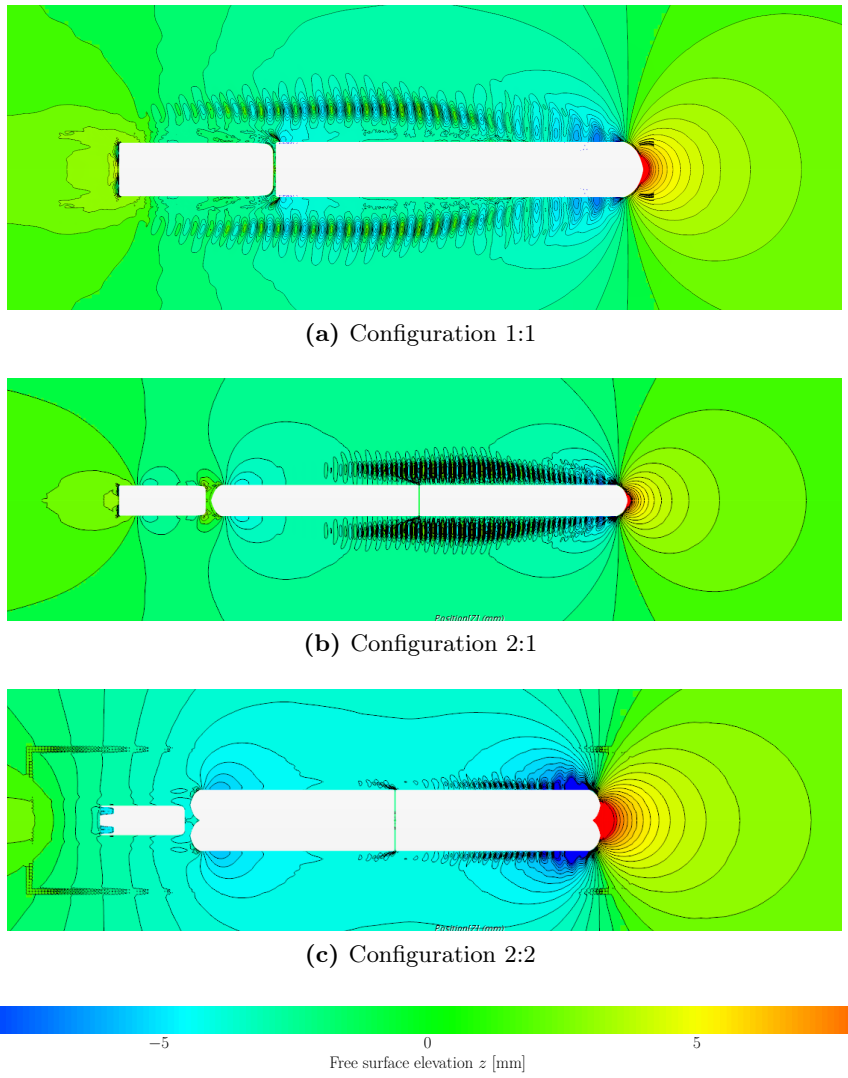

(a) Configuration 1:1

(b) Configuration 2:1

(c) Configuration 2:2

Figure 5.27: Free surface elevation z for configuration 1:1, 2:1 and 2:2 at $U = 0.556$ m/s and $h/T = 1.2$.

To analyze the gap flow and its effect on resistance, figure 5.28 depicts velocity contours on the longitudinal midship plane ($y = 0$) of configuration 1:1. In concordance with the wave pattern seen in figure 5.26, the distinctive velocity distribution around the convoy is visible. In all water depths, a lower velocity zone developed at the stagnation point around the bow of the barge. In the water depth of $h/T = 1.2$, the blockage effect occurring at the extreme narrow space between barge and channel bottom caused an expansion of this zone, thereby generating higher pressures and friction. Downstream, the velocities then quickly decreased, causing the flow to accelerate around that area. Similar to previous observations, the flow in the gap between pusher and barge was equally affected by water depth. Indeed, water depth had a drastic effect on the flow velocities around the pusher. As seen in figure 5.28, in deep water, the flow reattaches itself to the pusher at its half length. The velocity distribution around the pusher differs only slightly in water depths of $h/T = 2.0$ and 1.5. However, the flow changes drastically in water depth of $h/T = 1.2$. The recirculation zone is significantly larger, extending up to the pusher's transom. The flow passes through the narrow passage underneath the convoy, accelerates at the bow area, and exits in the gap area. The sudden variation in the geometry as well as the arrangement of the pusher behind the barge caused this abrupt change of flow velocities.

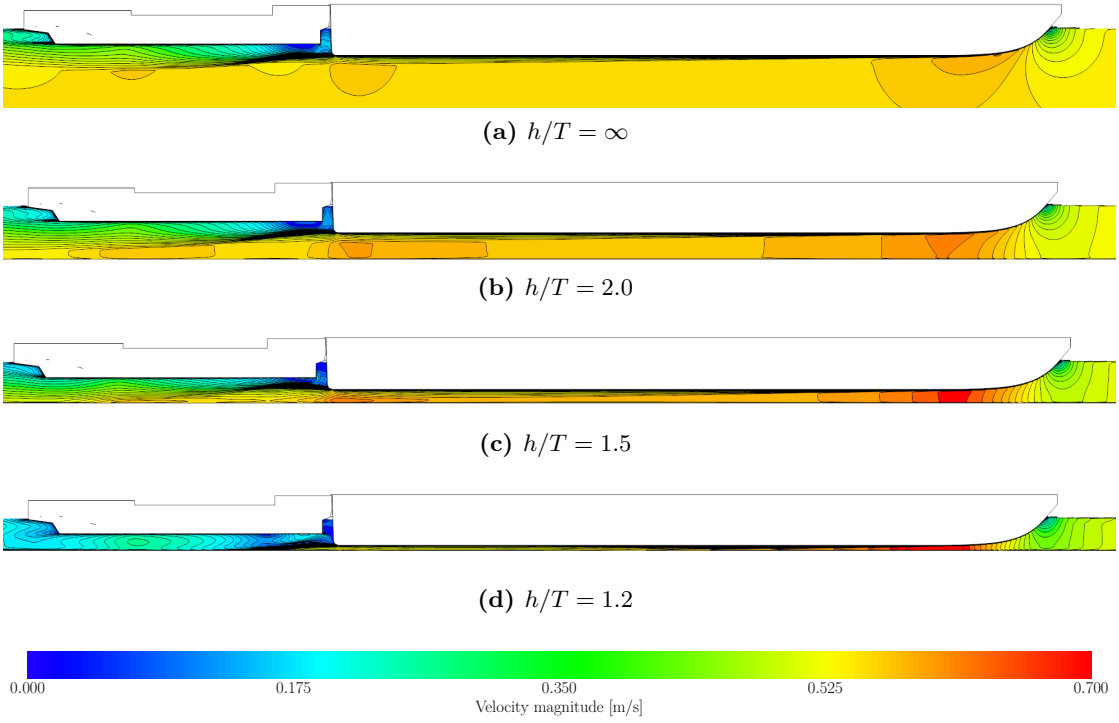

(a) $h/T = \infty$

(b) $h/T = 2.0$

(c) $h/T = 1.5$

(d) $h/T = 1.2$

Figure 5.28: Velocity magnitude contours at $y = 0$ for configuration 1:1 and $U = 0.556\,\mathrm{m/s}$ at different water depths.

The gap flow was significantly affected by water depth and barge or barges arrangement. Figure 5.29 portrays the velocity contours and streamlines in the pusher-barge gap for configuration 1:1, 2:1 and 2:2 at $U = 0.556$ m/s and $h/T = 1.2$. For all configurations, the flow around the pusher was greatly disrupted. In configuration 1:1, a vortex structure developed right under the pusher's bow. Indeed, the sudden change in geometry caused a massive flow separation at the barge's stern. This effect was however less present in configuration 2:1, despite the presence of a smaller vortex structure in the gap. In this case, a bow-bow coupling seemed to be more advantageous, causing less directional changes in the flow. The flow pattern around the pusher arranged in configuration 2:2 differed however drastically. As seen in figure 5.29c, vortices of different sizes developed from the gap and extended underneath the entirety of the pusher's bottom. The massive flow disruption caused by the gap and the shallow water poses a substantial challenge in terms of turbulence modeling. Indeed, the complex interaction between pusher and barge or barges, emphasize the need for more appropriate turbulence models to reliably predict the velocity distribution in the gap area and underneath the pusher. From an experimental point of view, the use of optical methods to quantitatively assess the gap flow would provide a robust validation basis for turbulence models.

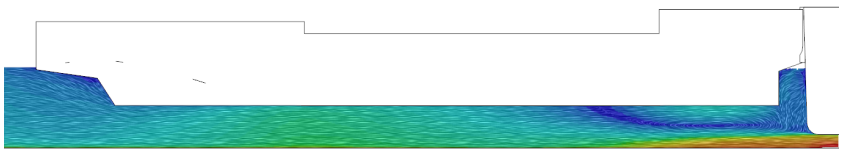

(a) Configuration 1:1

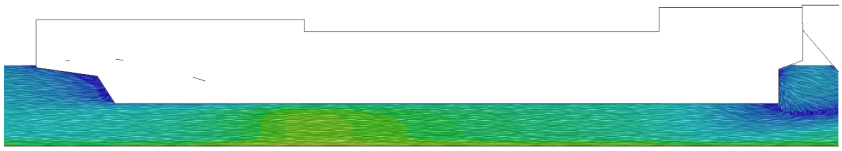

(b) Configuration 2:1

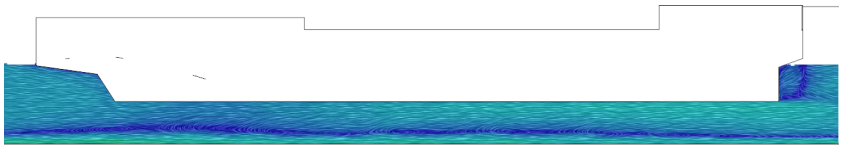

(c) Configuration 2:2

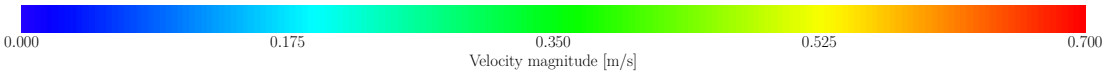

Figure 5.29: Velocity magnitude contours and line integral convolution around pusher boat at $y = 0$ for configurations 1:1, 2:1 and 2:2 at $U = 0.556$ m/s and $h/T = 1.2$.

To illustrate the gap's confinement effect on resistance and its consequences on propulsion, figure 5.30 depicts the ratio u_x/U distributed over the propeller inflow plane of configuration 1:1 advancing at $U = 0.556$ m/s in waters of $h/T = \infty, 2.0, 1.5$, and 1.2. Here, u_x is the flow velocity in the longitudinal x-direction, and U is the inlet velocity. The plane is located at a horizontal distance of 0.178 m from the pusher's transom. Under deep water conditions, ratios u_x/U were lower in the vicinity of the pusher. The effect of the center skeg located underneath the pusher's bottom can also be distinguished. Shallow waters caused ratios u_x/U to decrease in the immediate vicinity of the pusher, underlining the higher power requirements under such conditions, which was also substantiated by the experimental measurements. In shallow water of $h/T = 1.2$, a zone of lower u_x/U ratios than in the neighboring zones around the center plane at amidships can be distinguished. The light blue areas indicated a ratio of around 0.3 to 0.4. This observation is consistent, at least visually, with the velocity contours of figure 5.28, indicating the increasing gap effect in the propeller inflow plane with decreasing water depth.

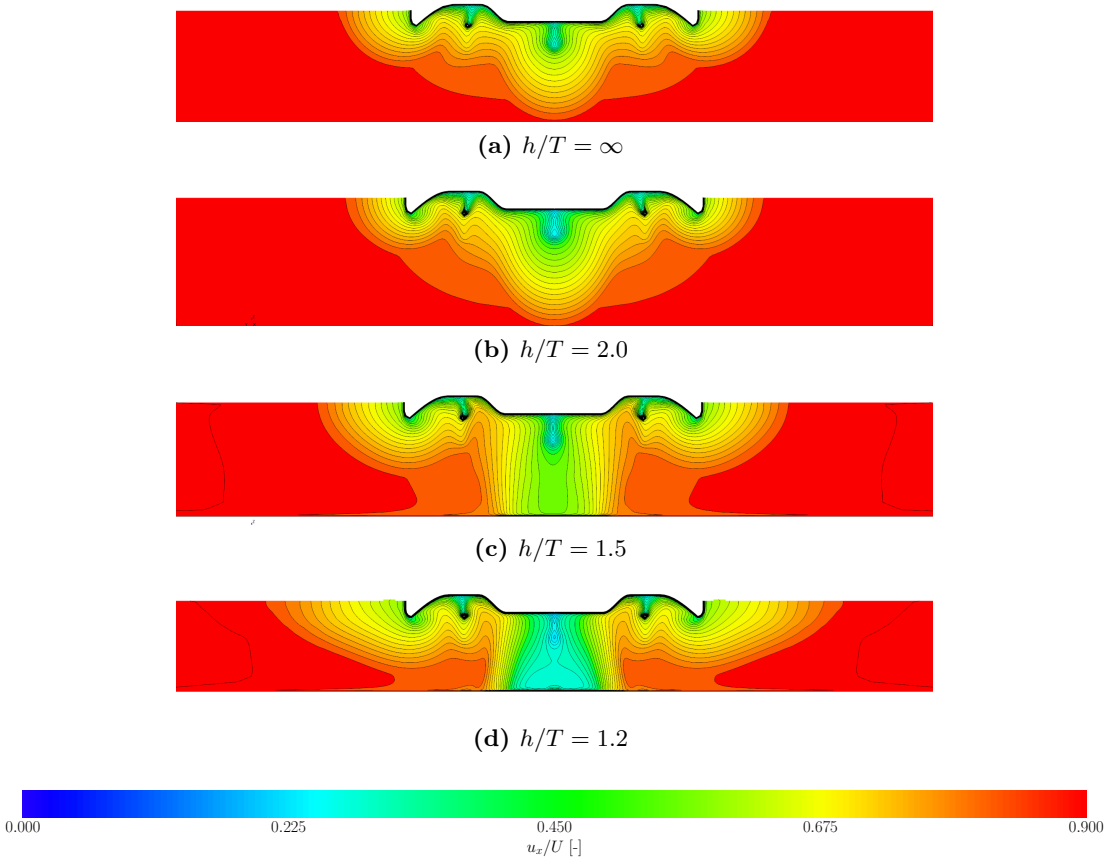

Figure 5.30: u_x/U at $x = 0.163$ m for configuration 1:1 and $U = 0.556$ m/s at different water depths.

Figure 5.31 depict the same ratios as in figure 5.30 for configuration 1:1, 2:1 and 2:2 at $U = 0.556$ m/s and $h/T = 1.2$. The combined effects of gap-flow and waterway blockage were clearly visible. The ratio u_x/U was lower in the vicinity of the pusher in all configurations. The distribution of u_x/U around configuration 1:1 resembled configuration 2:1, with some slight differences. Specifically, the interaction between bottom and waterway was accentuated for configuration 2:1, as seen in figure 5.31b. The overall length of the coupled barges in this configuration had a comparatively higher impact on the interaction between ship's bottom and waterway. The arrangement of four barges in configuration 2:2 presented the most unfavorable inflow condition. The large blue zone underneath the pusher's central area showed an almost zero velocity. This figure was consistent with the conclusions drawn on the basis of figure 5.29c. In other words, the flow disruption due the barge's arrangement in front of the pusher had a decisive impact on the propeller's inflow. Thus, the efficiency of the propulsive devices was greatly affected.

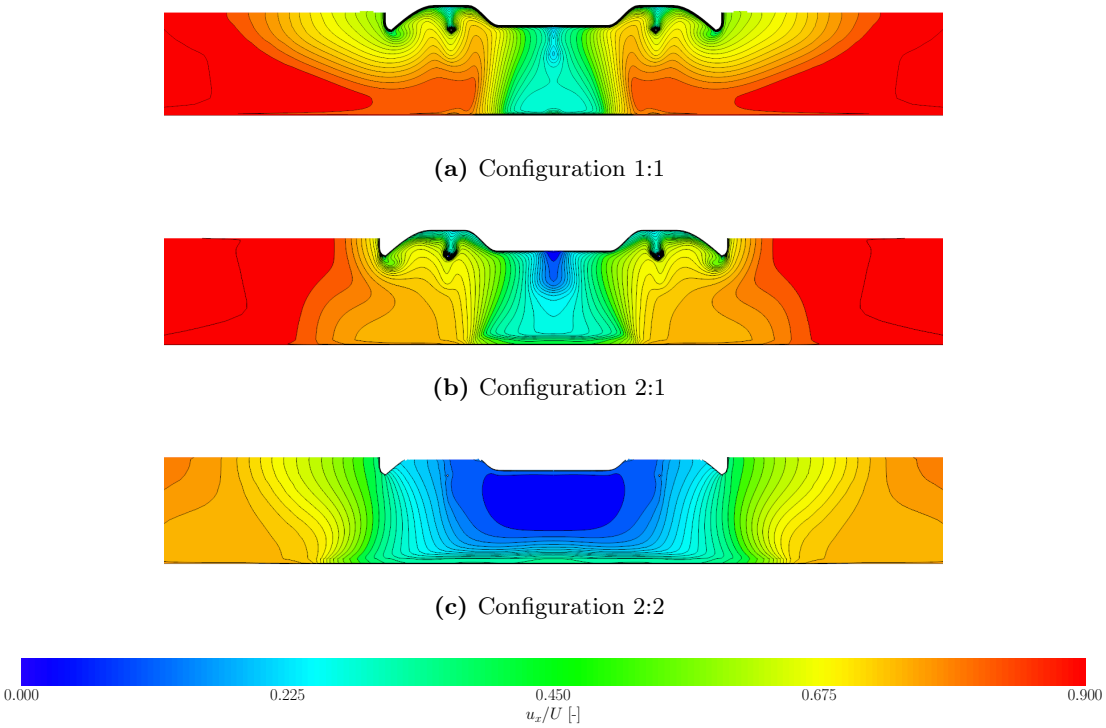

(a) Configuration 1:1

(b) Configuration 2:1

(c) Configuration 2:2

Figure 5.31: u_x/U at $y = 0.163$ m for configuration 1:1, 2:1 and 2:2 at $U = 0.556$ m/s and $h/T = 1.2$.

5.4 Concluding remarks

In this chapter, experimental results of resistance and propulsion tests in deep and shallow water were discussed. Resistance tests in deep water were conducted with bare hull models fitted only with the rudders. The target velocity U was varied successively in one single run to investigate three velocities. In shallow waters, the tests were conducted with appended models and a propeller delivering zero thrust. A single run for each velocity and configuration was then performed. Propulsion tests were performed using the British method in deep water. Residual force, propeller thrust, and propeller torque were measured. Linear interpolation determined self-propulsion points. In shallow water, while maintaining deep water propeller revolutions, additional resistance was measured.

Resulting resistances were presented as coefficient C_T. Although individual barges comprising the convoy configurations were identical, their arrangement significantly affected overall transport efficiency, represented by the power to move one unit of payload. This efficiency was lowest for configuration 2:2. In moderately deep and shallow waters, configuration 2:1 was the most efficient. Resistance test in deep and shallow waters were

replicated numerically using RANSE based computations. The free surface effects were accounted for by the VoF method. The models were constrained and adjusted to their floating position prior to the meshing process. Numerically predicted resistances compared favorably to experimentally measured resistances. Barge arrangement and shallow water effects on shear stresses, as well as on free surface elevation were assessed. The method proved to be reliable, for deep to moderately shallow waters. In extreme shallow waters, the complexity of the flow in the confined gap between barge or barges and pusher boat requires special attention regarding turbulence modeling.

6 Investigation of the Gap Flow Between Pusher and Barge

The experimental investigation of resistance and propulsion, as described in Chapter 5, offered useful insights into the hydrodynamic forces acting on the convoy in the straight ahead condition. However, the corresponding experimental setup was not designed to deliver quantitative data on the flow pattern around a convoy's body, especially in the gap region between the pusher and the barge or barges. While considering mean values of the overall longitudinal force may be sufficient for the validation of numerical resistance tests of seagoing vessels in deep water (as shown in Larsson et al. (2014)), the resistance simulations conducted in this work have shown that the uncertainty introduced by the gap demands special attention. Indeed, to numerically quantify the hydrodynamic forces and moments acting on a convoy's body with sastisfying accuracy, it is crucial to use an appropriate turbulence model that can accurately depict the complex flow pattern between pusher and barge or barges in both deep and shallow water.

In this work, PIV and LDV were used to experimentally capture the flow pattern between the pusher and the barge in a 1:1 configuration, in order to provide robust validation data to validate a suitable turbulence model. The main findings of this study can be used to determine whether RANSE coupled with two-equation turbulence models, which are widely used in the maritime community, are sufficient to accurately depict the complex flows around multibody vessels in deep and shallow water. The choice of the 1:1 configuration seemed natural, considering the ratio of the gap's length to the total convoy length. Indeed, this arrangement proved to be more sensitive to the flow disturbances induced by the bulkiness of the barge and the size of the gap.

The present chapter is organized as follows: First, the experimental setup is presented, including the test matrix and methods for quantifying uncertainties. Second, the numerical setup is described, including the meshing strategies and sensitivity analyses. Third, the experimental and numerical results for two water depths, corresponding to deep and moderately shallow waters, are presented and discussed. Fourth, the flow for water depths ranging from moderate to extremely shallow waters is analyzed numerically to assess the impact of water depth restrictions on the gap flow and convoy resistance. The content of this chapter has been partly published in Zentari et al. (2023), with partly exact wording.

6.1 Experimental setup

The primary objective of the experiments was to provide accurate quantitative flow measurements in the gap between a pusher and a barge for a characteristic 1:1 configuration. These measurements gave useful insights into the gap flow between these coupled bodies and provided high quality data required to validate the numerical method. A bow to stern coupling between pusher boat and barge characterized configuration 1:1. This configuration featured several geometric discontinuities and sharp angles, and it had a high block coefficient. The most prominent feature was obviously the gap between pusher boat and barge. At the front end of this gap, the stern of the barge ended abruptly, creating a large empty space between the coupled bodies. Consequently, the flow was not directed smoothly alongside the pusher's hull towards the propulsors. Therefore, in terms of the flow pattern, this configuration 1:1 was considered to be the worst-case scenario.

The convoy's geometry was identical to the pusher-barge system presented in chapter 4. The model scale was $\lambda = 60$, as opposed to $\lambda = 16$ used in the ambit of captive maneuvering tests. While a lager model offered more accurate results when investigating resistance and propulsion, Reynolds similarity was attempted between the PMM model and the PIV model, although the main focus was not on forces acting on the hull, but rather on how the geometry of the vessel disturbs the flow around it. As seen in figure 6.1, the system was modeled just up to its design waterline because only the flow surrounding the underwater part was of interest. This decision was supported by observations made during the PMM experimental campaign, where no noticeable deformation of the free surface occurred for the pusher-barge system advancing at a constant ship velocity U ranging between $U = 0.556$ to $1.156\,\mathrm{m/s}$, at a model scale of $\lambda = 16$. The corresponding Froude number Fn ranged between $Fn \approx 0.06$ to 0.116. Consequently, uncertainties associated with free surface effects and convoy's trim and sinkage were not considered.

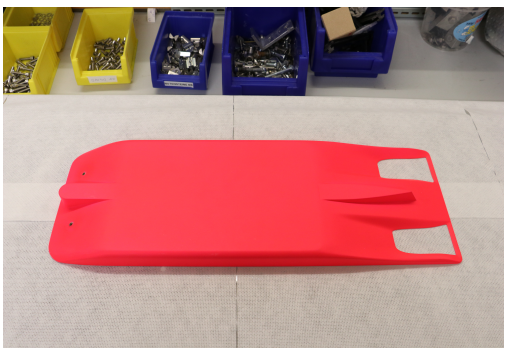

(a) Pusher at a model scale $\lambda = 60$.

(b) Barge at a model scale $\lambda = 60$.

Figure 6.1: Pusher and barge at model scale $\lambda = 60$. The ship's body is modeled up to the waterline.

The experiments were conducted in the circulating water channel of the Institute of Ship Technology, Ocean Engineering and Transport Systems of the University of Duisburg-Essen (**I**nstitut für **S**chiffstechnik, **M**eerestechnik und **T**ransportsysteme, ISMT, in German). The tank's maximum water depth is 645 mm, its width is 1476 mm, and its length is 6000 mm long. Along its measurement section, the tank's water depth could be varied by moving the bottom of the test section, enabling a water depth range between 100 and 645 mm. Thus, the deep water condition with $h/T = 13.82$ and the shallow water condition with $h/T = 2.14$ were possible. Here, h is the water depth, and T is the draft of the barge. The tank walls are made of glass to allow optical access for PIV and LDV measurements. A Perspex acrylic plastic plate covered the water surface to suppress free surface influences. As seen in figure 6.3a, underneath this Perspex plate the pusher-barge model was mounted longitudinally at the center of the measurement section. The bow of the barge was positioned 1478 mm from the inlet of the measurement section. The gap between pusher and barge was 8 mm wide at the water surface. Figures 6.3c and 6.3d show a detailed view of the gap between pusher and barge. For deep water conditions, the highest possible target flow velocity of $U_{in} = 2.09\,\mathrm{m/s}$ was considered; for shallow water conditions, the highest possible target flow velocity was $U_{in} = 1.91\,\mathrm{m/s}$. The latter velocity was slightly lower because the blockage effect in shallow water was larger. Each test was repeated five times to analyze the repeatability of the experiments. Table 6.1 lists these target velocities U_{in}, h/T ratios, and the number of repeated tests. Figure 6.2 shows a schematic representation of the measurement concept to capture the gap flow field as well as the inflow conditions and dynamic pressures downstream of the model. The LDV system, displayed in figure 6.3b, enabled measuring inflow velocities and the associated turbulence in front of the model. The 2D PIV system was set up to capture the flow in an area of interest, i.e., the region where the gap is located; see figure 6.3d. Here, two cameras equipped with special lenses captured the flow in this region from a different perspective. A centrally placed Pitot tube hooked up to a differential pressure sensor measured the dynamic pressures.

The LDV technique optically measures flow velocity components on a point-by-point basis. Here, an LDV system having a laser probe of 800 mm focal length as pictured in figure 6.3b was used. Four laser beams with a wave length of 488 and 514.5 nm and a diameter of 2.2 mm measured two velocity components, namely, the vertical component u_z and longitudinal component u_x. The inflow velocity and turbulence profiles were measured for the deep and the shallow water conditions. The velocity components were measured for 30 s at each point to obtain mean velocities required to calculate the turbulence. The vertical velocity component u_z was small compared to the main flow velocity u_x ($u_z \approx 2.5\,\% \cdot u_x$), so that it is neglected hereafter. For comparison, the measurement uncertainty of the LDV system was about 1.27% for velocities around 2.0 m/s. (These uncertainties were obtained during another measurement campaign, where the velocity of a towing carriage was compared with measured velocities, see Youssef et al. (2022).)

The PIV system consisted of a double cavity Nd:YAG InnoLas Compact Spitlight laser, two Phantom v9.1 high-resolution cameras, and a high-speed controller to monitor the

timing. The laser's pulse energy was 55 mJ, its wavelength was 532 nm, and its pulse rate was 100 Hz. The two cavities enabled illumination and captured two successive frames within a small time instant Δt. A light sheet optic transformed the laser beam into a light sheet with a thickness of about 5 mm. As seen in figure 6.4a, the laser was placed portside of the circulating water channel, and the light sheet was led horizontally inside the water channel. A mirror, placed in the transverse center of the channel, deflected the light sheet about 90° and directed it into the region of interest. For deep water conditions, the mirror was placed on top of the movable channel bottom; for shallow water conditions, it was hung underneath the bottom to avoid unwanted flow disturbances in the channel. To facilitate optical access, a window was cut in the bottom and covered by the Perspex plate. The two high-speed cameras were placed starboard side of the water channel to capture two different perspectives of the region of interest. Camera 1, equipped with a Zhongy Mitakon lens of 85 mm focal length, covered an area larger than the region of interest. Camera 2, equipped with an AF Micro-Nikkor lens of 200 mm focal length, covered a detailed view of the gap itself. Additionally, both lenses were equipped with a 532 nm band pass filter to capture only laser-induced light. The aperture of both lenses was set to f/4.0. Due to the perpendicularity between camera axis and light sheet (90° for camera 1 and 84.2° for camera 2), a prism or Scheimpflug adapter was not required to ensure adequate optical access. For PIV measurements, the time shift Δt between two frames had to be adjusted according to flow velocity, camera resolution, and field of view. Due to the different fields of view of both cameras, the time shift could only be optimized for one camera. Consequently, all tests had to be repeated for each camera. Figure 6.4a shows the arrangement of the PIV laser; figure 6.4b shows the arrangement of camera 1 and 2. As an additive, VESTOSINT polyamide 12 fine powder, with seeding particles having an average particle diameter of 100 μm were used. The captured pictures were post-processed using the proprietary LaVision software. A detailed description of the experimental setup and corresponding uncertainty quantification can be taken from Zentari et al. (2023).

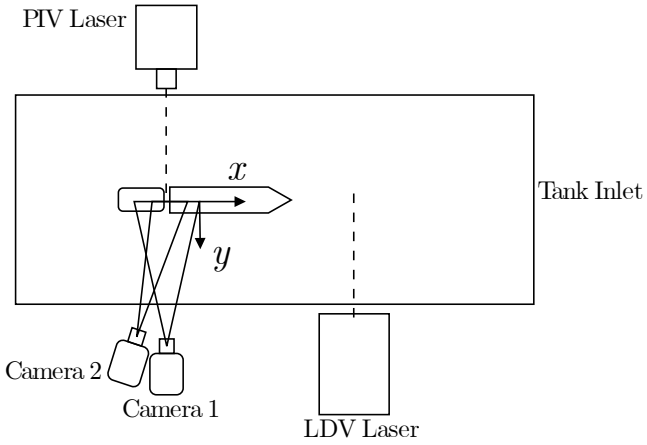

Figure 6.2: Schematic representation of the measurement concept.

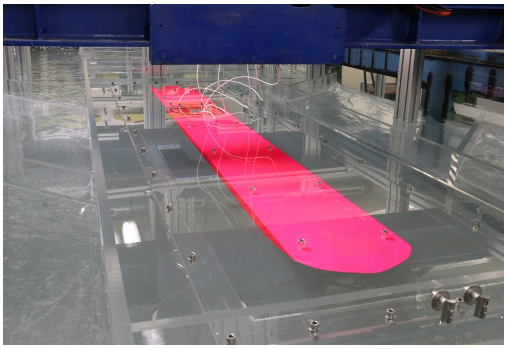

(a) Pusher barge model

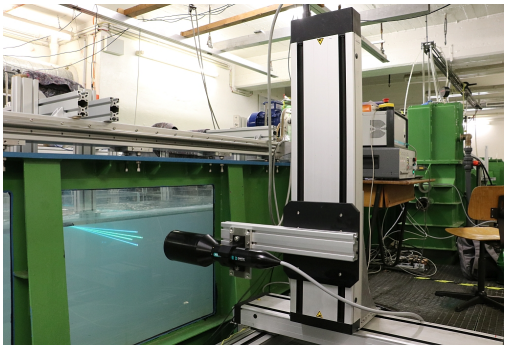

(b) LDV system

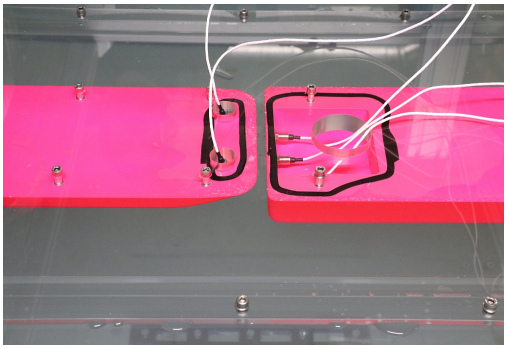

(c) Gap between pusher and barge

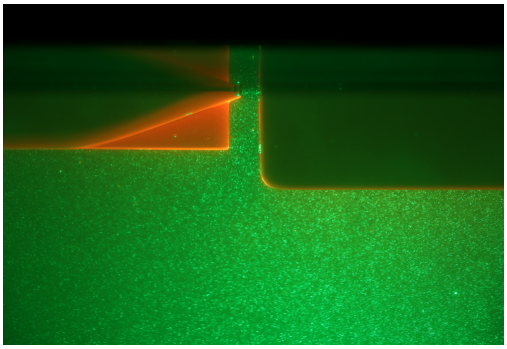

(d) Gap with light sheet

Figure 6.3: Experimental Setup for gap flow measurement in deep and shallow waters.

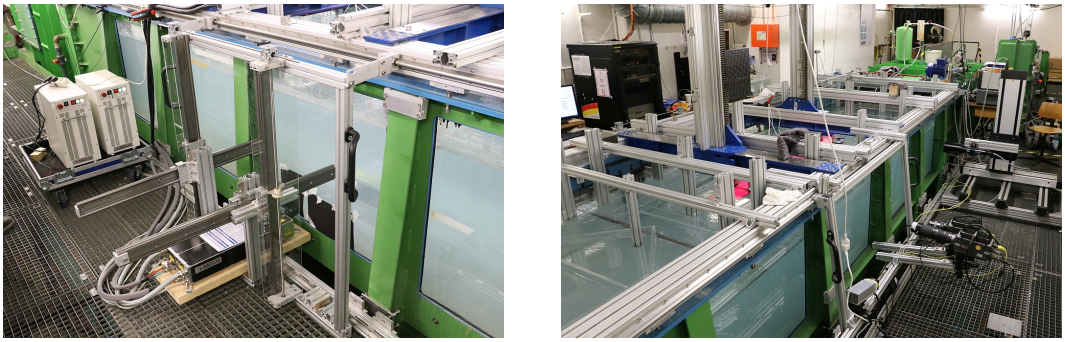

(a) Laser arrangement. **(b)** Camera arrangement.

Figure 6.4: PIV setup with laser and camera arrangement for gap flow measurement in deep and shallow waters.

Table 6.1: Overview of the test matrix, including investigated velocities and water depths variations.

Test condition	**Target velocities** U_{in} [m/s]	h/T [-]	**Repetitions**
Deep Water	2.09	13.82	5
Shallow Water	1.91	2.14	5

6.2 Computational procedure

The purpose of the numerical investigation was to reproduce the flow in the circulating water tank. By focusing on the gap flow, the suitability of different turbulence models was assessed. Two numerical methods were considered, both implemented in the commercial flow solver Simcenter STAR-CCM+. The first method was based on solving the RANS equations coupled with the $k-\omega-$SST and the $k-\varepsilon$ turbulence models, both of which were validated for a broad range of industrial applications. This model, known to yield satisfactory results for marine applications, constituted the starting point of the numerical study. The equations were solved in a segregated manner using the SIMPLE algorithm with seven inner iterations and a second order linear upwind differencing scheme for the convective term. The transient term was discretized using a second order implicit time discretization method and a time step of $\Delta t = 0.01$ s. A key criterion was keeping the CFL number below 0.5. The boundary layer was fully resolved in all cases, with associated y^+ values smaller than unity.

Preliminary calculations highlighted the extreme unsteadiness of the flow in the gap. The gap's particular geometric shape, and the generally poorly optimized barge shape, featuring numerous sharp edges, contributed to early flow separations and massive recir-

culation zones in the gap. This phenomenon was accentuated in shallow waters, owing to the mixing of two boundary layers and the blockage effect, which significantly influenced the velocity and pressure field around the hull. To account for these effects, a second method was employed, namely, the IDDES model of Gritskevich et al. (2012). Their formulation offered noteworthy advantages compared to the original DES formulation of Spalart et al. (1997) by introducing WMLES capabilities. Known issues associated with the original DES formulation, such as GIS and subsequent MSD were thus prevented. In the RANS region, the $k-\omega-$SST turbulence model provided closure of the system of equations. In all cases, a statistically converged RANS simulation constituted the starting point of an IDDES simulation. Reducing the time step to $2.0 \cdot 10^{-4}$ s resolved all relevant turbulent scales. Convective terms were discretized using the hybrid third order **M**onotonic **U**pstream-**C**entered **S**cheme for **C**onservation **L**aw (MUSCL) bounded-differencing scheme, which yielded more stable results in flows with larger gradients and discontinuities.

The dimensions of the circulating water tank defined the computational domains for the deep water case shown in figure 6.5 and for the shallow water case shown in figure 6.6. In the longitudinal direction, the body was positioned a distance of $2.5 \cdot L_{OA}$ from the inlet and a distance of $3.5 \cdot L_{OA}$ from the pressure outlet. A distance of 645 mm separated tank top from tank bottom for the deep water case; a distance of 100 mm, for the shallow water case. Top, bottom, and sides were defined as no-slip walls. As the correct distribution of LES and RANS zones in the IDDES simulations depended on grid size, refinement zones were arranged around the region of interest and around the pusher boat, where cell sizes were $\Delta x = \Delta y = \Delta z = 1.14$ mm. Figure 6.7 depicts sample meshes, although only for the deep water case, of the gap region, the bow of the barge, and the entire pusher-barge system. The correct implementation of both approaches in the solution domains used the IDDES blending function of Gritskevich et al. (2012). A blending function tending towards unity indicated a RANS zone; a blending function tending towards zero, a LES zone. In figure 6.8, a color scheme differentiates the zonal distribution of the blending function. Here, values approaching unity are colored red; values approaching zero are colored blue. As seen, in the area of interest, the RANS zone was limited to the vicinity of the walls of the submerged bodies. The selected grid spacing was hence appropriate for both deep and shallow water cases.

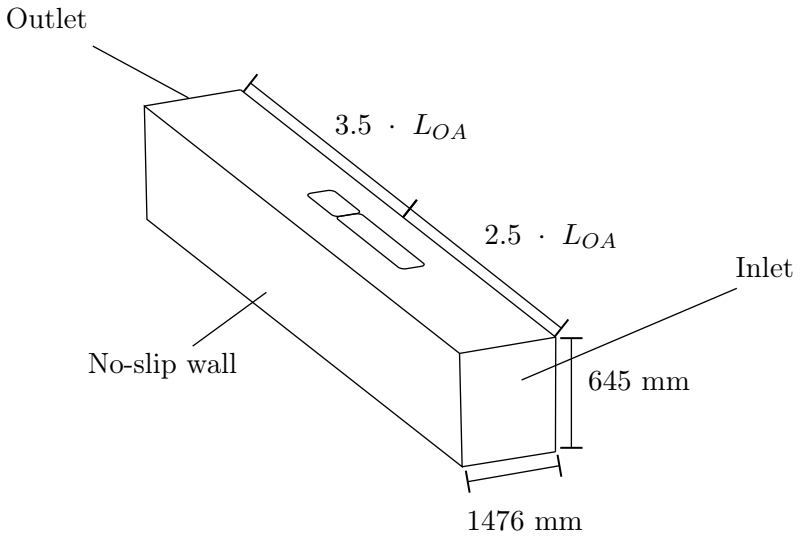

Figure 6.5: Schematic representation of numerical domain for deep water simulation.

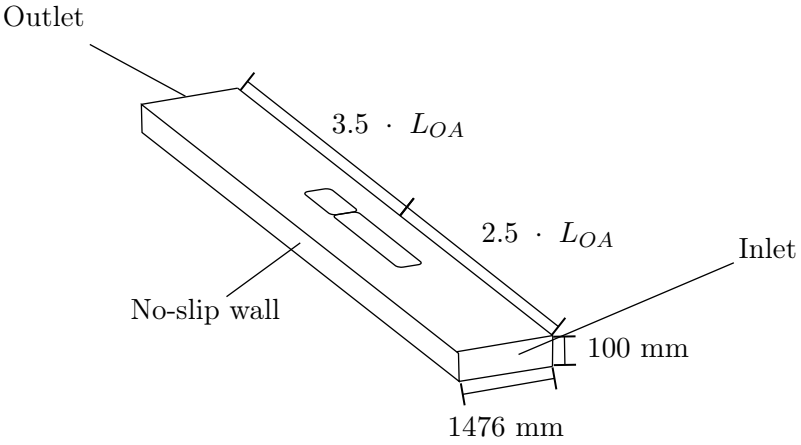

Figure 6.6: Schematic representation of numerical domain for shallow water simulation.

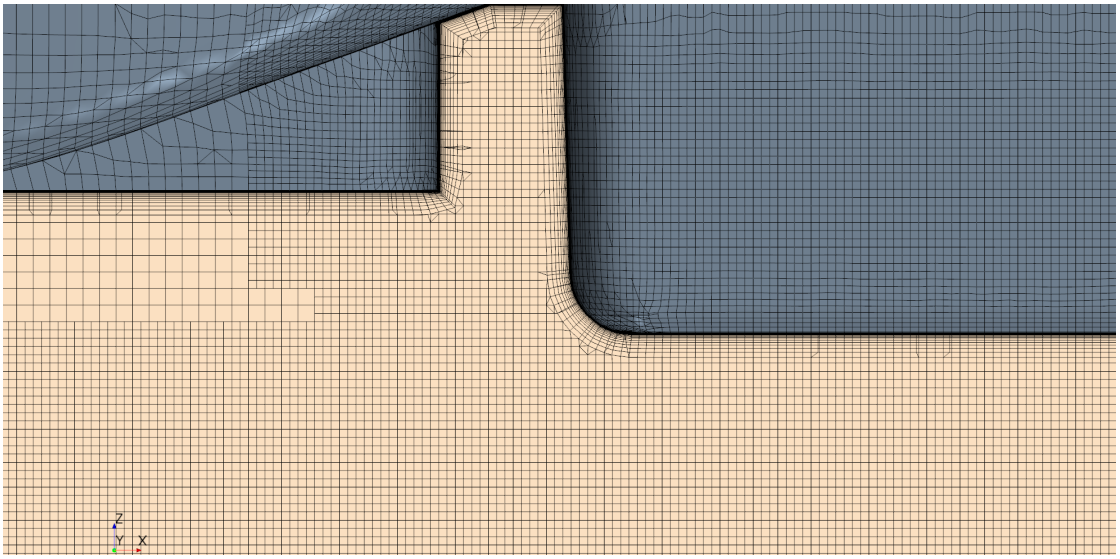

(a) Detailed view of the mesh on the area of interest for the deep water case.

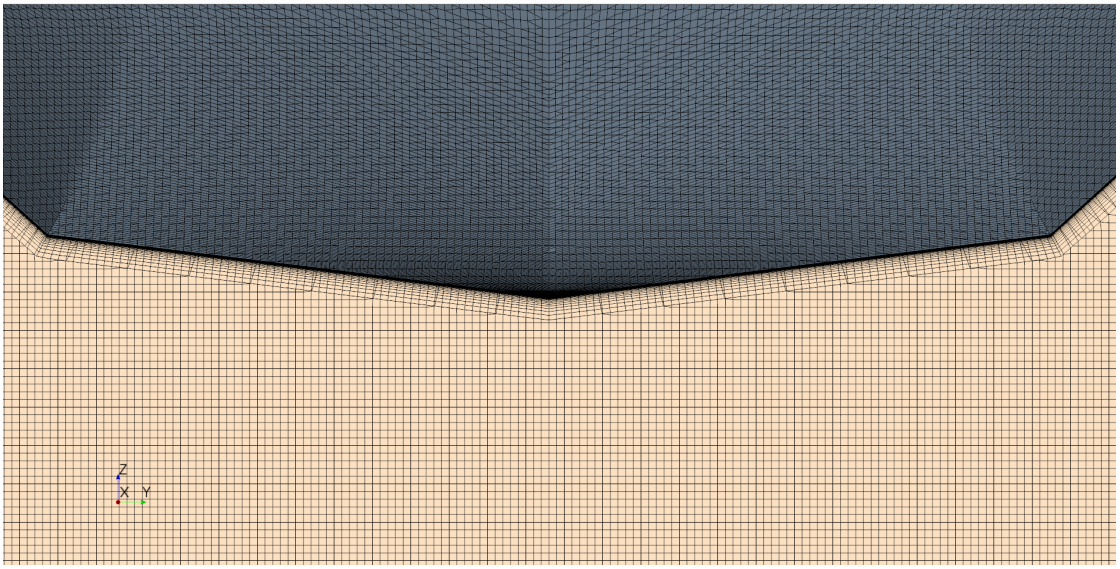

(b) Detailed view of the mesh on the bow area of the barge.

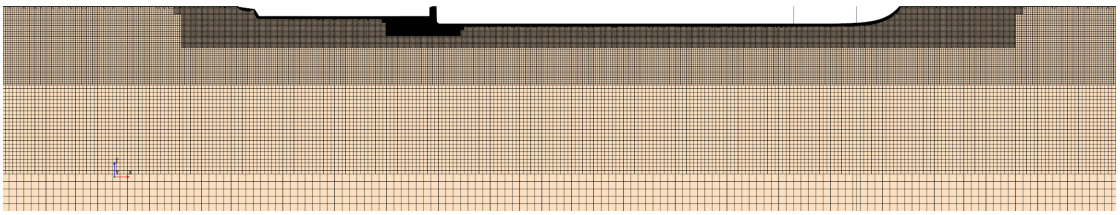

(c) Side view of the mesh around the hull for the deep water case.

Figure 6.7: Detailed view of the mesh for deep water simulation.

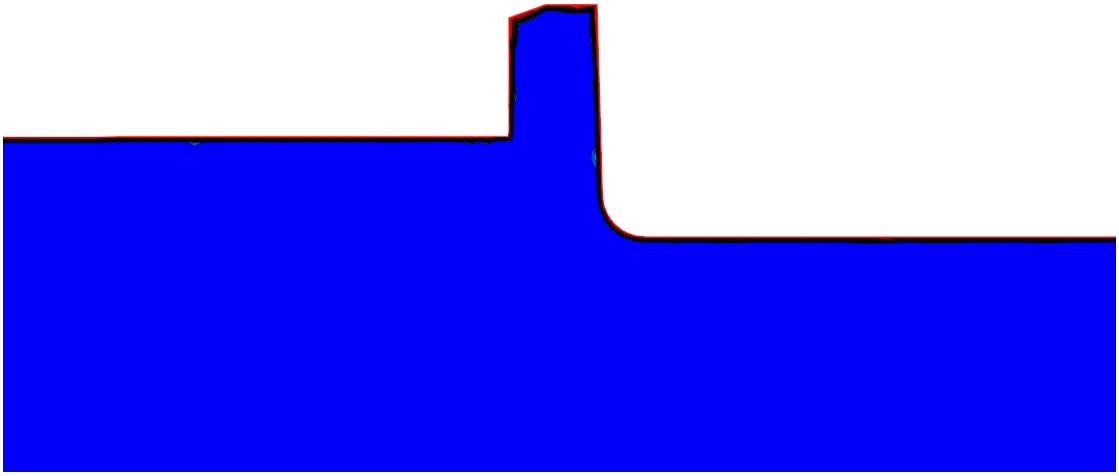

(a) Deep water.

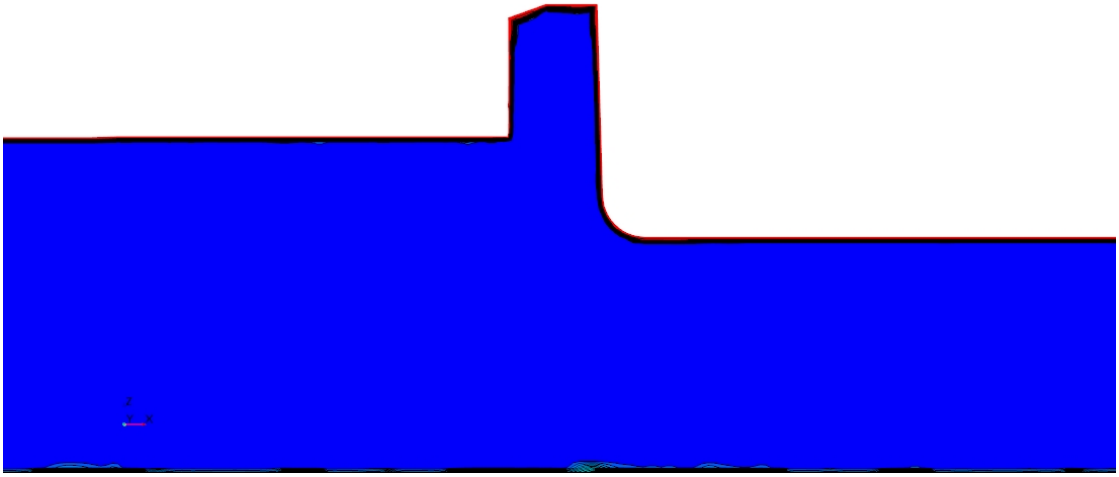

(b) $h/T = 2.14$

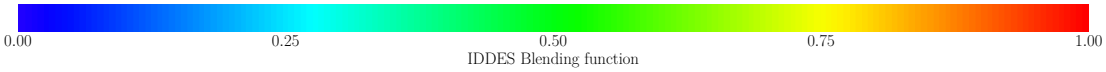

Figure 6.8: Zonal distribution of LES and RANS zones in area of interest for respectively deep water and $h/T = 2.14$ cases.

Convergence and sensitivity analyses were performed using the method of el Moctar et al. (2021) and Oberhagemann (2017). The grid refinement ratio was kept constant in both spatial and temporal refinements to ensure a constant CFL number throughout all simulations. The $k-\omega-$SST simulation was chosen for the discretization study because this kind of analysis was not suitable for an IDDES simulation. Indeed, a systematic refinement with an IDDES simulation might have led to an ambiguous zonal definition of LES

and RANS regions. The modeling error thus induced would have been superimposed on the discretization error, which would have prevented identifying the different error sources. Although Pereira et al. (2021), for example, documented an exhaustive classification and quantification of numerical errors in scale resolving simulations, a simulation was conducted on three successively refined grids with a uniform spatial and temporal refinement ratio $r_k = 2$. Oscillatory convergence was acceptable when the difference between the solutions obtained on successively refined grids was small. The coarsest grid comprised approximately $1.36 \cdot 10^6$ control volumes; the finest grid, $21.79 \cdot 10^6$ control volumes. For the deep water case, Table 6.2 lists the number of control volumes CV, the time step size Δt, the resulting total longitudinal force acting on the convoy X, and the percentage difference between this force and the force obtained on the finest grid. According to the resulting ratio of $R_k = 0.436$, the solution's convergence was monotonic. Figure 6.9 illustrates the application of the method by el Moctar et al. (2021) and Oberhagemann (2017), as a function of the non-dimensional grid spacing Υ. Herein, the grid and time-step independent solutions S_1 and S_2 were determined using equations 3.64 and 3.65. With grid independent solutions of $S_1 = -5.2371\,\mathrm{N}$ and $S_2 = -5.2519\,\mathrm{N}$, the percentage deviation from the solution obtained on the finest grid was only of respectively $\approx 1.29\,\%$ and $\approx 1.06\,\%$. Given this small difference, all successive simulations were conducted using the finest grid. The mesh samples in figure 6.7 and the zonal RANS and LES distributions of the blending function in figure 6.8 hold for the finest grid.

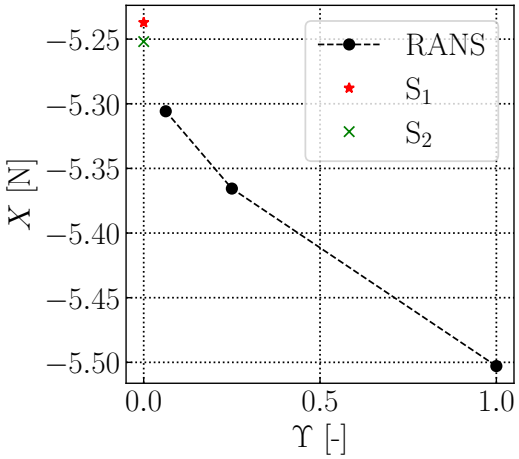

Figure 6.9: Extrapolation of the grid and time step independent solutions S_1 and S_2 determined via the procedure by el Moctar et al. (2021).

Table 6.2: Sensitivity analysis for longitudinal force X, $h/T = 13.82$, $U_{in} = 2.09\,\mathrm{m/s}$.

CV $\cdot\ 10^6$	Δt [s]	X [N]	Diff. in %	R_k
1.36	0.04	-5.5029	3.71 %	
10.04	0.02	-5.3656	1.12 %	
21.79	0.01	-5.3058		
-	-	-		0.436

Using the el Moctar et al. (2021) and Oberhagemann (2017) method, the grid convergence of the numerical simulation based on the RANS and $k-\omega-$SST equations was demonstrated. Nonetheless, the time-step Δt used on the finest grid in table 5.1 is almost one order of magnitude higher than the one required for the IDDES simulation. Furthermore, in all RANS simulations, the total longitudinal force X exhibited a steady behavior. Figure 6.10 depicts a comparison of time series of X for RANS with $k-\omega-$SST with two different time-steps and the IDDES method. All time series show the last 10 s of converged simulations. The red line symbolizes IDDES based X time series, with a Δt of $2 \cdot 10^{-4}$ s; the blue line RANS with $k-\omega-$SST based X time history with a Δt of $2 \cdot 10^{-4}$ s; the green line RANS with $k-\omega-$SST based X time series with a Δt of 0.01 s. The RANS based time series hardly differed from another, exhibiting both a steady behavior. As expected, the X time history obtained from the IDDES simulation demonstrated a noticeable unsteady behavior, with a standard deviation of almost 5% of the averaged value of X.

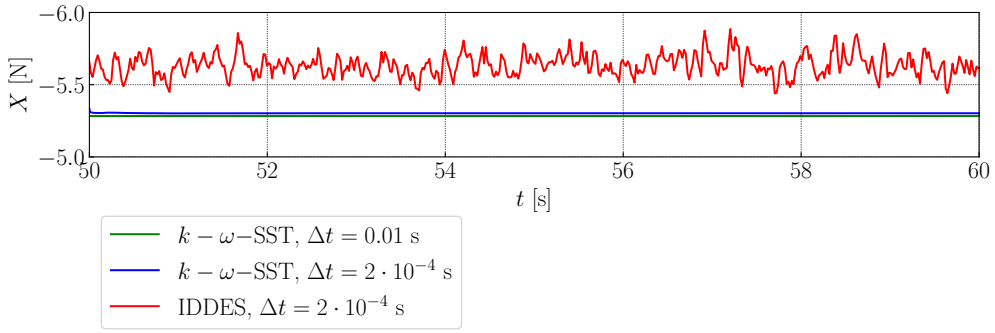

Figure 6.10: Time series comparison of total longitudinal force X obtained from RANS $k-\omega-$SST based simulations and IDDES based simulation.

6.3 Experimental results

Figures 6.11 and 6.12 depict experimentally measured mean velocity fields as contour plots of the normalized 2D time-averaged velocity magnitude $|U|/U_{\mathrm{in}}$. These figures show the mean velocity field in deep and shallow water as measured by the PIV method.

The vectors only indicate the averaged direction of the flow. The coloring from blue to green to red corresponds to the lowest velocity in blue to the highest velocity in red. Both figures discerned a relatively large recirculation zone extending from the barge's transom, engulfing the pusher's bow longitudinally between $x/L_{OA} \approx -0.2$ and -0.26 and vertically between $z/T \approx 0.8$ and 1.2. The transition zone, colored green, marks the separation between the recirculation zone and the free stream flow. In shallow water, the tank bottom is clearly identified as the velocity drastically decreased in its vicinity. In deep water, the flow detached itself at the barge transom, creating a small vortex structure located inside the gap. The water then escaped from the gap, where a larger separation bubble was generated. As seen in figure 6.11, the velocity vectors under the pusher's bow showed a smaller recirculation zone between $z/T \approx 0.6$ and 0.8. The flow reattached itself at about the pusher's half length. The transition zone grew larger further downstream, indicating the influence of the gap on the flow along the length of the pusher.

A similar flow pattern was observed in shallow water, albeit with some differences ensuing from the blockage effect. Consequently, the free stream region, where the flow reached its maximum velocity, was constrained between ship model and tank bottom. In addition, the recirculation zone and the transition region were somewhat smaller. Nonetheless, the same vortex structures as in deep water occurred, i.e., the boundary layer on the barge's bottom is similar in both cases. According to Zeng et al. (2019), who investigated this blockage effect in shallow water and its effect on the boundary layer for a typical inland waterway vessel, the flow is accelerated past the vessels bow, creating an under-pressure region. Here, the flow was altered by the shear forces and decelerated upon reaching a detachment point and, as seen in figures 6.11 and 6.12, this occurred at the barge's transom in this study. However, the bulkiness of the pusher-barge configuration, and the barge's vertical transom and sharp edges induced a major change in the flow pattern compared to the flow pattern of a conventional vessel. It is known that the flow pattern between two interacting floating bodies adds substantial complexity to the flow. Arslan et al. (2015), who analyzed the lateral flow between two tanker sections of different dimensions, identified two main vortices, one located directly in the gap between the two bodies and the other located below the body of lesser draft. Although only moderately comparable to this study, their arrangement between the two bodies is relatively close to the arrangement of pusher and barge in configuration 1:1.

From a broader point of view, the principal flow features in the current case resembled the canonical flow over bluff bodies. Flow characteristics past the barge's transom were similar to those for the so-called **B**ackward **F**acing **S**tep (BFS) case, exhaustively described by Chen et al. (2018). They highlighted three main parts of the flow. Similar to this case, they distinguish between a free stream region, a large separation region, and a reattachment/recovery region. The main separation bubble, located behind the step, is clearly visible in both deep and shallow water cases. According to Nadge and Govardhan (2014), a clear relation exists between the height of the step, the height of the channel, and the Reynolds number. Specifically, the combination of these parameters distinctly

influence the size of the separation bubble and its reattachment length. In this case, despite a Reynolds number of similar magnitude, the separation bubble was smaller in shallow water. Analogous to the conclusions of Nadge and Govardhan (2014) for the BFS case, a smaller UKC had a drastic effect on the size of the separation bubble and its reattachment length.

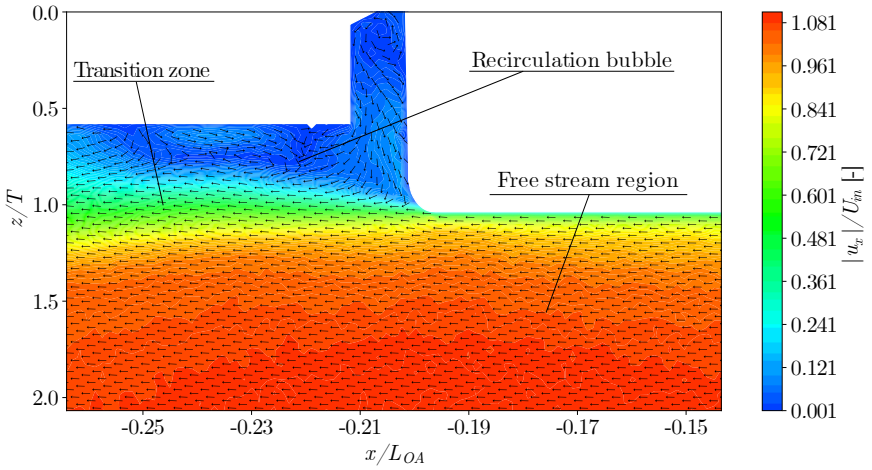

Figure 6.11: Velocity magnitude contour $|u_x|/U_{\text{in}}$ and vectors from PIV measurements for area of interest in $h/T = 13.82$ and $U_{in} = 2.09\,\text{m/s}$.

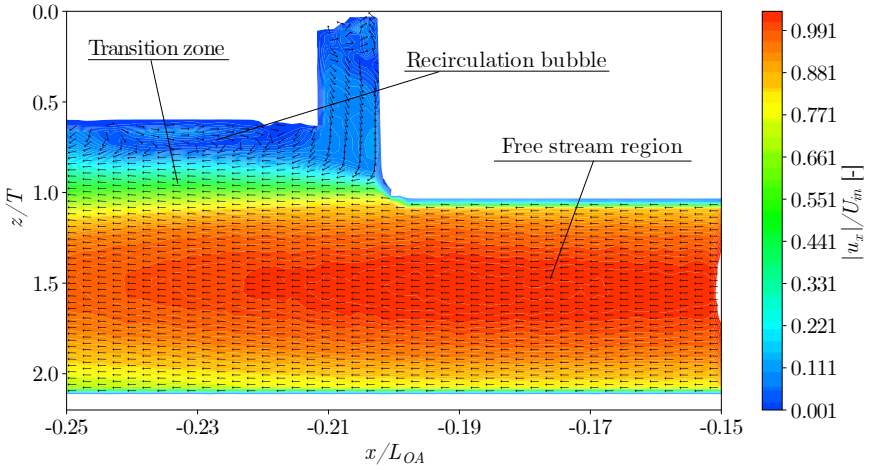

Figure 6.12: Velocity magnitude contour $|u_x|/U_{\text{in}}$ and vectors from PIV measurements for area of interest in $h/T = 2.14$ and $U_{in} = 1.91\,\text{m/s}$.

6.4 Numerical results

Figures 6.13 and 6.14 plot comparative computed and measured mean longitudinal velocity profiles u_x/U_{in} obtained for the deep water case and for the shallow water case, respectively. (The u_x/U_{in} values were multiplied by 20 to improve data visualization.) These profiles, referred to the amidships section at $y = 0$, were located between $x/L_{OA} = -0.15$ and -0.544, with a distance of $\Delta x = 20$ mm between each profile. The profile located at $x/L_{OA} = -0.207$ lies directly in the gap between pusher and barge. The numerically obtained velocity profiles represent the time averaged solution over the PIV measurement time. The green dashed line connects RANS based profiles using the $k-\omega-$SST turbulence model; the blue dash-dotted line, RANS based profiles using the $k-\varepsilon$ turbulence model; the solid line, profiles obtained using the IDDES method; and the red circles, experimentally measured values.

Analogous to figures 6.11 and 6.12, three main regions were identified. One region, located between $x/L_{OA} = -0.164$ and -0.207, comprised profiles located underneath the barge leading to its transom; a second region, located between at $x/L_{OA} = -0.207$ and -0.221, covered the gap; and a third region, located between $x/L_{OA} = -0.221$ and -0.263, included the velocity field underneath the pusher boat. As seen in figure 6.13, in deep water, all numerical methods accurately predicted the mean streamwise velocity in the region underneath the barge. Predictions based on the IDDES method were in closest agreement with measurements in all three regions. Specifically, in the gap region, where the velocities were almost zero, the transition between gap flow and free stream flow was accurately captured. Moreover, the IDDES based velocity profiles representing the boundary layer underneath the pusher boat compared excellently to the experiments. The RANS based velocity profiles also agreed favorably with experimental results. However, some discrepancies occurred in the wake of the barge underneath the pusher boat. The transition of the velocity profiles between $x/L_{OA} = -0.221$ and -0.263 and $z/T \approx 0.7$ and 1.5 deviated slightly from experimental data, revealing overpredicted transition velocities determined by the RANS based methods. Also, predictions based on the $k-\varepsilon$ turbulence model of streamwise velocity profiles in the wake region were somewhat more accurate than those based on the $k-\omega-$SST model.

In shallow water, the velocity profiles extended from ship's keel to tank bottom; see figure 6.14. Here, the numerical simulations yielded profiles that agreed satisfactorily with those based on experimental data. Indeed, the profiles underneath the barge matched the experimental data, although the streamwise velocities between bottom and barge's keel were slightly overestimated. The largest differences occurred in the gap and in the transition region between $x/L_{OA} = -0.207$ and -0.263. The transition into the free stream region of the experimentally obtained profile located in the gap at about $x/L_{OA} = -0.207$ was somewhat smoother. Indeed, between $z/T \approx 0.75$ and 1.00, the numerically predicted transition of this profile was very sudden. This kind of transition occurred in the majority of the numerically obtained velocity profiles underneath the pusher boat.

Nonetheless, the numerical results clearly differed. Specifically, the detachment bubble, located longitudinally between $x/L_{OA} = -0.235$ and -0.263 and vertically between $z/T \approx 0.75$ and 1.00, compared more favorably to experimental data when predicted by the IDDES method than its RANS based counterparts. The $k-\varepsilon$ model also yielded a satisfactory agreement with the experimental data in this area. All methods accurately captured the velocity profiles in the free stream region underneath the barge.

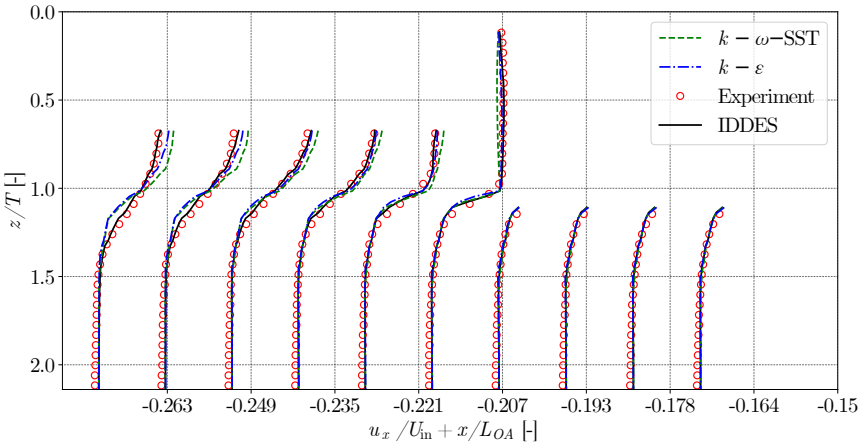

Figure 6.13: Comparison between computed and experimental streamwise velocity profiles $u_x/U_{in} + x/L_{OA}$ in deep water and $U_{in} = 2.09\,\text{m/s}$

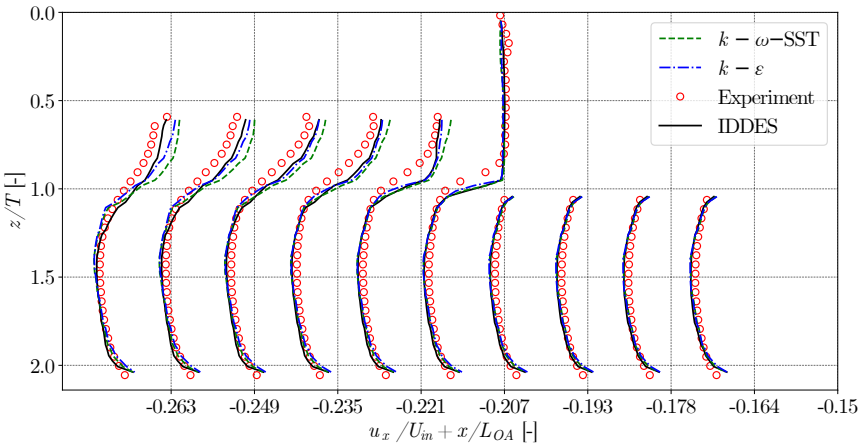

Figure 6.14: Comparison between computed and experimental streamwise velocity profiles $u_x/U_{in} + x/L_{OA}$ in shallow water and $U_{in} = 1.91\,\text{m/s}$

Guilmineau et al. (2018) analyzed streamwise velocity profiles to validate various turbulence models to predict the flow in the wake of the Ahmed body. The bulkiness of their test body bears some resemblance to a typical inland barge. They compared numerical data obtained using RANS coupled with the **E**xplicit **A**lgebraic **R**eynolds **S**tress **M**odel (EARSM) turbulence model and a DDES and IDDES approach combined with the $k-\omega-$SST turbulence model. They concluded that IDDES is best suited when predicting the flow pattern in the wake, a heavily separated region. Similar conclusions can be drawn in this case. Results from the numerical simulations using the IDDES method agreed best with experimental data for both deep and shallow water conditions.

Figures 6.15 plots the total mean pressure coefficient C_p along the length of the convoy for the deep water case and for the shallow water case, respectively. Here, $C_p = p/0.5\rho U_{in}^2$ is referred to the amidships section at y = 0, where p is the pressure, ρ the water density, and U_{in} is the inlet velocity. The blue dash-dotted line connects RANS based coefficients using the $k-\omega-$SST model; the green dashed line, RANS based coefficients using the $k-\varepsilon$ model; the black dotted line, coefficients obtained from the IDDES simulation.

For the deep water case (figure 6.15a), all three numerical methods predicted almost identical C_p values alongside the convoy's hull. The flow at the bow of the barge decelerated, creating a high pressure zone. Immediately after the bow, the flow accelerated, creating a low pressure zone. Underneath the barge, between $x/L_{OA} \approx 0.26$ and 0.75, the pressure remained relatively stable. In the gap region, a sudden pressure drop occurred, corresponding to the low pressure region at the transom of the barge. The variation of C_p underneath the pusher boat after the gap characterized the separation region. Some minor differences occurred in the gap at $x/L_{OA} \approx 0.26$. Here, the coefficients obtained via the IDDES method were slightly lower than the RANS predicted coefficients.

On the other hand, larger differences characterized the shallow water pressure coefficients plotted in figure 6.15b. Generally, the IDDES method yielded somewhat lower C_p values than the RANS method. The same trend was observed in the recirculation region alongside the pusher's hull. Besides, the discrepancies between RANS and IDDES methods and comparative C_p values obtained from deep and shallow water simulations clearly highlighted the blockage effect. Indeed, the shallow water case was characterized by higher pressures alongside the barge's hull and a larger pressure variation in the gap area. Moreover, the interaction between tank bottom and the barge's boundary layer also contributed to discrepancies between the methods.

For the deep water case and for the shallow water case, table 6.3 lists the total computed longitudinal force X acting on the convoy's hull determined using the RANS based method with the $k-\varepsilon$ turbulence model, the RANS based method with the $k-\omega-$SST turbulence model, and the IDDES method. Values of this force X represent averages obtained over the last 20 s of the corresponding statistically converged simulations. This table lists also the percentage difference between the RANS based force and the IDDES

based force. For the deep water case, the force X obtained from the IDDES simulation was approximately 7.5% higher than the RANS based force with the $k-\omega-$SST turbulence model and about 11.4% higher than the RANS based force with the $k-\varepsilon$ turbulence model. For the shallow water case, this difference still persisted, albeit to a lesser extent, where the peak difference between the IDDES based force and the RANS based force with the $k-\omega-$SST turbulence model and the RANS based force with the $k-\varepsilon$ turbulence model of was 6.9% and 6.8%, respectively. Zentari et al. (2022), using a RANS based force with the $k-\omega-$SST turbulence model underpredicted this force X, with larger deviations from the experimental values in shallow water. The lack of experimental measurements of the overall longitudinal force acting on the hull in this particular experiment could not substantiate the above findings. Nonetheless, it was concluded that the scale resolving IDDES method yielded a higher resistance for pusher-barge systems than RANS based methods, which suggests that the former is more accurate.

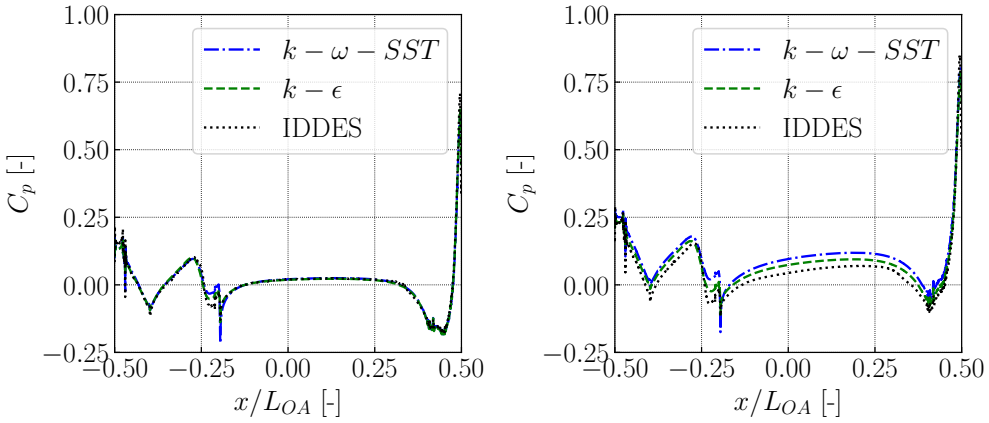

(a) $h/T = 13.82$ **(b)** $h/T = 2.14$

Figure 6.15: Pressure coefficient C_p alongside the center line of hull surface over non dimensional pusher-barge length x/L_{OA}.

Table 6.3: Values of total computed longitudinal force X acting on the convoy's hull in deep and shallow water. The velocity in deep water is 2.09 m/s and 1.91 m/s in shallow water. The last row shows the difference of X from RANS simulations to the value computed from IDDES simulation.

h/T [-]	**Method**	X[N]	**Diff. in %**
	$k-\varepsilon$	-5.064	11.4
13.82	$k-\omega-$SST	-5.288	7.5%
	IDDES	-5.713	-
	$k-\varepsilon$	-6.379	6.8
2.14	$k-\omega-$SST	-6.378	6.9
	IDDES	-6.848	-

Figures 6.16 and 6.17 portray 2D contour plots of average velocity, defined as $|u_x|/U_{in}$, on the system's center plane in the region of interest for, respectively, the deep and shallow water cases. Here, u_x is the velocity components in the x-direction. The four graphs in two figures depict velocities based on the RANS method with the $k-\varepsilon$ turbulence model, the RANS method with the $k-\omega-$SST turbulence model, the IDDES method, and the experimental data. These graphs are convenient to qualitatively compare the numerical results with measurements. The color scheme varies from blue to green to red, representing lower to higher velocity regions. All graphs distinguish the free stream region underneath the barge up to its transom, the gap region, and the separated wake starting at the barge's transom.

In deep water, the boundary layer underneath the barge turned out to be similar in all graphs, thus confirming the velocity profiles plotted in figure 6.13. However, figures 6.16a and 6.16b demonstrate that the RANS simulations predicted a somewhat larger separation bubble, indicated by the light blue region at $x/L_{OA} \approx -0.23$, which also identifies the center of the separation bubble. Moreover, the two RANS based contours show a similar transition from the separation region to free stream, colored green. Nevertheless, in figures 6.16c and 6.16d the IDDES based contours compare best to the experimentally based contours. Overall, the numerically simulated separation bubble, transition zone, and boundary layer at the barge's bottom agreed favorably to those from experiments depicted in figure 6.16d.

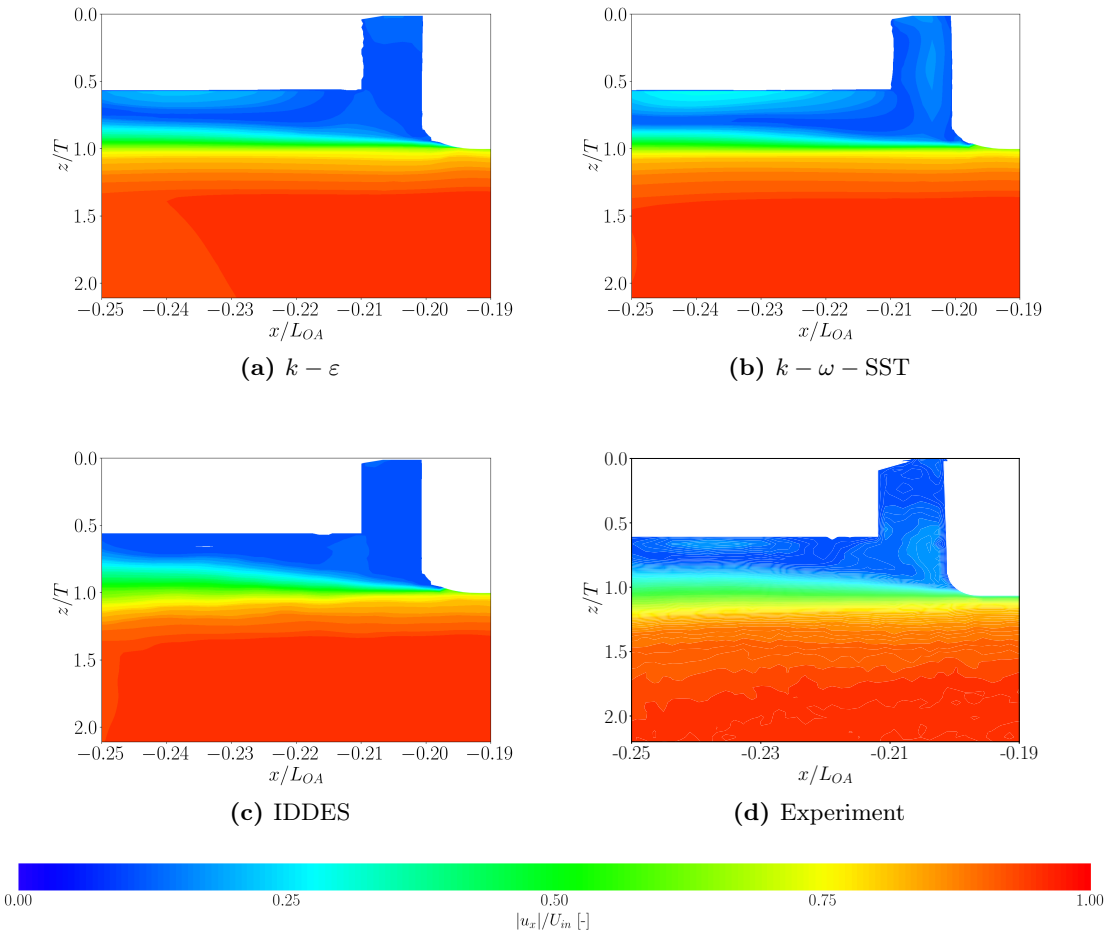

(a) $k-\varepsilon$ **(b)** $k-\omega-$SST

(c) IDDES **(d)** Experiment

Figure 6.16: Two dimensional contour plot of the velocity $|u_x|/U_{in}$ in area of interest for respectively $k-\varepsilon$, $k-\omega-$SST, IDDES and experiment at $h/T = 13.82$.

In shallow water, the numerical methods captured the boundary layer on the tank's bottom and underneath the barge with satisfactory accuracy, as confirmed by the velocity profiles plotted in figure 6.14. On the other hand, as seen in figures 6.17a and 6.17b, the RANS based methods overpredicted the separation bubble, which was comparatively smaller in shallow water. Consequently, the size of the green region depicting the transition from separation bubble to free stream was underpredicted compared to the experimental data in figure 6.17d. Furthermore, the free stream region predicted by the RANS methods are somewhat larger. The IDDES method yielded an improved concurrence with the experiments. Despite a visible difference in the immediate vicinity of the barge's transom, the size of the separation zone turned out to be similar. Not only the extent of the transition zone, but also the size of the free stream region compared favorably to experimental results. In both deep and shallow water, the qualitative com-

parison of the numerical and experimental results confirmed the conclusions drawn on the basis of the quantitative comparison of the velocity profiles depicted in figures 6.13 and 6.14.

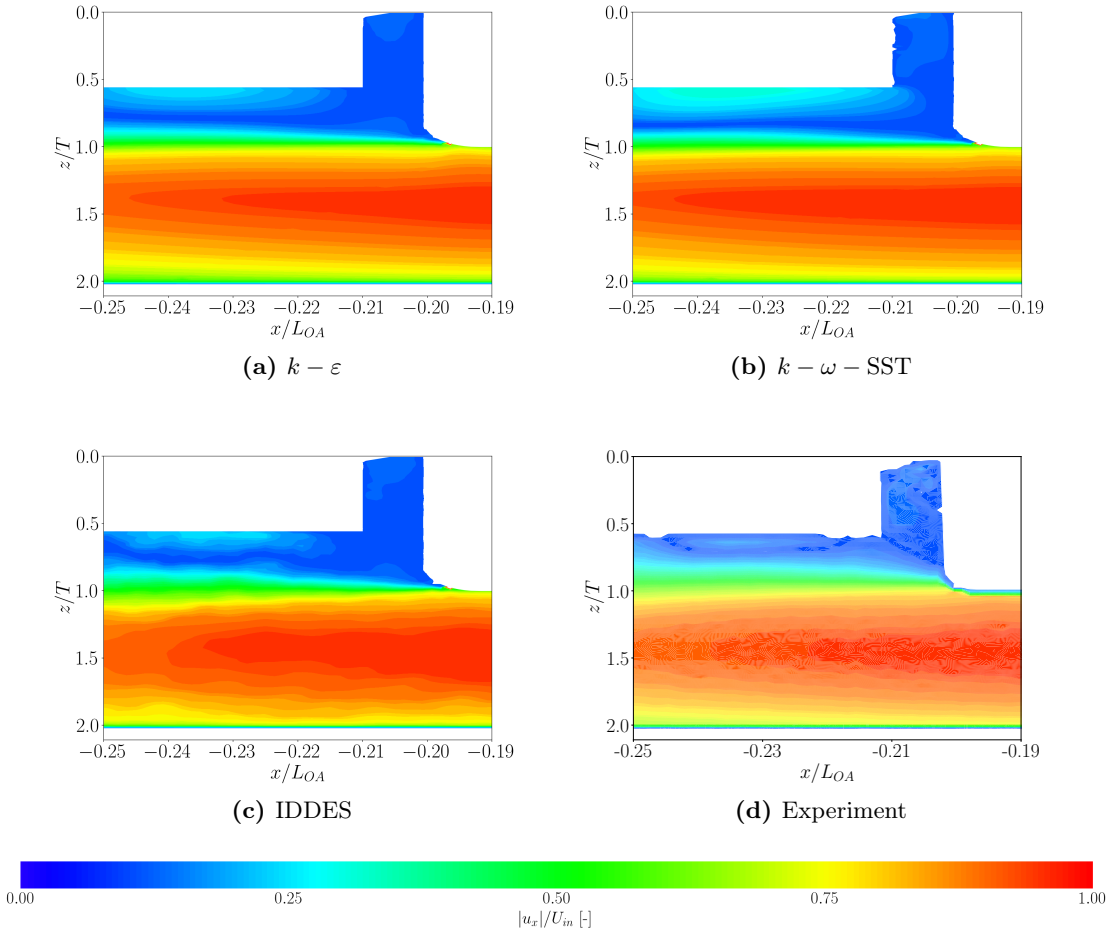

Figure 6.17: Two dimensional contour plot of the velocity $|u_x|/U_{in}$ in area of interest for respectively $k-\varepsilon$, $k-\omega-$SST, IDDES and experiment at $h/T = 2.14$.

Although the analysis of the velocity field covering the regions of interest allowed a qualitative comparison with the experimental results, it was useful to also trace the evolution of the flow at transverse sections. Figures 6.18 and 6.19 plot the averaged axial velocity ratio $|u_x|/U_{in}$ at three different transverse sections. The section at $x/L_{OA} = -0.19$ was located before the barge's transom; the section at $x/L_{OA} = -0.202$, inside the gap between barge and pusher; and the section at $x/L_{OA} = -0.23$, underneath the pusher on the level of the separation bubble. As the PIV technique did not measure velocities at these sections, only numerical predictions were compared.

In deep water, computed axial velocity contours were fairly similar at all three sections, regardless of the numerical method used. However, some differences are visible. First, a distinct vortex-like structure was generated alongside the barge's bilge radius at $x/L_{OA} = -0.19$, as seen in figures 6.18a, 6.18b and 6.18c. While the RANS based distributions are similar, the distributions from the IDDES simulation differed in some points. At $x/L_{OA} = -0.2$, the contours of u_x/U_{in} differed mostly inside the area marked in blue. The color distribution in this detached region shows the generation of a differently shaped recirculation bubble in the immediate vicinity of the barges transom. Here, the bilge vortex is still visible. Finally, the axial velocity distribution at section $x/L_{OA} = -0.23$ depicts a deep blue area alongside this section's center. Figures 6.18g and 6.18h demonstrate that the RANS predicted velocity fields with the $k-\varepsilon$ and the $k-\omega-$SST RANS turbulence models formed a larger recirculation bubble. The corresponding IDDES based velocity field in figure 6.18i obtained a substantially smaller recirculation bubble. Moreover, the bilge vortex, present in all figures, is somewhat larger. In conclusion, the pressure coefficient distribution C_p plotted in figure 6.15a substantiated the similarity of the computed axial velocity contours.

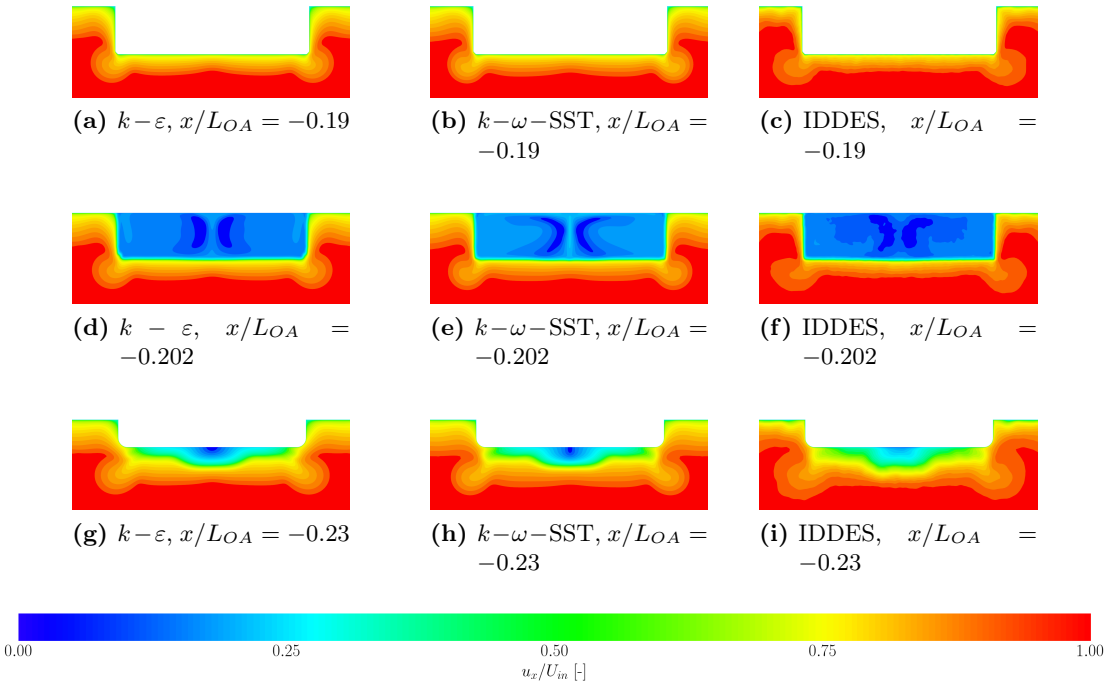

(a) $k-\varepsilon$, $x/L_{OA} = -0.19$ **(b)** $k-\omega-$SST, $x/L_{OA} = -0.19$ **(c)** IDDES, $x/L_{OA} = -0.19$

(d) $k-\varepsilon$, $x/L_{OA} = -0.202$ **(e)** $k-\omega-$SST, $x/L_{OA} = -0.202$ **(f)** IDDES, $x/L_{OA} = -0.202$

(g) $k-\varepsilon$, $x/L_{OA} = -0.23$ **(h)** $k-\omega-$SST, $x/L_{OA} = -0.23$ **(i)** IDDES, $x/L_{OA} = -0.23$

Figure 6.18: Two dimensional contour plot of the non-dimensional axial velocity u_x/U_{in} in the area of interest for respectively $k-\varepsilon$, $k-\omega-$SST and IDDES simulations in deep water.

In shallow water, the computed axial velocity contours obtained from the RANS method and the IDDES technique differed. As seen in figure 6.19c, at $x/L_{OA} = -0.19$ the IDDES method generated a larger bilge keel vortex, whereas the RANS based contours, shown in Figs. 6.19a and 6.19b were similar, regardless of the turbulence model used. In the gap section, at $x/L_{OA} = -0.202$, the contours differed, depending on the method used. The pressure coefficient distribution C_p in figure 6.15b also supports these discrepancies. However, the largest differences, seen in figures 6.19g , 6.19h and 6.19i, occurred underneath the pusher. Here, the velocity contours show that the IDDES based separation bubble, marked blue in these figures, is smaller than the RANS based bubble. Indeed, the contour plots at the longitudinal sections presented in 6.17 show that the RANS based simulations overestimated the separation region. Also, the IDDES based simulations in figure 6.19i indicated a certain amount of mixing occurring between the boundary layer flow underneath the pusher and the flow near bottom of the tank.

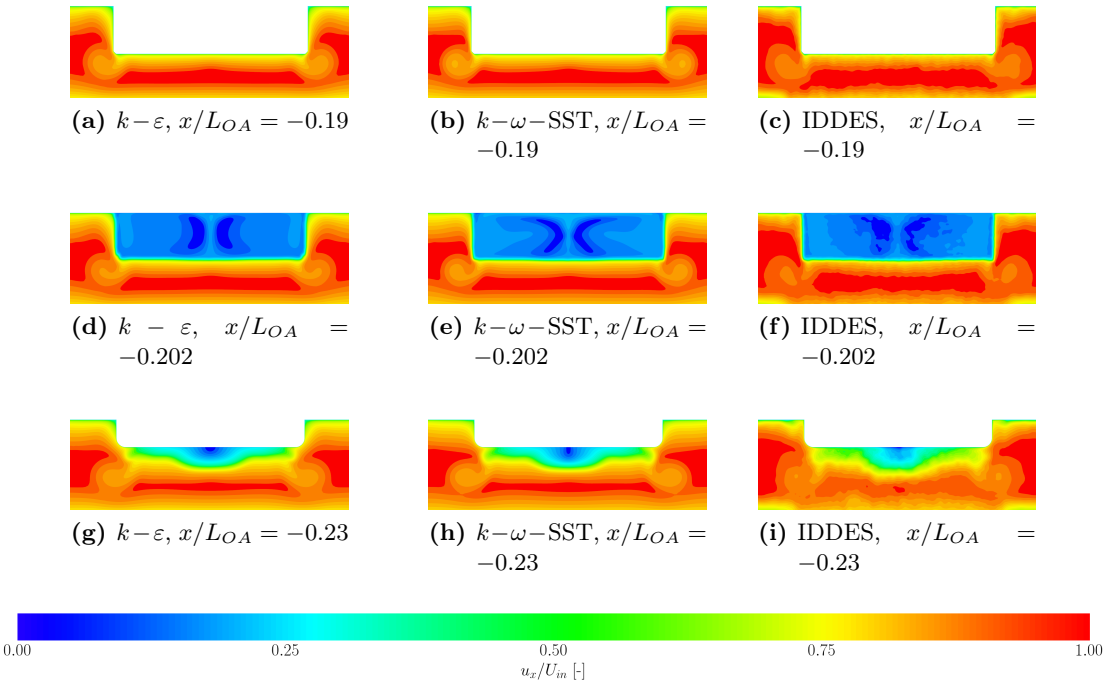

(a) $k-\varepsilon$, $x/L_{OA} = -0.19$ **(b)** $k-\omega-$SST, $x/L_{OA} = -0.19$ **(c)** IDDES, $x/L_{OA} = -0.19$

(d) $k-\varepsilon$, $x/L_{OA} = -0.202$ **(e)** $k-\omega-$SST, $x/L_{OA} = -0.202$ **(f)** IDDES, $x/L_{OA} = -0.202$

(g) $k-\varepsilon$, $x/L_{OA} = -0.23$ **(h)** $k-\omega-$SST, $x/L_{OA} = -0.23$ **(i)** IDDES, $x/L_{OA} = -0.23$

Figure 6.19: Two dimensional contour plot of the non-dimensional axial velocity u_x/U_{in} in the area of interest for respectively $k-\varepsilon$, $k-\omega-$SST and IDDES simulations in $h/T = 2.14$.

Figures 6.18 and 6.19 demonstrated that large vortices were generated alongside the barge and around its bilge keels. To visualize that these flow structures developed around the

entire convoy's hull, figures 6.20 and 6.21 depict for the deep water and the shallow water cases, respectively, isosurfaces of the averaged dimensionless λ_2-vortex criterion computed with a λ_2 value of 15. Their colors, ranging from blue to green to red, correspond to the vorticity. Blue areas denote a negative vorticity; red areas, a positive vorticity. Figures 6.20 and 6.21 depict comparative vortex structures obtained from the RANS method with the $k-\varepsilon$ and $k-\omega-$SST turbulence models and from the IDDES technique.

In deep as well as in shallow water, the vortex structures turned out to be similar. In the barge's bow area, a vortex developed at the edge of the barge alongside the bilge keel until finally reaching the transom area. Here, the flow detached, and separation occurred. Consequently, the small vortices generated in the recirculation zone extended until well behind the pusher's bow. In deep water, the vortex obtained from the RANS method with the $k-\varepsilon$ and $k-\omega-$SST turbulence models, represented in figures 6.20a and 6.20b, were nearly identical. The main difference occurred on the edges of the barge at about amidships as the simulation with the $k-\omega-$SST model yielded a somewhat elongated bilge keel vortex. The IDDES based vortex structure in figure 6.20c differed considerably from its RANS based counterparts. At first glance, the IDDES based isosurface enclosed the entire hull. As seen in this figure, the barge's bow vortex was noticeably larger. Along the bilge keel of the barge, the flow detached earlier, inducing a highly turbulent zone reaching the transom of the barge. Similar to the RANS based simulations, the separation region formed at the gap although, as seen in figure 6.20c, was substantially larger.

In shallow water, the flow patterns were similar, especially those predicted by the RANS simulations. However, some disparities occurred. Comparing figures 6.20a and 6.21a and figures 6.20b and 6.21b, it can be seen that, in shallow water, the vortex structures along the edges of the barge were larger, nearly maintaining their size up to the barge's transom area. The recirculation zone around the pusher was also noticeably larger, extending to a comparatively longer distance behind the pusher. Figure 6.21c shows more drastic differences when comparing RANS based flow patterns with those from IDDES simulations. Here, the blockage effect and the associated boundary layer interaction caused the isosurface to span from the barge's hull to the tank's bottom. Although developed at the barge's bow and at its edges, at about $L_{OA}/2$ these flow structures around the hull and on the tank's bottom differed from each another. The IDDES based flow pattern in figure 6.19i confirms this observation.

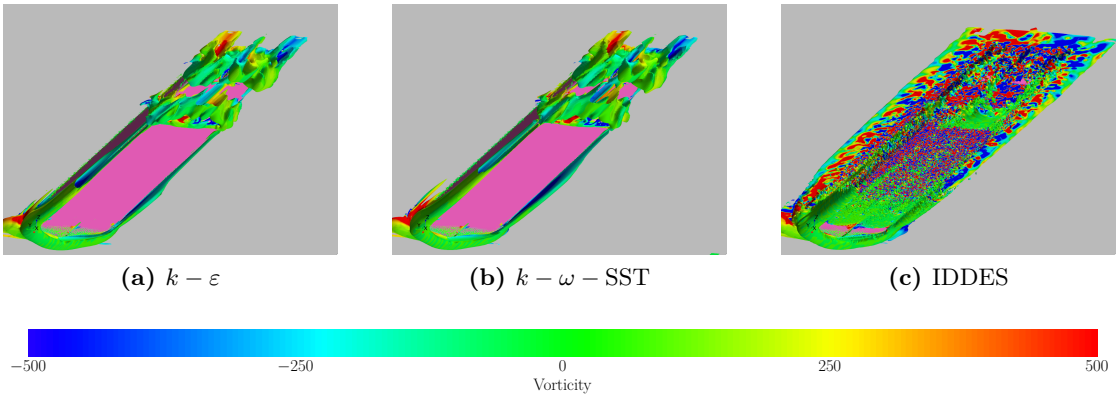

(a) $k-\varepsilon$ **(b)** $k-\omega-$SST **(c)** IDDES

Figure 6.20: Vorticity on vortex structures visualized by the λ^2 criterion around the pusher-barge model in deep water, criterion for respectively $k-\varepsilon$, $k-\omega-$SST and IDDES.

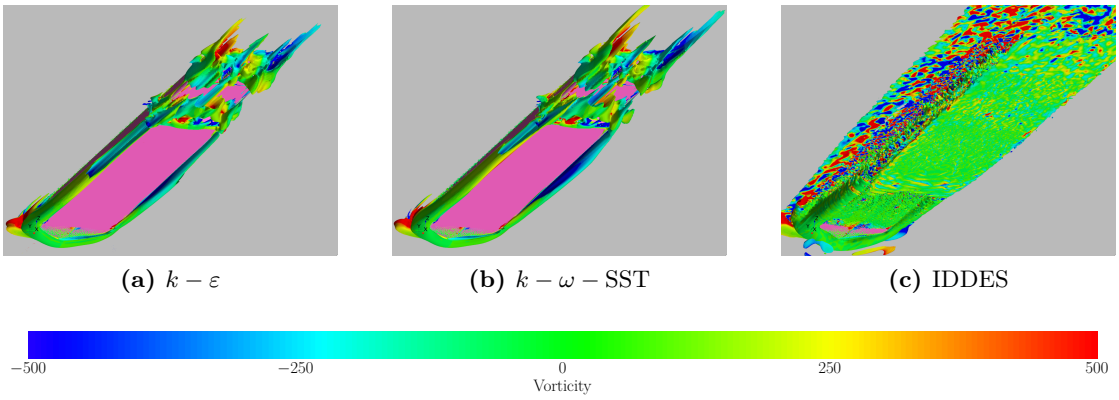

(a) $k-\varepsilon$ **(b)** $k-\omega-$SST **(c)** IDDES

Figure 6.21: Vorticity on vortex structures visualized by the λ^2 criterion around the pusher-barge model in shallow water of $h/T = 2.14$, criterion for respectively $k-\varepsilon$, $k-\omega-$SST and IDDES.

The hydrodynamic mechanism governing the gap flow was influenced by flow velocities and water depth restrictions. Under the straight ahead condition, a lower velocity zone developed at the stagnation point around the bow of the barge. The accelerated flow beneath and around the barge created a lower pressure zone. In the transom area, due to the abrupt change in geometry, the flow detached suddenly and, hence, generated a larger separation bubble between the barge's transom and the pusher's bow. This turbulent region caused a sudden pressure drop and a subsequent increase in overall resistance of the system. Additionally, the recirculation zone around the pusher's bow was sensitive to the water depth restriction. In deep water, as illustrated in figure 6.11, the gap flow

comprised three main areas: first, a recirculation bubble engulfing the pusher's bow, characterized by lower flow velocities; second, a shear layer transition zone, separating the recirculation bubble and the free stream region; third, a free stream region, in which the magnitude of the flow velocities almost equaled those of the inflow velocities. The restricted water depth significantly influenced the gap flow. Figure 6.22 depicts the computed mean velocity field $|u_x|/U_{in}$ and the averaged flow direction alongside the pusher's center line for three water depths to draft ratios $h/T = 2.14$, 1.5, and 1.2. The line integral convolution indicates the averaged flow direction. The coloring, ranging from blue to green to red, marks the velocity variation. All the computations were performed using the IDDES technique. The blockage effect induced by the lower UKC caused an extension of the recirculation bubble. Additionally, the velocity in the free stream area decreased in shallower waters. At the shallowest water depth ratio of $h/T = 1.2$, the recirculation bubble was comparatively larger with the pusher operating in the lowest velocity region. As seen in figure 6.22c, the separation bubble further downstream was extended, reaching almost to the pusher's half-length. The gap effect, combined with the blockage effect, thus had a comparatively greater influence on the flow around the pusher in the shallowest water depth.

Figure 6.23 plots averaged flow velocities in directions u_z and u_y and contours of pressure coefficient C_p on a vertical transverse plane located in the middle of the gap at $x/L_{OA} = -0.2$. Figure 6.23a plots these quantities for the convoy at the moderately shallow depth ratio $h/T = 2.14$; Figure 6.23b, for the convoy at the shallower water depth ratio $h/T = 1.5$; Figure 6.23c, for the convoy at the shallowest water depth ratio $h/T = 1.2$. Generally, in all water depths, the area located near the barge's transom was characterized by comparatively lower pressures. Furthermore, regardless of water depth, in this area the water was pushed to the sides of the pusher. Consequently, the restricted water depth distinctly affected the bilge keel vortices. As a result of the decreasing UKC, these vortices wandered further sideways. Moreover, at lower h/T ratios, a noticeable effect on the hull/bottom interaction was observed. Indeed, for the convoy at $h/T = 1.5$ and 1.2, smaller vortices were generated below the barge.

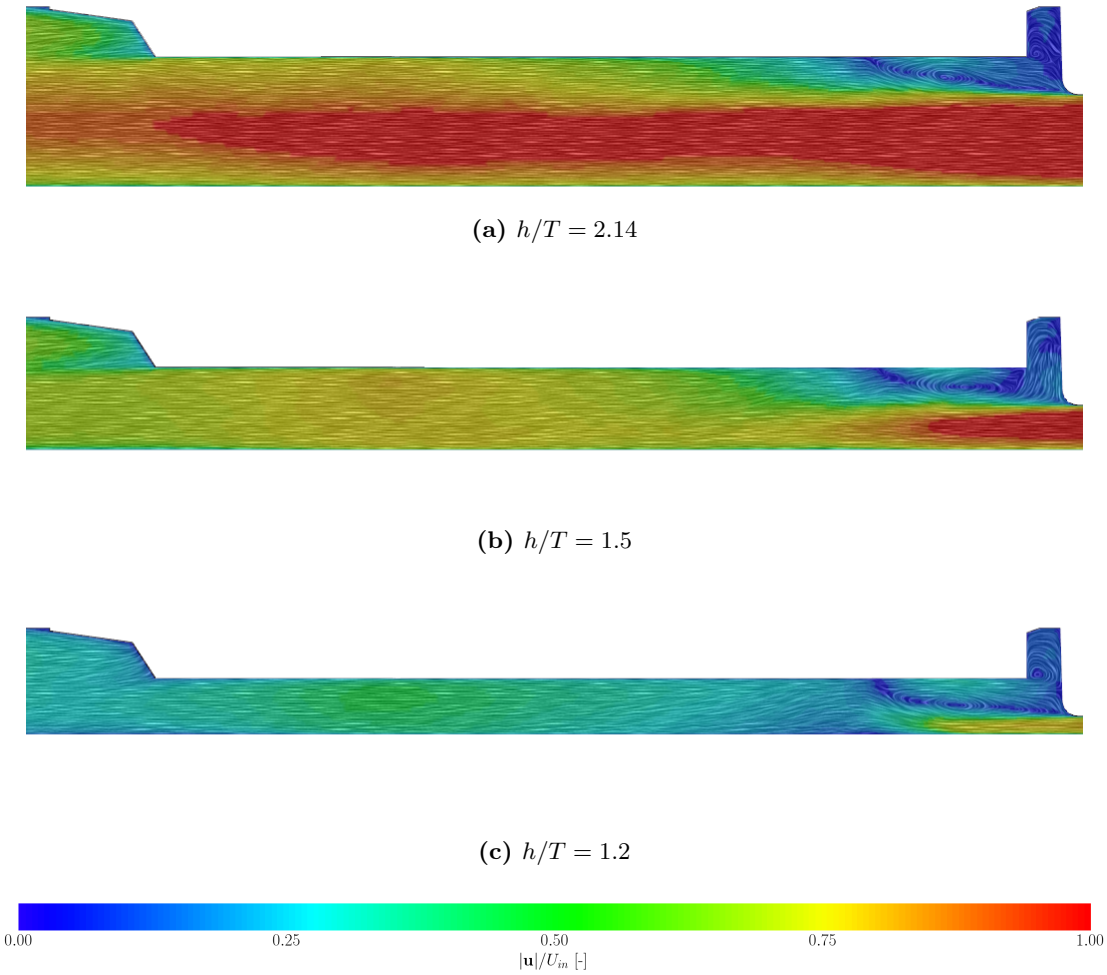

(a) $h/T = 2.14$

(b) $h/T = 1.5$

(c) $h/T = 1.2$

Figure 6.22: Velocity magnitude contour $|\mathbf{u}|/U_{in}$ and line integral convolution over pusher's midplane at different water depths to draft ratios h/T and $U_{in} = 1.91\,\mathrm{m/s}$.

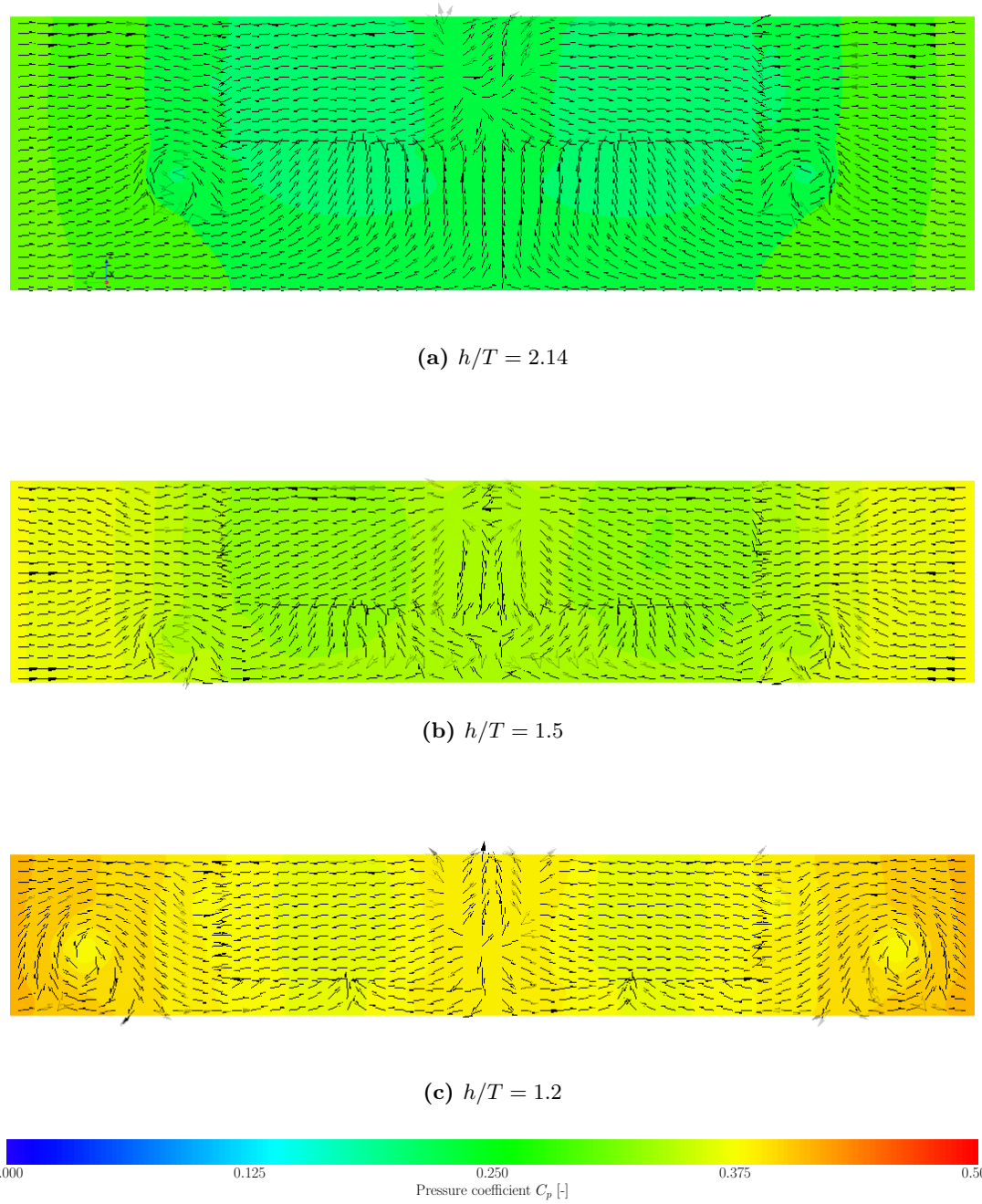

(a) $h/T = 2.14$

(b) $h/T = 1.5$

(c) $h/T = 1.2$

Figure 6.23: u_y and u_z averaged velocity vectors and pressure coefficient C_p contours over transversal plane at $x/L_{OA} = -0.2$ at different water depths to draft ratios h/T and $U_{in} = 1.91\,\mathrm{m/s}$.

Conclusions based on the plots presented in figure 6.22 were also substantiated by the shear stresses distributed on the pusher's hull shown in figure 6.24. This figure shows views of shear stresses distributed over the bottom surfaces of the pusher and the barge's transom in water depths of $h/T = 2.14, 1.5$, and 1.2. The effect of decreasing water depth on the recirculation bubble is clearly visible. In the junction area between pusher and barge, the low shear stress zone corresponded to the flow separation with its recirculating zone occurring in the gap between pusher and barge. This zone increased significantly with decreasing water depth. In the shallowest water depth, i.e., at $h/T = 1.2$, a large portion of the pusher's bottom was surrounded by dead water. This unfavorable arrangement of the pusher behind the vertical transom of the barge, coupled with the water-depth restriction, was a decisive factor.

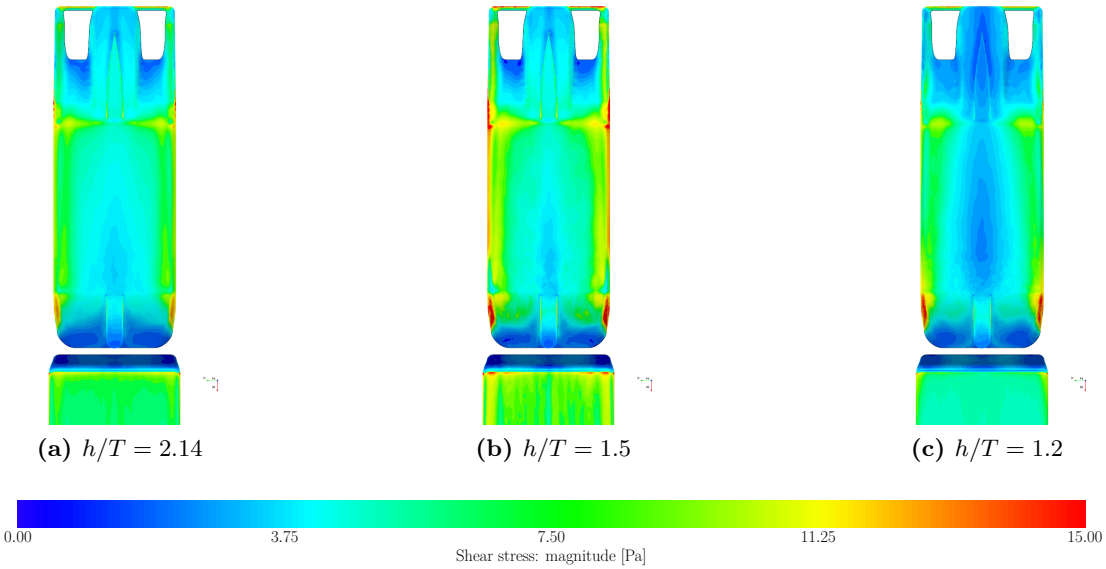

(a) $h/T = 2.14$ **(b)** $h/T = 1.5$ **(c)** $h/T = 1.2$

Figure 6.24: Shear stress distribution over the pusher's hull at different h/T ratios and $U_{in} = 1.91\,\mathrm{m/s}$.

The most notable effect on a vessel sailing in shallow waters is the massive increase in resistance. This effect was well documented Mucha et al. (2017), Zeng et al. (2018) and Chillcce and el Moctar (2022). This holds equally true for a pusher-barge convoy, see Zentari et al. (2022). Figure 6.25 plots computed resistance coefficient C_T obtained from the numerical method versus water depth to draft ratio h/T. As seen, the resistance computed for the convoy at $h/T = 1.2$ and $U_{in} = 1.91\mathrm{m/s}$ showed a percentage increase of 66.5 % compared to the resistance computed for the convoy at $h/T = 2.14$. However, to quantitatively assess the effect of the gap flow on resistance, we modified the pusher-barge model by closing the gap by inserting a relatively simple prism with a triangular profile covering the gap between pusher and barge. One of the sides of the prism was

attached to the barge's transom at the flow detachment point, while the other side was attached to the pusher's flat bottom. Thus, the gap was completely covered. Figure 6.26 shows a perspective view of the pusher-barge model, here colored in pink, and of the triangular prism, here colored in green. With this modified model, a resistance simulation for the convoy at $h/T = 1.2$ and $U_{in} = 1.91\,\mathrm{m/s}$ was performed, using the IDDES technique and the numerical setup described above.

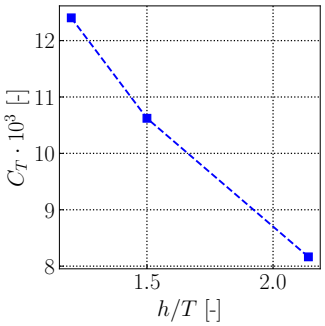

Figure 6.25: Resistance coefficients C_T versus h/T ratio for configuration 1:1 at $U_{in} = 1.91$ m/s obtained from IDDES simulations.

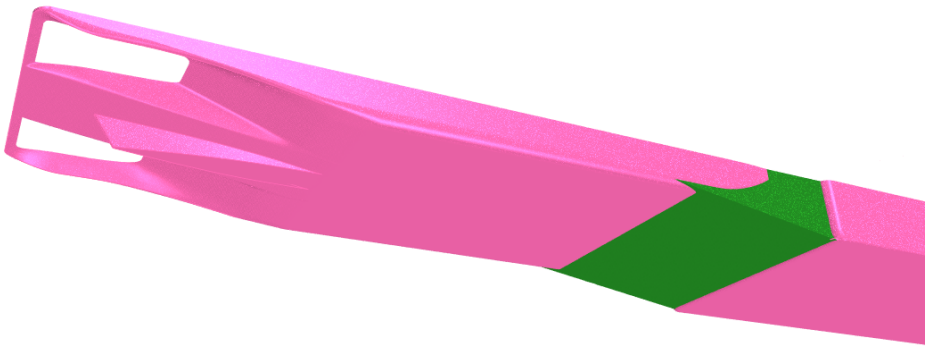

Figure 6.26: Perspective rendered view of the modified pusher-barge model with a triangular prism closing the gap between pusher and barge.

Figure 6.27 presents comparative mean velocities distributed on the $y = 0$ plane for the baseline model and the modified model. These velocities are shown as line-integral convolution to indicate their directions, and the associated color bar specifies the flow's velocity. As seen, the modification of the baseline model had an immediate effect on the flow. The large recirculation zone in the gap completely disappeared and, for the modified model, the flow was naturally directed alongside the gap cover, thus avoiding a

detachment of the flow at the barge's transom. Also, the coloring identifies the various velocities alongside the pusher's midplane. The flow velocity below the pusher's bottom was comparatively higher. Table 6.4 lists the computed resistance X, the corresponding resistance coefficients C_T, and the gap flow model's percentage deviation of resistance from the baseline model. Simply covering the gap reduced the longitudinal resistance by 6.59% compared to the resistance of the baseline model. The results of this simulation clearly demonstrated the effect of the gap flow on the total longitudinal force acting on a pusher-barge convoy's bull in shallow water.

(a) $h/T = 1.2$, Baseline design.

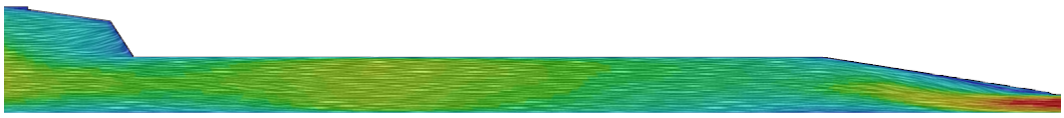

(b) $h/T = 1.2$, Gap covered.

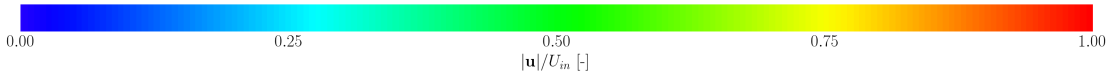

Figure 6.27: Velocity magnitude contour $|\mathbf{u}|/U_{in}$ and line integral convolution over pusher's midplane at different water depth to draft ratios h/T and $U_{in} = 1.91\,\mathrm{m/s}$.

Table 6.4: Values of total computed force X acting on the convoy's hull with and without gap in the shallowest water depth of $h/T = 1.2$. The velocity in both cases is $1.91\,\mathrm{m/s}$.

Model	X[N]	$C_T \cdot 10^3$ [−]	**Diff. in %**
Baseline	10.403	12.403	-
Gap covered	9.720	11.637	−6.58

6.5 Concluding remarks

Experimental and numerical investigations of the gap flow between a pusher and a barge in deep and shallow water helped gain a quantitative insight of the flow in this region, thereby obtaining suitable benchmark data used to validate a numerical approach that reproduced the complex flow patterns. A PIV technique and an LDV system assessed the flow conditions inside the gap. Considered were the two water depth to draft ratios h/T of 13.82 and 2.14 with their respective inflow velocities 2.09 m/s for the deep water case and 1.91 m/s for the shallow water. A Perspex acrylic plastic plate covered the water surface to suppress free surface influences.

The experiments identified the complex flow regime consisting of three main regions, namely, a free stream region underneath the barge, a separation bubble induced by the abrupt geometric changes at the junction of pusher and barge, and a shear layer between them. In shallow water, these regions were distinctly altered by the blockage effect of the gap and the mixing of boundary layers at the hull and the tank's bottom.

To predict the measured flow patterns, numerical simulations used the RANS method implemented with $k-\varepsilon$ and the $k-\omega-$SST turbulence models and the hybrid scale resolving method IDDES. In the latter, the RANS based solutions in the near body region were complemented with LES solutions in the far field. The numerical results compared favorably to experimental measurements of mean streamwise velocity profiles in the gap area. In deep water, the IDDES based results yielded accurate velocity profiles in the free stream and in the gap region, whereas the RANS based results overpredicted the size of the separation bubble. In shallow water, both methods predicted the velocity profiles in the free stream region of satisfactory accuracy. In shallow water, the IDDES method obtained the most accurate predictions in the gap region as well as in the transition region. Nonetheless, at the barge's transom, larger discrepancies between numerical results and experiments occurred. Indeed, due to the blockage effect, the flow was more complex than in deep water. A qualitative comparison of the numerical and experimental 2D velocity contours in the gap region confirmed that the IDDES based predictions compared more favorably to experimental measurements.

The influence of water depth restriction on gap flow and convoy's resistance was assessed using the IDDES technique. The numerical setup based on the IDDES technique was utilized to investigate the gap flow in water depth to draft ratios h/T of 2.14, 1.5 and 1.2. These ratios ranged respectively from moderately shallow to extreme shallow water. With decreasing water depth, the recirculation region was extended alongside the pusher's hull, delaying thus the flow reattachment. Additionally, the velocity of the free-stream region was significantly lower, with the lowest values observed in $h/T = 1.2$. These observations were substantiated by the shear stresses distribution on the pusher. As expected, the overall longitudinal force acting on the convoy was highest at $h/T = 1.2$, with an increase of 66.5% compared to $h/T = 2.14$. Furthermore, the numerical method

was used to quantify the effect of the gap on resistance in shallow waters. For this purpose, the gap was covered with a simple geometry to ease the flow alongside the pusher and to prevent generating larger recirculation zones. The numerical analysis of the flow passing by this modified model at $h/T = 1.2$ yielded a reduced resistance of about 6.5%.

7 Shallow Water Effect on Maneuvering Forces

The experimental and numerical studies described in the previous chapters laid the groundwork for further investigations on hydrodynamic forces and moments acting on a convoy's hull in maneuvering situation. Resistance and propulsion forces are essential for mathematical models. However, the main contributions to the equation of motion are given by the terms corresponding to transversal force Y and yaw moment N, as stated by Gronarz (1997), Eloot (2006) and Mucha (2017). In this ambit, resistance and propulsion tests were part of a larger experimental campaign, aiming to provide robust validation data for numerical methods. For sea-going vessels, numerous benchmark data are available to validate numerical simulations of virtual captive maneuvering tests. The SIMMAN 2008 results provide useful resources for numerous representative vessels, ranging from container ships such as the **K**RISO **C**ontainer **S**hip (KCS), to bulkier vessels such as the **J**apan **B**ulk **C**arrier (JBC), see Stern et al. (2011). Nevertheless, at this moment, benchmark data for pusher-barge models are scarce. The present chapter provides experimental results of steady drift tests and steady rudder variation tests for a pusher-barge convoy in different configurations, in deep and shallow water. Times series of respective tests, error sources and standard deviations are provided. Furthermore, the aforementioned experimental results were replicated numerically using the techniques presented in chapter 3. This chapter is organized as follows: first, the computational setup for steady drift and rudder variation tests is described. Second, the experimental and numerical results of steady drift tests are described and discussed, with an emphasis on the effect of water depth restriction on the resulting hydrodynamic forces and moments. Third, the experimental and numerical results of rudder variation tests are described and discussed. Finally, main findings are presented and discussed.

7.1 Steady drift forces

7.1.1 Computational procedure

The numerical procedure used to replicate the experimental steady drift tests is based on the solution of the RANS equations coupled with the $k-\omega-$SST turbulence model. The aim of the simulations was to validate a computational procedure adopted to predict steady drift forces and moments acting on a pusher-barge convoy in deep and shallow water. The simulations were conducted using a double-body single phase setup, as preliminary investigations revealed that the free surface effect was limited for lateral force Y'

and yaw moment N' fo the considered range of drift angles. Pusher and barge or barges were adjusted to the floating position and drift angle as measured in the experiment, prior to the meshing process. In the shallow water cases, the dimensions of the domain replicated the shallow water basin of MARIN as to include wall effects, as demonstrated by Oud and Bedos (2022). Figures 7.1 and 7.2 depict a schematic representation of the domain utilized in deep and shallow water simulations, respectively. A distance of $2.5 \cdot L_{OA}$ was included between inlet and ship; a distance of $3.5 \cdot L_{OA}$, between ship and outlet. For shallow water cases, a distance of 7.54 m was specified between convoy and outer domain wall; for deep water cases, this distance was $3.5 \cdot L_{OA}$, and a distance of $3.5 \cdot L_{OA}$ was specified between a test body's keel and the domain's bottom. In shallow water, the distance between ship and tank bottom was given by the corresponding h/T ratio. Refinement boxes were defined around the barge's bow and around the gaps between floating bodies. Finer mesh sizes were specified around the pusher's transom to allow a better resolution of the flow around propulsion and steering devices. A large refinement box was defined around the ship to capture vortex structures shedding from both sides of the vessel, see figure 7.3. In shallow water, a refinement box with a minimum of 20 cells was arranged between convoy's keel and tank bottom, as to capture the complex interaction between the respective boundary layers. Tank sides and bottom were assigned a no-slip wall condition, with a relative velocity equal to the inlet velocity. The free surface was defined as a symmetry plane. The boundary layer was fully resolved in all simulations, aiming for a y^+ value below unity. The simulations were run with an appended vessel with fully resolved ducted propellers at propulsion point. The **M**oving **R**eference **F**rame method (MRF) was used to simulate the motion of the propellers inside a separated subdomain without physically rotating the grid, as seen in figure 7.4. An interface between main domain and subdomains ensured the correct transfer of field variables.

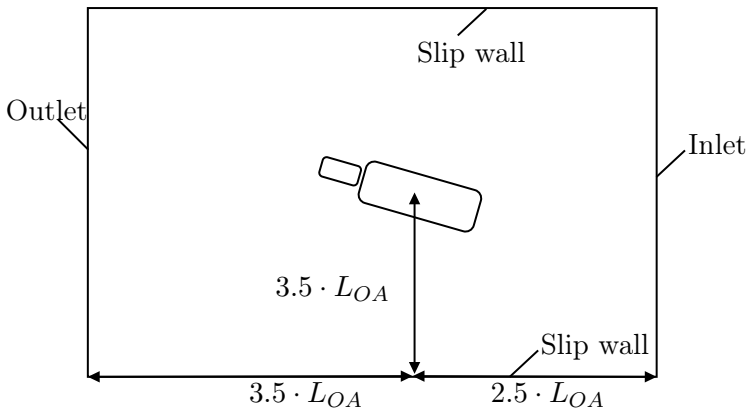

Figure 7.1: Schematic representation of the numerical domain for deep water drift simulations.

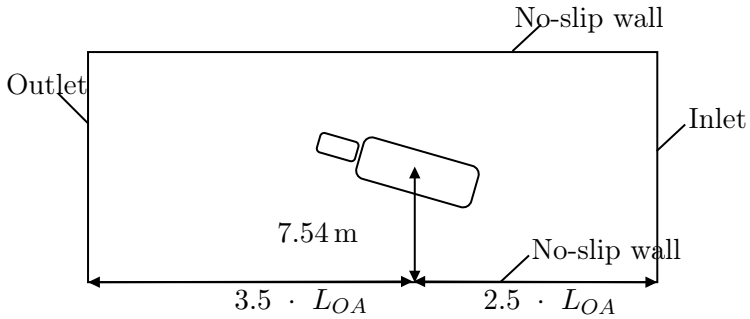

Figure 7.2: Schematic representation of the numerical domain for shallow water drift simulations.

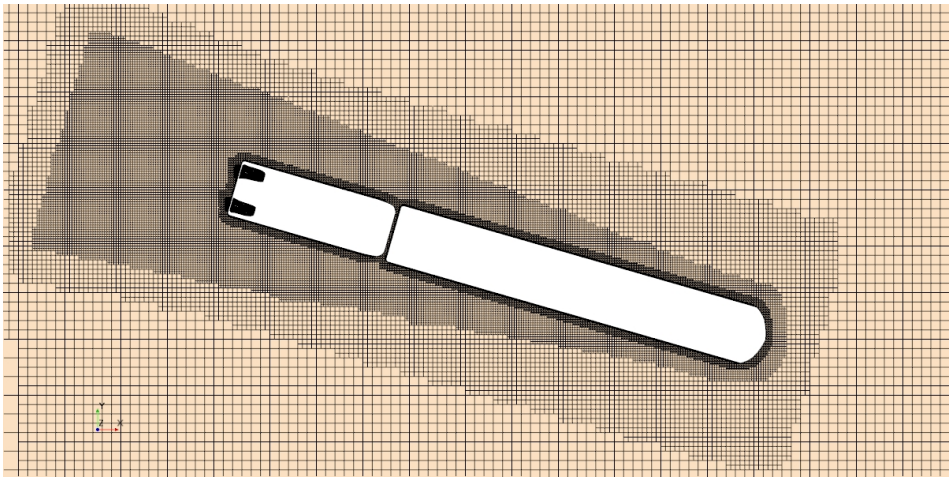

Figure 7.3: Top view of the mesh around configuration 1:1 at a drift angle of $\beta = 16°$.

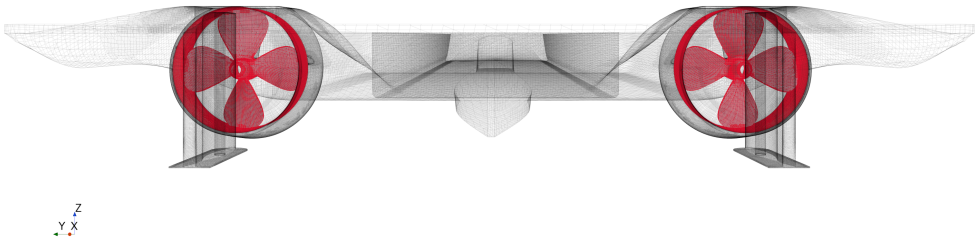

Figure 7.4: Perspective view of the surface mesh of configuration 1:1 for shallow water drift simulation at $h/T = 1.2$ and a drift angle of $\beta = 16°$.

The procedure described by el Moctar et al. (2021) and Oberhagemann (2017) was used to perform sensitivity and convergence analysis. Here, a grid refinement ratio $r_k = \sqrt{2}$ was used to generate three successively finer grids. The same refinement ratio was used to refine the time step Δt. For each time-step, six outer SIMPLE iterations were considered. Forces X, Y and moment N were the quantities of interest. For this purpose, and in an effort to remain consistent with the analyses performed in previous chapters, configuration 1:1 in steady drift condition at $\beta = 16°$, a water depth to draught ratio of $h/T = 1.2$ and a carriage velocity of $U = 0.556$ m/s were considered. Integral values were obtained by averaging over the last 50 s of a converged simulation. Figure 7.5 depicts the time history of total computed yaw moment N over simulation time t on the finest grid for configuration 1:1, $\beta = 16°$, $h/T = 1.2$ and $U = 0.556$ m/s. Herein, the simulation converged to nearly constant mean values after approximately 50 s. Figure 7.6 shows the interval used to obtain the averaged value of N compared to the experimental time series for the same case. Some oscillations measured in the experiment were not visible in the numerical time series. Free surface effects, carriage vibrations, vortex shedding and complex interaction between ship model and tank bottom may have caused this behavior. Table 7.1 gives an overview of the grids and time steps considered. The coarsest grid comprised $4.2 \cdot 10^6$ control volumes; the finest grid, $16.7 \cdot 10^6$. For these three grids, this table lists also the number of control volumes CV, the time step size Δt, the resulting overall total longitudinal force X, the overall total side force Y and the total yaw moment N. The difference in percentage between the respective quantity and its value obtained on the finest grid is also given. Oscillatory convergence was achieved for Y and N, with associated convergence ratios R_k of -0.98. Divergence was observed for X. Nevertheless, oscillatory convergence may be acceptable if the difference between the integral values computed on each grid are small. While pressure forces were dominant in Y and N, shear forces amounted for more than 40% of X. These forces were more sensitive to turbulence and were hence highly impacted by grid and time-step refinements.

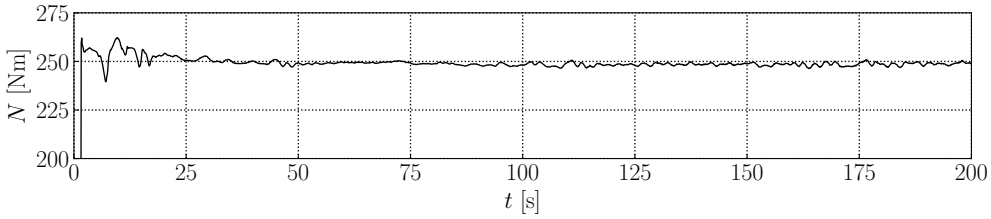

Figure 7.5: Convergence of computational total yaw moment N over time t for configuration 1:1 at a drift angle of β=16° and $h/T = 1.2$.

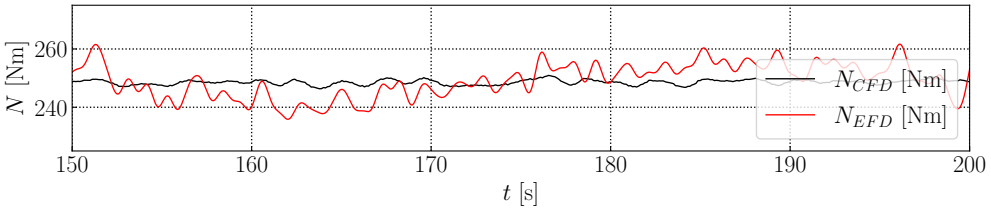

Figure 7.6: Time history of computational and experimental total yaw moment N for configuration 1:1 at a drift angle of β=16° and $h/T = 1.2$.

Table 7.1: Sensitvity analysis of total longitudinal force X [N] for configuration 1:1 at a rudder angle of δ=45° and $h/T = 1.2$.

CV·10^6	Δt [s]	X [N]	**Diff. in %**	Y [N]	**Diff. in %**	N [N m]	**Diff. in %**
4.2	0.01	27.848	-1.01	148.3131	1.68	250.085	0.52
8.5	0.007171	27.416	-2.60	146.204	0.27	247.892	-0.35
16.7	0.005	28.130	-	145.807	-	248.777	-
R_k	-	-1.01	-	-0.98	-	-0.98	-

7.1.2 Experimental results

The experimental campaign described in Chapter 4 yielded hydrodynamic forces and moments measurements resulting from steady drift tests in both deep and shallow water. Figures 7.7 and 7.8 present the time history of the total hydrodynamic longitudinal force X, total hydrodynamic lateral force Y, and total hydrodynamic yaw moment N measured during the steady drift tests for configuration 1:1 in deep water and shallow water of $h/T = 1.2$ and drift angle of $\beta = 16°$, respectively.

In deep water, the ship's drift angle was varied successively over one run to measure hydrodynamic forces and moments at a carriage velocity of $U = 0.556\,\text{m/s}$. The standard deviation of these tests indicated a relatively stable behavior of the force over the measurement time, although higher oscillations were observed for X. At a drift angle of $\beta = 16°$, the temporal progression of Y and N revealed that these quantities increased towards the end of the run. This surge may have been caused by wave reflections at the basin's end. To avoid such phenomena and quantify associated uncertainties, additional single run tests for higher drift angles in deep water are necessary.

In shallow water, each drift angle was investigated over a single run lasting approximately 300 s. Figure 7.8 displays the time history of X, Y, and N for a drift angle of $\beta = 16°$ at $h/T = 1.2$. Similar to resistance tests in $h/T = 1.2$, larger oscillations of forces and

moment were observed over the test run. The periodicity of these oscillations, specifically for Y and N, suggested the occurrence of vortex shedding.

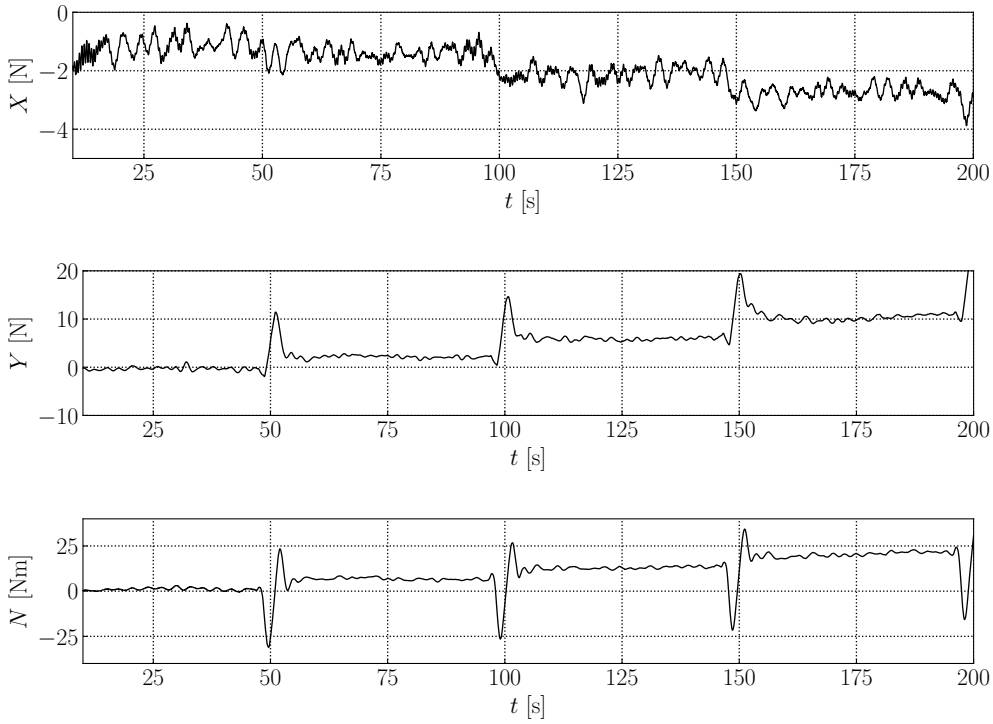

Figure 7.7: Time history of hydrodynamic forces and moment X, Y, and N during steady drift tests for configuration 1:1 in deep water at $U = 0.556$ m/s and drift angles ranging from 4° to 16°.

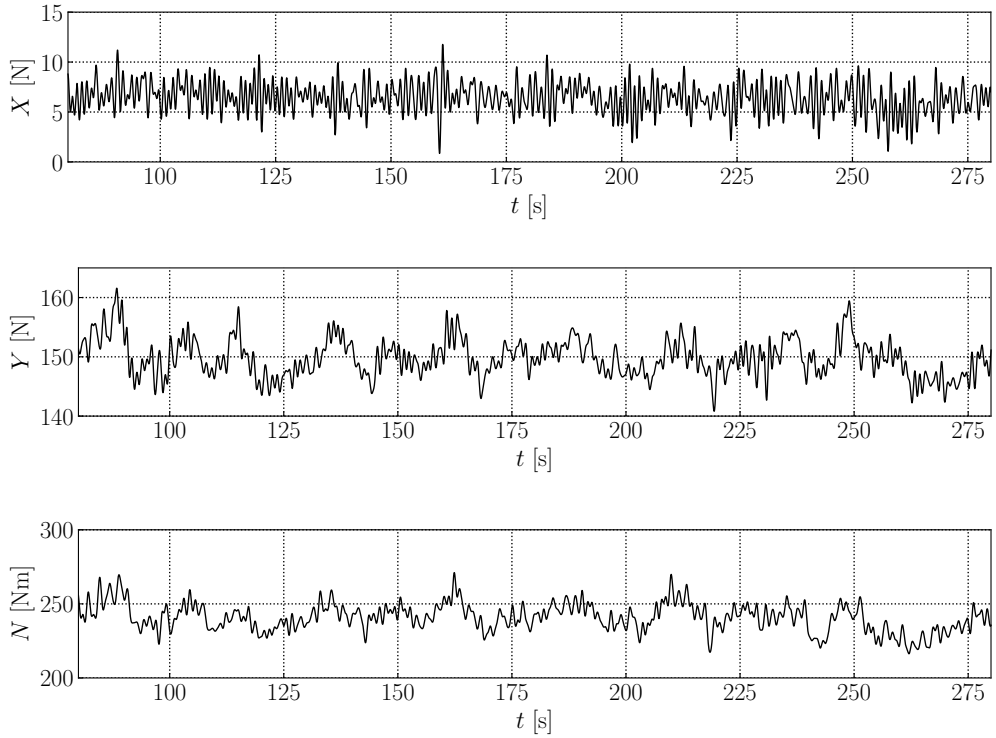

Figure 7.8: Time history of hydrodynamic forces and moment X, Y, and N during steady drift tests for configuration 1:1 in $h/T = 1.2$ at $U = 0.556$ m/s and drift angle of 16°.

Figures 7.9 and 7.10 present the results of steady drift tests conducted in deep and shallow water, respectively. Figure 7.9 shows the mean non-dimensional values of X', Y' and N' with their corresponding standard deviation for configuration 1:1 in deep and shallow water. These values were obtained via the following expressions:

$$X' = \frac{X}{0.5\rho U^2 L_{OA}^2} \qquad Y' = \frac{Y}{0.5\rho U^2 L_{OA}^2} \qquad X' = \frac{N}{0.5\rho U^2 L_{OA}^3} \tag{7.1}$$

where ρ is the water density, U the convoy's speed, and L_{OA} the convoy's length between perpendiculars. In figures 7.9 and 7.10, the black dashed line represents the results in deep water, while the blue, green and red dashed lines represent the results in shallow water for h/T ratios of 2.0, 1.5 and 1.2, respectively. The same quantities are depicted in figure 7.10 to compare forces and moments for each configuration in the shallowest water depth of $h/T = 1.2$.

For configuration 1:1 in deep water, the general behavior of X, Y and N with increasing drift angle showed a significant increase of these forces and moments. The measured total

longitudinal force X at 4 degrees drift angle was -1.381 N, increasing up to -3.341 N at $\beta = 16°$. The same behavior was observed for configuration 2:1, with an associated X value at $\beta = 16°$ of -3.031 N. The arrangement of four barges in front of the pusher as in configuration 2:2 resulted in a higher X value, peaking at -6.443 N at $\beta = 16°$. A similar trend was observed at the moderate water depth ratio of $h/T = 2$ for configuration 1:1, with the black and blue dashed lines being almost superimposed, as shown in figures 7.9 and 7.10.

At the shallowest water depth ratio of $h/T = 1.2$, X' became positive, indicating thrust in the direction of motion. This behavior has also been observed in monohulls; see Furukawa et al. (2016). The longitudinal and lateral components of the force in the earth-fixed coordinate system contributed to the X' value in ship-fixed direction. At higher drift angles, the lateral component of the force became dominant. This tendency was accentuated in the shallowest water depths, given the drastic increase of the lateral force Y. This tendency was observed moderately for configuration 2:1, but not for configuration 2:2 at the same h/T ratio. In the latter, the two front barges coupled side by side presented a large bow area. The resulting stagnation point caused a substantial surge in the hydrodynamic longitudinal force.

In deep water, the lateral force Y' exhibited a linear behavior for configuration 1:1. The maximum value of $Y' = 16.303$ N at this water depth for configuration 1:1 was measured at a drift angle of $\beta = 16°$. Higher Y values were observed for the other configurations under the same test conditions, specifically $Y = 22.563$ N and $Y = 23.947$ N for configurations 2:1 and 2:2, respectively. The difference between these values was negligible, which can be justified by the equal lateral area in the y direction shared by configurations 2:1 and 2:2. The same was true for the total yaw moment N, which had measured values of $N = 56.109$ N m and $N = 56.577$ N m for configurations 2:1 and 2:2, respectively.

Figure 7.9 illustrates the influence of shallow water on both Y and N for configuration 1:1. At the lowest tested drift angle of $\beta = 4°$, the difference in total lateral force and yaw moment was barely noticeable. However, with increasing drift angle, the difference between the forces measured at different h/T ratios increased significantly, peaking at $\beta = 16°$ and $h/T = 1.2$. At this point, Y and N had associated values of $Y = 149.97$ N and $N = 250.7$ N m, respectively, representing a percentage increase of approximately 620% for Y and 440% for N from the deep water values. This surge in the side force and yaw moment was almost exponential, highlighting the combined influence of water depth restriction and drift angle on the pressure field surrounding the vessel, which was accentuated by the bulkiness of the barge or barges. These results align with previous research by Gronarz (1997), Eloot (2006) and Oud and Bedos (2022).

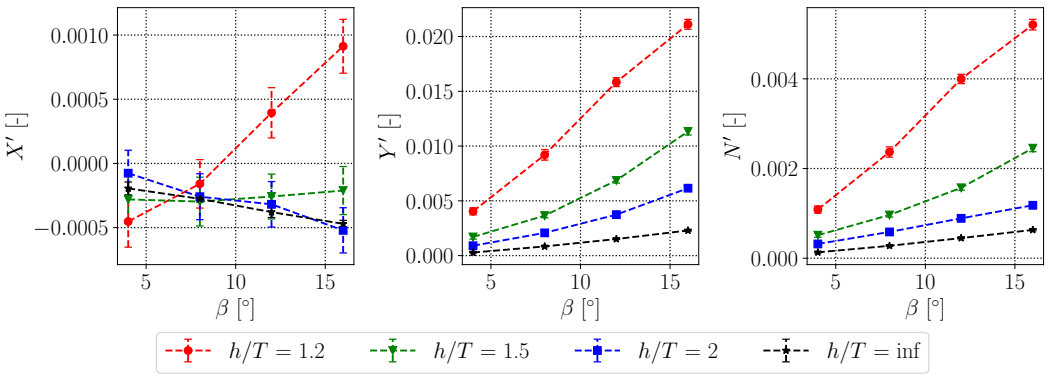

Figure 7.9: Experimental results of steady drift tests at $U = 0.556$ m/s for configuration 1:1 at water depths of $h/T = \infty$, 2.0, 1.5 and 1.2.

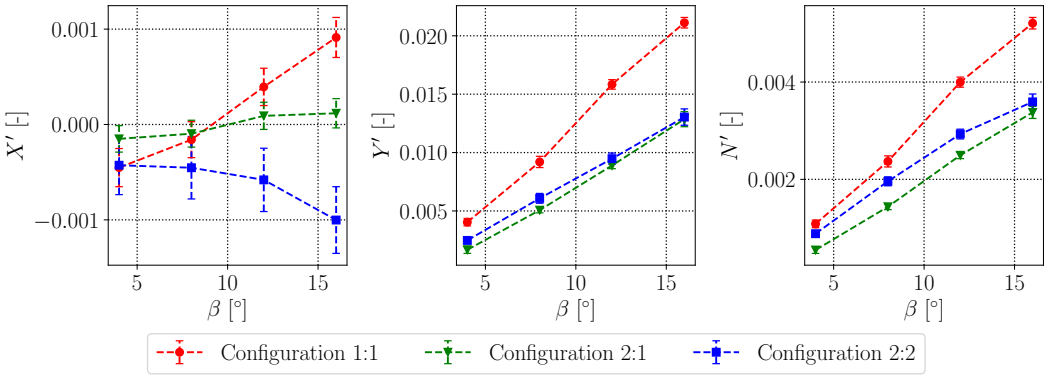

Figure 7.10: Comparison of experimental results of steady drift tests at $U = 0.556$ m/s and $h/T = 1.2$ for configuration 1:1, 2:1 and 2:2.

7.1.3 Numerical results

Accurately modeling propulsion forces is crucial for reproducing steady drift tests at the propulsion point. The complexity of this task depends on available computing resources. The actuator disk model, which uses open water propeller characteristics to calculate thrust and torque based on inflow velocity, might be used if computing power is limited. However, the fully resolved propeller geometry and dedicated subdomain in which the propeller rotates provide a more accurate method, albeit requiring a higher grid density around the propeller. According to Aram and Mucha (2023), the actuator disk method may also underestimate thrust if propeller inflow conditions deviate significantly from the straight ahead condition. Similar findings have been substantiated by Durasevic et al. (2022). To adapt the actuator disk method to larger drift angles, separate propeller curves

can be determined depending on operational conditions such as drift angle, rotation rate, or water depth, as noted by Yao (2015).

In the case of pusher-barge convoys, the use of an actuator disk was limited by the propeller operating inside a duct, which also contributed to thrust, and the highly disrupted propeller inflow due to the gap between the pusher and barge or barges. Therefore, the MRF method was utilized, which allows simulation of rotating regions without physically moving the subdomain grid. Although the propeller was fully modeled, the MRF method was less computationally expensive than a moving grid method while providing more accurate predictions than the actuator disk method.

Figure 7.12 shows the fully modeled propeller. Figure 7.11 compares modeled and measured total thrust T_T over drift angle β in steady drift conditions and deep water for configurations 1:1, 2:1, and 2:2. The red dashed line represents the computational results obtained using the numerical method described above, and the blue dashed line represents the experimental results measured during steady drift tests at HSVA. For configurations 2:1 and 2:2, the maximum difference between CFD and experimental thrust was approximately 10%, with the lowest deviation being only around 3%. For configuration 1:1, the numerically obtained thrust differed by approximately 21% for the largest drift angle of 16°. The lowest difference was determined for drift angles of 8° and 12°. However, the propeller performance was heavily impacted by the quality of the numerical prediction of the inflow at the propeller plane. The accuracy of the propulsion prediction can be improved by using more appropriate turbulence models, including free surface effects, and accounting for dynamic ship motions. For more resources on propulsion prediction in maneuvering situations, refer to Yao (2015).

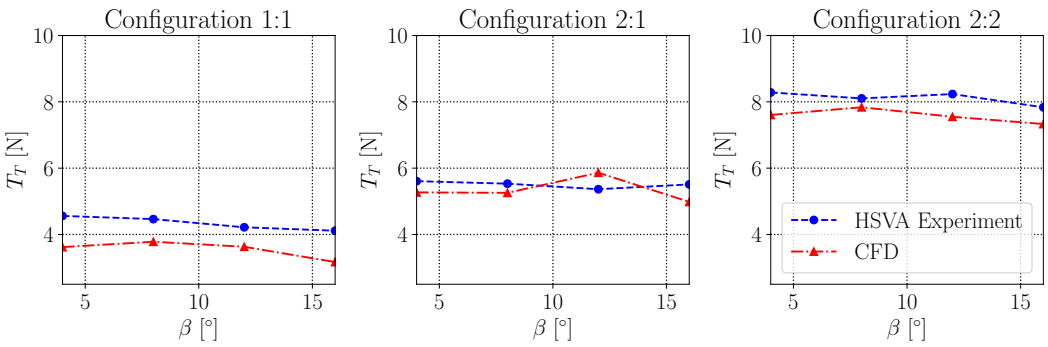

Figure 7.11: Validation of total thrust T_T computed for configurations 1:1, 2:1 and 2:2 in steady drift condition and deep water versus drift angle β.

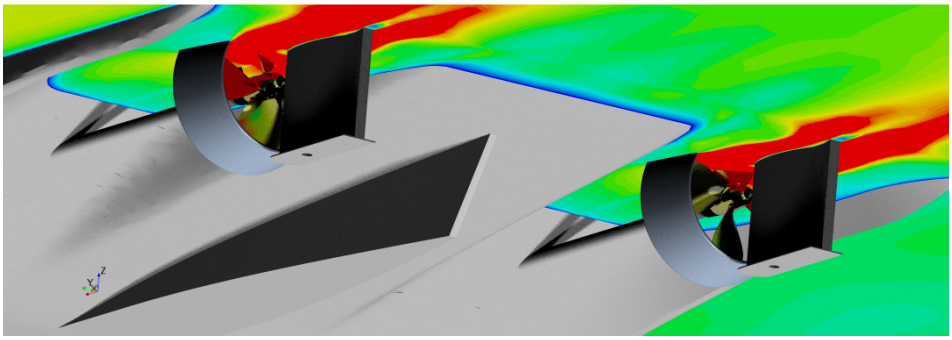

Figure 7.12: Velocity magnitude distribution on z-plane around the pusher's propulsive and steering devices in configuration 2:1 in deep water advancing at $U = 0.556\,\mathrm{m/s}$ with a drift angle of 4°.

Figures 7.13, 7.14, and 7.15 depict a comparison between the CFD-computed and experimentally measured non-dimensional total longitudinal force X', lateral force Y', and total yaw moment N' over drift angle β for all configurations and water depth to draft ratios h/T. Red markings indicate values computed on the finest grid, while blue markings represent experimental values with associated measured standard deviations as vertical bars.

In deep water, the computed non-dimensional longitudinal forces and moment agreed well with the experimental results. However, for configuration 1:1, the computed X' force showed deviations ranging from 1.2% to 13.1% for drift angles between 4° and 12°, and a deviation of approximately 16% for $\beta = 16°$, as shown in figure 7.13a. Similar deviations were observed for Y' and N'. Specifically, for drift angles ranging from 4° to 12°, the deviations were approximately 11.1%, 8.1%, and 2.13% for Y'; and 2.05%, 9.3%, and 2.15% for N'. At $\beta = 16°$, the deviations were around 19.8% and 17.07% for Y' and N', respectively.

The results obtained for configuration 2:1 and 2:2 were comparable. For configuration 2:1, the computed X' values (shown in figure 7.14a) satisfactorily captured the measured nonlinearity of the force, with associated deviations ranging from 4.3% to 10.1% for drift angles between $\beta = 4°$ and 16°. However, higher deviations were determined for Y', ranging from 10% to 15% for drift angles between 4° and 12°, with the greatest difference of approximately 18.4% at $\beta = 16°$. On the other hand, the computed N' values agreed very well with the experimental values, with a maximum difference of approximately 7.2% at $\beta = 12°$.

In configuration 2:2, the computed X' values exhibited the greatest deviation. The deviations were approximately 20% for all drift angles, except for $\beta = 4°$, where the deviation was only 1.1%. However, the computed Y' and N' values agreed very well with the experimental data, with a maximum deviation of 8.1%. The total lateral force for a drift angle of 16° showed a large deviation of 21% from the experimental data. The larger deviations at $\beta = 16°$ may be attributed to experimental uncertainty caused by the measurement method. The accuracy of the measurements could have been improved by conducting a single run for each drift angle. Similar results were obtained in shallow water.

Figure 7.13b shows the results for configuration 1:1 at a water depth to draft ratio of $h/T = 2.0$. The numerically computed forces and moment agreed with the experimental data with satisfactory accuracy. The highest deviation was 10.2% for Y' and 10.87% for N'. However, for X', there was clear divergence at $\beta = 16°$. Nonetheless, for drift angles ranging from $\beta = 4°$ to 12°, the computed values fell within the experimental error bars, with a maximum deviation of 23.1% at $\beta = 8°$. In shallower water depths of $h/T = 1.5$ and 1.2, the computed values of Y' and N' agreed remarkably well with the experimental values, as seen in figures 7.13c and 7.13d. Not only was the progression of Y' and N' captured, but the maximum deviation was also only approximately 6.1%.

The results obtained for configuration 2:1 in shallow waters showed good agreement between numerical and model test data. The computed values of X' at water depths of $h/T = 2.0$ and $h/T = 1.5$ were within the experimental uncertainty, with a maximum deviation of approximately 7.5% observed at $\beta = 16°$ and $h/T = 1.5$. The force progression was well captured by the numerical method, with other values not deviating from the experiment by more than 4%. For the shallowest water depth of $h/T = 1.2$, the simulation results showed satisfactory agreement with the experimental data for drift angles ranging from 4° to 12°, as shown in figure 7.14d. However, the total longitudinal force was overestimated in this water depth, with a deviation from the experimental value at $\beta = 16°$ of about 14 %. As for Y' and N', the simulations provided remarkably accurate predictions for moderately shallow water depths of $h/T = 2.0$ and $h/T = 1.5$, as seen in figures 7.14b and 7.14c. The non-linearity of the lateral force over the drift angle was outstandingly captured by the simulations, with a maximum deviation of only 8.5%. For the shallowest water depth of $h/T = 1.2$, the computed values of Y' and N' depicted in figure 7.14d agreed reasonably well with the model test data, although some discrepancies were observed for higher drift angles. Specifically, at drift angles of 12° and 16°, the deviations were respectively 9.1% and 12.3% for Y' and 11.8% and 12.1% for N'.

Figures 7.15b, 7.15c and 7.15d plot a comparison of experimental and numerical results in shallow water for configuration 2:2. The highest deviations from the experiment were observed for X'. In moderate shallow waters of $h/T = 2.0$ and $h/T = 1.5$, the numerical results lied within the experimental uncertainty. However, these amounted for almost 100 % of the mean force. Indeed, the behavior of the longitudinal force in the respective

experimental time series showed high oscillations. Configuration 2:2, characterized by a comparatively larger flat bottom and several geometrical discontinuities and gaps between floating boadies, caused a massive disturbance of the surrounding flow. This highly unsteady flow regime around configuration 2:2 may have caused numerous recirculation zones and vortex shedding. At $h/T = 1.2$, where the blockage effect is highest, the utilized numerical method may have not been entirely appropriate to completely resolve the flow passing by configuration 2:2 in steady drift condition. Nonetheless, the total non-dimensional lateral force Y' and yaw moment N' were very well predicted. Similar to configuration 2:1, in moderate shallow waters of $h/T = 2.0$ and $h/T = 1.5$, the trend of hydrodynamic force and moment was well captured, as seen in figures 7.15b and 7.15c. Herein, the highest deviation from the experiment is only about 11.1 % for Y' at $h/T = 1.5$ and $\beta = 12°$. Comparable results were achieved for the shallowest water depth of $h/T = 1.2$, where the maximum percentage difference of 10.47 % was observed for N' at $\beta = 12°$, as seen in figure 7.15d.

The results obtained from the computational procedure described in 7.1.1 were satisfactory for predicting hydrodynamic forces and moments acting on different inland convoy configurations in steady drift conditions in both deep and shallow waters. However, the performance of the RANSE setup varied greatly, depending on the configuration, water depth, and drift angle. A satisfactory agreement between computed and experimental values was achieved in deep water. The relatively higher deviations of forces and moments for the largest drift angle of 16°, as shown in figures 7.13a, 7.14a, and 7.15a, may have been caused by the experimental uncertainty associated with the HSVA method. The good agreements of numerical and experimental results for this drift angle in shallower water conditions indicated that it would have been preferable to conduct a single test run for each drift angle, which could have mitigated potential disturbances in the flow, such as memory effect, side, and front wall influence, as described in ITTC (2005).

In shallower waters, the numerical method delivered excellent results for the lateral force and side moment in all configurations. The progression of Y' and N' as a function of the drift angle, as well as the corresponding non-dimensional value, were well predicted. However, it should be noted that these quantities were sensitive to the floating position, as described in Toxopeus et al. (2013). To account for the free motion of the floating bodies, it is necessary to include the free surface and use an appropriate body motion solver.

Predicting the longitudinal force X' proved to be more complex. Firstly, the overall measured force in the experiment included the thrust. Although relatively well predicted using the MRF method, this quantity was greatly influenced by the quality of the inflow velocity and its fluctuation, as described in Aram and Mucha (2023). Considering a pusher-barge convoy, the flow disturbance induced by the gap, the ship's geometry, and the waterway confinement amounted to a substantial uncertainty. Specifically, for configuration 1:1 and 2:2, using a scale-resolving method, as described in chapter 6, might have delivered more accurate results. However, this conclusion should be considered under the

aspect of maneuverability, as the contribution of Y' and N' to the equation of motion is dominant when simulating maneuvers.

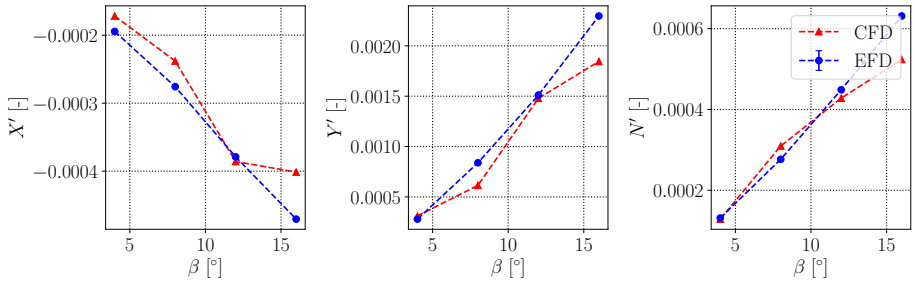

(a) $U = 0.556$ m/s, $h/T = \infty$.

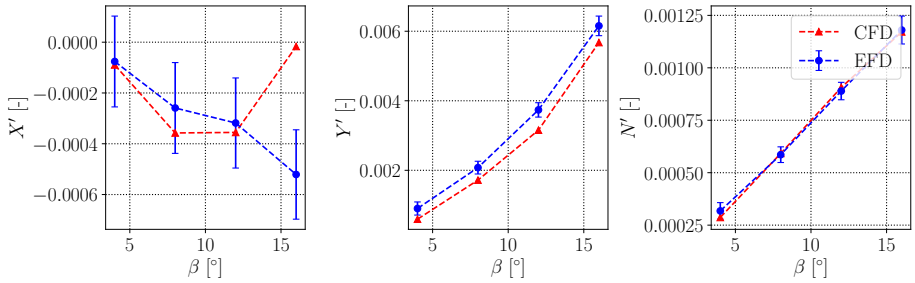

(b) $U = 0.556$ m/s, $h/T = 2.0$

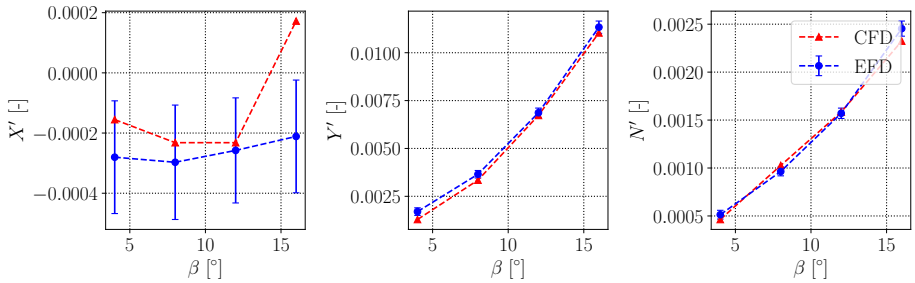

(c) $U = 0.556$ m/s, $h/T = 1.5$

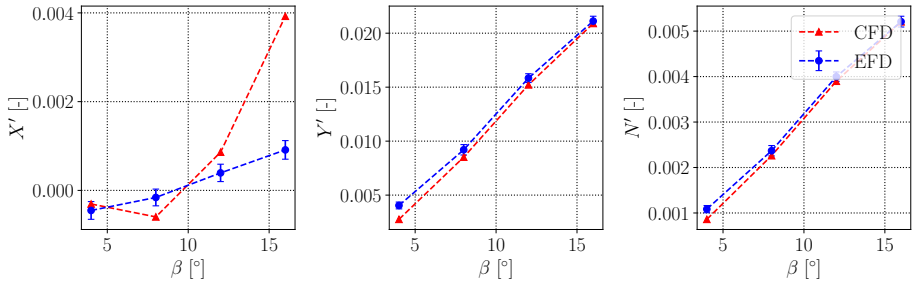

(d) $U = 0.556$ m/s, $h/T = 1.2$

Figure 7.13: Validation of numerical steady drift tests for configuration 1:1 in deep and shallow water. Deep water experiments were performed at HSVA, shallow water experiments at MARIN.

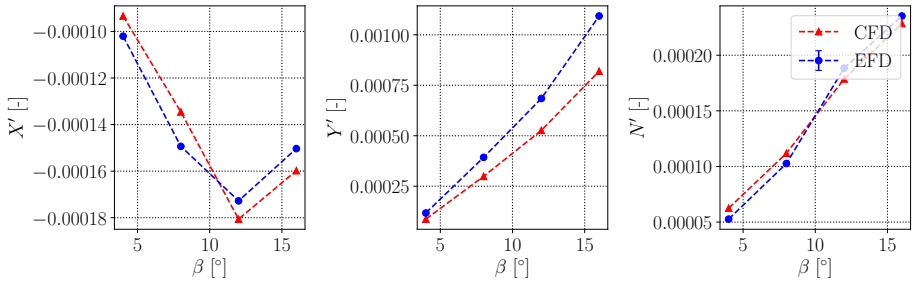

(a) $U = 0.556$ m/s, $h/T = \infty$.

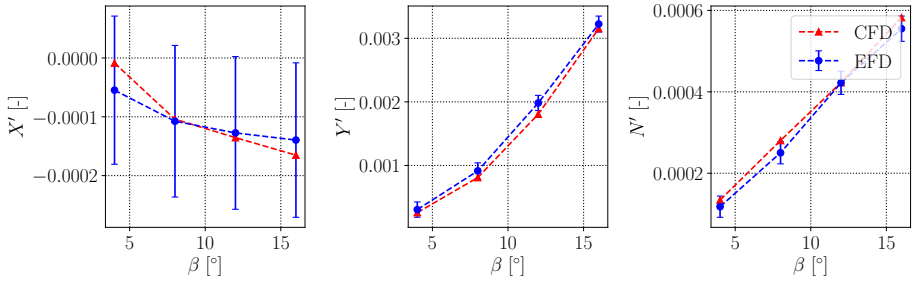

(b) $U = 0.556$ m/s, $h/T = 2.0$

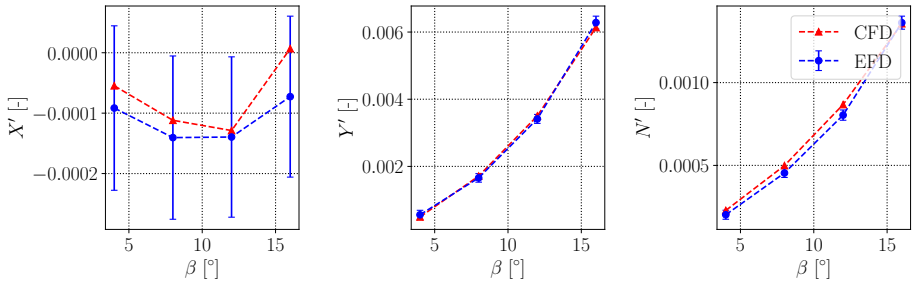

(c) $U = 0.556$ m/s, $h/T = 1.5$

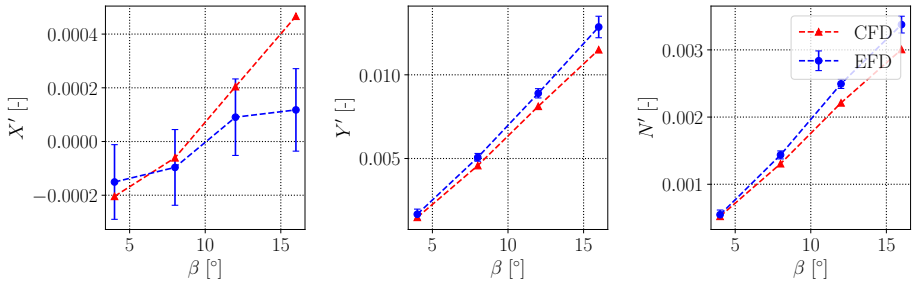

(d) $U = 0.556$ m/s, $h/T = 1.2$

Figure 7.14: Validation of numerical steady drift tests for configuration 2:1 in deep and shallow water. Deep water experiments were performed at HSVA, shallow water experiments at MARIN.

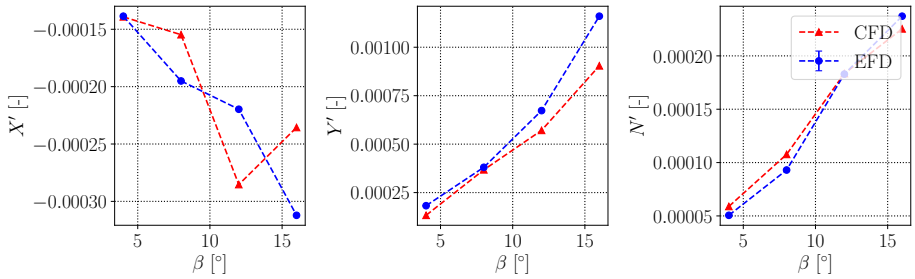

(a) $U = 0.556$ m/s, $h/T = \infty$.

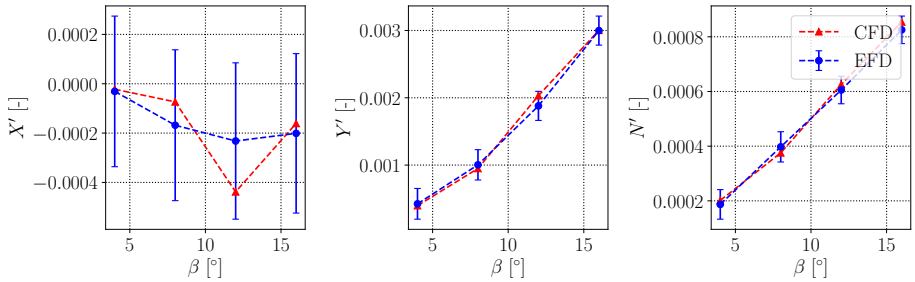

(b) $U = 0.556$ m/s, $h/T = 2.0$

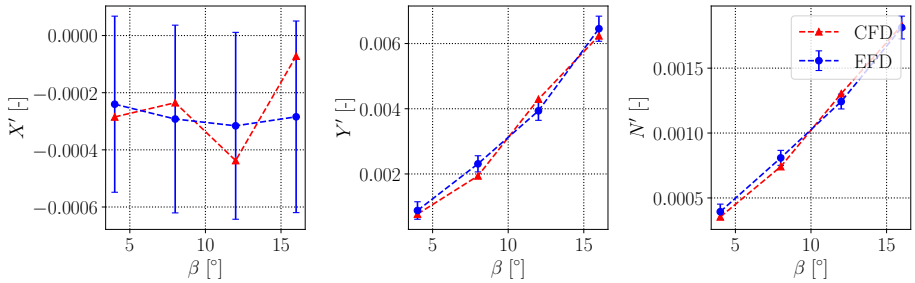

(c) $U = 0.556$ m/s, $h/T = 1.5$

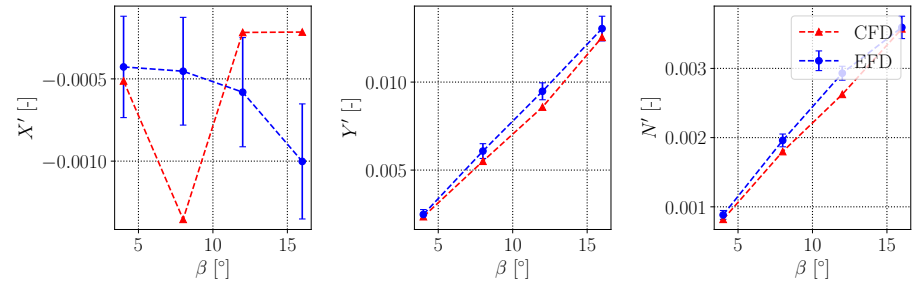

(d) $U = 0.556$ m/s, $h/T = 1.2$

Figure 7.15: Validation of numerical steady drift tests for configuration 2:2 in deep and shallow water. Deep water experiments were performed at HSVA, shallow water experiments at MARIN.

To put the numerical results into perspective, it is useful to analyze the pressure field around the vessels. Figure 7.16 presents the pressure coefficient distribution $C_p = (p/0.5\rho U^2)$ from a top-down view around configuration 1:1 for all the tested drift angles in deep water. p refers to pressure, U denotes inflow velocity, and ρ is water density. The section represented lies just below the idealized water surface. The color gradient ranges from blue to green to red, where blue regions indicate lower pressure and red marks higher pressure zones. At the lower drift angle of 4°, a higher pressure zone developed around the bow area, followed by a lower pressure zone at the fore shoulders. For higher drift angles, the low pressure zone on the suction side moved further downstream, as shown in figures 7.16b, 7.16c, and 7.16d. The pressure field around full-bodied tankers in steady drift conditions in deep water is similar, according to Carrica et al. (2016) and Mucha (2017). However, in the case of configuration 1:1, the drift angle and coupling between pusher and barge affected the pressure distribution. A small lower pressure region can be observed at the barge's transom, while a higher pressure zone can be noticed on the side edges of the pusher's bow. These zones appear in all plots of figure 7.16, and their location does not seem to vary. Higher drift angles tend to amplify this phenomenon.

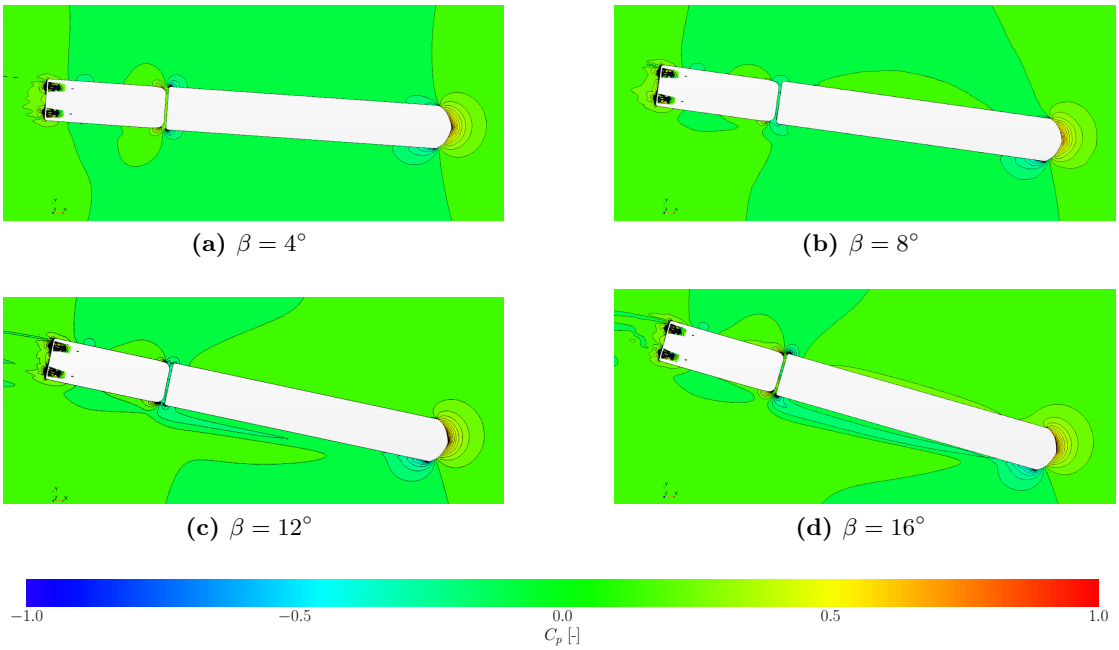

(a) $\beta = 4°$ **(b)** $\beta = 8°$

(c) $\beta = 12°$ **(d)** $\beta = 16°$

Figure 7.16: Pressure field around configuration 1:1 in deep waters and respectively $\beta = 4°$, 8°, 12° and 16° drift angle.

To gain further insights, the pressure coefficient distribution around configuration 1:1 at a drift angle of 16° was compared in different water depth to draft ratios h/T, as shown in figure 7.17. For comparability, the same scale as in figure 7.16 was used. In all figures, a clear low pressure zone was visible. Figure 7.17b depicts the moderately shallow water depth at $h/T = 2.0$. Here, relatively small differences from the deep water case in figure 7.16d were observed, although the blue region appeared somewhat elongated. The low pressure zone extended up to the junction point between the pusher and barge, while the high pressure zone was limited around the bow area. In the shallower water depth of $h/T = 1.5$, as shown in figure 7.17c, the low pressure zone, colored with a deeper shade of blue, hinted at a lower absolute pressure value. Additionally, a distinct lower pressure region developed on the opposite side around the pusher. In the shallowest water depth of $h/T = 1.2$, depicted in figure 7.17d, the pressure distribution underwent noticeable alterations compared to the other cases. The low pressure zone on the barge's side did not show the elongated shape visible in $h/T = 2.0$ and 1.5, but was significantly larger, revealing some kind of vortex shedding. Moreover, the high pressure zone was located further downstream on the pressure side of the barge.

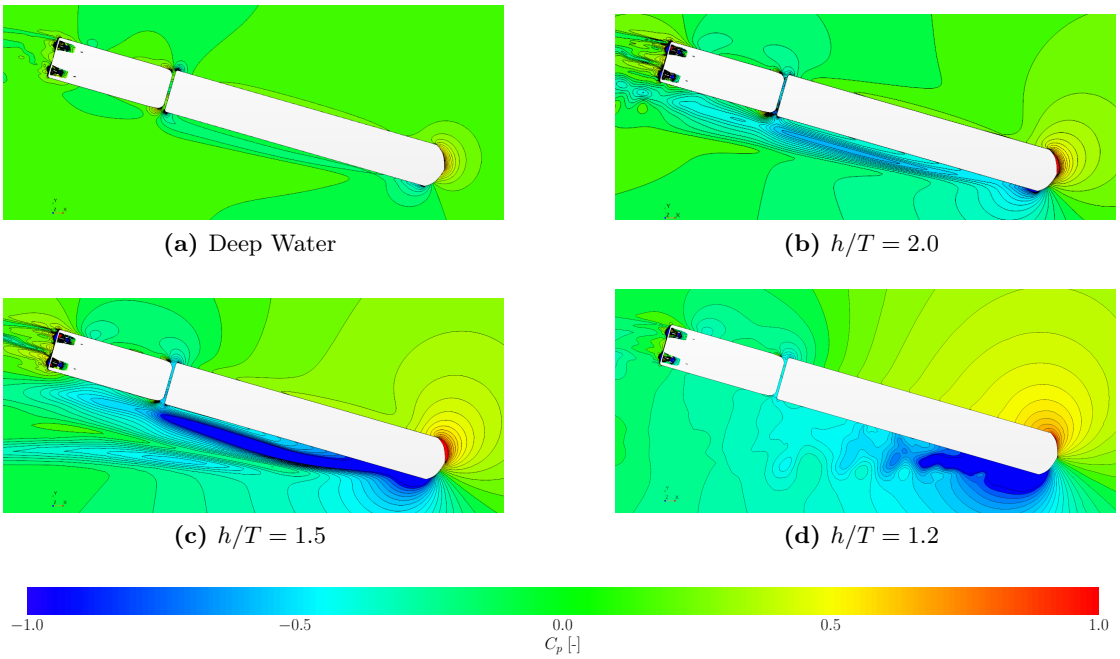

(a) Deep Water **(b)** $h/T = 2.0$

(c) $h/T = 1.5$ **(d)** $h/T = 1.2$

Figure 7.17: Pressure field around configuration 1:1 at $\beta = 16°$ drift angle and respectively deep water, $h/T = 2.0$, $h/T = 1.5$ and $h/T = 1.2$.

Figure 7.18 illustrates the distribution of pressure coefficient C_p on an idealized water surface for all tested configurations at the shallowest water depth of $h/T = 1.2$ and a drift angle of 16°. Similar to figure 7.17, this comparison focuses on the influence of

extreme water restriction and barge arrangement on the pressure distribution around different configurations. Configuration 1:1 is shown in figure 7.18a, configuration 2:1 in figure 7.18b, and configuration 2:2 in figure 7.18c. A consistent distribution of C_p is observed in all images, with a higher pressure zone on the port side of the bow area, corresponding to the stagnation point. The location of this high-pressure zone varied slightly for configuration 2:2 due to the side-by-side arrangement of the two front barges. However, in configuration 2:1, the high-pressure area was larger, extending up to the transom of the fore barge. In all cases, the flow accelerated on the suction side of the fore barge or barges, creating a low-pressure zone. The vortex shedding phenomenon, observed in configuration 1:1, was more pronounced in configuration 2:1 and 2:2 due to the sharp edges at the barge's bow, which accelerated the flow disruption. This caused numerous instabilities on the starboard side of the barge or barges. Additionally, in configuration 2:1 and 2:2, the sharp edges caused an early flow separation, leading to an earlier transition to turbulent flow. As a result, the pusher, located behind two or four barges, operated in turbulent waters. This effect was particularly evident in the wake of configuration 2:2, where the breadth of the side-by-side arranged barges exceeded the pusher's breadth by a factor of 2.

Figure 7.19 presents a perspective view of the C_p distribution on the suction side of the hull for all tested configurations in the shallowest water depth of $h/T = 1.2$ and drift angle of 16°. The color scheme ranges from blue to green to red, indicating lower to higher pressure zones. Across all configurations, the sharp edge located amidship of the front barge or barges significantly impacted the pressure distribution. Specifically, this design feature acted as a divider between pressure zones. In configuration 2:2, the larger low pressure zone extended from the central sharp edge to the suction side of the starboard barge, as shown in figure 7.19c. For configuration 2:1, the low pressure region on the front barge extended to the starboard side of the barges bow, where two sharp edges defined an almost flat area. Configuration 1:1 shared this feature, as the barges were identical across all configurations. However, in all configurations, these sharp edges caused significant flow detachment, leading to relatively poor propeller inflow downstream.

According to Mucha (2017), a reduced UKC results in increased lift and drag forces on the ship hull. The pressure imbalance between the suction and pressure sides, induced by the drift angle, is further accentuated by the water depth restriction. This conclusion holds true for all pusher-barge configurations considered in this chapter. However, the flow disturbance caused by the gap, in addition to the design features of the pusher and barge or barges, differed from the pressure distribution around slender vessels in steady drift condition.

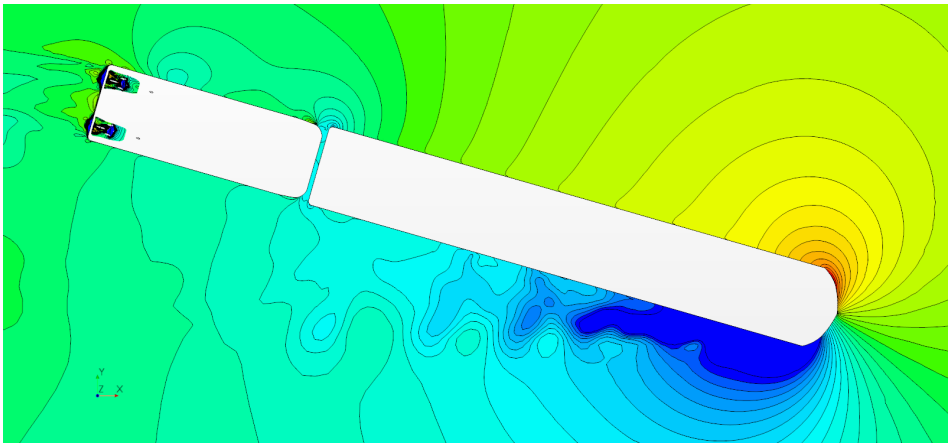

(a) Configuration 1:1

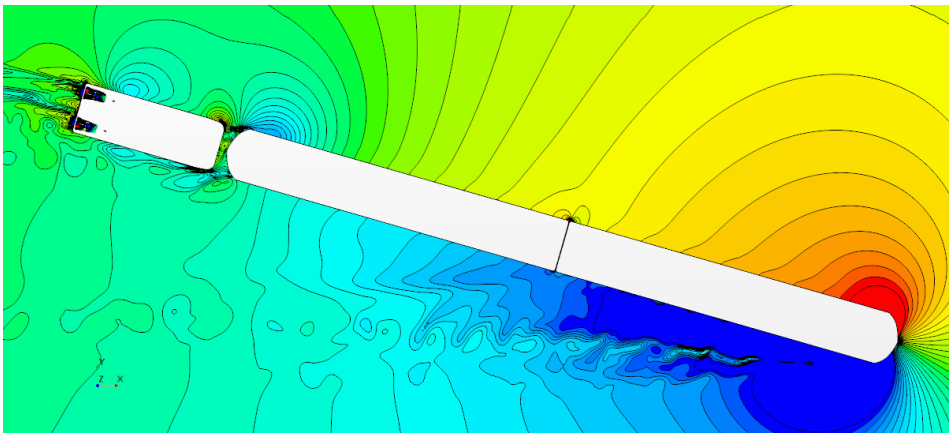

(b) Configuration 2:1

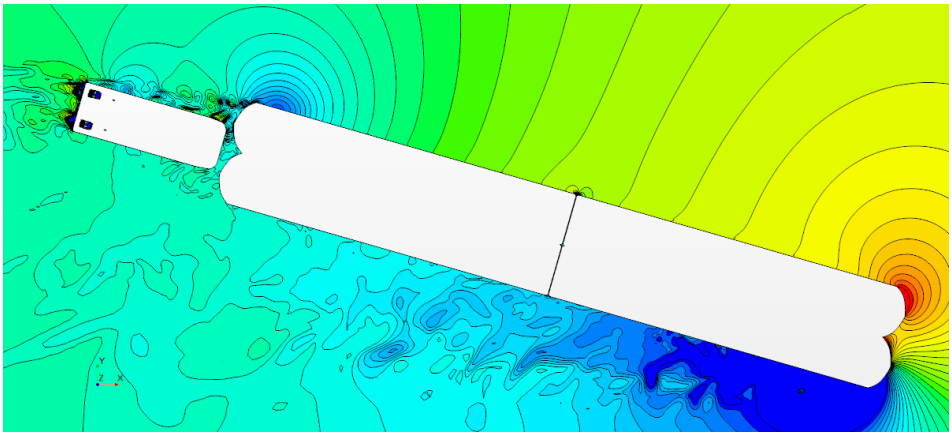

(c) Configuration 2:2

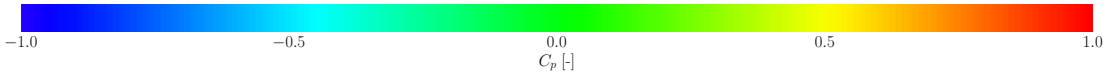

Figure 7.18: Pressure field around configuration 1:1, 2:1 and 2:2 at $\beta = 16°$ drift angle and $h/T = 1.2$.

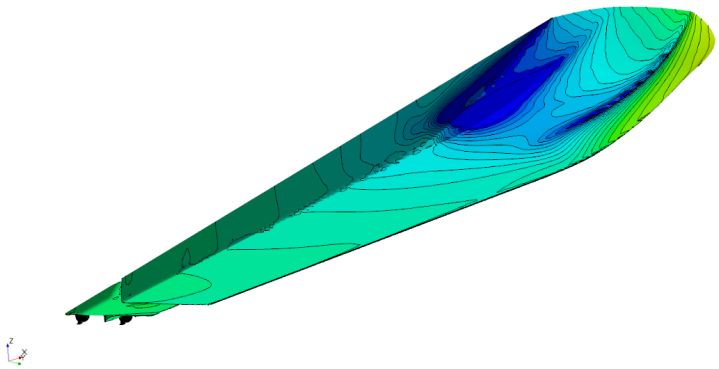

(a) Configuration 1:1

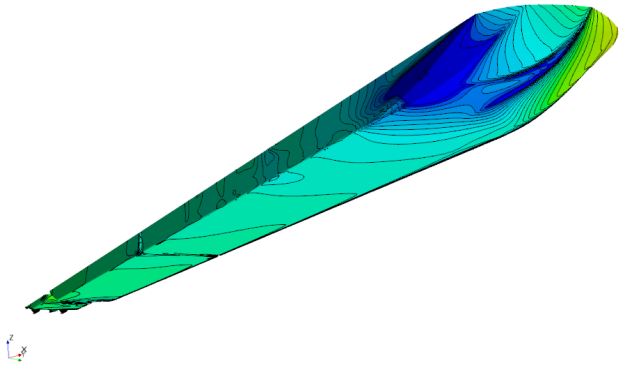

(b) Configuration 2:1

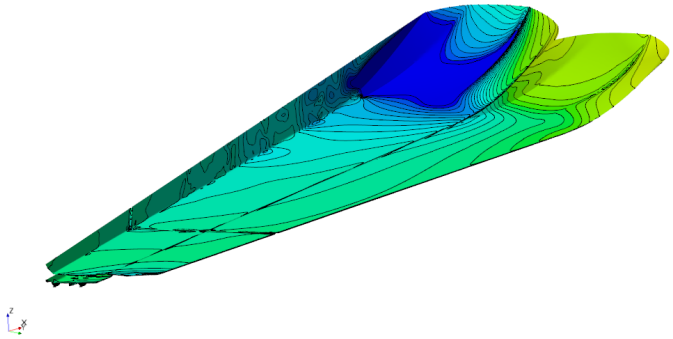

(c) Configuration 2:2

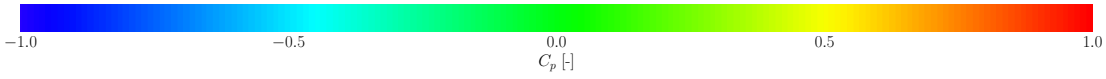

Figure 7.19: Pressure distribution on the hull of configuration 1:1, 2:1 and 2:2 at $\beta = 16°$ drift angle and $h/T = 1.2$.

Figure 7.20 shows a top-down view of the velocity magnitude $|\mathbf{u}|/U$ in the idealized water plane, with colors ranging from blue to green to red indicating low to high velocity regions. Figures 7.20a, 7.20b, and 7.20c present the velocity distribution for configuration 1:1, 2:1, and 2:2, respectively. In all configurations, two distinct regions can be observed near the bow of the vessel: a low velocity region on the port side corresponding to the stagnation point, followed by a high velocity region on the starboard side where the flow accelerates. On the port side of the barge or barges, the velocity distribution appears relatively smooth, with no notable disruptions. However, a higher velocity zone is visible on the aft edge of the barge or barges, especially in configuration 2:2. Around the pusher's transom, two jet-like red regions indicate the propeller-induced velocity. On the starboard side of all configurations, the vortex shedding region is clearly recognizable, occurring immediately after the barge's bow. For configuration 1:1, this zone extends up to the pusher's transom, as shown in figure 7.20a. In configuration 2:1, in addition to the turbulence induced by the drift angle and the barge's sharp bow, an extra disturbance can be traced back to the wider gap between the rear barge and the pusher, as shown in figure 7.20b. Configuration 2:2 exhibits significantly larger flow disruptions, with smaller vortices visible on the port side of the rear barge in figure 7.20c. As a result, the pusher operates in a low velocity zone. In conclusion, the arrangement of four barges has a significant impact on the pusher's performance, altering the velocity distribution and inducing more flow disruptions.

The axial velocity ratio u_x/U_{in} at four different transverse sections along configurations 1:1, 2:1, and 2:2 are presented in figures 7.21, 7.22, and 7.23. These figures show the convoys in a drift condition at a 16° angle and a water depth of $h/T = 1.2$. The four sections are located at different positions: in the forepart of the foremost barge or barges; $x/L_{OA} = 0.0$ at the midship section; inside the gap between barge or barges and pusher; and in the wake of the convoys. The color scheme ranges from blue to green to red, representing lower to higher velocity regions. Additionally, normalized velocity vectors are superimposed on the figures to indicate the direction of the transverse velocity and to identify recirculation zones and vortices.

Figure 7.21a shows a clear vortex identified on the suction side of configuration 1:1, around the bow. This vortex was highlighted by the lower velocity zone on the suction side of configuration 1:1 and the tangential velocity vectors rotating clockwise around it. This turbulent structure was observed to be growing downstream alongside the hull of the convoy, as seen in figures 7.21b, 7.21c, and 7.21d. The flow pattern, highlighted by the tangential velocity vectors, supported this observation. Additionally, the gap between the barges and pusher caused a noticeable disruption in the flow, as seen in the figure 7.21d. The deep blue-colored low velocity region induced by the gap was clearly identifiable. The velocity vectors on this section revealed a rather large recirculation region on the suction side, while the vectors inside the gap were pointing in different directions. In the wake of configuration 1:1, the propellers, gap, and shallow water effects caused a significant disturbance in the flow field. Figure 7.21d shows vortices of different sizes, as well as low and high velocity regions, which corroborated this observation.

Figure 7.22 illustrates the flow behavior around configuration 2:1. At $x/L_{OA} = 0.35$, near the bow of the front barge, a low velocity zone, indicative of a bow vortex, was identified, as shown in figure 7.22a. Similar to configuration 1:1, the presence of the bow vortex was confirmed by the clockwise rotating tangential velocity vectors. As the flow progressed downstream, a larger low velocity zone formed, as seen in figures 7.22b and 7.22c. In figure 7.22c, which depicts the section in the gap between the rear barge and pusher, multiple vortices of varying sizes were observed. Moreover, the deep blue zero velocity region, which corresponds to the dead water zone in the pusher-barge gap, was relatively smaller compared to configuration 1:1. This is due to the smooth transition between the pusher and rear barge in configuration 2:1, as they are coupled bow-to-bow, resulting in a more streamlined flow and a wider gap, allowing for more from port to starboard side through the gap, due to pressure difference. This is in contrast to configuration 1:1, where the gap between the pusher and barge is narrower and prevents the cross flows from port to starboard side. However, in the wake of configuration 2:1, multiple vortices and velocity regions were still observed.

Similar to configurations 1:1 and 2:1, a bow vortex formed on the suction side of configuration 2:2, as observed in figure 7.23a. Moving downstream, a larger recirculation zone appeared, as shown in figure 7.23b. However, in this section, the tangential velocity vectors did not exhibit any well-defined turbulent structures. This disordered flow behavior was also observed in the gap section between the rear barges and the pusher, as seen in figure 7.23c. Here, a larger dead water zone, colored deep blue, was noticeable. Despite the bow-bow coupling of the pusher and the rear barges in configuration 2:2, the convoy's large overall width caused a more significant gap effect. Moreover, the water restriction, drift angle, and bulkiness of the convoy resulted in several flow detachments and recirculation zones. As in configurations 1:1 and 2:1, vortices of different sizes were superimposed in the wake of configuration 2:2. In addition, figures 7.21d, 7.22d, and 7.23d highlighted the impact of propeller rotation on the wake, as shown by the deep red marked regions.

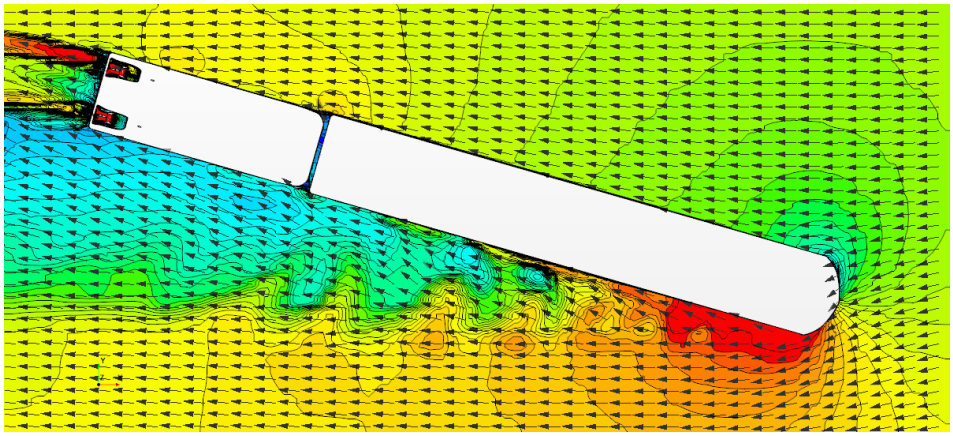

(a) Configuration 1:1

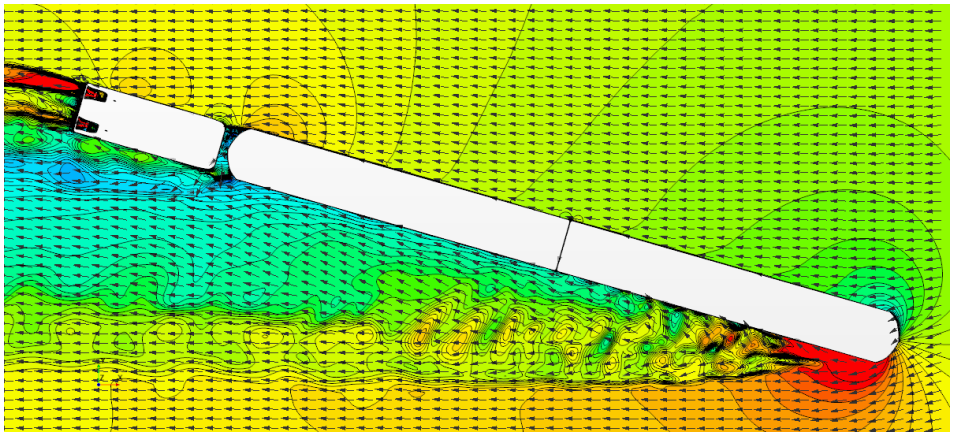

(b) Configuration 2:1

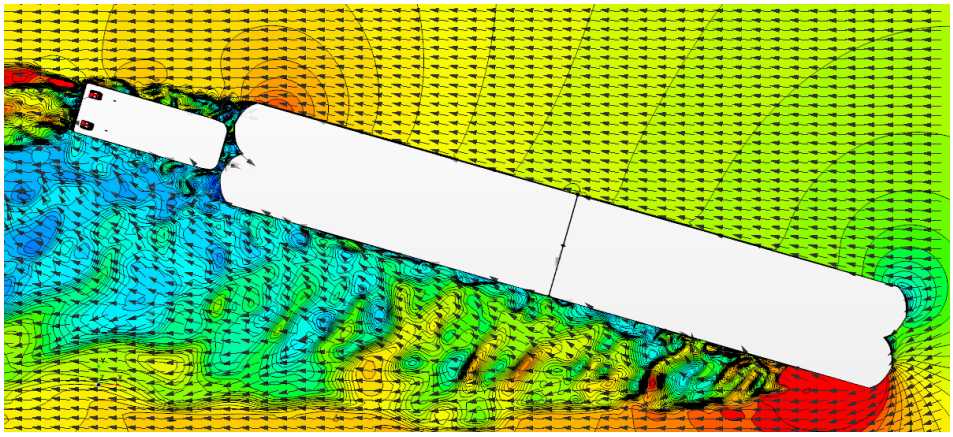

(c) Configuration 2:2

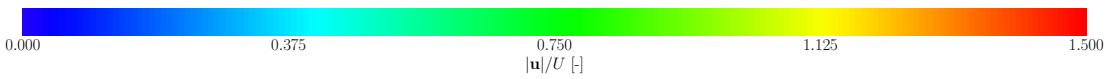

Figure 7.20: Velocity magnitude $|\mathbf{u}|/U$ and normalized velocity vectors at idealized water plane for configuration 1:1, 2:1 and 2:2 at $U = 0.556$ m/s and $h/T = 1.2$.

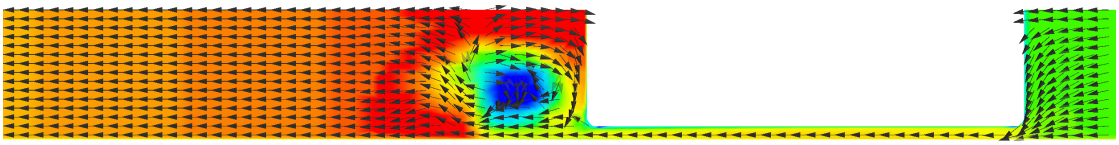

(a) Configuration 1:1, $x/L_{OA} = 0.35$

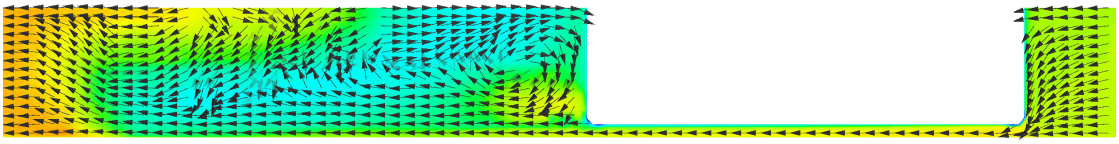

(b) Configuration 1:1, $x/L_{OA} = 0.0$

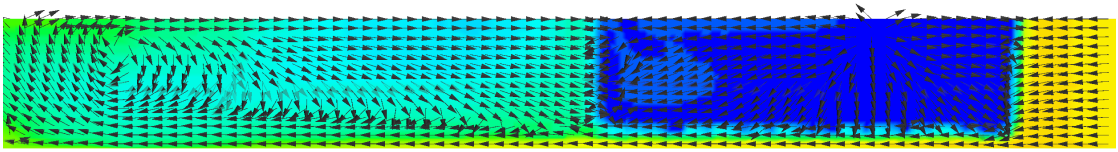

(c) Configuration 1:1, $x/L_{OA} = -0.20$

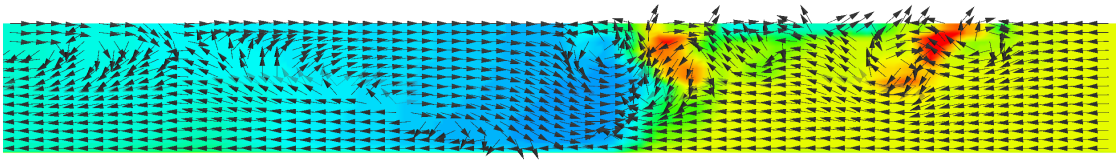

(d) Configuration 1:1, $x/L_{OA} = -0.53$

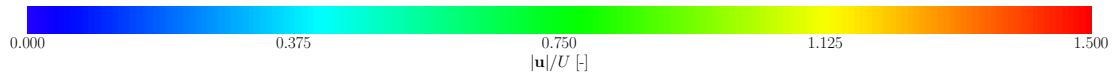

Figure 7.21: $|\mathbf{u}|/U$ and normalized velocity vectors in different sections alongside configuration 1:1 at $U = 0.556$ m/s and $h/T = 1.2$.

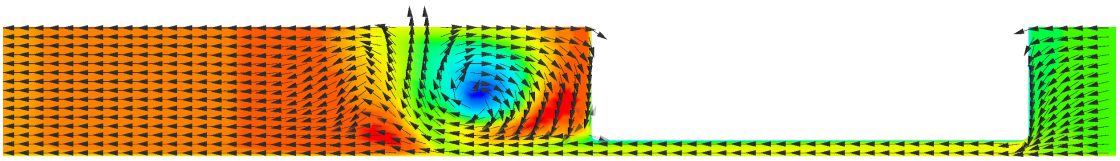

(a) Configuration 2:1, $x/L_{OA} = 0.38$

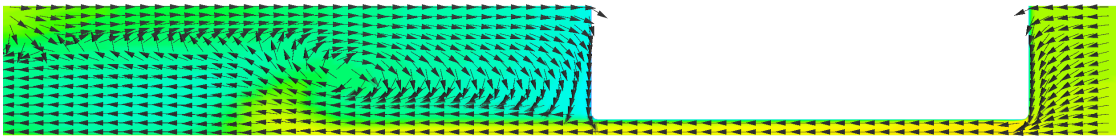

(b) Configuration 2:1, $x/L_{OA} = 0.29$

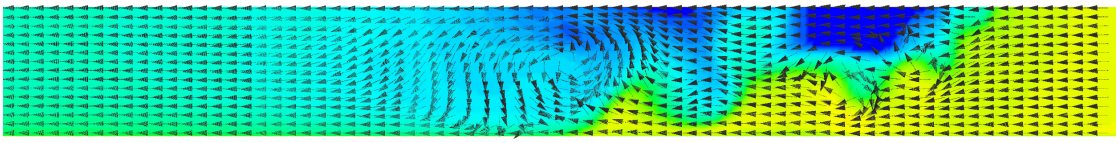

(c) Configuration 2:1, $x/L_{OA} = -0.32$

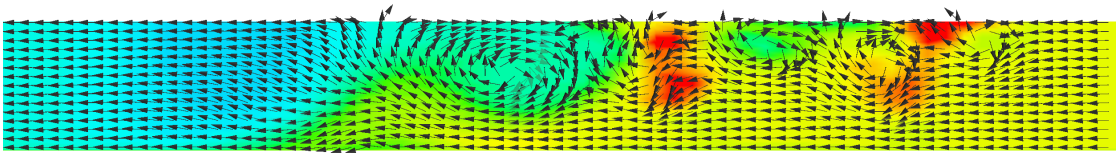

(d) Configuration 2:1, $x/L_{OA} = -0.52$

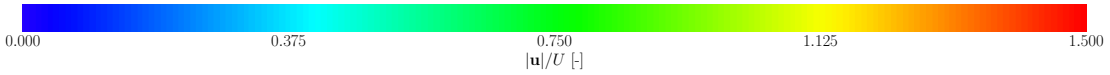

Figure 7.22: $|\mathbf{u}|/U$ and normalized velocity vectors in different sections alongside configuration 2:1 at $U = 0.556$ m/s and $h/T = 1.2$.

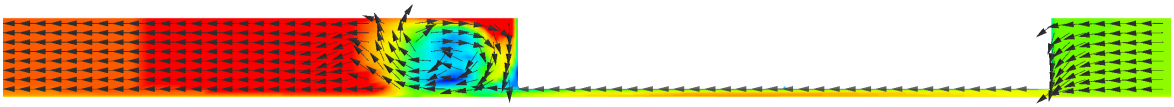

(a) Configuration 2:2, $x/L_{OA} = 0.38$

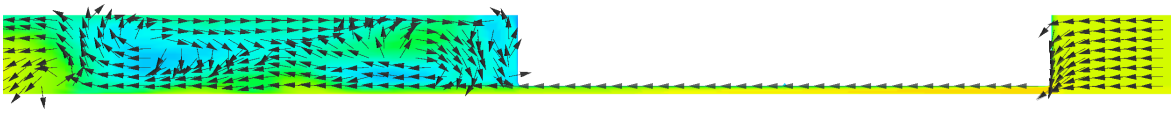

(b) Configuration 2:2, $x/L_{OA} = 0.29$

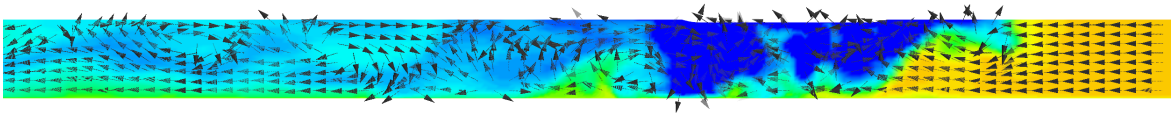

(c) Configuration 2:2, $x/L_{OA} = -0.32$

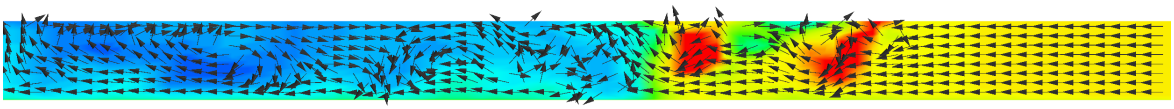

(d) Configuration 2:2, $x/L_{OA} = -0.52$

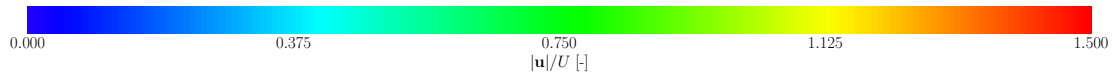

Figure 7.23: $|\mathbf{u}|/U$ and normalized velocity vectors in different sections alongside configuration 2:2 at $U = 0.556$ m/s and $h/T = 1.2$.

Understanding the formation of vortices around drifting vessels is crucial for assessing their impact on the pressure distribution around the hull, and consequently, on hydrodynamic forces and moments acting on the hull. Xing et al. (2012) conducted a comprehensive analysis of turbulent structures around a KVLCC drifting at 0°, 16°, and 30° in deep water. They identified three primary vortices, each forming at different points on the hull. The first vortex, known as the **f**ore **b**ody **s**ide **v**ortex (FBSV), detached around the bow of the ship on the suction side. The second vortex, the **a**ft **b**ody **a**ide **v**ortex (AFBS), developed in the aft body part of the vessel on the pressure side, near the stern. Finally, the aft body bilge vortex formed in the wake of the vessel. Similar structures were observed by Feder et al. (2022).

Although the convoys analyzed in this study differed significantly from the monohulls studied in the studies cited above, some similarities were identified. Figure 7.24 presents a visualization of the vortex structures obtained using the λ_2 criteria at a drift angle of 16° and a h/T ratio of 1.2. The colors ranging from blue to green to red represent the vorticity. In all configurations, an FBSV separated on the suction side of the bow of the front barge or barges. Additionally, similar vortex structures detached from the gaps around the floating bodies. However, in configuration 2:2, a substantial amount of mixing occurred, which made the identification of coherent vortex structures rather difficult. Moreover, in the wake of all configurations, a larger structure engulfed the pusher, substantiating to some extent the complexity of propeller inflow.

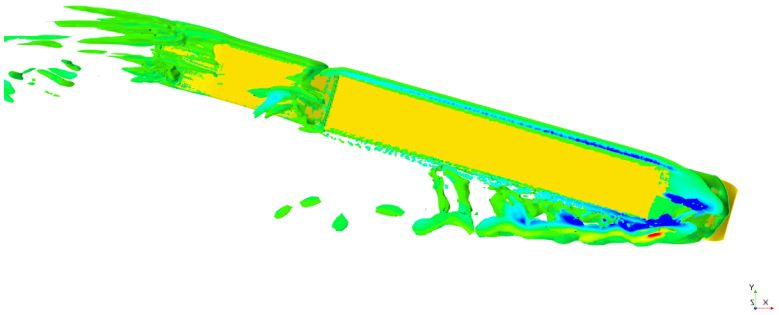

(a) Configuration 1:1

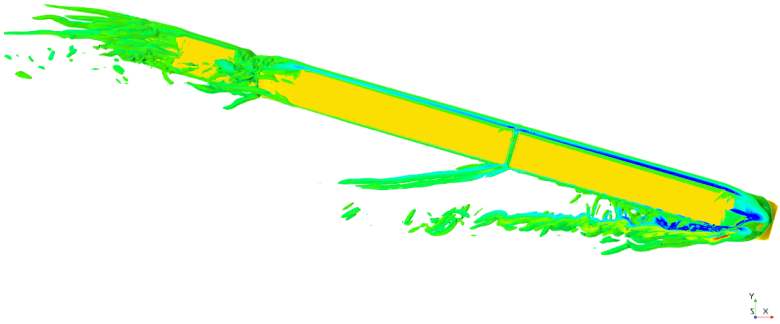

(b) Configuration 2:1

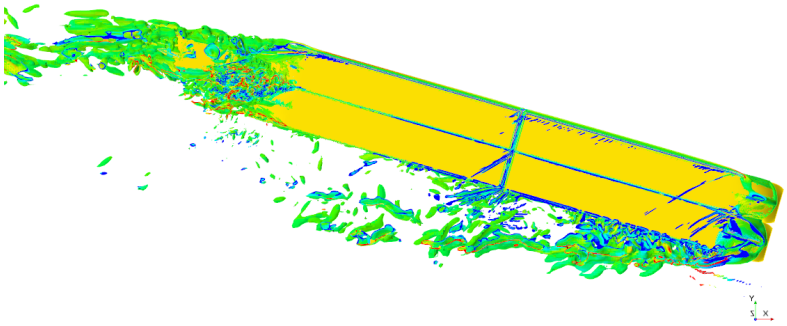

(c) Configuration 2:2

Figure 7.24: Vorticity on vortex structures around configuration 1:1, 2:1 and 2:2 in steady drift condition at $\beta = 16°$, $U = 0.556$ m/s and $h/T = 1.2$ visualized by the λ^2 criterion.

In addition to analyzing the velocity and pressure fields around different configurations, the distribution of the total lateral hydrodynamic force Y' is a useful quantity for assessing the impact of water depth and drift angle on a vessel's hull. The convoy's hull was subdivided into transversally arranged stripes, and the force was obtained through pressure and shear-stress integration on these stripes. Figure 7.25 illustrates this quantity for configuration 1:1 in deep water, with drift angles ranging from 4° to 16° over the non-dimensional ship length ratio x/L_{OA}. Consistent with the pressure distribution represented in figure 7.19a, a force imbalance due to the drift angle was observed between $0.2 < x/L_{OA} < 0.5$. Moreover, the gap effect between the pusher and barge at $-0.2 < x/L_{OA} < -0.4$ led to a higher opposite lateral force. Here, the flow accelerated between the pusher and barge, inducing lower and higher pressure zones, as shown in figure 7.16.

The impact of shallow water on the lateral force distribution for configuration 1:1 at $\beta = 16°$ is illustrated in figure 7.26. As expected, the shallowest water depth at $h/T = 1.2$ caused the largest increase in force, with a maximum value that was 450% higher than that in deep water conditions. The lateral force distribution on the hulls of configurations 1:1, 2:1, and 2:2 at $\beta = 16°$ and $h/T = 1.2$ is depicted in figure 7.27. The large force at the bow and the gap effect were also visible here. However, the behavior of the green dotted line representing configuration 2:2 was somewhat different. Specifically, the gap effect was more pronounced, with a distinctive surge of the lateral force in both negative and positive directions between $-0.4 < x/L_{OA} < 0.2$. The arrangement of four barges in front of the pusher in configuration 2:2 disrupted the flow, causing a larger pressure imbalance around the pusher, which was reflected in the lateral force distribution.

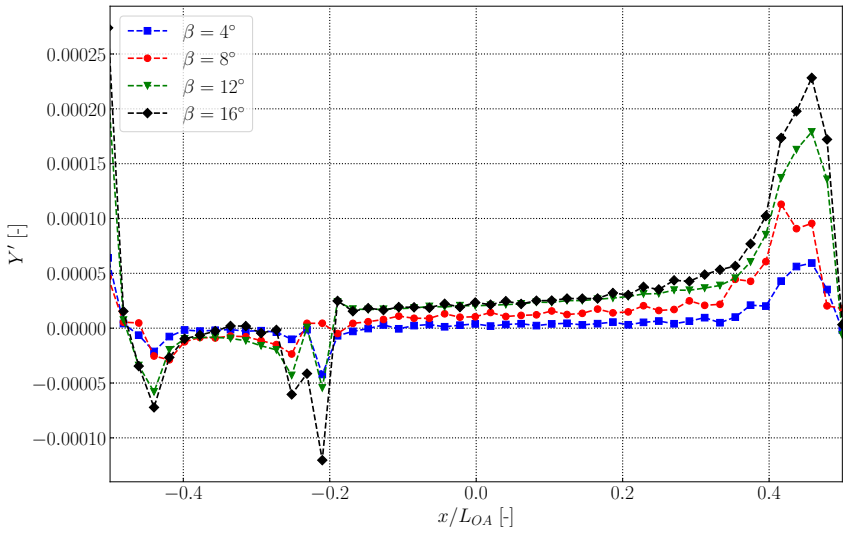

Figure 7.25: Lateral force Y' distribution on configuration 1:1 in deep water and a drift angle of respectively $\beta = 4°$, $8°$, $12°$ and $16°$.

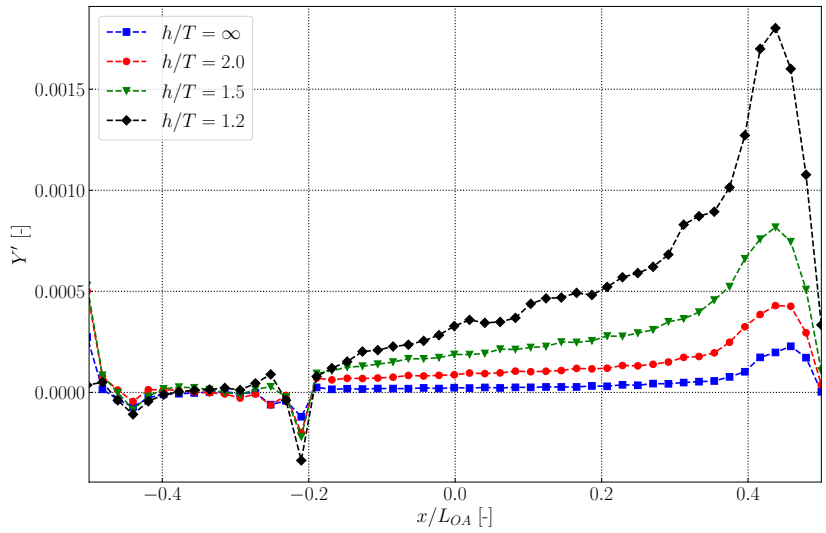

Figure 7.26: Lateral force Y' distribution on configuration 1:1 at a drift angle of $\beta = 16°$ and respectively deep water, $h/T = 2.0$, $h/T = 1.5$ and $h/T = 1.2$.

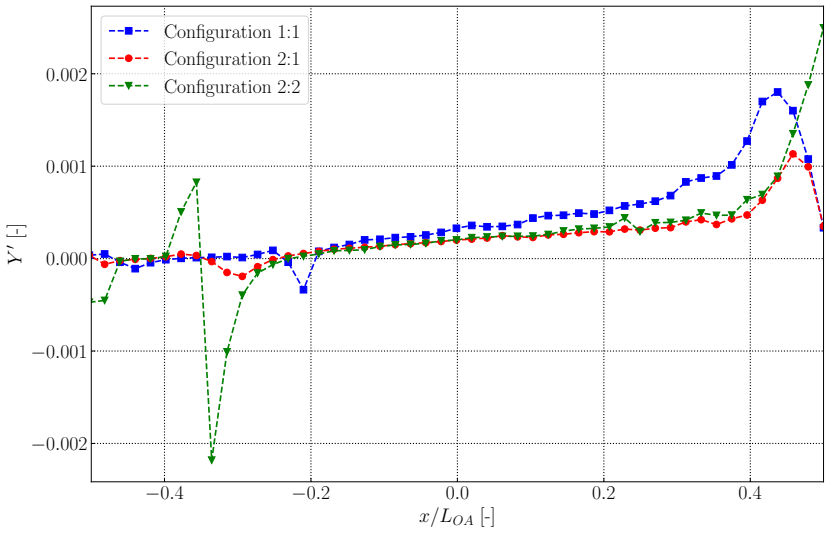

Figure 7.27: Lateral force Y' distribution on configuration 1:1, 2:1 and 2:2 at a drift angle of $\beta = 16°$ and $h/T = 1.2$.

7.2 Steady rudder variation

7.2.1 Computational procedure

Steady rudder variation tests were conducted using the same computational procedure and domain as the steady drift simulation. Prior to meshing, the floating position of the vessels was adjusted, and the free surface was omitted. The main objective of these tests was to validate the maneuvering forces obtained from numerical steady rudder variation tests in both deep and shallow waters. The mesh was constructed around the vessel at a drift angle of 0°, and the rudder angle was varied before each simulation. Refinement boxes were set up around the appendages, with special attention given to the rudders. The surface mesh's resolution was increased for the ducts and rudders to accurately represent the steering and propulsive devices geometrical features. Figure 7.29 provides a top view of the mesh around the appendages connected to the pusher in configuration 1:1. The simulations aimed for a fully-resolved boundary layer with a y^+ below unity. The MRF method simulated the propeller's rotation, and the corresponding subdomains are shown in a schematic arrangement in figure 7.28.

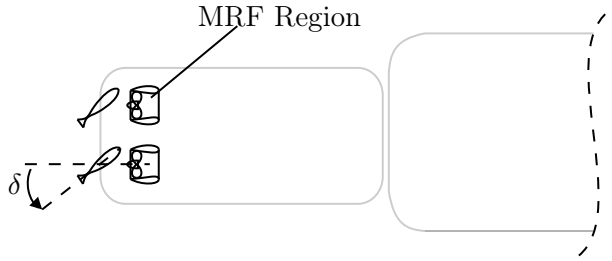

Figure 7.28: Schematic representation of numerical setup for numerical steady rudder variation tests.

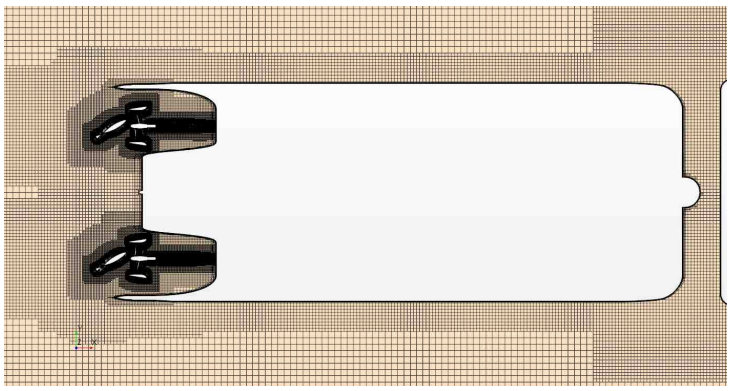

Figure 7.29: Top view of the mesh around the fully appended pusher in configuration 1:1 with a rudder angle of $\delta = 45°$.

The sensitivity analysis for the numerically obtained integral forces and moment (X, Y, and N) acting on configuration 1:1, with a rudder deflection angle of $\delta = 45°$, a water depth to draft ratio of $h/T = 1.2$, and an inlet velocity of $U = 0.556$ m/s, was performed using the el Moctar et al. (2021) and Oberhagemann (2017) procedure. The grid refinement ratio r_k was set to $\sqrt{2}$ for refining the mesh and time step simultaneously. The mean values of X, Y, and N were obtained by averaging over the last 20 s of a converged simulation. Figure 7.30 shows the time history of N over simulation time t for the case considered in this section, which converged to a statistically steady state after approximately 20 s. The numerical simulation failed to reproduce the substantial unsteadiness of the flow observed in the experimental time history of N (shown in figure 7.31). The almost steady flow behavior of the numerically obtained yaw moment may be attributed to the omission of the free surface, constraints of ship motions and inherent simplification of the $k-\omega$-SST turbulence model. Table 7.2 provides an overview of the grids and time steps considered for the sensitivity and convergence analysis. The coarsest grid comprised $4.2 \cdot 10^6$ control volumes; The finest grid had $16.7 \cdot 10^6$ control volumes. All quantities demonstrated oscillatory convergence, with associated convergence ratios R_k of -0.901 for X, -0.98 for Y and -0.97 for N.

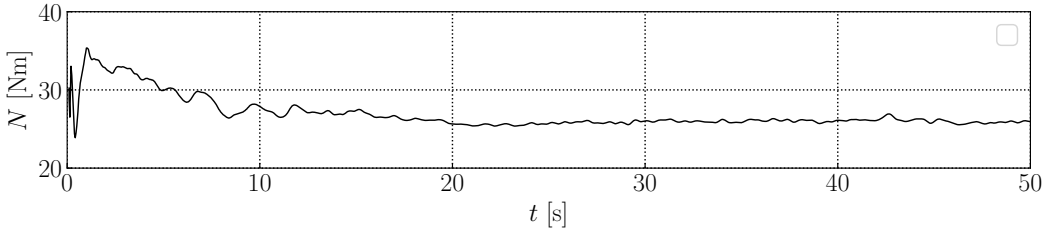

Figure 7.30: Convergence of computational total yaw moment N over time t for configuration 1:1 with rudders deflected at an angle of δ=45° and $h/T = 1.2$.

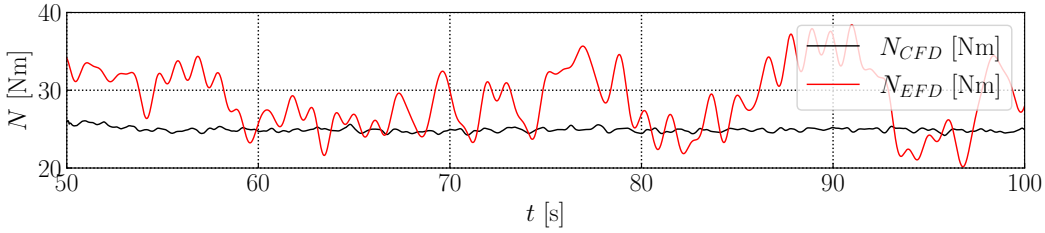

Figure 7.31: Time history of computational and experimental total yaw moment N over time t for configuration 1:1 with rudders deflected at an angle of δ=45° and $h/T = 1.2$.

Table 7.2: Sensitivity analysis of total longitudinal force X [N] for configuration 1:1 at a rudder angle of δ=45° and $h/T = 1.2$.

CV·10^6	Δt [s]	X [N]	**Diff. in** %	Y [N]	**Diff. in** %	N [N m]	**Diff. in** %
4.2	0.01	-2.694	-1.01	-10.594	-4.40	26.126	-4.72
8.5	0.007171	-2.472	-2.60	-10.147	-2.99	24.948	-2.96
16.7	0.005	-2.429	-	-10.285	-	25.374	-
R_k	-	-0.901	-	-0.98	-	-0.97	-

7.2.2 Experimental results

The rudder variation tests were conducted as part of the experimental campaign described in chapter 5. The experimental procedure consisted in towing the convoys in a straight-ahead position at propulsion point, and deflecting the rudders at an angle δ. The time histories of the experiments conducted in deep water and shallow water of $h/T = 1.2$ are presented in figures 7.32 and 7.33, respectively. The ship model was towed at a velocity of $U = 0.556$ m/s. In deep water, a wider range of rudder angles were tested. The rudders were deflected incrementally by 5° during a single run until reaching the maximum angle of 60°. Although this method was advantageous in terms of execution time, it resulted in highly oscillating forces due to the relatively short testing interval. Nonetheless, the increase of total non-dimensional longitudinal force X', lateral force Y' and yaw moment N' over time was evident until the rudder stalled at approximately 200 s. In shallow water, two rudder angles δ per run were investigated. The oscillations observed in shallow water, as depicted in figure 7.33, were extreme. However, it is important to note that the observed oscillations may not be solely caused by rudder deflection. The blockage effect and massive vortex shedding induced by the interaction between the rudder, propeller, and waterway may also have played a significant role.

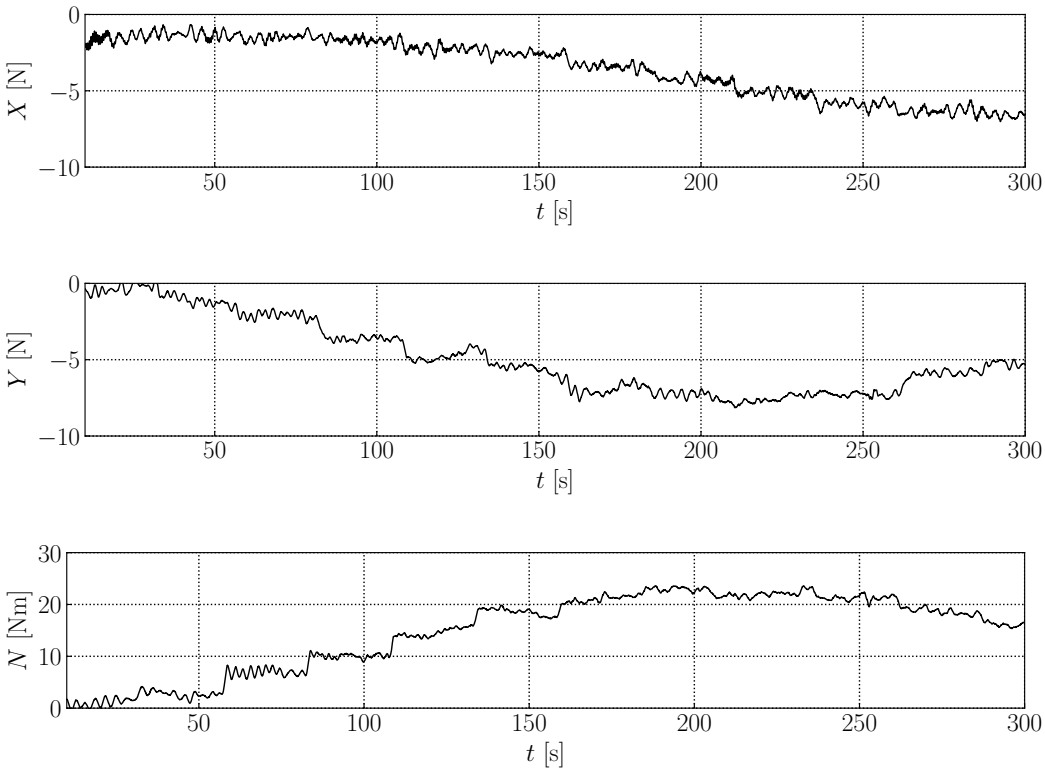

Figure 7.32: Time history of hydrodynamic forces and moment X, Y, and N during steady rudder variation tests for configuration 1:1 in deep water at $U = 0.556$ m/s and rudder angles ranging from 5° to 60° in steps of 5°.

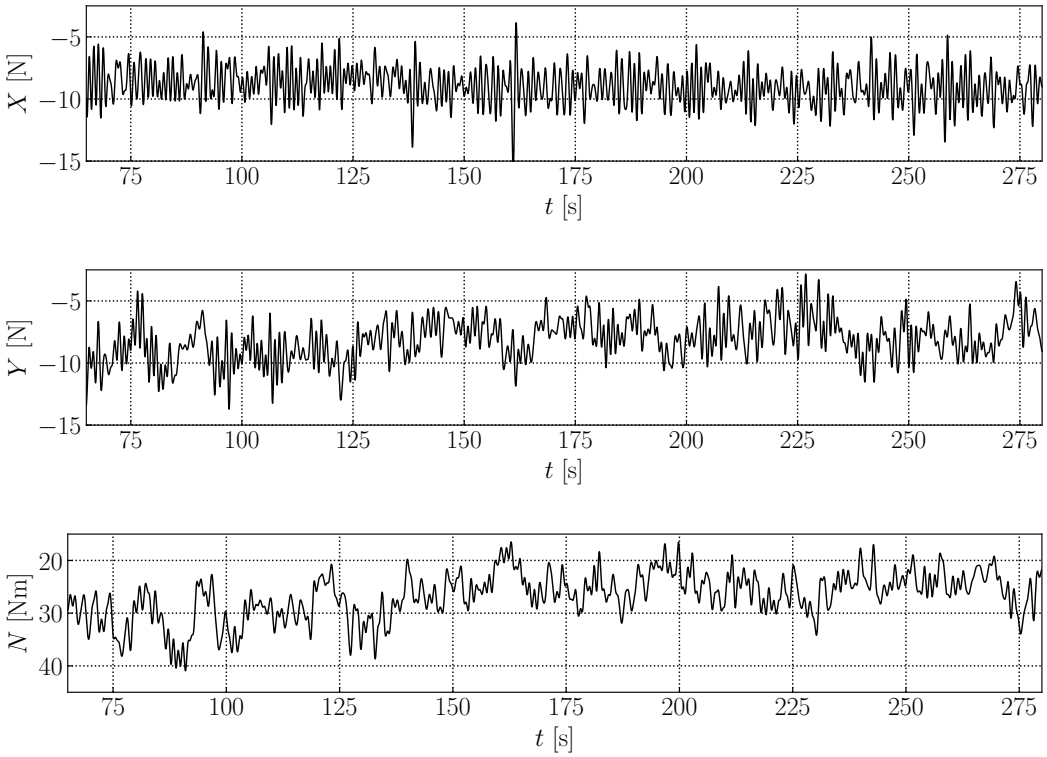

Figure 7.33: Time history of hydrodynamic forces and moment X, Y, and N during steady rudder variation tests for configuration 1:1 in $h/T = 1.2$ at $U = 0.556$ m/s and rudder angles of 45° and 60°.

The operational conditions of inland waterway vessels require specific rudder geometry and arrangement to ensure maneuverability in restricted waterways. As noted in Radojčić et al. (2021), shallow waters and frequent course changes impose a higher maneuverability requirement on steering devices compared to seagoing vessels, which are subject to seaway and waves. To meet these requirements, rudders on inland waterway vessels are dimensioned to generate higher forces and delay the stall angle. According to Liu et al. (2016), this results in lower aspect ratios but higher lift coefficients. However, this design choice also leads to comparatively higher drag coefficients.

Figure 7.34 presents the experimental results of rudder variation tests for configuration 1:1 at all tested water depths. Herein, the black dashed line represents deep water tests; the blue line represents a water depth to draft ratio of $h/T = 2.0$; the green line represents $h/T = 1.5$; and the red line represents $h/T = 1.2$. Error bars are provided to show the standard deviation. The graphs from left to right display the non-dimensional overall hydrodynamic longitudinal force X', lateral force Y', and yaw moment N' acting on a convoy's hull plotted against rudder deflection angle δ. For all water depths, X' increased gradually. At lower deflection angles, the overall longitudinal force was close to

zero for deep to moderately shallow waters, while in shallow to extremely shallow waters ($1.5 > h/T > 1.2$), the shallow water effect was more pronounced. The progression of the curves was almost identical, and in the straight-ahead position, the hull contribution to X' remained unchanged regardless of the rudder angle. The contribution of δ to the total longitudinal force was relatively unaffected by the water depth, and the rudder was always operating in deep to moderately shallow waters as the ratio h/T was determined with the barge's draft. The non-dimensional lateral force Y' and yaw moment N' displayed minor differences between the values measured at different water depths, with the black marking for deep water differing the most. However, this may be attributed to the different test condition, justifying the discrepancy. The highest values for Y' and N' at all water depths were attained at a deflection angle of $\delta = 45°$, confirming the observations made by Liu et al. (2016).

Figure 7.35 compares experimentally obtained total non-dimensional forces and moment X', Y' and N' in rudder variation tests for three different configurations, 1:1, 2:1, and 2:2, in the shallowest water depth of $h/T = 1.2$. The red markings represent configuration 1:1, green markings represent configuration 2:1, and blue markings represent configuration 2:2. The operational conditions for each configuration, i.e., the revolution rate and resulting thrust, were different. Furthermore, the quality of the inflow heavily depended on the arrangement of barges in front of the pusher.

Considering the results for lateral force Y' and yaw moment N', the maximum lateral force was achieved at a deflection angle of $\delta = 45°$ for all configurations. Configuration 1:1 resulted in higher non-dimensional forces, which is likely due to using the same steering devices to maneuver a comparatively smaller convoy. While lateral force Y' was almost equal for configurations 2:1 and 2:2, the measured values of N' for configuration 2:1 were comparatively smaller. This could be because configuration 2:2 operated at a higher propulsion point than configuration 2:1.

According to Maimun et al. (2011), the turning behavior of pusher-barge convoys may improve in shallow waters compared to deep water. The increase in rudder forces in shallow water may partly explain this observation. In fact, in figure 7.34, Y' was higher in the shallowest water depth of $h/T = 1.2$. This phenomenon has also been observed by Yasuo and Hitoshi (1988) on wide vessels fitted with twin-screws and twin-rudders.

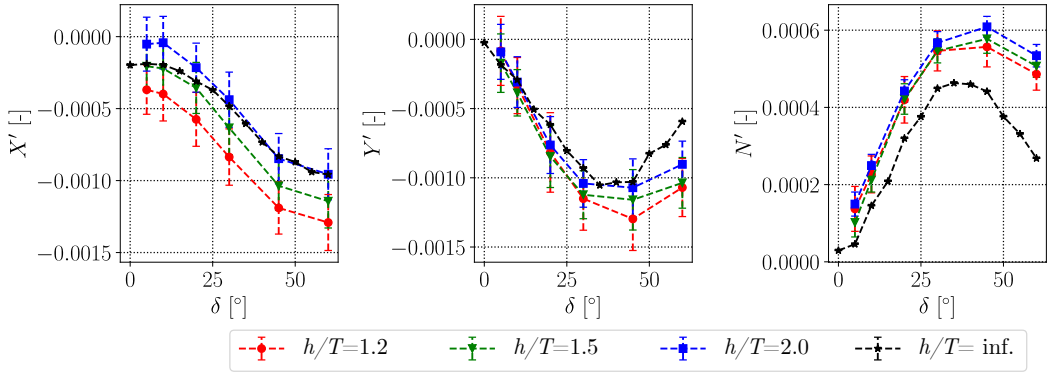

Figure 7.34: Experimental results of steady rudder variation tests at $U = 0.556$ m/s for configuration 1:1 in water depths of $h/T = \infty$, 2.0, 1.5 and 1.2.

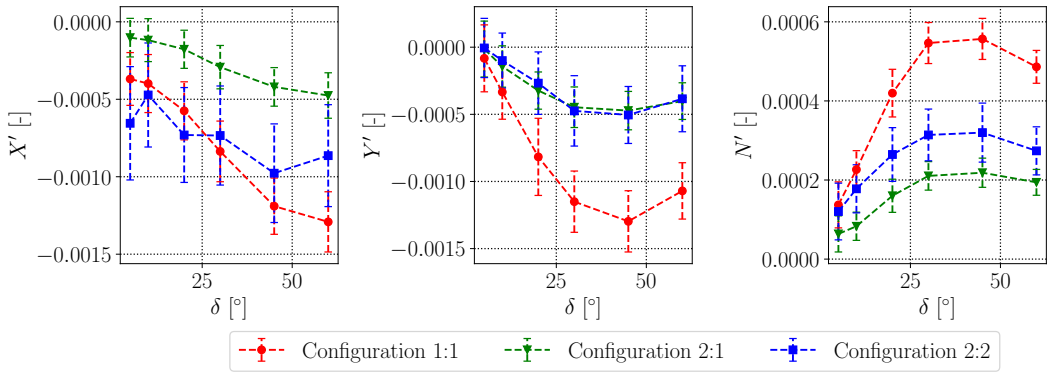

Figure 7.35: Comparison of experimental results of steady rudder variation tests at $U = 0.556$ m/s and $h/T = 1.2$ for configuration 1:1, 2:1 and 2:2 in $h/T = 1.2$.

The experiments conducted in this study provided valuable insights into the hydrodynamic forces and moments acting on a convoy's hull induced by rudder deflection in both deep and shallow water. These findings can be utilized to derive hydrodynamic derivatives for the maneuvering method outlined by Cura-Hochbaum (2006) and Mucha (2017).

7.2.3 Numerical results

Figures 7.36, 7.37, and 7.38 illustrate the comparison between computed and measured total hydrodynamic forces X', Y', and moment N' acting on the hulls of configurations 1:1, 2:1, and 2:2 in both deep and shallow water. The red markings indicate the com-

puted values, while the blue markings represent the measured forces. The experimental data is supplemented by an error bar, which symbolizes the standard deviation of the corresponding quantity.

For the deep water cases, the numerically obtained total lateral force Y' and yaw moment N' agreed well with the experimentally measured data. However, the quality of the numerical results was highly dependent on the rudder deflection angle and the considered configuration. In the case of configuration 1:1, the highest deviation of approximately 30% was determined for Y' computed at the lowest rudder angle of $\delta = 50°$. Although the computed value was -1.105 N, and the absolute experimental value of Y was -1.523 N, the absolute difference between both values was less than 0.5 N. Furthermore, the time history of Y shown in figure 7.7 indicates that the time interval considered to obtain forces and moments associated with each rudder angle was relatively small, contributing to a higher level of uncertainty. Nevertheless, Y' and N' values computed for larger drift angles for configuration 1:1 agreed with satisfactory accuracy with the experimental data, with all computed values differing from experimental data by a maximum of approximately 10%. The computational method also captured the non-linearity of Y' and N' well. Similar results were obtained for Y' and N' acting on the hulls of configurations 2:1 and 2:2, with the highest deviations determined for the largest rudder angles at 60°. For these rudder deflections, the computed Y' and N' values differed by respectively 15.1% and 18.2% for configuration 2:1 and 19.8% and 18.2% for configuration 2:2. For lower rudder angles, numerically obtained Y' and N' agreed well with experimental values, deviating by less than 10%.

On the other hand, computing the total non-dimensional longitudinal hydrodynamic force X' acting on a convoy's hull proved to be more complex. The complexity of the rudder geometry, combined with the gap effect and rudder-propeller interaction, may explain the large discrepancy observed between the experimental and computed X' forces, particularly for larger rudder angles, as seen in figures 7.36a, 7.37a, and 7.38a.

In shallow waters, the experimental investigation covered fewer drift angles. Figure 7.8 shows that X, Y, and N were measured for two rudder angles during a single run of 300 s. When the water depth ratio was $h/T = 2.0$, the computed values of Y' and N' showed good agreement with the experimental data. For configuration 1:1, the largest deviations occurred at rudder angles greater than $\delta = 30°$. At $\delta = 60°$, Y' deviated by approximately 19.5% and N' deviated by approximately 30%. For all other rudder angles, the deviations did not exceed 12%. Moreover, the computed values were within the experimental uncertainty, as indicated by the error bars on the blue dashed line in figure 7.36b. Similar results were obtained for configuration 2:1, as shown in figure 7.37b, where the computed values of Y' and N' agreed well with the experimental values. The largest deviation occurred at $\delta = 60°$, with percentage differences of 27.04% and 19% for Y' and N', respectively. For other rudder angles, the deviations from the experiments were less than 8%. The results for configuration 2:2 were similar, with the largest deviations observed only at the lowest rudder angle of $\delta = 5°$. Specifically, Y' and N' diverged by

approximately 30%, but the absolute difference between the computed and measured Y was less than 1.0 N. However, the tests in shallow water were characterized by large standard deviations, which amounted to more than 20% of the corresponding mean value.

At a water depth ratio of $h/T = 1.5$, the numerically computed values of Y' and N' showed satisfactory agreement with the experimental data. For configuration 1:1, the majority of the investigated rudder angles exhibited a percentage difference between the numerically obtained and measured values of less than 11%. The largest deviation of approximately 15.1% for Y' was observed at the lowest rudder angle of $\delta = 5°$, with an absolute difference between the computed and measured Y value smaller than 0.3 N. N' deviated by approximately 26.5% for the largest rudder angle of $\delta = 60$ °. Nevertheless, all computed Y' and N' values generally fell within the uncertainty interval. For configuration 2:1, the maximum deviation of approximately 31.1% for Y' was observed at a rudder angle of $\delta = 10°$, while the difference was approximately 20% for N' for the same rudder angle. However, for the majority of cases, the percentage difference from the experiments did not exceed 10%. All computed values fell within the experimental uncertainty. Regarding configuration 2:2, some discrepancies in the trend were observed for rudder angles higher than $\delta = 25°$. As shown in figure 7.38c, a larger non-dimensional hydrodynamic lateral force Y' was computed at drift angles of $\delta = 30°$ and $\delta = 45°$, with deviations from the corresponding experimental data of approximately 20.3% and 13.1%, respectively. Nevertheless, the standard deviations of the experimental data were relatively large. Again, all computed values were within the experimental uncertainty.

At the shallowest water depth ratio of $h/T = 1.2$, the flow passing by the different convoys was severely disrupted. In addition to blockage and gap effects, larger rudder deflections caused significant disturbances in the velocity and pressure fields. Generally, simulations of the flow around fish-tail rudder profiles are challenging, as noted by Liu et al. (2016). Consequently, the deviations between the computed Y' and N' values and the experimentally obtained data were larger than those at moderately shallow waters. For configuration 1:1, the largest percentage difference of 30% was observed for a rudder angle of $\delta = 10°$. The maximum deviation for N' was approximately 20.5%, which occurred for the largest rudder angle of $\delta = 60°$. In the case of configuration 2:1, computed values agreed comparatively well with experimental data, as depicted in figure 7.37d. All computed Y' and N' values deviated by a maximum of 14%, and the computed force and moment were within the experimental uncertainty interval. Configuration 2:2 at this water depth presented an additional challenge, compared to configuration 2:1. The numerous gaps, water depth restrictions, and barge arrangement caused several recirculation zones and vortex shedding, resulting in larger deviations for Y' and N'. Nevertheless, all computed values lied within the experimental uncertainty interval. It is however important to note that X' was significantly underestimated at higher rudder deflection angles for all tested configurations.

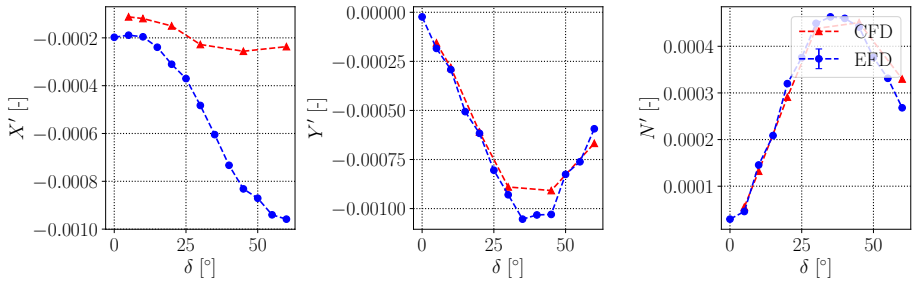

(a) $U = 0.556$ m/s, $h/T = \infty$.

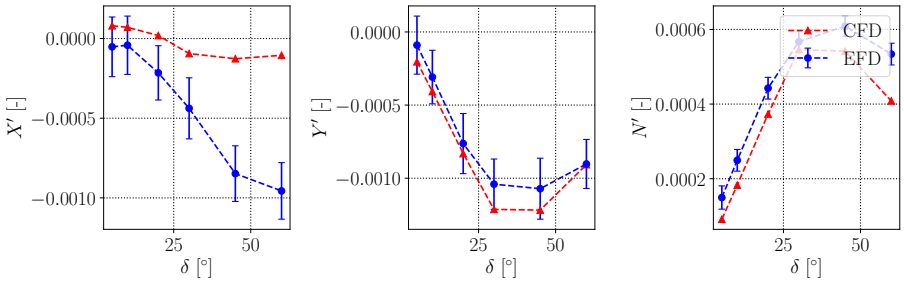

(b) $U = 0.556$ m/s, $h/T = 2.0$.

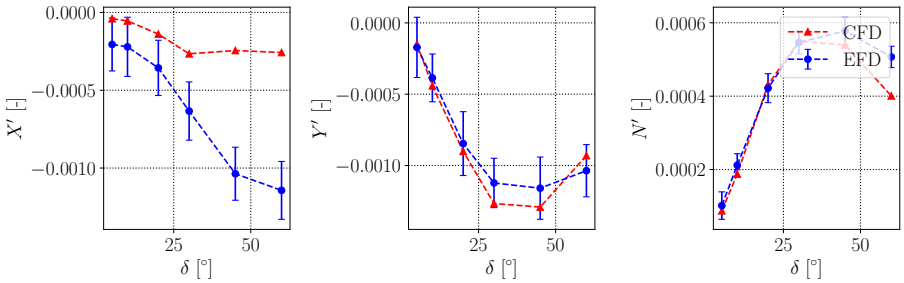

(c) $U = 0.556$ m/s, $h/T = 1.5$.

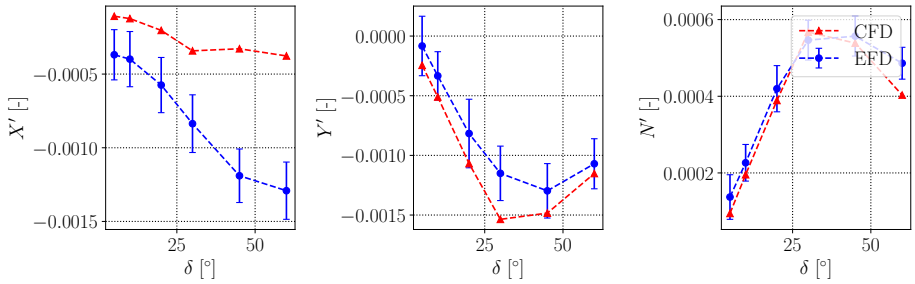

(d) $U = 0.556$ m/s, $h/T = 1.2$.

Figure 7.36: Validation of numerical steady rudder variation tests for configuration 1:1 in deep and shallow water. Deep water experiments were performed at HSVA, shallow water experiments at MARIN.

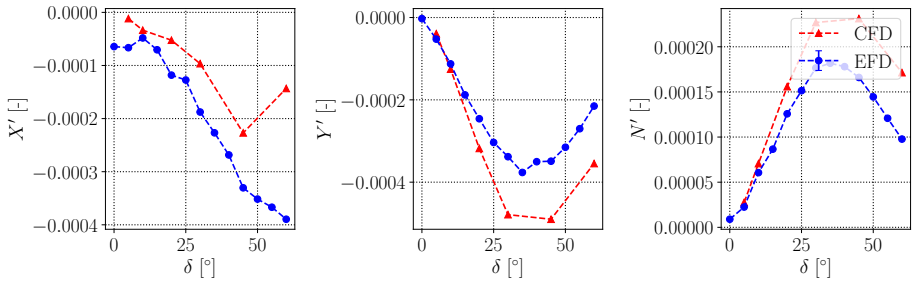

(a) $U = 0.556$ m/s, $h/T = \infty$.

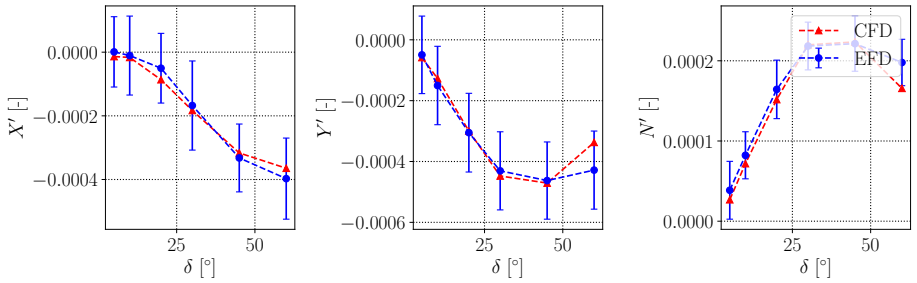

(b) $U = 0.556$ m/s, $h/T = 2$.

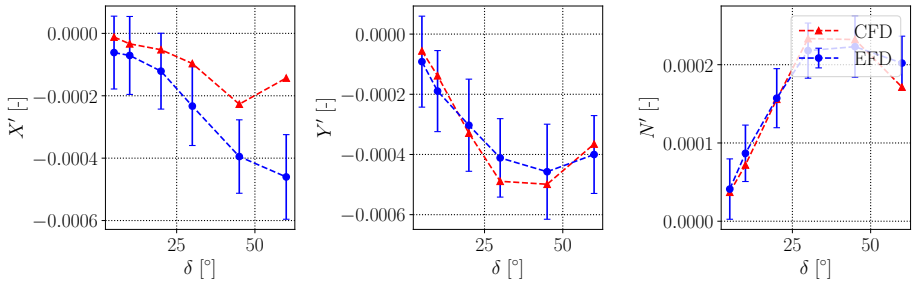

(c) $U = 0.556$ m/s, $h/T = 1.5$.

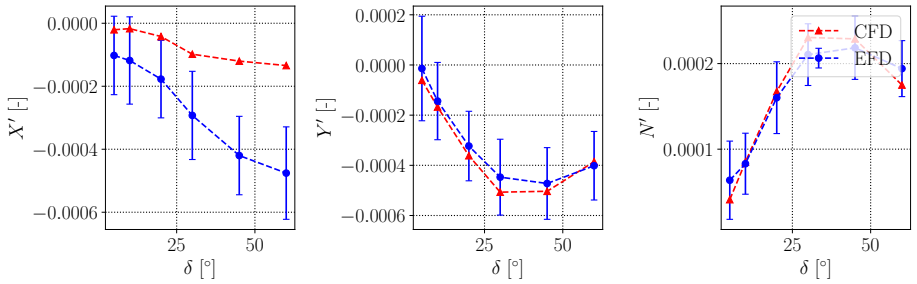

(d) $U = 0.556$ m/s, $h/T = 1.2$.

Figure 7.37: Validation of numerical steady rudder variation tests for configuration 2:1 in deep and shallow water. Deep water experiments were performed at HSVA, shallow water experiments at MARIN.

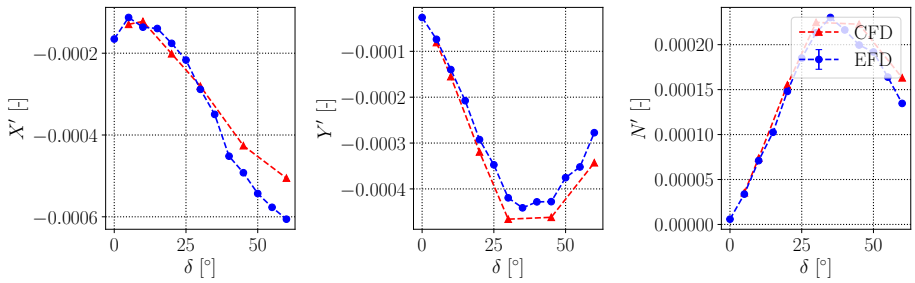

(a) $U = 0.556$ m/s, $h/T = \infty$.

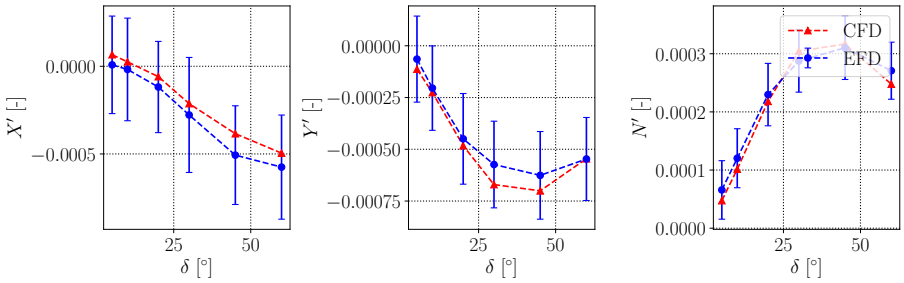

(b) $U = 0.556$ m/s, $h/T = 2$.

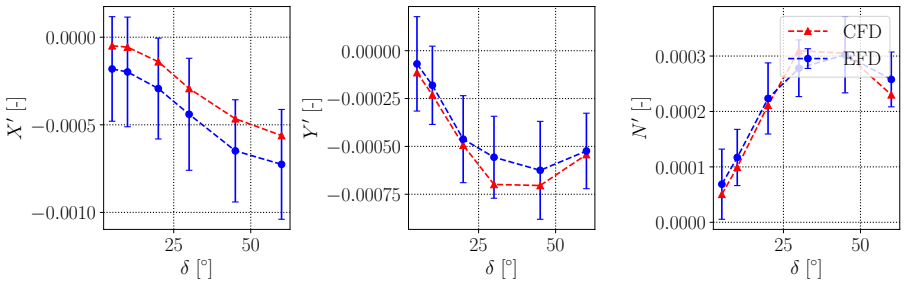

(c) $U = 0.556$ m/s, $h/T = 1.5$.

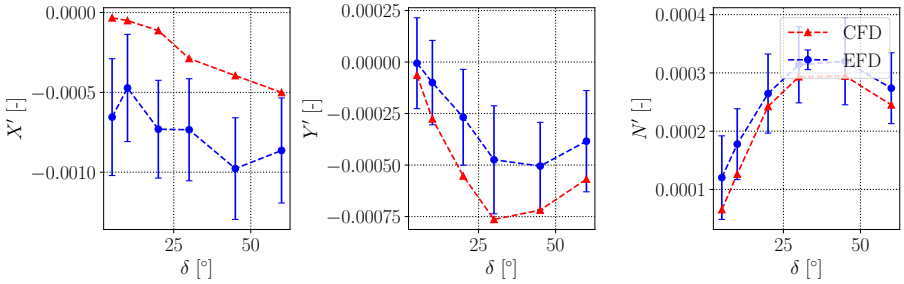

(d) $U = 0.556$ m/s, $h/T = 1.2$.

Figure 7.38: Validation of numerical steady rudder variation tests for configuration 2:2 in deep and shallow water. Deep water experiments were performed at HSVA, shallow water experiments at MARIN.

The pressure distribution on the surface of a rudder is a valuable metric for evaluating the effectiveness of steering devices positioned in the transom region of a pusher boat. Figure 7.39 illustrates the pressure coefficient C_p on the starboard-side rudder surface with a deflection angle of $\delta = 60°$, at varying water depths. C_p is computed as $p/(0.5U^2\rho)$, where p denotes pressure, ρ is water density, and U is the inlet velocity. The pressure and suction side of the rudder are compared, with red areas indicating high pressure zones and blue areas representing lower pressure zones. The pressure distribution reveals a higher pressure zone on the pressure side of the rudder at mid-chord and the base, which aligns with the propeller and rudder configuration. In shallower waters, this high-pressure zone appears to be proportionally larger. Conversely, the pressure distribution on the suction side is consistent across all water depths. Despite these minor variations, the hull forces obtained from the rudder variation tests were similar for all water depths. This similarity in pressure distribution, as seen in figure 7.39, supports this trend.

To provide context for the results obtained in configuration 1:1, figure 7.40 compares the pressure coefficient distribution on the starboard rudder surface at a deflection angle of $\delta = 45°$ and the shallowest water depth of $h/T = 1.2$ for different configurations. Figures 7.40a and 7.40b show this quantity for configuration 1:1, with the suction and pressure side highlighted, while figures 7.40c and 7.40d display the same metrics for configuration 2:1. Lastly, figures 7.40e and 7.40f show the corresponding data for configuration 2:2. The difference in scales between the figures emphasizes the variations in the pressure coefficient distributions between the configurations. As expected, larger high-pressure zones were observed near the chord and the base of the rudder in configuration 2:1, as shown in figure 7.40d. A larger blue area corresponding to lower pressure is clearly visible on the suction side in figure 7.40c. This pressure distribution pattern can be explained by the higher propeller loading needed to maintain this configuration at propulsion point, which results in a higher pressure on the rudder's surface. Conversely, figures 7.40e and 7.40f display smaller high and low-pressure areas for configuration 2:2. This trend can be attributed to the lower propulsive efficiency of configuration 2:2. Despite these differences, the hull forces measured in the experimental tests for both configurations 2:1 and 2:2 were similar, indicating lower rudder performance for configuration 2:2.

Figure 7.41 illustrates the dimensionless velocity magnitude $|\mathbf{u}|/U$ in a plane located at $z = -0.015$ at the transom of the pusher boat with rudders deflected at an angle of $\delta = 45°$. Tangential vectors are displayed on top to indicate the flow direction, while the color scheme varies from blue to green to red, indicating increasing $|\mathbf{u}|/U$ values. Configuration 1:1 is shown in figure 7.41a, configuration 2:1 in figure 7.41b, and configuration 2:2 in figure 7.41c. In all these figures, a red zone was observed in the vicinity of the propellers, which caused higher velocity zones. The rudder deflection caused the propeller stream to split, resulting in a larger recirculation zone behind the rudders. These areas, marked blue in figures 7.41a, 7.41b, and 7.41c, show a significant disturbance in the wake of the pusher boat. Furthermore, the velocity vectors behind the rudders indicated the occurrence of vortex shedding.

The flow induced by the rudder deflection is quite complex, owing to the unique design of the rudders and the constraints imposed by the water depth and barge arrangement. In a study by Liu et al. (2016), it was found that wedge-tailed rudders, also known as fish-tailed rudders, are preferred for ships that are required to perform complex maneuvers in constrained waterways. The study investigated various rudder profiles and compared their performance using a modular maneuvering model developed by Yasukawa and Yoshimura (2015). The authors concluded that wedge-tailed rudders generate comparatively higher lift and allow for faster response times. Additionally, they have a lower aspect ratio than conventional rudders used in sea-going vessels. However, for sea-going vessels, good rudder performance is demonstrated by the course-keeping ability of the vessel. In contrast, inland waterway vessels, including pusher-barge convoys, require enhanced maneuvering performance. Consequently, the rudder stall angles for low aspect ratio wedge-tailed rudders are comparatively higher. The main disadvantage of such rudder profiles are the comparatively larger drag forces and, because of the particular geometrical features, the added complexity when computing rudder-induced forces and moments. Similar conclusions were drawn on the basis of experimental data; see Molland and Turnock (2007).

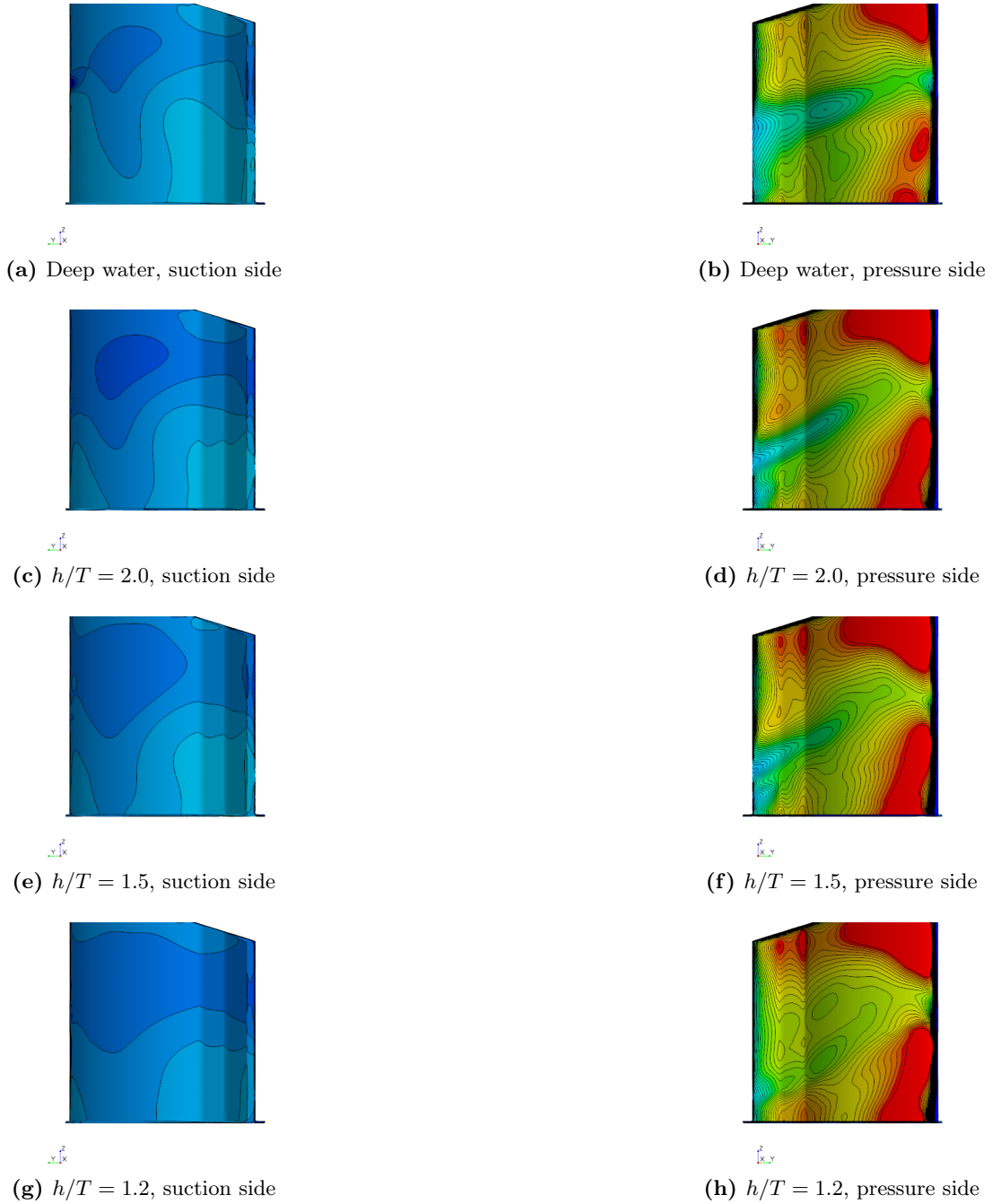

(a) Deep water, suction side

(b) Deep water, pressure side

(c) $h/T = 2.0$, suction side

(d) $h/T = 2.0$, pressure side

(e) $h/T = 1.5$, suction side

(f) $h/T = 1.5$, pressure side

(g) $h/T = 1.2$, suction side

(h) $h/T = 1.2$, pressure side

Figure 7.39: Instantaneous pressure coefficient C_p on rudder surface at a deflection angle of $\delta = 45°$ at different water depths for configuration 1:1.

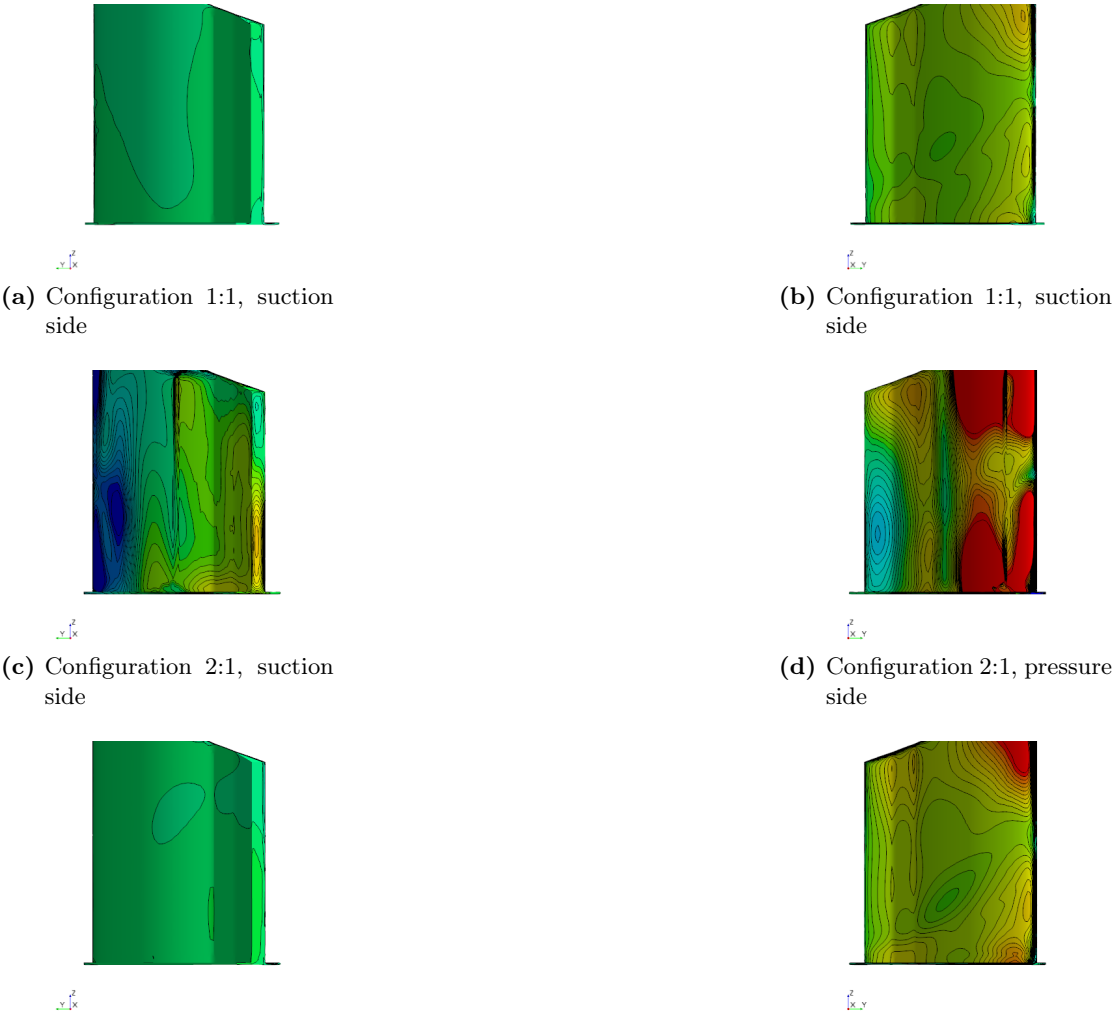

(a) Configuration 1:1, suction side

(b) Configuration 1:1, suction side

(c) Configuration 2:1, suction side

(d) Configuration 2:1, pressure side

(e) Configuration 2:2, suction side

(f) Configuration 2:2, pressure side

Figure 7.40: Instantaneous pressure coefficient C_p on rudder surface at a deflection angle of $\delta = 45°$ and $h/T = 1.2$ for configuration 1:1, 2:1 and 2:2.

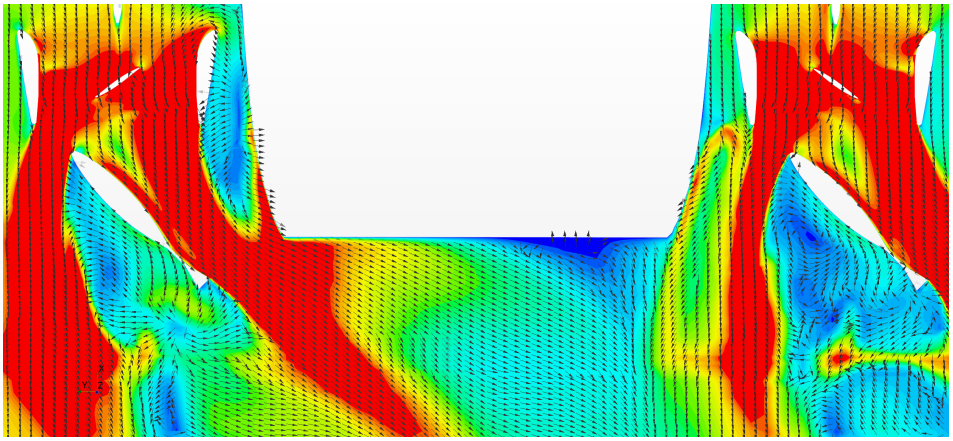

(a) Configuration 1:1

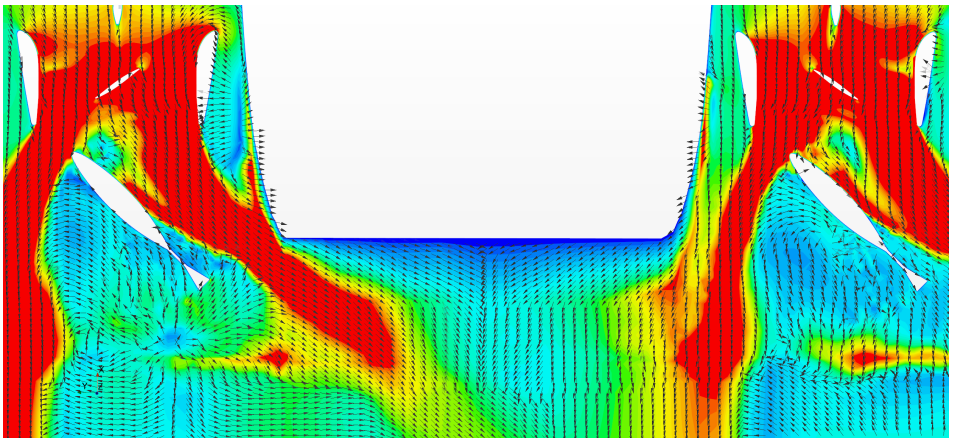

(b) Configuration 2:1

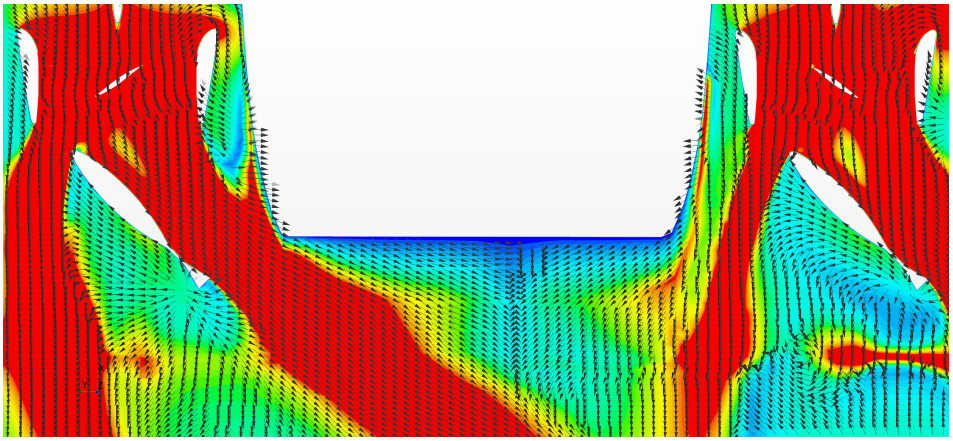

(c) Configuration 2:2

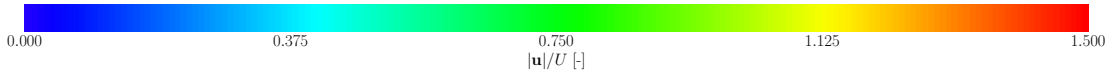

Figure 7.41: Instantaneous $|\mathbf{u}|/U$ distribution on z-plane at rudder half height for configuration 1:1, 2:1 and 2:2 at $\delta = 45°$, $U = 0.556$ m/s and $h/T = 1.2$.

7.3 Concluding remarks

Hydrodynamic forces and moments acting on pusher-barge convoys were analyzed through steady drift and steady rudder variation tests. The experiments were conducted at varying water depths, ranging from deep to extremely shallow waters. In steady drift conditions, the depth restriction effect resulted in a significant surge in overall longitudinal hydrodynamic force X, overall hydrodynamic lateral force Y, and overall yaw moment N. This trend was most pronounced at the highest drift angle of $\beta = 16°$. During steady rudder variation tests, the differences in measured hydrodynamic forces and moments between deep and shallow waters were less apparent than in the steady drift tests. Rudder-induced hydrodynamic forces and moments were more sensitive to variations in propeller revolution rate and propeller inflow, rather than water depth restrictions. Due to its smaller draft compared to the barges, the pusher always operated in moderately shallow water.

The numerical simulations revealed that the hydrodynamic forces resulting from steady drift simulations in deep and shallow waters showed a satisfactory agreement with experimental results for lateral force Y' and yaw moment N'. However, some deviations were noticed for total longitudinal force X' depending on drift angle, h/T ratio, and barge arrangement. These deviations can be attributed to the increased uncertainty associated with water depth restriction, poor geometrical optimization of the barges, and complex propeller-hull interactions. The double-body setup used in the simulations, which omitted the free surface and the floating body motions, may also have contributed to the underprediction of certain quantities. Moreover, the presence of massive vortex shedding around all configurations, especially for larger drift angles, often engulfed the pusher, leading to higher uncertainty for propulsion forces.

On the other hand, total lateral force Y' and yaw moment N' were predicted with great accuracy since these forces and moments were more pressure-dependent. Additionally, the major contribution to overall lateral force Y' occurred around the bow area, where trailing vortices were not fully developed, and pressure and velocity fields were not fully altered by turbulent structures.

Numerical rudder variation tests showed good agreement with measured overall lateral force Y and overall yaw moment N. However, depending on the rudder angle and the convoy configuration, total longitudinal hydrodynamic force X was underpredicted, especially for larger rudder angles. An accurate representation of the flow passing by steering and propulsive devices was essential for predicting the hydrodynamic forces induced by rudder deflection in steady rudder variation tests.

Around the considered pusher-barge convoys, the stern region of the pusher was subject to flow disturbances induced by the particular geometry of the pusher, the influence of the gap on the propeller inflow plane, as well as the water depth restriction. A correct

representation of the flow field may have required more complex turbulence models and optical method for appropriate validation.

8 Conclusion

8.1 Summary

This work presented a comprehensive investigation of hydrodynamic forces and moments acting on pusher-barge convoys in deep and shallow waters. Experimental and numerical aspects were covered, with an emphasis on validation of hydrodynamic loads in deep and shallow water. Particular attention was given to the flow in a gap between pusher and barge. The experiments consisted of a thorough investigation of steady maneuvering forces of three representative pusher barge combinations, by means of captive tests such as resistance and propulsion tests, steady drift tests and steady rudder variation tests. Furthermore, the flow in the gap was measured for one configuration by means of PIV and LDV measurement techniques. The experimental data were used to validate a numerical procedure based on the RANS equations. In select cases, the flow was resolved using different turbulence approaches, including two-equations models and the IDDES technique. Generally, the numerically obtained forces and moments agreed favorably with the experiments. The numerical investigation allowed to highlight the complexity of the flow surrounding multi-body vessels in shallow waters, and the impact thereof on the hydrodynamic performance of such multibody ships.

Drawing upon the need for maneuvering mathematical models adapted to inland waterways vessels sailing in shallow waters, this thesis made a decisive contributions towards a better understanding of the hydrodynamic mechanisms governing the flows passing by maneuvering pusher-barge vessels in deep and shallow waters. The next sections present a detailed summary of this thesis, highlighting the main findings, the author's contribution as well as suggestion for future work.

8.2 Main findings

The key research questions that motivated this study were to quantify the hydrodynamic forces and moments acting on pusher-barge convoys and investigate the impact of water depth restriction on these forces, and hence, on the overall hydrodynamic performance of pusher-barge convoys. This thesis had two objectives: first, to conduct captive maneuvering tests to quantify hydrodynamic forces and moments acting on pusher-barge convoys in different configurations in both deep and shallow waters; second, to validate a

numerical procedure based on the RANS equations that could provide a robust and reliable virtual captive test environment to gain detailed insights into the flow surrounding multi-body vessels.

An Abkowitz-type maneuvering mathematical model constituted the starting point of this work. Indeed, captive maneuvering tests, intended originally for the derivation of maneuvering coefficients, offer a useful method to analyze the flow around a vessel in quasi steady condition under the systematic variation of relevant kinematic parameters. In chapter 2, the model's derivation and theoretical considerations for its application in deep and shallow waters were briefly discussed. Relevant captive tests were then used to obtain the test matrix. In chapter 3 the numerical techniques needed to replicate captive tests virtually were presented, including the Navier-Stokes equations, turbulence modeling, and the VoF method. Discretization methods, solution algorithms, and error quantification procedures were also described and discussed, with the discretization error estimated throughout the work using the procedures of el Moctar et al. (2021) and Oberhagemann (2017).

In Chapter 4, the test cases and experimental campaigns conducted in deep and shallow waters were detailed. The pusher-barge convoy configurations investigated in this work consisted of a typical pusher-boat with two fish-tail rudders and two ducted propellers arranged in a tunnel located inside the aft part of the pusher, necessary for operating in shallow waters. The barges used were typical Europe II Type-b barges, non-motorized vessels often coupled with pusher-boats or monohulls and mainly operating on the Rhine and Danube rivers. Three main configurations were considered: Configuration 1:1 with one barge stern bow coupled with the pusher-boat; Configuration 2:1 with two barges coupled stern to stern and the rear barge coupled bow to bow with the pusher boat; and Configuration 2:2 with four barges coupled stern to stern, while the two rear barges were coupled bow to bow with the pusher boat. The deep water captive tests were performed at HSVA in Hamburg, Germany, while shallow water tests were conducted at MARIN in Wageningen, the Netherlands. Both experimental campaigns consisted of resistance and propulsion tests, steady drift tests, and steady rudder variation tests. In deep waters, steady drift and rudder tests were conducted by varying relevant parameters, such as drift angle or rudder angle, during one run. In shallow waters, due to the low UKC associated with the investigated h/T ratios, experimental uncertainties were more pronounced, and multiple runs were necessary to cover one set of parameters. Repeatability studies were performed to quantify experimental uncertainties. A total of four representative h/T ratios were considered: $h/T = 18.14$ in deep water, restricted by the HSVA Basin depth, and h/T ratios of 2.0, 1.5, and 1.2 in shallow waters.

Chapter 5 provides a detailed analysis of resistance and propulsion using both experimental and numerical methods. Resistance tests were conducted on bare hull models with only rudders attached. In deep water, the target velocity U was varied successively in one single run. In shallow waters, a single run was performed for each velocity and configuration. Propulsion tests were carried out using the British method in deep

water, measuring residual force, propeller thrust, and propeller torque. Self-propulsion points were determined using linear interpolation. In shallow water, added resistance was measured while maintaining the deep water propeller revolution rate. Although the individual barges in the convoy configurations were identical, their arrangement significantly affected overall transport efficiency, which was represented by the power required to move one unit of payload. Configuration 2:2 had the lowest efficiency, while configuration 2:1 was most efficient in moderately deep and shallow waters. Numerical simulations of resistance tests in deep and shallow waters were performed using RANSE-based computations. The VoF method accounted for free surface effects, and the models were constrained and adjusted to their floating position prior to the meshing process. The numerically predicted resistances were found to be in good agreement with the experimentally measured resistances. Barge arrangements and shallow water effects on shear stresses and free surface elevation were also assessed. The method proved to be reliable for deep to moderately shallow waters. However, in extremely shallow waters, the flow requires special attention regarding turbulence modeling.

Chapter 6 presents an investigation of the flow in the gap between a pusher and a barge in configuration 1:1. The study utilized PIV and LDV techniques to obtain optical measurements of the flow in the gap for two water depths with ratios of $h/T = 13.04$ and $h/T = 2.14$. The experiments revealed the existence of three distinct regions, namely, a free stream region beneath the barge, a recirculation zone between the pusher and barge, and a separation region near the pusher's half-length, where a separation bubble reattached itself. Numerical simulations were also conducted using the RANS technique with different turbulence models, namely $k - \varepsilon$ and $k - \omega - \mathrm{SST}$, as well as the hybrid scale-resolving IDDES method. The numerical results were compared with experimental data of mean streamwise velocity profiles in the gap area. Overall, a satisfactory agreement between numerical and experimental data was reached. Furthermore, it was concluded that the IDDES method provided more accurate predictions in both the gap and transition regions. However, in shallow waters, larger discrepancies between numerical and experimental results were observed at the barge's transom and in the transition region. To further assess the effect of extreme water depth restriction on the gap flow and convoy's resistance, additional numerical simulations using the IDDES technique were performed. The investigations were carried out for water depth to draft ratios of 2.14, 1.5, and 1.2, corresponding to moderately shallow to extremely shallow water. As water depth decreased, the recirculation region extended alongside the pusher's hull, delaying flow reattachment. Additionally, the velocity of the free-stream region decreased, with the lowest values observed in $h/T = 1.2$. The analysis of the flow passing by a modified model covering the gap in shallow waters at $h/T = 1.2$ yielded a reduced resistance of approximately 6.5%, demonstrating the impact of the gap on resistance in shallow waters.

Chapter 7 offers a detailed experimental and numerical investigation of hydrodynamic forces and moments acting on pusher convoys in deep and shallow waters by means of steady drift and steady rudder variation tests. During one run in deep water at a design

velocity U, four different drift angles were investigated. In shallow water, hydrodynamic forces and moments were measured with one single drift angle in each run. All tests were performed with appended models at a predetermined propulsion point, measuring the overall longitudinal force X, lateral force Y, and yaw moment N acting on the convoy's hull. Under steady drift conditions, the impact of shallow water on Y and N was substantial, with an increase of up to 650% for Y and 450% for N, compared to deep water values. Additionally, at the smallest h/T of 1.2, the overall longitudinal force X turned positive at higher drift angles for configurations 1:1 and 2:1. Numerical computations using a double-body RANSE setup replicated the drift tests with favorable comparison of the numerically obtained thrust values to the measured thrust values in deep water. The free surface was not accounted for in steady drift computations; however, sinkage and trim were considered by adjusting the convoy's floating position prior to the meshing process. Generally, in deep and shallow waters, computed values of X, Y, and N agreed well with experimental results. However, the prediction of the overall longitudinal force X proved more challenging as it was more sensitive to propeller inflow condition, gap effects, restricted water effects and turbulence modeling. Velocity vectors and contours alongside the convoy's hull under drift conditions revealed early flow separation, large vortex shedding, and recirculation zones. Steady rudder variation tests were performed with appended models at their propulsion point and zero drift angle. The rudder angle δ was varied successively in one run in deep water, while two single rudder angles were investigated in one run in shallow water. The latter method proved to be more effective, as strong memory effects affected the force measurements in deep water. The rudder deflection induced hydrodynamic forces X, Y, and N acting on the convoy's hull depended strongly on the propeller's rotation rate and the convoy's barge arrangement rather than on the water depth restriction. The steady rudder variation tests were numerically replicated using RANSE. The numerical setup was identical to the steady drift computations. Generally, the computed overall lateral force Y and yaw moment N agreed favorably to experimentally obtained values. However, the overall longitudinal force X was more challenging to compute due to sensitivity to propeller inflow conditions, gap effects, water depth restriction and turbulence modeling. Furthermore, due to the complex interaction between hull, rudders, ducts and propellers, the flow was characterized by larger recirculation zones in the wake of the pusher, strongly affecting the numerical prediction.

The main findings of this thesis, which align with the research questions outlined in chapter 1, can be summarized as follows:

- The experimental captive tests proved to be accurate in quantifying hydrodynamic forces and moments acting on pusher-barge convoys in deep and shallow waters. The resulting measurements of motions, forces, and moments delivered valuable validation data. In certain tests, such as steady drift and steady rudder variation tests, it was found that investigating a single parameter variation per run was preferable due to the memory effect, which affected certain results. Furthermore, in extremely shallow waters, repetitions were necessary to quantify the experimental

uncertainty, as water depth restrictions significantly impacted the force measurements.

- Throughout this work, around 160 simulations were conducted. In general, the numerical results obtained using a RANSE setup with a $k-\omega-$SST turbulence model showed good agreement with experimental data. This was particularly true for predicting pressure-dominated forces, such as lateral hydrodynamic force and yaw moment. However, due to the complex nature of the flow in extremely shallow waters and the interaction between the floating bodies and the waterway, accurately predicting the hydrodynamic longitudinal force acting on the convoys' hull proved to be challenging in certain cases.

- The use of optical flow measurement methods in a novel experimental procedure revealed the complexity of the flow in the gap between the pusher and barge, which negatively impacted the convoy's overall hydrodynamic efficiency, specially in shallow waters. These measurements were valuable for quantitatively assessing the flow surrounding configuration 1:1. In addition, the numerical procedure based on the IDDES technique was found to be the most accurate in capturing the highly complex flow phenomena occurring in the gap. This hybrid scale-resolving technique also predicted comparatively higher resistances than RANSE based methods.

- The experimental and numerical analyses presented in this thesis lead to the conclusion that water depth restrictions had a major impact on all aspects relevant to the navigation of pusher-barge convoys. Firstly, a smaller UKC resulted in a drastic increase in resistance for all tested configurations, negatively affecting propulsive efficiency and leading to a diminished transport efficiency in shallow waters. Secondly, hydrodynamic forces and moments acting on a pusher-barge convoy in quasi steady maneuvering condition were comparatively much higher in shallow waters. Moreover, due to the poor hydrodynamic shape optimization of the barges, early flow separations and large recirculation zones characterized the flow around pushed-convoys in such conditions. Lastly, in shallow waters, the gap between floating bodies had a more pronounced negative effect on the hydrodynamic performance of such multibody vessels.

8.3 Suggestion for future works

In the light of recent extreme weather events, inland waterway vessels are likely to navigate in extreme shallow waters for extended periods of time. Therefore, it is of primary interest to prioritize navigational safety related issues, especially from a policy making standpoint. Thus, research towards the prediction of pushed convoys trajectories using improved maneuvering mathematical models is expected to draw attention. Hence, it is

suggested to articulate future research around the development of mathematical modeling of shallow water maneuvering forces acting on such vessels.

From an experimental point of view, quantification of hydrodynamic forces and moments acting on pushed convoys should not be limited to the measurement of overall mean forces and moments, but complemented with optical measurements of the flow surrounding floating bodies. By these means, hydrodynamic interactions between rudders, propellers, hulls, and waterway restrictions should be further investigated.

From a computational standpoint, the use of hybrid RANS/LES methods should be extended to predict hydrodynamic forces and moments in maneuvering conditions, especially in extreme shallow waters. Using such hybrid numerical methods, the gap-flow effect on the hydrodynamic performance of pushed convoys should be further investigated, using a fully appended model in quasi steady maneuvering condition.

Bibliography

[1] Abkowitz, M. Lectures on ship hydrodynamics - steering and manoeuvrability. Technical report, Hydro- og aerodynamisk laboratorium, Lyngby, Denmark, 1964.

[2] Aram, S. and Mucha, P. Computational fluid dynamics analysis of different propeller models for a ship maneuvering in calm water. *Ocean Engineering*, 276:114226, 2023. ISSN 0029-8018. doi: 10.1016/j.oceaneng.2023.114226.

[3] Arslan, T., Pettersen, B., and Andersson, H. I. Investigation of the flow around two interacting ship-like sections. *Journal of Fluids Engineering*, 137, 4 2015. doi: 10.1115/1.4028876.

[4] Arslan, T., Pettersen, B., and Andersson, H. I. Large-eddy simulation of cross-flow around ship sections. *Journal of Marine Science and Technology (Japan)*, 21: 552–566, 9 2016. ISSN 09484280. doi: 10.1007/s00773-015-0366-6.

[5] Bechthold, J. and Kastens, M. Robustness and quality of squat predictions in extreme shallow water conditions based on RANS-calculations. *Ocean Engineering*, 197, 2 2020. doi: 10.1016/j.oceaneng.2019.106780.

[6] Bertram, V. *Practical Ship Hydrodynamics*. Butterworth-Heinemann, 2012. ISBN 978-0-08-097150-6. doi: 10.1016/B978-0-08-097150-6.10008-9.

[7] Boussinesq, J. *Essai sur la théorie des eaux courantes* -. Imprimerie nationale, Paris, 1877.

[8] Brix, J. *Manoeuvring Technical Manual*. Seehafen-Verlag, 1993. ISBN 9783877439029.

[9] Bundesverband der Deutschen Binnenschifffahrt e.V. Daten und Fakten 2021/2022, 2022. https://www.binnenschiff.de/wp-content/uploads/2022/11/Daten-Fakten_2021-22_Ansicht-002.pdf, Last accessed on 20/02/2023.

[10] Carrica, P. M., Mofidi, A., Eloot, K., and Delefortrie, G. Direct simulation and experimental study of zigzag maneuver of KCS in shallow water. *Ocean Engineering*, 112, 1 2016. doi: 10.1016/j.oceaneng.2015.12.008.

[11] Chen, L., Asai, K., Nonomura, T., Xi, G., and Liu, T. A review of Backward-Facing Step (BFS) flow mechanisms, heat transfer and control. *Thermal Science*

and Engineering Progress, 6:194–216, 6 2018. doi: 10.1016/j.tsep.2018.04.004.

[12] Chillcce, G. and el Moctar, O. Viscous effects on squat. *Applied Ocean Research*, 125:103252, 2022. doi: 10.1016/j.apor.2022.103252.

[13] Cura-Hochbaum, A. Virtual PMM Tests for Manoeuvring Prediction. In *Proceedings of the 26th ONR Symposium on Naval Hydrodynamics, Rome, Italy, 17-22 September 2006*, 2006.

[14] Delefortrie, G., Villagomez, J., and Verwilligen, J. Maneuvring Behavior of Push Convoys in Different Barge Configurations. *Journal of Ship Research*, 66(03):231–249, 09 2022. doi: 10.5957/JOSR.1220005.

[15] Du, P., Ouahsine, A., Sergent, P., and Hu, H. Resistance and wave characterizations of inland vessels in the fully-confined waterway. *Ocean Engineering*, 210(July 2019): 107580, 2020. doi: 10.1016/j.oceaneng.2020.107580.

[16] Durasevic, S., Gatin, I., Uroic, T., and Jasak, H. Numerical analysis of self-propulsion flow characteristics in model scale. *Ocean Engineering*, 259:111885, 07 2022. doi: 10.1007/s00773-013-0221-6.

[17] el Moctar, B. O., Schellin, T. E., and Söding, H. *Numerical Methods for Seakeeping Problems*. Springer International Publishing, 2021. ISBN 978-3-030-62560-3. doi: 10.1007/978-3-030-62561-0.

[18] el Moctar, O. M. *Numerische Berechnung von Strömungskräften beim Manövrieren von Schiffen*. PhD thesis, Technische Universität Hamburg-Harburg, Hamburg, 2001.

[19] el Moctar, O., Lantermann, U., Mucha, P., Höpken, J., and Schellin, T. E. RANS-Based Simulated Ship Maneuvering Accounting for Hull-Propulsor-Engine Interaction. *Ship Technology Research*, 61, 8 2014. doi: 10.1179/str.2014.61.3.003.

[20] Eloot, K. *Selection, experimental determination and evaluation of a mathematical model for ship manoeuvring in shallow water*. PhD thesis, Ghent University, Ghent, 2006.

[21] Eloot, K., Delefortrie, G., Vantorre, M., and Quadvlieg, F. Validation of Ship Manoeuvring in Shallow Water Through Free-Running Tests. In *Proceeding of the ASME 2015 34th International Conference on Ocean, Offshore and Arctic Engineering, St John's, Newfoundland, Canada. May 31 – June 5, 2015*, 05 2015. doi: 10.1115/OMAE2015-41912.

[22] Eça, L. and Hoekstra, M. Evaluation of numerical error estimation based on grid refinement studies with the method of the manufactured solutions. *Computers & Fluids*, 38(8):1580–1591, 2009. doi: 10.1016/j.compfluid.2009.01.003.

[23] Feder, D.-F., Shevchuk, I., Sahab, A., and Abdel-Maksoud, M. Characteristics and consequences of vortex wandering around a ship hull at drift: a numerical study. *Ocean Engineering*, 255:111220, 05 2022. doi: 10.1007/s00773-013-0221-6.

[24] Ferziger, J. H., Perić, M., and Street, R. L. *Computational Methods for Fluid Dynamics*. Springer, Berlin / Heidelberg, 2019. ISBN 978-3-319-99693-6.

[25] Fossen, T. I. *Handbook of marine craft hydrodynamics and motion control*. Wiley-Blackwell, Hoboken, NJ, 2nd edition, 2021. ISBN 978-1-119-57505-4.

[26] Friedhoff, B., Hoyer, K., List, S., and Tenzer, M. Investigation of the nominal and effective propeller inflow for a family of inland waterway vessels. *Ocean Engineering*, 187, 9 2019. doi: 10.1016/j.oceaneng.2019.106180.

[27] Furukawa, Y., Ibaragi, H., Nakiri, Y., and Kijima, K. Shallow Water Effects on Longitudinal Components of Hydrodynamic Derivatives. In *Proceedings of 4th International Conference on Ship Manoeuvring in Shallow and Confined Water (MASHCON), 23-25 May 2016, Hamburg, Germany*, pages 295–303, 2016. doi: 10.18451/978-3-939230-38-0_33.

[28] Germano, M., Piomelli, U., Moin, P., and Cabot, W. A dynamic subgrid-scale eddy viscosity model. *Physics of Fluids A*, 3:1760–1765, 1991. doi: 10.1063/1.857955.

[29] Grassi, A. G. F., Lavieri, R. S., Pereira, A. A. P., and Tannuri, E. A. CFD and Experimental Analysis of Current Forces of Pusher-Barge Systems. In *Proceedings of the 32nd International Conference on Ocean, Offshore and Arctic Engineering, June 9-14 2013, Nantes, France*, 2013. doi: 10.1115/omae2013-10404.

[30] Gritskevich, M. S., Garbaruk, A. V., Schütze, J., and Menter, F. R. Development of DDES and IDDES formulations for the $k-\omega$ shear stress transport model. *Flow, Turbulence and Combustion*, 88(3):431–449, 2012. doi: 10.1007/s10494-011-9378-4.

[31] Gronarz, A. *Rechnerische Simulation der Schiffsbewegung beim Manövrieren unter besonderer Berücksichtigung der Abhängigkeit von der Wassertiefe*. PhD thesis, Gerhard-Mercator-Universität - Gesamthochschule Duisburg, Duisburg, 1997.

[32] Guesnet, T. Entwurf und Modellkonstruktion für einen Schubverband. Technical Report 2213, Development Centre for Ship Technology and Transport Systems DST e.V., Duisburg, 2017.

[33] Guilmineau, E., Deng, G. B., Queutey, P., and Visonneau, M. Assessment of hybrid LES formulations for flow simulation around the ahmed body. *Notes on Numerical Fluid Mechanics and Multidisciplinary Design*, 135:171–176, 2018. doi: 10.1007/978-3-319-60387-2-18.

[34] Hadzic, I. *Second-Moment Closure Modelling of Transitional and Unsteady Turbulent Flows*. PhD thesis, Delft University of Technology, Delft, 1999.

[35] Jones, W. and Launder, B. The prediction of laminarization with a two-equation model of turbulence. *International Journal of Heat and Mass Transfer*, 15(2):301–314, 1972. ISSN 0017-9310. doi: 10.1016/0017-9310(72)90076-2.

[36] Kim, D., Tezdogan, T., and Incecik, A. Hydrodynamic analysis of ship manoeuvrability in shallow water using high-fidelity URANS computations. *Applied Ocean Research*, 123, 04 2022. doi: 10.1016/j.apor.2022.103176.

[37] King, K. K., Yasukawa, H., Hirata, N., and Kose, K. Maneuvering simulations of pusher-barge systems. *Journal of Marine Science and Technology*, 13:117–126, 2008. ISSN 09484280. doi: 10.1007/s00773-007-0267-4.

[38] Lackenby, H. The effect of shallow water on ship speed. *Shipbuilder and Marine Engine Builder*, pages 446–450, 1963.

[39] Larsson, L., Stern, F., Visonneau, e. L., Michel", Oñate, E., García-Espinosa, J., Kvamsdal, T., and Bergan, P. *CFD in Ship Hydrodynamics—Results of the Gothenburg 2010 Workshop*, pages 237–259. Springer Netherlands, 2013. ISBN 978-94-007-6143-8. doi: 10.1007/978-94-007-6143-8_14.

[40] Larsson, L., Stern, F., and Visonneau, M. *Numerical Ship Hydrodynamics - An assessment of the Gothenburg 2010 Workshop*. Springer Nature, 2014. ISBN 978-94-007-7188-8.

[41] Launder, B. and Sharma, B. Application of the energy-dissipation model of turbulence to the calculation of flow near a spinning disc. *Letters in Heat and Mass Transfer*, 1(2):131–137, 1974. doi: 10.1016/0094-4548(74)90150-7.

[42] Liefvendahl, M. and Fureby, C. Grid requirements for LES of ship hydrodynamics in model and full scale. *Ocean Engineering*, 143:259–268, 2017. ISSN 0029-8018. doi: 10.1016/j.oceaneng.2017.07.055.

[43] Liu, J. *Impacts of Rudder Configurations on Inland Vessel Manoeuvrability*. PhD thesis, TU Delft, Delft, 2017.

[44] Liu, J., Quadvlieg, F., and Hekkenberg, R. Impacts of the rudder profile on manoeuvring performance of ships. *Ocean Engineering*, 124:226–240, 08 2016. doi: 10.1016/j.oceaneng.2016.07.064.

[45] Maimun, A., Priyanto, A., Muhammad, A. H., Scully, C. C., and Awal, Z. I. Manoeuvring prediction of pusher barge in deep and shallow water. *Ocean Engineering*, 38:1291–1299, 2011. ISSN 00298018. doi: 10.1016/j.oceaneng.2011.05.011.

[46] Menter, F. R. Two-equation eddy-viscosity turbulence models for engineering applications. *AIAA Journal*, 32:1598–1605, 1994. doi: 10.2514/3.12149.

[47] Menter, F. R. and Kuntz, M. Adaptation of eddy-viscosity turbulence models to unsteady separated flow behind vehicles. In McCallen, R., Browand, F., and Ross, J., editors, *The Aerodynamics of Heavy Vehicles: Trucks, Buses, and Trains*, pages 339–352, Berlin / Heidelberg, 2004. Springer Berlin Heidelberg. ISBN 978-3-540-44419-0.

[48] Mewes, S. *Numerical Prediction of Hydrodynamic Damping and Loads on a Floating Offshore Wind Turbine*. PhD thesis, Universität Duisburg-Essen, Duisburg, 2021.

[49] Millward, A. The effect of water depth on hull form factor. *Int. Shipbuilding Progress*, 36:283–302, 1999.

[50] Molland, A. and Turnock, S. *Marine Rudders and Control Surfaces*. Butterworth-Heinemann, 2007. doi: 10.1016/B978-0-7506-6944-3.X5000-8.

[51] Mucha, P. *On Simulation-based Ship Maneuvering Prediction in Deep and Shallow Water*. PhD thesis, Universität Duisburg-Essen, Duisburg, 2017.

[52] Mucha, P., Deng, G., Gourlay, T., and el Moctar, O. Validation studies on numerical prediction of ship squat and resistance in shallow water. In *Proceedings of 4th International Conference on Ship Manoeuvring in Shallow and Confined Water (MASHCON), 23-25 May 2016, Hamburg, Germany*, 2016. doi: 10.18451/978-3-939230-38-0_33.

[53] Mucha, P., el Moctar, O., Dettmann, T., and Tenzer, M. Inland waterway ship test case for resistance and propulsion prediction in shallow water. *Ship Technology Research*, 64(2):106–113, 2017. doi: 10.1080/09377255.2017.1349723.

[54] Mucha, P., el Moctar, O., Dettmann, T., and Tenzer, M. An experimental study on the effect of confined water on resistance and propulsion of an inland waterway ship. *Ocean Engineering*, 167:11–22, 2018. doi: 10.1016/j.oceaneng.2018.08.009.

[55] Mucha, P., Dettmann, T., Ferrari, V., and el Moctar, O. Experimental investigation of free-running ship manoeuvers under extreme shallow water conditions. *Applied Ocean Research*, 83(11-22):155–162, 2019. doi: 10.1016/j.apor.2018.09.008.

[56] Muzaferija, S. and Perić, M. Computation of free-surface flows using the finite-volume method and moving grids. *Numerical Heat Transfer, Part B: Fundamentals*, 32:369–384, 1997. doi: 10.1080/10407799708915014.

[57] Nadge, P. M. and Govardhan, R. N. High Reynolds number flow over a backward-facing step: structure of the mean separation bubble. *Experiments in Fluids*, 55: 1657, 1 2014. doi: 10.1007/s00348-013-1657-5.

[58] Norrbin, N. H. Theory and observations on the use of a mathematical model for ship manoeuvering in deep and confined waters. Technical report, Publications of the swedish state shipbuilding experimental tank, 1971.

[59] Oberhagemann, J. *On Prediction of Wave-Induced Loads and Vibration of Ship Structures with Finite Volume Fluid Dynamic Methods*. PhD thesis, University of Duisburg-Essen, Duisburg, 2017.

[60] Oltmann, P. and Sharma, S. D. Simulation of combined engine and rudder maneuvers using an improved model of hull-propeller-rudder interactions. *Schriftenreihe Schiffbau*, 20, 1984. doi: 10.15480/882.929.

[61] Oud, G. and Bedos, A. CFD investigation of the effect of water depth on manoeuvring forces on inland ships. *Journal of Ocean Engineering and Marine Energy*, 8, 2022. doi: 10.1007/s40722-022-00253-y.

[62] Patankar, S. V. *Numerical heat transfer and fluid flow*. Series on Computational Methods in Mechanics and Thermal Science. Hemisphere Publishing Corporation (CRC Press, Taylor & Francis Group), 1980. ISBN 978-0891165224.

[63] Pereira, F. S., Eça, L., Vaz, G., and Girimaji, S. S. Toward Predictive RANS and SRS Computations of Turbulent External Flows of Practical Interest. *Archives of Computational Methods in Engineering*, 28:3953–4029, 8 2021. doi: 10.1007/s11831-021-09563-0.

[64] Pompée, P.-J. About modelling inland vessels resistance and propulsion and interaction vessel - waterway, key parameters driving restricted/shallow water effects. In *Proceedings of the PIANC SMART RIVERS Conference, 7-11 September 2015, Buenos Aires, Argentina*, 2015.

[65] Pope, S. B. *Turbulent Flows*. Cambridge University Press, 2000. doi: 10.1017/CBO9780511840531.

[66] Quadvlieg, F., Willemsen, C., and de Boer, W. Manoeuvring simulation models for inland ships. In *Proceedings of the 5th International Conference on Ship Manoeuvring in Shallow and Confined Water (MASHCON), 19-23 May 2019, Ostend, Belgium*, 2018.

[67] Radojčić, D., Simić, A., Momčilović, N., Motok, M., and Friedhoff, B. *Design of Contemporary Inland Waterway Vessels - The Case of the Danube River*. Springer International Publishing, 2021. ISBN 978-3-030-77324-3. doi: 10.1007/978-3-030-77325-0.

[68] Raven, H. C. A new correction procedure for shallow-water effects in ship speed trials. In *Proceedings of the 13th International Symposium on Practical Design of*

Ships and Other Floating Structures (PRADS'2016), 4-8 September 2016, Copenhagen, Denmark, 9 2016.

[69] Sagaut, P. *Large eddy simulation for incompressible flows : an introduction*. Springer-Verlag, Berlin / Heidelberg, 2006. ISBN 978-3-540-26344-9.

[70] Sano, M., Yasukawa, H., Okuda, A., and Hamaguchi, T. Maneuverability of a pusher and barge system under empty and full load conditions. *Journal of Marine Science and Technology (Japan)*, 23:464–482, 2017.

[71] Schevchuk, I. *Study of unsteady hydrodynamic effects in the ship stern area under shallow water conditions*. PhD thesis, Universität Rostock, Rostock, 2018.

[72] Schilchting, O. Schiffswiderstand auf beschränkter Wassertiefe. *STG Jahrbuch*, 35: 2–35, 1934.

[73] Schlichting, H. and Gersten, K. *Boundary-layer Theory*. Springer, Berlin / Heidelberg, 8th revised edition, 2000. ISBN 3-540-66270-7.

[74] Shur, M. L., Spalart, P. R., Strelets, M. K., and Travin, A. K. A hybrid RANS-LES approach with delayed-DES and wall-modelled LES capabilities. *International Journal of Heat and Fluid Flow*, 29:1638–1649, 12 2008. doi: 10.1016/J.IJHEATFLUIDFLOW.2008.07.001.

[75] Siemens. *Simcenter STAR-CCM+ User guide*. Siemens PLM Softwares, 2022.

[76] Smagorinsky, J. General circulation experiments with the primitive equations. *Monthly Weather Review*, 91:99–164, 3 1963. doi: 10.1175/1520-04932.

[77] Spalart, P. R., Jou, W.-H., Strelets, M., Allmaras, S. R., Liu, C., Liu, Z., and Sakell, L. Comments on the Feasibility of LES for Wings, and on a Hybrid RANS/LES Approach. In *Advances in DNS/LES: Direct numerical simulation and large eddy simulation, 1st International conference*, pages 137–148. Greyden Press, 1997. ISBN 1570743657.

[78] Spalart, P. R., Deck, S., Shur, M. L., Squires, K. D., Strelets, M. K., and Travin, A. A new version of detached-eddy simulation, resistant to ambiguous grid densities. *Theoretical and Computational Fluid Dynamics*, 20:181–195, 7 2006. doi: 10.1007/S00162-006-0015-0.

[79] Spalart, P. and Allmaras, S. A One-Equation Turbulence Model for Aerodynamic Flows. *La Recherche Aérospatiale*, 1:5–21, 01 1994. doi: 10.2514/6.1992-439.

[80] Statistisches Bundesamt. "Ein Viertel der Güterverkehrsleistung 2020 Entfallen auf Eisenbahn und binnenschifffahrt", 2022. https://www.destatis.de/DE/Presse/Pressemitteilungen/2022/04/PD22_148_463.html, Last accessed on

20/02/2023.

[81] Stern, F., Agdrup, K., Kim, S. Y., Hochbaum, A. C., pyo Rhee, K., Quadvlieg, F., Perdon, P., Hino, T., Broglia, R., and Gorski, J. Experience from SIMMAN 2008 — The First Workshop on Verification and Validation of Ship Maneuvering Simulation Methods. *Journal of Ship Research*, 55:135–147, 2011.

[82] Strelets, M. Detached eddy simulation of massively separated flows. In *39th Aerospace Sciences Meeting and Exhibit, RENO, NV, USA, 8 - 11 January, 2001*, 01 2001. doi: 10.2514/6.2001-879.

[83] Sutulo, S. and Guedes Soares, C. *Mathematical models for simulation of manoeuvring performance of ships*, pages 661–698. Taylor and Francis Group, London, 01 2011. ISBN 978-0-415-69808-5.

[84] Tezdogan, T., Incecik, A., and Turan, O. A numerical investigation of the squat and resistance of ships advancing through a canal using cfd. *Journal of Marine Science and Technology*, 21, 3 2016. doi: 10.1007/s00773-015-0334-1.

[85] The International Towing Tank Conference. 1978 ITTC performance prediction method. Recommended Procedures and Guidelines 7.5-02-03-01.4, 1999.

[86] The International Towing Tank Conference. Testing and extrapolation methods manoeuvrability. Recommended Procedures and Guidelines 7.5-02-06-01, 2005.

[87] Toxopeus, S. L., Simonsen, C. D., Guilmineau, E., Visonneau, M., Xing, T., and Stern, F. Investigation of water depth and basin wall effects on KVLCC2 in manoeuvring motion using viscous-flow calculations. *Journal of Marine Science and Technology*, 18:471–496, 12 2013. doi: 10.1007/s00773-013-0221-6.

[88] Tuck, E. O. Hydrodynamic problems of ships in restricted waters. *Annual Review of Fluid Mechanics*, 10:33–46, 1 1978. ISSN 0066-4189. doi: 10.1146/annurev.fl.10.010178.000341.

[89] Vantorre, M., Eloot, K., Delefortrie, G., Lataire, E., Candries, M., and Verwilligen, J. Maneuvering in shallow and confined water. In *The encyclopedia of Marine offshore engineering*, pages 1–17. 2017. ISBN 978-1-118-47635-2. doi: {10.1002/9781118476406.emoe006}.

[90] von Kármán, T. Mechanische Ähnlichkeit und Turbulenz. *Nachrichten von der Gesellschaft der Wissenschaften zu Göttingen, Fachgruppe 1 (Mathematik)*, 5:58–76, 1930.

[91] Wilcox, D. C. Reassessment of the scale-determining equation for advanced turbulence models. *AIAA Journal*, 26, 11 1988. doi: 10.2514/3.10041.

[92] Wolff, K. Ermittlung der Manövriereigenschaften fünf repräsentativer Schiffstypen mit Hilfe von CPMC-Modellversuchen. *Schriftenreihe Schiffbau*, 1981. doi: 10.15480/882.841.

[93] Xing, T., Bhushan, S., and Stern, F. Vortical and turbulent structures for KVLCC2 at drift angle 0, 12, and 30 degrees. *Ocean Engineering*, 55:23–43, 12 2012. doi: 10.1016/j.oceaneng.2012.07.026.

[94] Yao, J. *On the propeller effect when predicting hydrodynamic forces for manoeuvring using RANS simulations of captive model tests.* Phd thesis, Technische Universität Berlin, Berlin, 2015.

[95] Yasukawa, H. and Yoshimura, Y. Introduction of MMG standard method for ship maneuvering predictions. *Journal of Marine Science and Technology*, 20, 3 2015. ISSN 0948-4280. doi: 10.1007/s00773-014-0293-y.

[96] Yasuo, Y. and Hitoshi, S. Mathematical Model for the Manoeuvring Ship Motion in Shallow Water (3rd Report), Manoeuvrability of a Twin-propeller Twin-rudder ship. *The Journal of The Kansai Society of Naval Architects*, 211:115–126, 1988.

[97] Yoon, H., Simonsen, C. D., Benedetti, L., Longo, J., Toda, Y., and Stern, F. Benchmark CFD validation data for surface combatant 5415 in PMM maneuvers – Part I: Force/moment/motion measurements. *Ocean Engineering*, 109:705–734, 2015. doi: 10.1016/j.oceaneng.2015.04.087.

[98] Youssef, M., El Moctar, O., El Sheshtawy, H., Tödter, S., and Schellin, T. E. Passive flow control of vortex-induced vibrations of a low mass ratio circular cylinder oscillating in two degrees-of-freedom. *Ocean Engineering*, 254, 04 2022. doi: 10.1016/j.oceaneng.2022.111366.

[99] Yuba, D. T. G. and Tannuri, E. A. Analysis of Pusher-Barge System With Different Maneuvering and Propulsion Devices. In *Proceedings of the 32nd International Conference on Ocean, Offshore and Arctic Engineering, June 9-14 2013, Nantes, France*, 2013. doi: 10.1115/omae2013-10404.

[100] Zeng, Q., Hekkenberg, R., and Thill, C. A benchmark test of ship resistance in extremely shallow water. In *Progress in Maritime Technology and Engineering - Proceedings of the 4th International Conference on Maritime Technology and Engineering, MARTECH 2018*, 2018. doi: 10.1201/9780429505294-26.

[101] Zeng, Q., Hekkenberg, R., and Thill, C. On the viscous resistance of ships sailing in shallow water. *Ocean Engineering*, 190:106434, 2019. doi: 10.1016/j.oceaneng.2019.106434.

[102] Zentari, L., el Moctar, O., Lassen, J., Hallmann, R., and Schellin, T. E. Experimental and numerical investigation of shallow water effects on resistance and propulsion of coupled pusher-barge convoys. *Applied Ocean Research*, 121:103048, 2022. doi: 10.1016/j.apor.2022.103048.

[103] Zentari, L., Tödter, S., el Moctar, O., Neugebauer, J., and Schellin, T. E. Experimental and numerical investigation of the gap flow between a pusher and a barge in deep and shallow water. *Applied Ocean Research*, 132:103466, 2023. doi: 10.1016/j.apor.2023.103466.

[104] ZKR - Zentrale Komission für die Rheinschifffahrt. Jahresbericht 2020 der Zentralkommission für die Rheinschiffahrt. Report, Europäische Kommission, 2003.

DOI: 10.17185/duepublico/81430
URN: urn:nbn:de:hbz:465-20240126-145203-1